Multi-messenger and Multi-wavelength study of Galactic sources

AGNIBHA DE SARKAR[1]

Thesis Submitted for The Degree of

Doctor of Philosophy

to

Jawaharlal Nehru University[3],
New Delhi 110067, India

Thesis Supervisor:

NAYANTARA GUPTA[1]

Thesis Co-Supervisor:

DIEGO F. TORRES[2]

[1]RRI
Bengaluru 560080
Karnataka, India

[2]ICE-CSIC
08193 Cerdanyola del Vallès
Barcelona, Spain

[3]JNU
New Delhi 110067
Delhi, India

Submitted: June, 2023

Declaration

I, ***Agnibha De Sarkar*** (Enrolment No.: RRI/2017/001), declare that the work reported in this thesis titled '***Multi-messenger and Multi-wavelength study of Galactic sources***', is entirely original. This thesis is composed independently by me at ***Raman Research Institute (RRI)*** under the supervision of ***Prof. Nayantara Gupta*** and the co-supervision of ***Prof. Diego F. Torres***, and is the result of my own work unless otherwise stated. I further declare that the subject matter presented in this thesis has not previously formed the basis for the award of any degree, diploma, membership, associateship, fellowship or any other similar title of any university or institution. I also declare, this thesis has been checked through the plagiarism software OURIGINAL.

Signature of Supervisor	Signature of Co-Supervisor	Signature of Candidate
Prof. Nayantara Gupta	**Prof. Diego F. Torres**	**Agnibha De Sarkar**
Professor, RRI	Director, ICE-CSIC	Senior Research Fellow, RRI

Astronomy & Astrophysics Group
Raman Research Institute (RRI)
Bengaluru 560080, Karnataka, India

Date:
Place:

Certificate

This is to certify that the work contained in the thesis titled '***Multi-messenger and Multi-wavelength study of Galactic sources***', submitted by ***Agnibha De Sarkar*** (Enrolment No.: RRI/2017/001) to the Jawaharlal Nehru University for the award of the degree of ***Doctor of Philosophy (Ph.D.)*** in Physical Sciences, is the bonafide record of original research work carried out by the candidate from August 2017 — May 2023, under our guidance and supervision at Raman Research Institute (RRI), Bengaluru, India. The results embodied in the thesis have not been submitted to any other University or Institute for the award of any degree or diploma.

Signature of Director	Signature of Supervisor	Signature of Co-Supervisor
Prof. Tarun Souradeep	**Prof. Nayantara Gupta**	**Prof. Diego F. Torres**
Director, RRI	Professor, RRI	Director, ICE-CSIC

Astronomy & Astrophysics Group
Raman Research Institute (RRI)
Bengaluru 560080, Karnataka, India

Date:
Place:

Acknowledgements

First and foremost, I would like to express my sincere gratitude to my thesis supervisor Prof. Nayantara Gupta (Professor, Raman Research Institute, Bengaluru, India), for her continuous support, invaluable advice and patience during my Ph.D. journey. She supported me during my darkest times, without which, I would have left academia a long time ago. Her creative ingenuity and deep insight towards research have, in turn, helped me immensely in becoming an independent researcher. She has taught me to become fearless in the face of adversities, and to keep my spine straight at all times. I am what I am because of her, and I can not thank her enough for being my guiding light throughout all these years.

I am deeply grateful and would like to extend my sincere thanks to my co-supervisor, Prof. Diego F. Torres (Director, Institute of Space Sciences, Barcelona, Spain) for all his treasured support and tutelage. His immense knowledge and abundant experience have encouraged me in all the time of my academic research life. I want to thank him for letting me visit him at Barcelona, which had been a wonderful and productive experience. I am looking forward to my PostDoc journey ahead, under his supervision, in the near future.

I would also like to thank all of my collaborators, especially Dr. Pratik Majumdar (Associate Professor, Saha Institute of Nuclear Physics, Kolkata, India), Dr. Nirupam Roy (Associate Professor, Indian Institute of Science, Bengaluru, India), Prof. Karl M. Menten (Director, Max Planck Institute for Radio Astronomy, Bonn, Germany), Dr. Jonatan Martin (former PostDoc, Institute of Space Sciences, Barcelona, Spain), among many, for their invaluable suggestions and constructive criticism regarding the work that went to construct this thesis. I look forward to continue my collaboration with them, hopefully producing interesting scientific output along the way.

I have made many friends and acquaintances during my six years worth of stay in RRI, and I thank all of them for being a part of my life. I have learnt a great deal from all of them. I am especially thankful to my brothers, Maheswar da, my favorite partner-in-crime, and Tanuman, my first roommate and friend in RRI. I want to thank Saikat da for providing me with great insights and motivation about research, as well as life, in general. A special thanks to Sanhita for always being there for me from the start. Hemanth, Avik da, Rishab da, Sagar da, Subha da, Shovan, Bapan da, Sandeep, Anirban da, Dipak da, and all of the members of RRI Bongiyo Samiti, have left a deep impact in my day-to-day life, and I am thankful to all of them. I further wish all the best to all my juniors, Sovan, Soumen, Sayantan, Jasim, Puneet, and others for their academic journey ahead.

I acknowledge the support received from the Library Section, RRI, which maintains a vast volume of the digital repository, online resources, and a massive collection of print version books. I especially thank Manju KP and Nagaraj sir for their help. I also thank the computer section for providing facilities related to computation and networking, institute canteen facility and Vyalikaval hostel mess cooks for providing food, and administrative department of RRI for timely processing of official documents and other essential tasks. I am obliged for the fellowship grant, travel allowance, accommodation facility, etc., provided by RRI.

Finally, I want to thank my baba and maa, for their unwavering love and support through the uncertainties, accomplishments, doubts, joy, ups and downs of my academic journey. Without them, this day would not have been possible. A very special thanks to Ushali, for being a constant support, especially during the last three tough and tumultuous months of my Ph.D. years. I am looking forward to our life together in the future. I dedicate this thesis to them.

Agnibha De Sarkar

June, 2023

Contents

Synopsis

Introduction

Energetic particles, traditionally called cosmic rays (CRs), were discovered nearly a hundred years ago by V. Hess and W. Kohlhörster in the beginning of the twentieth century. Cosmic rays are mainly charged particles that contribute an energy density in the Galaxy of about 1 eV cm^{-3}. Their constituents are mainly protons (Hydrogen nuclei), with about 10% fraction of Helium nuclei, and smaller abundances of heavier elements. There are also electrons, positrons and antiprotons. The flux of all nuclear components present in the cosmic rays (all-particle spectrum) extends over energies from a few hundred MeV up to about 300 EeV. The spectral slope of differential spectrum is about $\sim$ -2.7, but there is a prominent steepening at around energy 3 PeV, which is called the Knee region, where the spectral slope changes from $\sim$ -2.7 to $\sim$ -3.1. Below the Knee region, it is conventionally assumed that the cosmic rays are produced by highly energetic Galactic sources, whereas beyond 3 EeV energy, the CR particles have to be extragalactic in origin. CRs with energy in between this range are considered to be a mixture of both Galactic and extragalactic origins.

In this thesis, we focus on the study of highly energetic Galactic sources, capable of accelerating CR particles to PeV energies. Various astrophysical objects observed in the Milky Way Galaxy, like Supernova Remnants (SNRs), Pulsar Wind Nebulae (PWNe), gamma-ray binaries, Giant Molecular Clouds (GMCs) are considered to be potential candidates for high energy CR acceleration. We study the origin, nature, spatial morphology and acceleration mechanism of these CR sources situated in our Galaxy. We also use various signatures of gamma-rays and neutrinos, as they can be important probes for studying the nature and emission of these Galactic CR sources. We carry out analytical and computational studies to understand the mechanism of high energy CR production in Galactic sources and subsequent propagation of CRs in the Galaxy. We also perform analysis of multi-wavelength (gamma-ray, X-ray) data observed from the sources, accumulated by different observatories (*Fermi*-Large Area Telescope (LAT), NuSTAR) to understand their spatial and spectral features.

Positron excess explained by Galactic Molecular Clouds

"Positron excess" is a spectral feature of the positron flux observed at Earth by Alpha Magnetic Spectrometer (AMS-02), in which the positron flux rises with energy, shows a peak near a few hundred GeV, and then subsequently falls off. We have explored the possibility of explaining the excess using the secondary positrons produced in nearby Galactic Molecular Clouds (GMCs). Apart from considering the catalogued GMCs observed in our Galaxy through large scale CO survey, we have also

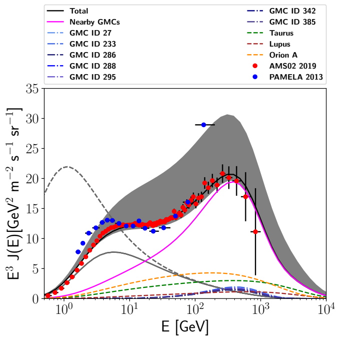

Figure 1 The model positron flux plotted against the observational data reported by AMS-02 and PAMELA (De Sarkar, A. et al. 2021, JHEAp).

considered 7 nearby (< 1 kpc) GMCs detected in optical/IR dust extinction measurements separately, and assumed that reacceleration due to magnetic turbulence is occuring inside these nearby GMCs. These GMCs are yet to be detected by *Fermi*-LAT due to their particular $M_5/d^2_{kpc} < 0.2$ value. We have shown that even if a small portion of cosmic ray protons injected in these GMCs are reaccelerated, then the resulting secondary positron flux will be able to explain the observed positron excess. Our self-consistent model also reproduces the observed proton, electron, antiproton spectra, as well as B/C, ^{10}Be/^{9}Be and $e^+/(e^+ + e^-)$ ratios. We also show that the $(e^+ + e^-)$ anisotropy of these nearby GMCs does not violate the *Fermi*-LAT upper limits.

Discovery of an accreting High Mass Gamma-Ray binary HESS J1828-099

HESS J1828-099 is a point-like, unidentified Galactic source, with no apparent association with any object detected at other wavelengths. We have investigated the nature and association of HESS J1828-099 with multi-wavelength observational data. A high mass X-Ray binary (HMXB), comprising of pulsar XTE J1829-098 and a companion star, has been observed earlier in the X-ray and infrared bands, which shows frequent outbursts and is primarily accreting. Through X-ray data analysis, we found a sub-dominant power law component depicting shock, the presence of which is typical in gamma-ray binaries. By analyzing 12 years of *Fermi*-LAT gamma-ray data, a GeV counterpart 4FGL J1830.2-1005 was also detected. Existing radio frequency surveys revealed a steep spectrum plausible radio counterpart. By fitting the multi-wavelength spectrum, we showed that HESS J1828-099, 4FGL J1830.2-1005 and the HMXB system have a common origin and HESS J1828-099 might be a first ever detected, accreting, high mass gamma-ray binary source.

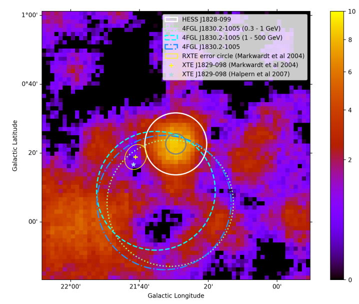

Figure 2 HESS J1828-099 source morphology (De Sarkar, A. et al. 2022, ApJL).

Hadronic origin of ultra high energy gamma-ray source LHAASO J1908+0621

We have studied Galactic ultra high energy gamma-ray source LHAASO J1908+0621, and explored the origin of gamma-ray emission from this source. We have explained the multi-TeV, very high energy gamma-ray emission observed from the direction of LHAASO

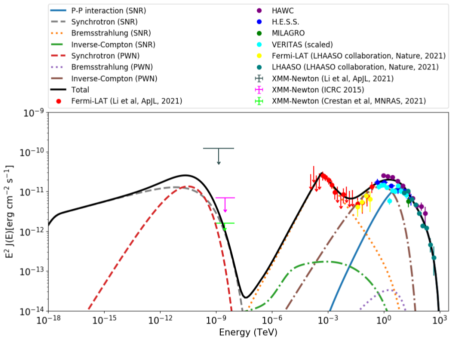

Figure 3 Multi-wavelength Spectral Energy Distribution of LHAASO J1908+0621 (De Sarkar, A. et al. 2022, ApJ).

J1908+0621, by the hadronic interaction between accelerated protons that escaped from the middle-aged radio SNR G40.5-0.5 shock front and cold protons present inside the dense molecular clouds, as well as the leptonic emission from the pulsar wind nebula (PWN) associated with the pulsar J1907+0602. Moreover, we have explained comparatively lower energy gamma-ray emission by considering the radiative cooling of the electrons that escaped from SNR G40.5-0.5. An IceCube hotspot of neutrino emission was found to be spatially associated with LHAASO J1908+0621. We have also showed that the second generation IceCube observatory will be able to detect neutrinos from this source, thus confirming the hadronic origin of sub-PeV gamma-ray emission observed from LHAASO J1908+0621.

Pulsar Wind Nebula interpretation of ultra high energy gamma-ray source LHAASO J2226+6057

We have explored the pulsar wind nebula interpretation of Galactic ultra high energy gamma-ray source LHAASO J2226+6057. By solving a time-energy-dependent diffusion-loss equation, we have performed a leptonic, time-dependent modeling of the pulsar wind nebula (PWN) associated with PSR J2229+6114. Particle injection, energy losses, and escape of particles were considered to balance the time-dependent lepton population. We have also included the dynamics of the PWN and the associated supernova remnant and their interaction via the reverse shock to study the reverberation phase of the system. We have explored the effects of considering different values of braking index and true age on the multi-wavelength (MWL) spectral energy distribution (SED) of LHAASO J2226+6057. We have χ^2-fitted the MWL SED of the LHAASO source and provided the best-fit PWN model parameters and their 1σ confidence intervals. We have also demonstrated the impact of reverberation on the MWL SED with increasing time. Additionally, we have discussed the resultant large radius and low magnetic field associated with the PWN as caveats of considering PWN as the primary source behind the observed emission from LHAASO J2226+6057.

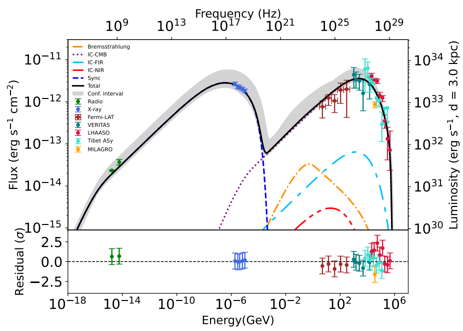

Figure 4 Multi-wavelength Spectral Energy Distribution of LHAASO J2226+6057 (De Sarkar, A. et al. 2022, A&A).

Summary & Outlook

In this thesis, we emphasize on the currently ongoing research topics in the field of high energy cosmic ray and gamma-ray astrophysics in the Galaxy, from both theoretical and observational perspectives. Although it has long been known that the Galactic sources can accelerate particles up to very high energies and subsequently contribute to the "Galactic CR sea", the exact nature and emission of these sources are yet to be properly understood. Since gamma-rays are not charged particles, they do not get deflected by the large scale Galactic magnetic field. Consequently, gamma-rays are excellent probes for CR acceleration and emission from Galactic sources. To that end, data obtained by current generation Imaging Atmospheric Cherenkov Telescopes such as MAGIC, H.E.S.S. etc., have proven to be of utmost importance to decipher the nature, acceleration and emission mechanism of various Galactic sources. Moreover, Large High Altitude Air Shower Observatory (LHAASO) has recently provided conclusive proof of the existence of sources that accelerate particles up to PeV energies, thus opening a new era of ultra high energy gamma-ray astronomy. The existence of PeVatrons indicates that particle acceleration in Galactic sources are far more complicated than previously perceived, and further observations and subsequent theoretical modeling are needed to properly understand the Galactic sources. Furthermore, more sensitive next generation gamma-ray observatories such as Cherenkov Telescope Array (CTA) and Southern Wide-field Gamma-ray Observatory (SWGO) will be able to accurately detect various Galactic sources, which will help us understand the nature and emission of Galactic sources with unprecedented detail. Similarly, next generation neutrino observatories such as IceCube-Gen2 and KM3NeT will also help understand the emission mechanism at play in a diverse class of Galactic sources.

Signature of Supervisor	Signature of Co-Supervisor	Signature of Candidate
Prof. Nayantara Gupta	**Prof. Diego F. Torres**	**Agnibha De Sarkar**
Professor, RRI	Director, ICE-CSIC	Senior Research Fellow, RRI

Astronomy & Astrophysics Group
Raman Research Institute (RRI)
Bengaluru 560080, Karnataka, India

List of Publications

1. **Agnibha De Sarkar**, Sayan Biswas, and Nayantara Gupta
   Positron excess from cosmic ray interactions in galactic molecular clouds[1]
   Journal of High Energy Astrophysics **29**, 1 (2021)
   arXiv.org identifier: arXiv:1911.12977 [astro-ph.HE]

2. **Agnibha De Sarkar**, Nirupam Roy, Pratik Majumdar, Nayantara Gupta, Andreas Brunthaler, Karl M. Menten, Sergio A. Dzib, Sac Nicté X. Medina, and Friedrich Wyrowski
   Possible TeV Gamma-Ray Binary Origin of HESS J1828-099[2]
   The Astrophysical Journal Letters **927**, L35 (2022)
   arXiv.org identifier: arXiv:2202.13376 [astro-ph.HE]

3. **Agnibha De Sarkar**, and Nayantara Gupta
   Exploring the Hadronic Origin of LHAASO J1908+0621[3]
   The Astrophysical Journal **934**, 118 (2022)
   arXiv.org identifier: arXiv:2205.01923 [astro-ph.HE]

4. **Agnibha De Sarkar**, Wei Zhang, Jonatan Martín, Diego F. Torres, Jian Li, and Xian Hou
   LHAASO J2226+6057 as a pulsar wind nebula[4]
   Astronomy & Astrophysics **668**, A23 (2022)
   arXiv.org identifier: arXiv:2209.13285 [astro-ph.HE]

Other publications (not included in the thesis):

1. **Agnibha De Sarkar**
   Supernova connection of unidentified ultra-high-energy gamma-ray source LHAASO J2108+5157
   Monthly Notices of the Royal Astronomical Society: Letters, Volume **521**, Issue 1, May 2023, Pages L5-L10
   arXiv.org identifier: arXiv:2301.13451 [astro-ph.HE]

2. **Agnibha De Sarkar**, Nayana A. J., Nirupam Roy, Soebur Razzaque, and G. C. Anupama
   Lepto-hadronic interpretation of 2021 RS Ophiuchi nova outburst
   The Astrophysical Journal **951**, 62 (2023)
   arXiv.org identifier: arXiv:2305.10735 [astro-ph.HE]

[1]Chapter 2 of the thesis is based on this paper.
[2]Chapter 3 of the thesis is based on this paper.
[3]Chapter 4 of the thesis is based on this paper.
[4]Chapter 5 of the thesis is based on this paper.

3. **Agnibha De Sarkar**, and Pratik Majumdar
   Dissecting the emission from LHAASO J0341+5258: implications for future multi-wavelength observations
   Astronomy & Astrophysics, DOI: 10.1051/0004-6361/202347258
   arXiv.org identifier: arXiv:2309.04729 [astro-ph.HE]

Conference Proceedings:

1. **Agnibha De Sarkar**, Sayan Biswas, and Nayantara Gupta
   Galactic molecular clouds as sources of secondary positrons
   Proceedings of the 37th International Cosmic Ray Conference (ICRC 2021)
   arXiv.org identifier: arXiv:2202.13333 [astro-ph.HE]

2. **Agnibha De Sarkar**, and Nayantara Gupta
   Supernova remnants as Galactic PeVatron candidates
   Advances in Astroparticle Physics and Cosmology (AAPCOS-2023)

Signature of Supervisor	Signature of Co-Supervisor	Signature of Candidate
Prof. Nayantara Gupta	**Prof. Diego F. Torres**	**Agnibha De Sarkar**
Professor, RRI	Director, ICE-CSIC	Senior Research Fellow, RRI

Astronomy & Astrophysics Group
Raman Research Institute (RRI)
Bengaluru 560080, Karnataka, India

List of Figures

List of Tables

1

Introduction

Ever since the discovery of radioactivity at the beginning of the twentieth century, the ionization of air-producing atmospheric current was attributed to the radiation from the decay of radioactive elements near the surface of the Earth. However, during the early 1900s, further measurements with the electroscope, a device that measures ionization produced by the radiation at different heights, indicated that ionizing current dropped at low altitudes while it kept on increasing as the electroscope was taken vertically upwards and away from the surface of the Earth. This increment of ionization with height was first established by Victor Hess in 1912 when he carried three electroscopes at an altitude of 5300 meters in his famous free balloon flight. The flight was taken during a near-total eclipse, thus effectively ruling out the Sun as the radiation source. The rising radiation with increasing altitude made Hess believe that this increasing ionization must be due to a source of radiation of highly penetrative power entering our atmosphere and not the radioactivity caused by the Earth. In 1913-1914, Hess's initial finding was confirmed by Werner Kolhörster by measuring the increasing ionization at an altitude of 9 km. Initially, it was believed to be a radiation of electromagnetic nature, specifically a highly penetrative form of gamma-rays [1, 2]; hence Robert Millikan first coined the term 'Cosmic rays.' But it was confirmed to be a flux of electrically charged particles from their deflection in the Earth's magnetic field. Victor Hess received the Nobel Prize in Physics in 1936 for his discovery. One can find more information on the history of cosmic rays in many books and reviews; for example, see [3–9].

Since the discovery of cosmic rays, this phenomenon has been studied extensively, and some characteristic properties of these highly energetic charged particles were assembled. Especially the energy spectrum, composition, and abundances of cosmic rays provide us with more clues regarding their origin. After getting accelerated from astrophysical accelerators, primary cosmic ray particles, which are composed of protons, alpha particles ($\sim$ 9 %), heavier nuclei ($<$ 1 %), leptons ($<$ 1 %), gamma rays and antimatter particles as well, propagate throughout the Galaxy, and reach us homogenously due to having undergone many interactions during their propagation. These charged cosmic ray particles also interfere with the Sun and the Earth's magnetic fields, modifying their spectra. Detecting these cosmic rays on the Earth's surface is of great interest, as they can tell a lot about our Galaxy, e.g., the structure and composition of matter, radiation, and magnetic field of our Galaxy, which can be inferred from the observed secondary-to-primary ratio. We can also study the interactions that occur while cosmic rays particles propagate in our Galaxy.

The primary cosmic ray all-particle spectrum is remarkably featureless, with little deviations from a constant power law,

$$\frac{dN(E)}{dE} \propto E^{-\gamma}, \tag{1.1}$$

across a large energy range. The observed flux of cosmic ray particles falls off rapidly as the energy increases. Particles with energy below 10^6 electronvolt (eV) mainly originate in the solar wind. The solar modulation dominates the observed cosmic ray spectrum until the energy range of 10 Giga-electronvolt (1 GeV $\approx 10^9$ eV). The rate of particles arriving with energy $\geq 10^6$ eV is about 10^4 per square meter per second. In the energy range above 1 Tera-electronvolt (1 TeV $\approx 10^{12}$ eV), the rate comes down to 1 particle per square meter per second. There is a small change in slope at 3×10^{15} eV, from $E^{-2.7}$ to $E^{-3.1}$, which is also known as the "knee" of the cosmic ray spectrum. Beyond the knee, the rate decreases to 1 particle per square meter per year. The origin of the knee is not quite understood as to why the spectrum experiences an abrupt change in slope at that point. There is also another spectral change at a point called "ankle" of the spectrum around 10^{19} eV, where the slope changes to -2.8. The rate of arrival of particles decreases even further to 1 particle per square kilometer per year. At a threshold energy of 5×10^{19} eV, a cutoff in the energy spectrum is expected due to a theoretical upper limit, known as the GZK limit, of the cosmic rays from distant sources [10, 11]. This indicates that extragalactic cosmic rays with energies greater than this threshold should never be observed on Earth. Finally, due to the featureless nature of the cosmic ray energy spectrum, the same mechanism below the knee is expected to govern cosmic ray acceleration and propagation, and the same or another one works above the knee. The differential cosmic ray flux is shown in the left panel of Figure 1.1.

The chemical abundances of cosmic rays also provide important clues to their origin and propagation processes from their sources to the Earth. Figure 1.1 right panel compares the relative abundances of cosmic rays with that of the elements in the solar system. Both cosmic rays and the solar system shows similarities in terms of the odd-even effect, with the more tightly bound, even Z nuclei being more abundant, which could be explained by the fact that cosmic ray particles must have been accelerated from the material of quiet similar chemical composition to the Solar System abundances. Nevertheless, the two compositions show two differences. First, nuclei with $Z > 1$ are much more abundant relative to protons in the cosmic rays compared to that found in the solar system. This can be chalked up due to the fact that hydrogen is relatively hard to ionize for injection into the acceleration process, or it could reflect a genuine difference in composition at the source. The second difference is that two groups of elements Li, Be, B, and Sc, Ti, V, Cr, and Mn, are many orders of magnitude more abundant in the cosmic ray than that found in the solar system, which can be a result of spallation of the more abundant primary cosmic ray nuclei, especially carbon and oxygen, and of iron. Hence from a knowledge

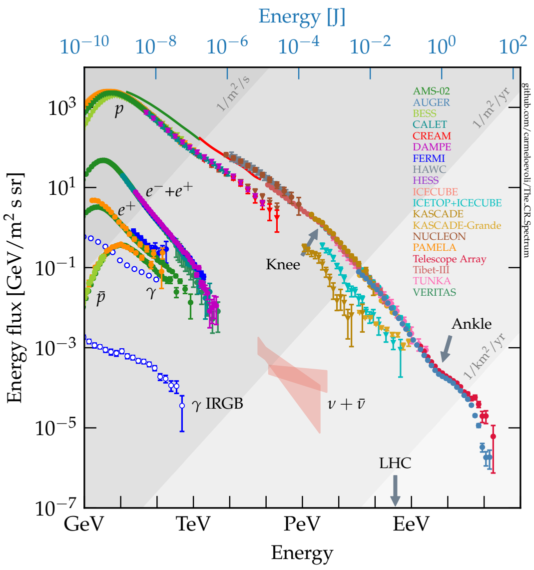

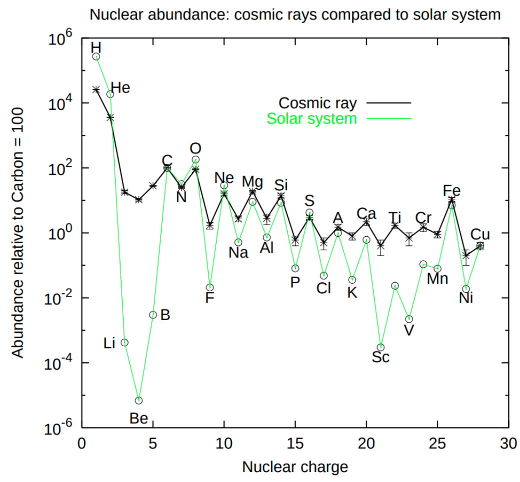

Figure 1.1 *Left Panel:* Spectra of various cosmic ray components [12], *Right Panel:* Relative chemical abundances of cosmic rays and of the solar system, normalized to Carbon [13].

of cross-sections for spallation, the amount of matter traversed by cosmic rays between production and observation can be estimated.

In order to reproduce the observed abundances of stable nuclei, the cosmic rays should have traversed 10 g cm^{-2} amount of material, also known as grammage [14]. Assuming the number density of interstellar medium to be $n_{ISM} \sim 1$ cm^{-3}, the total distance traversed by cosmic rays particles would be,

$$L = \frac{\text{grammage}}{n_{\text{ISM}} m_p} \approx 10^4 \text{ kpc}, \tag{1.2}$$

which is larger than the size of the Galaxy. This indicates the cosmic ray particles must circulate within the Galaxy for a long time ($\sim 10^7$ years) before escaping the Galaxy. This can be explained by the fact the cosmic rays, being charged particles, diffuse through the Galaxy due to the turbulent magnetic field that threads through the entire Galaxy, which has a value in μG, as obtained from the secondary-to-primary ratio. So in the Galaxy, the Larmor radius of the cosmic ray particles (r_L) in the magnetic field can be given by,

$$r_L = \frac{E}{ZeB} \sim 110 \text{ kpc } Z^{-1} \left(\frac{E}{10^5 \text{ PeV}}\right)\left(\frac{B}{\mu\text{G}}\right)^{-1}. \tag{1.3}$$

Now, the Larmor radius must be smaller than the Galactic size for the cosmic rays particles to be confined within the Galaxy. The value of r_L in Galactic magnetic fields is comparable to the Galactic disk thickness only if the maximum energy of the cosmic ray particles is almost equal to 10^{15} eV, which also coincides with the energy at which the "knee" of the cosmic ray spectrum is observed. This is why it is generally believed that Galactic sources might be responsible for the observed spectrum below the "knee", whereas extragalactic sources might be responsible for the spectrum above the "knee". In this thesis, we have addressed different theoretical and observational aspects of the Galactic sources situated within the Milky Way Galaxy.

In 1934, Fritz Zwicky showed that stars with enough mass collapse at the end of their lives, producing an explosion of cosmic rays while leaving behind compact objects such as neutron stars, white dwarfs, or even black holes. It has been argued that the energy released by the supernovae explosion ($\sim 10^{51}$ ergs, assuming a rate of explosions of 1/30 years^{-1}) is about ten times larger than the energy measured for cosmic rays, which is consistent with the efficiency we expect for cosmic ray acceleration. Later in the 1950s, synchrotron emission was also detected from cosmic ray electrons, consequently shifting the paradigm from supernovae (SNe) to supernova remnants (SNRs) [15, 16]. Currently, SNRs are widely accepted to be the acceleration sites of cosmic rays, and this is also supported by recent gamma-ray observations [17], produced from cosmic ray interaction from SNRs associated with molecular clouds [15, 16], e.g., the case of gamma-ray detection from Tycho SNR [18–23]. Nevertheless, no decisive proof has been confirmed yet.

Pulsars are also a probable source of cosmic ray acceleration [24, 25]. They are extreme, compact objects which show high spin down and large magnetic fields associated with them. Their spin-down is caused by dipolar emission. As an effect, a fraction of this rotational energy loss can be transferred into energy required to accelerate particles. Consequently, pulsars and their nebulae are able to accelerate particles up to energy corresponding to the "knee", although they are unable to considerably accelerate heavy nuclei to very high energies. So these objects essentially play an important role in explaining the observed lepton flux [26–29]. Additionally, there are convincing pieces of evidence in which young massive stellar clusters (OB associations, and generally SN occuring in superbubbles) [30, 31], X-ray binaries that can accelerate particles up to very high energies, producing gamma rays (also known as gamma-ray binaries) [32], are also found to be efficient particle accelerators observed in the Galaxy.

After being accelerated in Galactic sources, the cosmic rays propagate in the Galaxy before reaching us while also producing secondary particles through various interactions. The propagation and interaction of primary cosmic rays can be realized by the diffusion-transport equation (discussed in later sections). The Galactic magnetic field plays an important role in cosmic ray propagation. There are many ways of constraining the intensity and orientation of the magnetic field, e.g., Zeeman splitting observations [33], starlight polarisation studies [34–36], and most importantly, Faraday rotation measurements [37, 38]. The Galactic magnetic field can be divided into two different components: large-scale, regular magnetic field and small-scale, turbulent magnetic field. The accelerated charged cosmic ray particles diffuse owing to the turbulent magnetic field threading the Galaxy. Apart from this, the material of ISM also plays a crucial role in the interaction and subsequent production of secondary cosmic ray particles. During propagation, primary cosmic ray particles interact with different components of ISM gas, which are 1) atomic Hydrogen (HI), 2) ionized hydrogen (HII), and 3) molecular hydrogen (H_2). HI can be detected by the observation of Lyman α and 21-cm line [39–42]. Information about HII can be obtained by radio signals from pulsars and other Galactic and extragalactic compact objects [43–46]. Finally, the H_2 distribution can be indirectly studied from the radio observations of CO molecules as CO molecules show a rotational transition from J = 1 to J = 0 at 2.6 mm radio wavelength [43, 47–51]. Primary cosmic rays interact with ISM gas distribution, producing secondary particles, as well as gamma-rays and neutrinos through various interaction mechanisms (discussed in later sections). Due to this interlink, the study of gamma-ray gives us an indirect glimpse at the large and small-scale features and distribution of Galactic cosmic rays, in general, in the Galaxy. Not only that, the study of Galactic sources at different wavelengths, such as gamma-ray, X-ray, radio, etc., provides us with great insight regarding the nature and emission of the said sources. Apart from the study of cosmic rays and photons, astrophysical messengers such as neutrinos can also indicate the signature of the emission occuring in certain Galactic cosmic ray accelerators. This fact clearly indicates that a multi-messenger and multi-wavelength study of different Galactic sources is important to unravel the exact properties, structure, and radiation of the sources, as well as the study of Galactic cosmic ray distribution or "Galactic Cosmic Ray Sea" in general. To that end, in this thesis, we have provided a study of the nature and emission of the Galactic sources, as well as the study of different features of the large-scale Galactic cosmic ray distribution in a multi-messenger and multi-wavelength context.

In the following sections of this chapter, we discuss multiple facets of high energy Galactic cosmic ray astrophysics, in general, as well as different aspects of multi-messenger and multi-wavelength study associated with it. In section 1.1, we provide a brief overview of cosmic ray acceleration, propagation, and subsequent interaction processes. In section 1.2, we account for the ongoing multi-messenger and multi-wavelength experiments and briefly discuss the observatories responsible for detecting these astrophysical messengers. In this section, we also focus on the observatories responsible for the detection of photons in multiple wavelengths and briefly discuss the detection techniques employed in those cases. In section 1.3, we provide a discussion regarding various Galactic sources that have been particularly studied in this thesis. Finally, in section 1.4, we illustrate the motivation and the structure of this thesis.

1.1 Acceleration, propagation and interaction

In this section, we discuss the processes typically used to explain the acceleration of primary cosmic ray particles in various Galactic sources. After the acceleration, the cosmic ray particles escape from the acceleration site and interact with different components, e.g., interstellar gas, magnetic field, etc, while propagating. So, we also discuss the propagation and subsequent interaction mechanisms required to produce the radiation of gamma-rays, neutrinos, etc., that have been employed in studies reported in this thesis.

1.1.1 Acceleration of cosmic rays

In the 1950s, Enrico Fermi put out the idea of an acceleration process that explains the power law spectrum via the interaction of moving clouds [52, 53]. These randomly moving clouds have magnetic fields embedded in them. As cosmic rays scatter in the clouds, they can exchange energy and momentum. Since the cosmic ray particle scatters via the Lorentz force associated with the magnetic field inside the cloud, the energy of the said particle does not change in the cloud's reference frame. Assuming E_0 to be the initial energy of the particle in the laboratory frame, μ_1 to be the cosine of the angle θ_1 between the particle and direction of motion of the cloud at the point of approach, and β (= v/c) to be the speed of the cloud in units of speed of light, then the energy of the particle in cloud's frame before the scattering, can be calculated with a Lorentz transformation as $E' = \gamma E_0(1 - \beta \mu_1)$.

After the scattering, the particle energy still remains the same in the cloud's frame, and the final energy in the laboratory frame can be given by $E'' = \gamma E'(1 + \beta\mu_2')$, where μ_2' is the cosine of the exit angle θ_2. So, the fraction of the change in energy can be calculated by,

$$\frac{E'' - E_0}{E_0} = \frac{1 - \beta\mu_1 + \beta\mu_2' - \beta^2\mu_1\mu_2'}{1 - \beta^2} - 1. \tag{1.4}$$

For non-relativistic clouds ($\beta \ll 1$), and assuming the exit angle θ_2 is random ($<\mu_2'> = 0$), then equation 1.4 reduces to,

$$\left\langle \frac{E'' - E_0}{E_0} \right\rangle \approx \frac{1 - \beta \langle \mu_1 \rangle}{1 - \beta^2} - 1. \tag{1.5}$$

Since head-on collisions are more frequent than tail-in ones,i.e., $-1 < \langle \mu_1 \rangle < 0$, this results in an energy gain. After calculating $<\mu_1>$, by averaging over the scattering angle, assuming the probability distribution of the angles is proportional to the relative speed, the previous equation yields,

$$\Xi \equiv \left\langle \frac{E'' - E_0}{E_0} \right\rangle_{\mu_1} \sim \frac{4}{3}\beta^2. \tag{1.6}$$

After repeated encounters, the average particle energy after the n-th collision is given by $E_n = E_{n-1} + \Xi E_{n-1}$, where E_{n-1} is the average energy after the (n-1)-th collision. If E_0 is the initial particle energy, then the energy after the n-th collision will be,

$$E_n = (1 + \Xi)^n E_0. \tag{1.7}$$

Hence, the number of encounters needed for the particle to reach an energy E is given by,

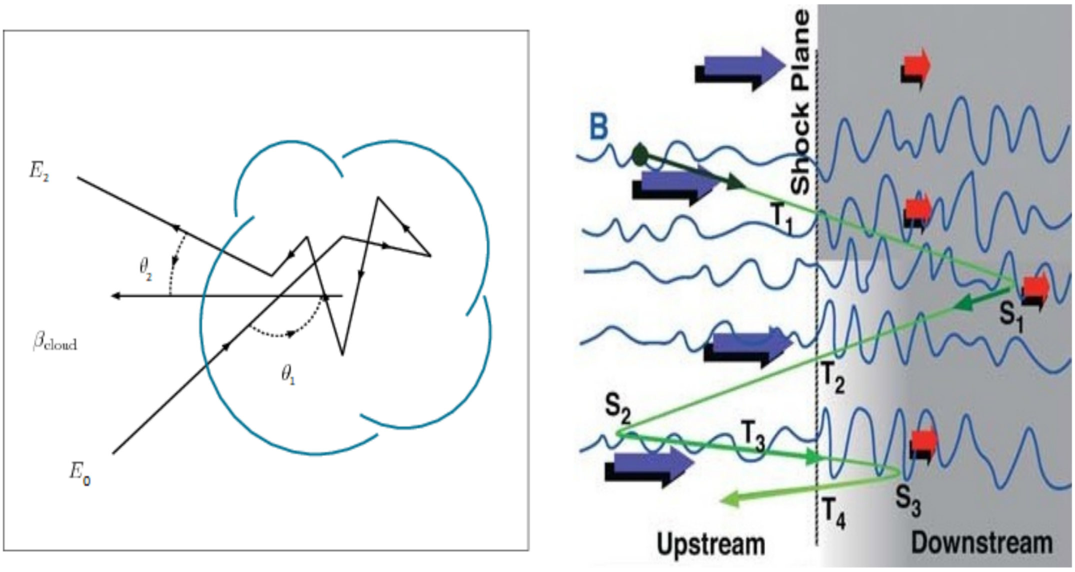

Figure 1.2 *Left Panel:* Magnetic clouds accelerating charged particles, according to Fermi 2-nd order mechanism [58], *Right Panel:* Particle acceleration in the shock wave, according to Fermi 1-st order mechanism, taken from [59].

$$n = \frac{log\left(\frac{E}{E_0}\right)}{log(1+\Xi)}. \tag{1.8}$$

If P_{esc} is the probability for the particle to leave the acceleration site after each scattering, then the integral energy spectrum, i.e., the fraction of particles with energy E > E_n, is given by,

$$f(E > E_n) \propto \sum_{m=n}^{\infty}(1-P_{esc})^m = \frac{(1-P_{esc})^n}{P_{esc}}. \tag{1.9}$$

Then, using equation 1.8, we get that,

$$(1-P_{esc})^n = \left(\frac{E_n}{E_0}\right)^{-\gamma}, \tag{1.10}$$

with γ = - $\frac{log(1-P_{esc})}{log(1+\Xi)} \approx \frac{P_{esc}}{\Xi}$, in the limit of P_{esc}, $\Xi \ll 1$.

Although this mechanism, also known as "*Fermi 2-nd order acceleration*", explains the power law in the energy spectrum, the assumption of the clouds being non-relativistic ($\beta \ll 1$) and small in dimensions (~ 1 pc) leads to an inefficient acceleration mechanism to explain the observed cosmic ray spectrum [54–57].

Next, another iterative method was pointed out by Fermi, which is effective in the case of SNRs since it is based on the idea of a shock wave traversing in a hydromagnetic medium such as the one produced by the SNRs. A shock wave is defined as a discontinuity in the ambient medium that is propagating out in the smooth medium. A sketch of this phenomenon has been shown in the right panel of Figure 1.2. See [60] for an extensive review.

From an external viewpoint, a shock would be seen to be moving with a speed v_{sh} towards the undisturbed upstream region. Due to the shock, the downstream region would have a density ρ_d, and the upstream region would have a density ρ_u. This essentially implies a misalliance in the velocity of the two regions, v_d and v_u. Now, since the continuity equation, $\frac{\partial \rho}{\partial t} + \vec{\nabla}(\rho \vec{v}) = 0$, holds true across the shock front, integrating this equation from one side of the shock to the other, we get,

$$v_d \rho_d = v_u \rho_u, \tag{1.11}$$

which leads to a compression ratio of,

$$R = \frac{\rho_d}{\rho_u} = \frac{v_u}{v_d} = \frac{(\tilde{\gamma}+1)M_u^2}{(\tilde{\gamma}-1)M_u^2+2}, \tag{1.12}$$

where $\tilde{\gamma}$ (= 5/3 for monoatomic gases) is the adiabatic index, and M_u (= v_u/c_s) is Mach number of the upstream region, and c_s is the velocity of the sound in the medium. In the strong shock limit (M » 1), and considering monoatomic gas in the shock environment, the compression ratio becomes R = 4.

In the frame of the shock, the charged particles oscillate back and forth from downstream to upstream regions due to magnetic interactions with plasma instabilities generated due to the movement of the shock through the ambient hydromagnetic medium, acting as a "magnetic mirror". Also, in this frame, v_u = - v_{sh}, and v_d = v_u/R. So, in this frame, the energy of the particle propagating towards the downstream region will be E′ = γE(1 + $\beta\mu$), where μ is defined as the cosine of the pitch angle (angle between incidence direction and shock front direction), and $\beta = \frac{v_u - v_d}{c}$, where c is the speed of light.

When a particle bounces back to the upstream region from the downstream region, the energy remains conserved in the downstream reference frame, as particle energy does not get changed by magnetic interactions. But to an external observer, it will come back to the upstream region with an energy E″ = E′γ(1 - β μ'), as E′ is conserved in the interaction. So, the fractional energy is given by,

$$\frac{\Delta E}{E} = \gamma^2(1+\mu\beta)(1-\mu'\beta) - 1. \tag{1.13}$$

Averaging equation 1.13 over μ and μ', taking into account that the probability of a particle entering (or exiting) with a given direction is the probability of crossing a wall,

$$\Xi = \left\langle \frac{\Delta E}{E} \right\rangle_{\mu,\mu'} = \frac{4\beta}{3},\ for\ \beta << 1. \tag{1.14}$$

Next, we calculate the flux of cosmic ray particles moving upstream from the downstream of the shock as $F_- = \int_{down \to up} d\Omega \frac{nc}{4\pi}\mu = \int_0^{2\pi} d\phi \int_0^1 d\mu \frac{nc}{4\pi}\mu = \frac{nc}{4}$, where n is the particle number density near the shock, and considering particles to be relativistic, in order to be able to cross the shock front. Since no particles escape from the upstream shock, the shock conservation of cosmic ray flux dictates that cosmic ray particles entering the shock from downstream (F_+) = particle flux escaping into the far downstream and not returning (F_∞) + particle flux returning to the upstream shock (F_-). Then, the escape probability can be given by $P_{esc} = \frac{F_-}{F_+} = \frac{F_-}{F_\infty + F_-} = 1 - P_{cycle}$. The escaping flux can be given by $F_\infty \sim n v_d$, assuming cosmic ray distribution downstream of the shock to be isotropic. So, the probability of completing a cycle of acceleration is given by,

$$P_{cycle} = 1 - P_{esc} = 4\frac{v_d}{c}. \tag{1.15}$$

Essentially, a particle will gain a fraction of energy Ξ in each cycle, transferred from the energy of the shock with a probability P_{cycle} of repeating the cycle. So after n number of cycles, a particle having an initial energy of E_0 will gain an energy of $E_n = (1 + \Xi)^n E_0$. From equation 1.8, we obtain,

$$(P_{cycle})^n = (1 - P_{esc})^{\frac{log(\frac{E_n}{E_0})}{log(1+\Xi)}} = \left(\frac{E_n}{E_0}\right)^{-\gamma}, \tag{1.16}$$

with γ = - $\frac{log(1-P_{esc})}{log(1+\Xi)} \approx \frac{P_{esc}}{\Xi}$ in the limit of P_{esc}, Ξ « 1.

This indicates that the differential flux with respect to the energy ($\frac{df(E>E_n)}{dE}$) of accelerated particles according to this process, has the form of Q(E) ∝ $E^{-\gamma-1} = E^{\alpha}$, which reproduces power law behavior of the observed cosmic ray spectrum. The exponent can be calculated to be $\alpha = \frac{P_{esc}}{\Xi} + 1 = \frac{\frac{4v_d}{c}}{\frac{4(v_u - v_d)}{3c}} + 1 = \frac{3}{R-1} + 1 = 2$, in the strong shock limit (R = 4). α can be larger, not considering the strong shock limit, as observed in the cases of old SNRs or cosmic ray reacceleration during propagation [61]. This acceleration process, also known as *"Fermi 1-st order acceleration"*, is roughly able to reproduce the shape of the observed spectra. However, this process faces problems in explaining the maximum energy achievable during the expansion of SNRs in its Sedov-Taylor phase [62–64].

Finally, we calculate the efficiency of this process in accelerating particles. The acceleration rate can be calculated as,

$$\frac{dE}{dt} = \frac{\Delta E}{\tau_{cycle}}, \tag{1.17}$$

where τ_{cycle} is the time required to complete a cycle of acceleration. We assume that a particle needs a time t_d to meet back the shock front while traveling a distance l_d using a diffusive motion, with a diffusion coefficient D, from the downstream region to the upstream region. This can be related by the equation $l_d \sim \sqrt{Dt_d}$. At the same time, the shock has also traveled the same distance of $l_d = v_{sh} t_d$. So, the diffusion time can be taken as an order of magnitude estimate of τ_{cycle} and can be written as $\tau_{cycle} \sim t_d \sim D / v_{sh}^2$. This means that the more energetic the particle, the more time it will take to complete an acceleration cycle. Also, taking the diffusion length l_d to be the order of the particle's gyroradius r_g, the diffusion coefficient must be $D \sim \frac{r_g c}{3}$. The gyroradius can be written as $r_g = \frac{p}{ZeB} \approx \frac{E}{ZeBc}$, with p being the momentum perpendicular to the magnetic field B, and Ze being the particle charge. From here, we get,

$$\frac{dE}{dt} \sim \frac{\Xi E v_{sh}^2}{\frac{r_g c}{3}} = \frac{3\Xi E v_{sh}^2}{\frac{E}{ZeB}} = 4\beta v_{sh}^2 ZeB. \tag{1.18}$$

Assuming the maximum timescale for a cycle to be the same as that of the typical timescale for the SNR Sedov-Taylor phase, maximum energy is calculated as $E_{max} = \frac{dE}{dt} t_{ST}$. We find that $E_{max} \sim Z\left(\frac{B}{3\mu G}\right) 6\times10^{13}$ eV, assuming $v_{sh} \sim 3\times10^{19}$ cm/s, $t_{ST} \sim 10^3$ years, and $\beta \sim 10^{-2}$. Using the same relation, the maximum energy achieved by the iron nuclei (Z = 26) will be $E_{max} \sim 1.6\times10^{15}$ eV, which is close to the energy corresponding to the "knee". This means that this acceleration process is able to explain the cosmic ray spectra below "knee" energy, although this estimation is pretty optimistic [65], and further sophisticated investigations found this estimate to be one order lower [66–68]. This also indicates the break at the "knee" is due to a change in acceleration mechanism, corresponding to different sources. However, the modern theory of *Diffusive Shock Acceleration* [69–72] suggests that acceleration efficiency of SNRs can change depending on the magnetic field orientation [73, 74], and the magnetic field, which experiences amplification [75–77]. [78] provides a review on this topic.

1.1.2 Propagation of cosmic rays

The cosmic ray propagation in Galaxy can be considered a diffusive transport process as a result of collisionless interactions with plasma waves generated in the Galactic medium. A complete picture of this propagation and interaction requires the knowledge of source distribution, interstellar radiation field, gas density distribution, regular and turbulent magnetic field, spallation and inelastic cross sections, as well as boundary conditions for all of the cosmic ray species considered. A coupled diffusive-transport equation involving all of the cosmic ray species is used to describe this propagation, which should also explain diffusion, and convection by the Galactic wind, energy losses and reacceleration process, as well as collisions with interstellar gas, and the decay of radioactive isotopes.

From the description stated above, the full diffusion-transport equation for any given cosmic ray species i, can be written as,

$$\begin{aligned}\frac{\partial N_i}{\partial t} + \vec{\nabla}.(\vec{J}_i - \vec{v}_\omega N_i) + \frac{\partial}{\partial p}\left[p^2 D_{pp}\frac{\partial}{\partial p}\left(\frac{N_i}{p^2}\right)\right] &= Q_i + \frac{\partial}{\partial p}\left[\dot{p}N_i - \frac{p}{3}\left(\vec{\nabla}.\vec{v}_\omega N_i\right)\right] - \frac{N_i}{\tau_i^f} \\ &+ \sum_j \Gamma^s_{j\to i}(N_j) - \frac{N_i}{\tau_i^r} + \sum_j \frac{N_j}{\tau^r_{j\to i}},\end{aligned} \tag{1.19}$$

where the first term of the L.H.S. represents the time evolution of N_i, the number density of particles per unit momentum. In the second term of the L.H.S., flux $\vec{J}_i$ contains the information of the spatial diffusion obtained from Fick's law, i.e., $\vec{J}_i$ = -D_{ke} $\vec{\nabla} N_i$, where k and e correspond to the spatial components of the diffusion tensor, and $\vec{v}_\omega$ is the advection speed accounting for convection, which is important in lower energies, and also comparable with the kinetic energy of the Galactic wind. The third term of the L.H.S. corresponds to the diffusion in the momentum space (also important in the lower energies). The first term of the R.H.S. $Q_i \equiv Q(E, \vec{x}, t)$ represents the energy spectrum and spatial distribution of cosmic ray sources as a function of energy, position, and time. The second term of the R.H.S. corresponds to the momentum or energy losses. The final four terms in R.H.S. of the equation represent the spallation and decay of the cosmic ray particles during propagation. The subscript i indicates the primary cosmic ray species, whereas the subscript j represents other cosmic ray species produced as a result of these processes. Γ^s can be written for any species j and i using the relation $\Gamma^s_{j\rightarrow i} = \beta_j c n_H \sigma_{j\rightarrow i} N_j$, where n_H is the ISM density, β_jc is the velocity of species j, and finally, $\sigma_{j\rightarrow i}$ represents the interaction cross-section for the production of species i from species j. As the exact solution of the equation 1.19 is difficult to calculate analytically, approximate solutions can only be calculated under certain assumptions. Leaky box model [79–82], nested leaky box model [83], and weighted slab model [84–87] are some of the analytical frameworks explored in solving the simplified version of equation 1.19. However, we employ more elaborative numerical methods to solve the full diffusion-transport equation for the study reported in this thesis.

1.1.3 Interaction of cosmic rays

The hadrons accelerated in Galactic accelerators interact with the ambient matter and produce gamma-ray and neutrinos through the decay of neutral and charged pions. The accelerated leptons can also produce gamma-ray in GeV energies or above by inverse Compton and Bremsstrahlung processes. These high-energy leptons can also interact with the ambient magnetic field and produce photons having a wavelength corresponding to radio to X-ray. The newly produced photons may play an important role in the inverse Compton process. In this subsection, we provide a brief discussion of these radiation mechanisms.

Pion decay process

Inelastic *p-p* interactions between high energy protons and cold protons in the ambient matter lead to the production of π^0 and η mesons, which subsequently decay and produce high energy gamma-rays, see [88] for discussion and further references. [89] gives parametrized equations of the final gamma-ray/neutrino spectrum based on the Monte Carlo simulations of inelastic *p-p* interaction. For a proton spectrum $\frac{dN_p}{dE_p}$, the gamma-ray/neutrino produced per unit time $\frac{dN_{\gamma/\nu}}{dE_{\gamma/\nu}dt}$ can be calculated using,

$$\frac{dN_{\gamma/\nu}}{dE_{\gamma/\nu}dt} = cn_H \int_{E_\gamma/E_\nu}^{\infty} \sigma_{inel}(E_p)\frac{dN_p}{dE_p}F_{\gamma/\nu}\left(\frac{E_{\gamma/\nu}}{E_p}, E_p\right)\frac{dE_p}{E_p}, \tag{1.20}$$

where c is the speed of light, n_H is the ambient matter number density (dominantly proton), $\sigma_{inel}(E_p)$ is the inelastic *p*-*p* interaction cross-section, and $F_{\gamma/\nu}\left(\frac{E_{\gamma/\nu}}{E_p}, E_p\right)$ corresponds to the gamma-ray/neutrino number produced per unit interval of $\frac{E_{\gamma/\nu}}{E_p}$ per interaction of a proton of energy E_p with the ambient matter. For gamma-ray energies $E_\gamma \geq 1$ GeV, the parametrized form of $F_\gamma(x, E_p)$ (where, $x = \frac{E_\gamma}{E_p}$) is given by equations (58) to (61) of [89], whereas the inelastic cross section is given by equation (73) of [89]. In even lower energies, the "δ-functional approximation" for the pion production is considered [89], whereas an appropriate form of $\sigma_{inel}(E_p)$, given by equation (79) of [89], is taken into account. In case of neutrinos, the function $F_\nu(x, E_p)$ (where, $x = \frac{E_\nu}{E_p}$) explains the spectra of muonic neutrinos, $\nu_\mu^{(1)}$ and $\nu_\mu^{(2)}$, which get produced from the decays of charged pions ($\pi \rightarrow \mu\nu_\mu$) and muons ($\mu \rightarrow e\nu_\mu\nu_e$) respectively, and its parametrized form is given by the equation 62 - 69 of [89]. Equation 1.20 is used to calculate the total muonic neutrino flux, similar to gamma rays. [90] also reports updated parametrized equations for inelastic *p*-*p* interaction, which also have been used in work reported in this thesis.

Synchrotron process

An electron of energy $\gamma m_e c^2$ with pitch angle θ in a magnetic field B produces synchrotron photons with energy spectrum [91],

$$L_\nu^{sync} = \left(\frac{dE}{d\nu dt}\right)_{sync} = \frac{\sqrt{3}e^3 B sin\theta}{m_e c^2}\frac{\nu}{\nu_c}\int_{\frac{\nu}{\nu_c}}^{\infty} K_{5/3}(x)dx, \tag{1.21}$$

where e is the charge of the electron, and $\nu_c = \frac{3e\gamma^2}{4\pi m_e c}$ B $\sin\theta$ is the characteristic frequency of synchrotron radiation, and $K_{5/3}(x)$ is the modified Bessel function of order 5/3. Averaging over the pitch angle ($<\sin\theta> = \sqrt{2/3}$), we find synchrotron energy spectrum produced by electrons with an energy spectrum $\frac{dN_e}{d\gamma}$ to be,

$$(L_\nu^{sync})_{total} = \int_1^{\infty} d\gamma \frac{dN_e}{d\gamma_e} L_\nu^{sync}. \tag{1.22}$$

The magnetic field of the considered sources dictates the total observed synchrotron radiation produced in the source region, which can be observed in radio to X-ray wavelengths.

Inverse Compton Process

High-energy electrons transfer their energy to background low-energy photons through scattering, thus producing high-energy photons. If an electron of energy $\gamma m_e c^2$ takes part in this inverse Compton (IC) scattering, then high energy photons get produced with energy spectrum [91],

$$L_{\nu}^{IC} = \left(\frac{dE}{d\nu dt}\right)_{IC} = \frac{3}{4}\frac{\sigma_T c}{\gamma^2}h^2\nu\int_{\frac{h\nu}{4\gamma^2}}^{h\nu} d\epsilon \frac{n_b(\epsilon)}{\epsilon} f_{IC}(\epsilon,\nu,\gamma), \tag{1.23}$$

where σ_T is the Thomson scattering cross section, hν is the energy of photon post scattering, dϵ n$_b$ (ϵ) is the number density of soft photons in the energy interval ϵ and dϵ, and

$$f_{IC}(\epsilon,\nu,\gamma) = 2qlnq + (1+2q)(1-q) + \frac{1}{2}\frac{\left[4\epsilon\gamma q/m_e c^2\right]^2}{1+4\epsilon\gamma q/m_e c^2}(1-q), \tag{1.24}$$

where, q = $\frac{h\nu}{4\epsilon\gamma^2[1-h\nu/\gamma m_e c^2]}$.

The IC energy spectrum produced by electrons with an energy spectrum $\frac{dN_e}{d\gamma}$ can be given by,

$$(L_{\nu}^{IC})_{total} = \int_1^{\infty} d\gamma \frac{dN_e}{d\gamma_e} L_{\nu}^{IC}. \tag{1.25}$$

The low energy photons considered here can be a summation of different components, e.g., cosmic microwave background (CMB), interstellar radiation field (ISRF), emission from thermal dust, low energy synchrotron photons produced by electron population responsible for IC emission (synchrotron self-Compton process), etc. Apart from CMB (which is constant), other components may vary depending on the sources considered.

Bremsstrahlung process

This process can be visualized as the Compton scattering of electrons with virtual photons corresponding to the Coulomb field of a scattering point. When an electron traverses through a plasma of number density n$_s$, comprising of different species, i.e., atoms, ions, and electrons, then the corresponding produced bremsstrahlung radiation spectrum per electron can be given as [91],

$$\frac{dN_{\gamma}}{dtdK} = c\sum_s n_s \frac{d\sigma}{dK}, \tag{1.26}$$

where dN$_\gamma$ is the number of photons in the momentum interval between K and K + dK, emitted due to an electron in time dt. The differential bremsstrahlung cross section for an electron from a charge Ze is given by,

$$d\sigma = 4Z^2\alpha r_0^2 (dK/K)(E_i^2)^{-1}\left[(E_i^2+E_f^2) - \frac{2}{3}E_iE_f\right]\left[ln(2E_iE_f/K) - \frac{1}{2}\right], \tag{1.27}$$

where, E$_i$ and E$_f$ are initial and final energies of the electrons, K (= E$_i$ - E$_f$) is the energy of photon radiated, α is the fine structure constant, and r$_0$ is the classical radius of the electron.

So, the total bremsstrahlung radiation spectrum resulting from high energy electron distribution $\frac{dN_e}{dE}$ is given by,

$$\left(\frac{dN_\gamma}{dt dK}\right)_{total} = \int dE \frac{dN_e}{dE} \frac{dN_\gamma}{dt dK}. \tag{1.28}$$

Non-thermal bremsstrahlung is produced by relativistic electrons, which typically follow power law distribution. On the contrary, thermal bremsstrahlung is produced by electrons obeying Maxwell-Boltzmann distribution at thermal equilibrium. Non-thermal bremsstrahlung produces gamma-ray photons, whereas photons in X-ray energies are produced by thermal bremsstrahlung.

1.2 Multi-messenger & Multi-wavelength astrophysics

Here, we briefly discuss various detectors that are capable of observing astrophysical messengers, such as cosmic rays and photons across multiple wavelengths, arriving from different Galactic sources. In this thesis, we have focused on the observed photons having wavelengths corresponding to gamma-ray, X-ray, and radio energies in particular. We have also discussed the detection technique employed by one of the neutrino observatories dedicated to detecting astrophysical neutrinos from Galactic sources.

1.2.1 Cosmic rays

Cosmic rays are one of the primary astrophysical messengers studied in this thesis. In order to understand the features related to the acceleration and propagation of cosmic rays, it is essential that these messengers are detected in precise detail. To that end, here we provide a brief summary of two of the principle detectors currently operational to detect cosmic rays coming from Galactic sources. See corresponding references for other operational detectors such as balloon experiments [92], Voyager program [93–95], CAPRICE [96], HEAT [97], Balloon Experiment with Superconducting Spectrometer (BESS) [98], the cosmic ray energetic and mass (CREAM) [99], high-altitude balloon and Advanced Thin Ionization Calorimeter (ATIC) [100], and KASKADE-Grande [101], among others.

AMS-02

The Alpha Magnetic Spectrometer (AMS-02) is a general purpose, high energy particle detector operating aboard International Space Station (ISS) from 19th May 2011 [102]. Due to its large acceptance, long exposure time, and particle identification capabilities, this detector is fully capable of detecting cosmic ray nuclei, from hydrogen up to heavier cosmic ray nuclei such as iron, as well as cosmic ray leptons from MeV energies, up to multi-TeV energies. The detector consists of nine plates of precision Silicon tracker, a Transition Radiation Detector (TRD), four planes of Time of Flight (TOF) counters, a permanent magnet, an array of Anticoincidence Counters (ACC), a Ring Imaging Cherenkov detector (RICH), and Electromagnetic Calorimeter (ECAL) (see the left panel of Figure 1.3 for the structure of AMS-02). Some of the scientific goals of the AMS-02 mission are a) measuring cosmic ray spectra from proton to iron in GeV/n to TeV/n energy range to constrain the acceleration and propagation models, b) indirect search of dark matter through the

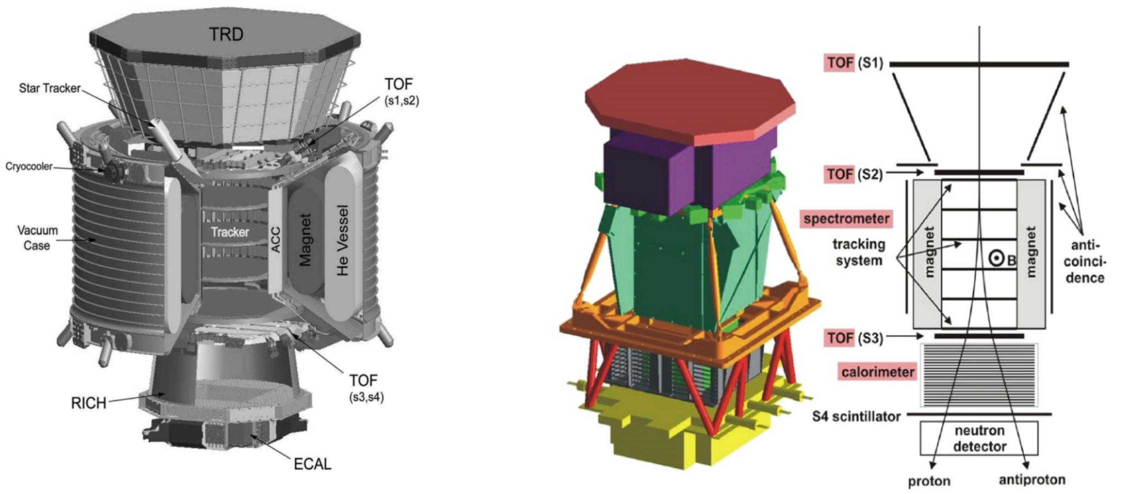

Figure 1.3 *Left Panel:* Structure of AMS-02 (https://ams02.space/), *Right Panel:* Structure of PAMELA (https://pamela.roma2.infn.it/).

detection of positrons, antiprotons, anti-deuterons, gamma-rays, etc., c) direct search of primordial antimatter and new forms of matter through the detection of anti-helium, anti-carbon, strangelets, etc., d) solar activity and modulation through the observation of cosmic ray spectra over 11 years of the solar cycle, and finally, e) contribute to the total space radiation [103–120]. AMS-02 generally collects about 1.5 billion cosmic rays during each month of operation. As one of the first significant results of AMS-02 obtained from the ~ 15 % of the total AMS sample, the positron fraction, i.e., the fraction of positron flux to the total electron plus positron fluxes, as well as individual electron and positron fluxes were measured. Apart from this, proton flux, secondary-to-primary ratios such as boron-to-carbon ratio, Beryllium isotope ratio, as well as antiproton to proton ratio, and lighter nuclei fluxes were also measured. An excess of positrons having energy greater than 10 GeV with respect to that theoretically expected from secondary production was the remarkable anomaly that was confirmed by AMS-02. This phenomenon has been typically explained by leptonic contribution from nearby pulsars and dark matter annihilation. AMS-02 also provided upper limits on the amplitude of dipole anisotropy for all cosmic ray species.

PAMELA

The Payload for Antimatter Matter Exploration and Light-nuclei Astrophysics (PAMELA) is a satellite experiment [121, 122] dedicated to the study of acceleration and propagation mechanisms of the cosmic rays in the Galaxy, the search of primordial antimatter and dark matter annihilation signals, long term study of solar modulation of Galactic cosmic rays, measurements of energetic particles from the Sun inside the heliosphere, and the radiation environment around the Earth [123–131]. PAMELA was launched with a Soyuz-U rocket on 15th June 2006, and it is hosted on Russian Resurs-DK1 satellite. The main scientific goals of PAMELA were measurements of a) antiproton spectrum up to 200 GeV, b) positron spectrum up to 200 GeV, c) electron spectrum up to 600 GeV, d) the proton and helium nuclei spectra up to 1.2 and 0.6 TeV/n, respectively, and e) the lighter nuclei spectra (from Li to O) up to 100 GeV/n. Apart from this, PAMELA also searches for antinuclei (with a $\overline{He}/He$ sensitivity of 10^7), possible features in cosmic ray spectra as a result of indirect evidence of dark matter or new astrophysical sources, and finally, some new forms of matter like strangelets. The detector itself is composed of a TOF system with segmented scintillators divided into three groups of planes, a magnetic spectrometer, an anticoincidence system with solid scintillators, an electromagnetic sampling calorimeter, a shower tail-catcher scintillator, and finally, a neutron detector as well (see the right panel of Figure 1.3 for the structure of PAMELA). High-precision measurements from PAMELA have revealed significant spectral features in cosmic ray spectra. Fluxes of H and He, which constitutes 98 % of the observed cosmic rays, shows gradual softening in the rigidity range 30-230 GV, whereas the same spectra also show spectral hardening at 232^{+35}_{-30} GV for H and 243^{+27}_{-31} GV for He. PAMELA has also provided flux measurements of boron, carbon nuclei, leptons, and that for the isotopes of hydrogen, helium, lithium, and beryllium. PAMELA measurements of positron flux also indicate the presence of an excess similar to that observed by AMS-02, thus further confirming the positron excess phenomena, which continues to remain a pertinent antiparticle puzzle.

1.2.2 Photons

Photons, produced from various interaction mechanisms occuring between high energy cosmic ray particles and the ambient medium, can also act as messengers of various Galactic astrophysical sources. As discussed earlier, cosmic rays are charged particles. Consequently, they get scattered and deflected in the large-scale Galactic magnetic field threaded throughout the Galaxy. But since photons are devoid of charge, they do not get deflected in the magnetic field. As a result, photons are very useful and efficient messengers to convey indirect pieces of evidence of various high-energy astrophysical phenomena associated with the acceleration of cosmic rays in the Galactic sources and their subsequent propagation. Photons with energy extending from low energy radio range to a very high-energy gamma-ray range can provide us with a detailed picture of the Galactic sources studied in this particular thesis. So, the multi-wavelength study is a fantastic way to study the structure and emission mechanisms at play, thus unveiling the nature of these sources. Here, we briefly discuss the detection mechanism of different observatories across multiple wavelengths, which have been particularly used in different studies reported in this thesis.

Gamma-ray

In this subsection, we discuss various space-based and ground-based detectors that observe high energy (HE) ($E_\gamma \leq 100$ GeV), very high energy (VHE) (100 GeV $< E_\gamma \leq$ 100 TeV) and ultra-high energy (UHE) ($E_\gamma > 100$ TeV) gamma-rays from Galactic and extragalactic objects. Space-based detectors are used to detect MeV-GeV gamma rays as they are comparatively abundant in number. On the other hand, gamma rays with higher energies are lesser in number, so ground-based observatories are needed to observe them, as they have a higher observational effective area to detect these VHE-UHE gamma rays.

***Fermi*-LAT** The *Fermi Gamma-ray Space Telescope* was launched on a Delta II Heavy launch vehicle on 11th June 2008 by NASA into an orbit at an altitude of about 550 km and with an orbital period of about 96 minutes. This telescope has the Large Area Telescope (LAT) as the primary instrument and Gamma-ray Burst Monitor (GBM) as the secondary instrument on board to observe various Galactic and extragalactic sources. LAT is used for long-term observation of astrophysical sources by operating in sky survey mode, whereas GBM is used for observing transient events such as gamma-ray bursts and solar flares.

LAT, being a pair conversion gamma-ray detector, tracks electron-positron pairs produced by an incident gamma-ray photon to measure the direction of the incident photons. CsI(T1) crystal calorimeter of LAT measures the energy of the same incident photons. The direction of the incident gamma-ray is constructed by an array of a total of sixteen trackers, and the energy of the incident photons is measured and stored by the calorimeter. The background rejection is done by a thin anticoincidence detector. Gamma-ray passes through this anticoincidence detector (ACD) and further interacts with the tungsten foils inside the detector to produce the electron-positron pairs. Silicon strip detectors (SSD) are used to track these pairs, which produce ions at the base of the detector. A cesium iodide calorimeter situated at the base of the detector is used to stop the charged particles and to measure the total deposited energy. Information from ACD, SSD, and CsI calorimeter are put together to measure the direction and energy of the incident gamma-ray. The effective energy range for observation by LAT is between 20 MeV to 300 GeV. LAT has a field of view of 2.4 sr and covers about 20% of the sky at a given point in time. LAT covers the entire sky every 3 hours, given LAT has an orbital period of 96 minutes. The point spread function (PSF), effective area, and angular resolution of LAT are functions of the energy of the incident gamma-ray, its incidence angle, and the event class. The PSF for an on-axis incident gamma-ray photon has a 68% containment radius of about 3 degrees at 100 MeV and about 0.04 degrees at 100 GeV. The photon count rate observed can be calculated as the product of the effective area of the LAT and the incident gamma-ray flux with livetime fraction. Essentially, the systematics associated with the measured gamma-ray flux is governed by the uncertainty in the effective area and the energy. The uncertainty of measured flux is 10% below 100 MeV, 5% between 316 MeV and 10 GeV, and 10% above 100 GeV. The schematic diagram of *Fermi*-LAT is given in Figure 1.4. The

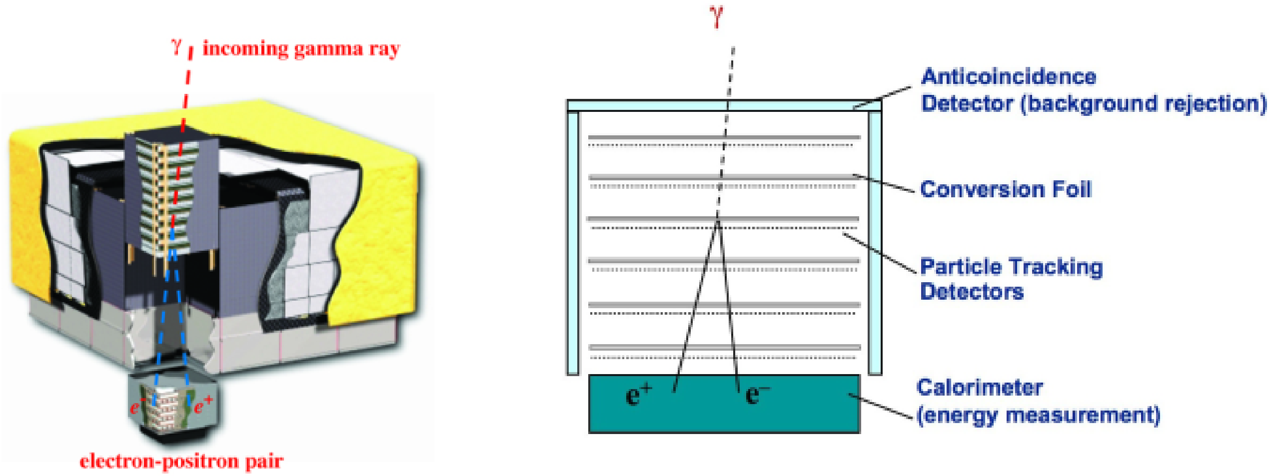

Figure 1.4 Schematic diagram of *Fermi*-LAT instrumentation (https://www-glast.stanford.edu/instrument.html).

details about the LAT instrumentation and performance can be found in [132].

H.E.S.S. High Energy Stereoscopic System (H.E.S.S.) is a system of imaging atmospheric Cherenkov telescopes (IACTs) dedicated to the study of VHE gamma-rays having an energy between 0.03 to 100 TeV [133, 134]. The observatory is situated in the Khomas region, Namibia, at an altitude of 1800 m. The name of the observatory was chosen in honor of Victor Hess. H.E.S.S., being a stereoscopic system, consists of five telescopes, four of which are made of mirrors with 12 m diameter arranged as a square with 120 m sides, and the fifth one with a mirror of 28 m located at the center of the array. Four 12 m telescopes have been operating since 2004, and the 28 m telescope (H.E.S.S. II) started its operation in 2012. H.E.S.S. has provided evidence of gamma-ray production in supernova remnants, pulsar wind nebulae, and active galactic nuclei. It is also looking for dark matter annihilation signals and testing the Lorentz invariance.

MAGIC Major Atmospheric Gamma Imaging Cherenkov Telescopes (MAGIC) is a system of two IACTs, situated at the Roque de los Muchachos Observatory on La Palma, Canary Islands, at an altitude of 2200 m [135, 136]. Each of the two telescopes has a reflecting mirror of 17 m in diameter, the first of which was built in 2004. The second MAGIC telescope started operating in 2009 at a distance of 85 m from the first telescope. Together they form the MAGIC stereoscopic system. MAGIC is sensitive to the gamma-rays with energy between 25 GeV to 30 TeV due to its large mirror. MAGIC observes gamma rays from different astrophysical sources, such as supernova remnants, pulsar wind nebulae, active galactic nuclei, and gamma-ray bursts, as well as an indirect study of dark matter annihilation.

VERITAS Very Energetic Radiation Imaging Telescope Array System (VERITAS) is a ground-based observatory consisting of an array of four 12-meter optical reflectors at an approximate separation of 100 m of each adjacent telescope, observing gamma-rays with energy from 50 GeV up to 50 TeV [137, 138]. VERITAS is located at the Fred Lawrence Whipple Observatory in southern Arizona, United States, at an altitude of 1268 m. VERITAS uses the IACT technique to observe gamma rays from astrophysical sources, and it started its operation in 2007. Each of the telescopes has a 3.5-degree field of view. VERITAS effectively complements LAT due to its large effective area, as well as coverage in a large energy band. Similar to H.E.S.S. and MAGIC, VERITAS observes gamma rays from supernova remnants, pulsar wind nebulae, active galactic nuclei, etc.

HAWC High Altitude Water Cherenkov (HAWC) observatory is a gamma-ray and cosmic ray observatory located in Mexico, at an altitude of 4100 m [139, 140]. HAWC observatory is based on the principle of indirectly detecting gamma rays using the water Cherenkov method. HAWC started its operation in 2015, and it consists of an array of 300 water Cherenkov detectors. It detects electromagnetic radiation from air showers produced by high energy cosmic rays and gamma rays hitting the atmosphere of the Earth. Furthermore, HAWC is sensitive to air showers produced by high-energy particles having energies between 100 GeV and 50 TeV. HAWC is dedicated to studying Galactic sources at high energies, Galactic diffuse emission, transient phenomena such as GRB, cosmic rays at TeV energies, and also to testing out the predictions of fundamental physics.

LHAASO Large High Altitude Air Shower Observatory (LHAASO) is a cosmic ray and gamma-ray observatory situated at Daocheng, Sichuan Province in China, at an altitude of 4410 m above sea level [141, 142]. The observatory is designed to detect air showers produced in the Earth's atmosphere by high energy gamma rays and cosmic rays using the water Cherenkov method. The observatory is expanded across an area of 360 acres, with three underground observing pools, each containing 100,000 tonnes of water. The pools also contain 12 telescopes to observe very high-energy gamma rays through the Cherenkov radiation technique. Recently in 2021, LHAASO discovered more than a dozen PeVatrons, by observing photons having sub-PeV energies, including one case in which the photon energy went up to 1.4 PeV.

Tibet-ASγ The Tibet-ASγ observatory is located in Tibet, China, at an altitude of 4300 m above sea level [143, 144]. This experiment consists of a 65,700 square meter surface air shower array and 3400 square meters of underground water Cherenkov muon detectors. The primary particle energy and direction are reconstructed by the surface air shower array, whereas the underground muon detectors are used to discriminate gamma-ray-induced muon-poor air showers from cosmic ray-induced muon-rich air showers. Tibet-ASγ has successfully observed gamma-rays in 100 TeV energies from some pointed and extended sources, as well as sub-PeV diffuse gamma-ray emission along the Galactic disk.

X-ray

Similar to gamma rays, X-ray photons also get emitted from astrophysical sources, albeit at lower energies. Typically X-ray photons have energies in the keV range. Nevertheless, X-ray photons reveal emission properties of different point-like, as well as extended astrophysical sources, as they can get produced from synchrotron cooling of accelerated leptons. To observe these X-ray photons, multiple space-based satellites have been employed throughout the years. Here, we briefly discuss one of those satellites pertinent to the study reported in this thesis.

NuSTAR The Nuclear Spectroscopic Telescope Array (NuSTAR) Small Explorer mission is the first astronomical space-based, direct-imaging X-ray telescope in an orbit that makes use of the new generation hard X-ray optics and solid state detector technologies to perform highly sensitive X-ray observations at energies significantly greater than ten keV, which is beyond the energies typically observed by Chandra X-ray observatory and XMM-Newton [145, 146]. NuSTAR focuses on the X-ray having energy in the range of 3 to 79 keV. NuSTAR started its detailed design phase in 2008 and was launched in low-Earth, near-equatorial orbit in 2012. The NuSTAR observatory consists of two co-aligned, hard X-ray telescopes pointed at astrophysical targets by a three-axis stabilized spacecraft. The NuSTAR science instrument consists of two depth-graded multilayer-coated Wolter-I conical approximation X-ray optics, which focus on two independent solid-state focal plane detectors separated from the optics by a focal length of approximately 10 m. The focal plane images are added together to gain sensitivity by designing the optics and the detector to be identical. NuSTAR was deployed to focus on measuring X-rays from astrophysical sources, especially for nuclear spectroscopy. The primary scientific goals of NuSTAR involve studying binary systems, compact objects, active galactic nuclei, etc., distributed across the Galaxy and beyond. The schematic diagram of NuSTAR is given in Figure 1.5.

Radio

Apart from observing astrophysical sources in gamma-ray and X-ray wavelengths, the properties of these sources can also be unveiled from radio observations. Low-energy radio observations can reveal the nature of emission occuring from the source, thermal or non-thermal, which, in turn, can confirm particle acceleration occuring in the source region, as non-thermal radio emission can occur due to the synchrotron cooling of accelerated leptons. We discuss two of many radio observatories currently operational, data of which have been used in the study reported in this thesis.

THOR The HI/OH/Recombination (THOR) line survey is a project that focuses on surveying the northern Galactic plane ($15^\circ < l < 67^\circ$ and $|b| < \pm 1^\circ$). The observatory surveys in HI, four OH and 19 Hα recombination lines, as well as the L band continuum from 1 to 2 GHz [147, 148]. THOR is able to provide a radio continuum image of $\sim$

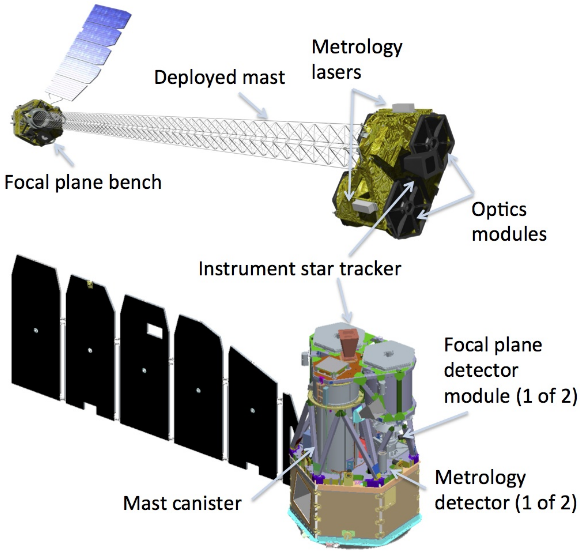

Figure 1.5 Schematic diagram showing the instrumentation of NuSTAR (https://heasarc.gsfc.nasa.gov/docs/nustar/nustar_about.html).

132 square degrees of the Galactic plane observed with the Karl G. Jansky Very Large Array (VLA) in C array configuration [149], where the spatial resolution of VLA in C array is about 20", which is essential for comparing the results with other Galactic plane surveys. This large multi-line and continuum Galactic plane survey addresses multiple topics, such as dynamics of the ISM, and cloud formation from the atomic to molecular phase, thus is useful for comparing with the theoretical cloud formation models. A study of HI and OH absorption/emission lines reveals the cold phases of the ISM. The nature of photodissociation regions can be unveiled by the combined study of THOR and Herschel/SOFIA C+ observations. The HII region recombination lines are used to study the dynamics of triggered star formation and to derive the kinematic distances. Additionally, unexpected and important results can also emerge from such a novel project.

GLOSTAR The Global View on Star Formation in the Milky Way (GLOSTAR) survey makes use of wide-band 4-8 GHz C-band receivers of the VLA and the Effelsberg 100-m telescope [149] to survey and characterize the star formation region in the Galaxy [150, 151]. GLOSTAR covers $\sim$ 145 square degrees of the Galactic plane with the VLA B and D configuration along with the Effelsberg 100-m data to study the large-scale structure. The survey of the Galactic plane also reveals information about the early phases of high-mass star formation, compact, ultra-compact, and hyper-compact HII regions, and traces of 6.7 GHz methanol (CH_3OH) masers used to study the early evolutionary stages of high mass star formation and to study the location of young stellar objects (YSOs).

The experiment also studies emission at 5.8 GHz, 4.8 GHz formaldehyde (H_2CO), and multiple radio recombination lines (RRLs).

1.2.3 Neutrinos

Another complementary messenger to cosmic rays and gamma rays is the neutrino. Having no mass and no electric charge, the neutrino is similar to photons, as the neutrinos do not get deflected by the Galactic magnetic field. However, there is one important difference in their attributes, i.e., unlike gamma rays, the interaction of neutrinos with matter is extremely feeble. As a result, neutrinos travel unscathed across large distances, thus conveying accurate information about their production site as an astrophysical messenger. Nevertheless, their weak interactions make them extremely difficult to detect. Here, we discuss one of the neutrino observatories dedicated to detecting astrophysical neutrinos from Galactic and extragalactic sources alongside the diffuse neutrino background spread all over the Galaxy.

IceCube

The IceCube neutrino observatory is situated at the South Pole and has been completely operational since 2011. In this observatory, a cubic kilometer of the Antarctic ice sheet at a depth between 1450 m and 2450 m has been instrumented, and it consists of 5160 Digital Optical Modules (DOMs) attached to 86 strings in a 3D hexagonal array. Cherenkov photons emitted by charged particles traveling at a speed greater than that of light are detected by these DOMs. These DOMs have a vertical separation of 17 m, and the strings are placed 125 m apart [152]. Following this configuration, IceCube is able to detect neutrinos with energies above 100 GeVs. Additionally, the IceTop surface array, consisting of 162 water tanks filled with clear and pure ice, is used to identify cosmic ray air shower that develops in the atmosphere. IceCube is also capable of measuring anisotropy in the cosmic ray arrival directions at TeV to PeV energies. IceCube DeepCore, a more densely instrumented volume at the deeper and the central part of the IceCube array, brings the operational threshold down to 10 GeV. DeepCore enables IceCube to probe neutrino oscillation properties and dark matter searches. IceCube is proving to be instrumental in detecting neutrinos from various astrophysical sources. A diagram of the IceCube observatory is given in Figure 1.6. Neutrinos are expected to be produced from the decay of charged pions, which are created from inelastic p-p interaction. As a result, high energy particles accelerated in supernova shocks can produce neutrinos over a much longer period when they diffuse through ISM to interact with the nearby molecular clouds. Star-forming regions provide all of the necessary ingredients for the efficient production of astrophysical neutrinos. Additionally, IceCube has also been responsible for establishing the existence of an astrophysical diffuse neutrino component above 100 TeV, which was first observed in 2013.

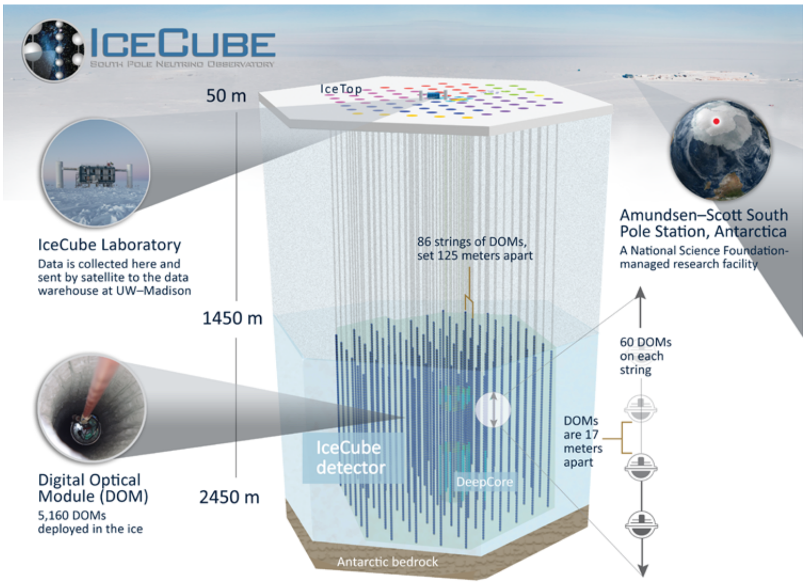

Figure 1.6 Schematic diagram showing the surface array IceTop, the IceCube array, and the low-energy sub-array DeepCore, i.e., components of IceCube Neutrino Observatory at South Pole ice (https://icecube.wisc.edu/science/icecube/).

1.3 Galactic sources

In this section, we discuss the Galactic sources that have been a direct or indirect part of the study reported in this particular thesis. The most ubiquitous sources found in the Galaxy that produce gamma rays are SNRs. Additionally, pulsar wind nebulae (PWNe) and high-mass X-ray binaries are also able to radiate gamma rays. Passive Galactic Molecular Clouds (GMCs), which are not associated with any SNRs, have also been observed to shine in gamma rays, contributing to the total cosmic ray sea. We briefly discuss these sources here.

1.3.1 Supernova remnants

SNR is the most credible source class for Galactic cosmic ray acceleration, and they have been observed to radiate in radio, X-rays, and gamma rays. The charged particles are accelerated in SNR shocks through Diffusive Shock Acceleration (DSA), and these accelerated cosmic rays are able to plausibly explain the observed cosmic ray spectra, up to "knee" energies [153, 154]. Typical kinetic energy of $\sim 10^{51}$ ergs is released in a supernova explosion. It has been found that if even ~ 10 % of this kinetic energy released goes into accelerating protons, heavier nuclei, as well as electrons, then SN explosion can power the cosmic rays that we observe. For the acceleration mechanism typically considered in SNRs to accelerate cosmic rays, please see subsection 1.1.1. For young, shell-type SNRs containing multiple numbers of shells, the outer shells of the SNRs are the most plausible place for accelerating high-energy leptons through DSA [155]. Detection of X-rays from shell-type SNRs confirmed the acceleration of high energy leptons in SNRs to

TeV energies [156, 157]. Non-thermal radio, X-rays, and even gamma-rays are produced in shell-type SNRs by high energy leptons via synchrotron, bremsstrahlung, and IC process (see subsection 1.1.3). On the other hand, direct evidence of proton acceleration are yet to be confirmed. Indirect proof of proton acceleration can be found by unambiguous gamma-ray detection from the SNRs resulting from neutral pion decay produced by the interaction between accelerated protons and protons present in the ambient matter.

1.3.2 Pulsar wind nebulae

Pulsars are rapidly rotating highly magnetized astrophysical objects. A pulsar is surrounded by wind nebulae and the associated SNR in the case of a pulsar wind nebulae (PWNe) system. Multiple PWNe have been detected in radio, X-ray, and gamma rays. Pulsars lose their rotational energy as they spin down, and the rotational energy lost converts into wind energy, which consists of leptons and ions. The expanding wind gets terminated by the matter in the surrounding nebula, creating the so-called wind termination shock. The radius of the shock can be determined by a balance between the pressure in the wind and the pressure of the nebula, which is created by the cumulative accumulation of energy that got injected over the duration of the age of the pulsar [158]. Leptons present in the pulsar wind get accelerated up to GeV energies through magnetohydrodynamic processes before they are stopped at the position of the termination shock. Thereafter, these accelerated leptons get randomized at the downstream region of the shock and further get accelerated even up to PeV energies through DSA at the termination shock. After that, these accelerated particles get injected into the surrounding medium, where they interact with the magnetic field, low energy photon field including the CMB, and ambient matter, and further emit from radio to ultra-high energy gamma-rays through synchrotron, bremsstrahlung, and IC processes. Reviews of the various theories of PWN, including the latest observation results, can be found, for example, in Ref. [159–161].

1.3.3 High mass X-ray binaries

Another type of Galactic object, known as high mass X-ray binaries, can also be potential gamma-ray emitters, typically known as gamma-ray binaries. The high-mass X-ray binaries consist of a compact object and a companion star. Depending on the nature of the compact object, there can be two types of X-ray binaries, namely binary pulsars, and microquasars. Binary pulsars comprise a pulsar orbiting around a main-sequence star with a circumstellar disc, e.g., a Be star. When the pulsar passes through the disc of the Be star, high energy emission results from the interaction between the wind of the pulsar and the material in the dense circumstellar disc of the Be star. On the contrary, microquasars have a stellar-mass black hole as their compact objects and a companion star that losses its mass by forming an accretion disc around the central black hole. High energy emissions are seen from the microquasars in the form of collimated jet outflows from the close region of the central compact objects of the binary system. Emissions can be produced when leptons accelerate to high energies at the jet and interact with the stellar UV photons through the IC process. LS I +61°303 is one of the few gamma-ray binaries observed, which not only emit gamma-rays but also show variability in their emission. Orbital modulation or varying absorption processes can be used to explain this variability [162].

1.3.4 Galactic Molecular Clouds

A significant fraction of interstellar gas in our Milky Way Galaxy, which is a spiral Galaxy, is molecular hydrogen (H_2) [163]. Most of the molecular hydrogen material is concentrated as large reservoirs in the Galaxy, also known as Giant Molecular Clouds (GMCs), which are objects with masses 10^4 - 10^6 $M_\odot$ and radii of 50 - 200 pc [164]. Although H_2 molecules have a permanent electric dipole moment, it is very difficult to observe them in cold and obscured interstellar regions, as optical and UV observations suffer from interstellar extinction. This is why a stable, diatomic model such as Carbon Monoxide (CO) is very important in detecting H_2 distribution in the Galaxy. CO acts as a tracer of H_2 molecules, as CO molecules have $J = 1 \rightarrow 0$ rotational transitions at a radio wavelength of 2.6 mm, which can be easily observed in very tenuous molecular gas, and CO-to-H_2 conversion factor (X_{CO}) is found to be a constant ($\sim 2 \times 10^{20}$ cm^{-2} (K km s^{-1})$^{-1}$ with ± 30% uncertainty). It has been found from radio continuum, optical and infrared observations, OB associations, and population I objects that essentially all star formation occurs in GMCs. GMCs can also be detected in other wavelengths. Gamma rays detected from GMCs carry direct evidence of spatial and energy distribution of cosmic rays in the Galaxy. The galactocentric radial distribution of GMCs points towards a homogenous sea of cosmic rays with a constant density and spectral shape of the locally measured flux of cosmic rays [165]. Despite that, a cosmic ray flux with a harder spectral index compared to that of the cosmic ray sea has been posited as a result of the reacceleration process due to magnetized turbulence inside some of the GMCs [166–168]. Although reacceleration has not been objectively confirmed by observations, evidence of cosmic ray excess inside local GMCs has been unveiled by *Fermi*-LAT data analysis [169], which essentially indicates that reacceleration might be a possibility in some of the GMCs yet to be observed.

1.4 Thesis Objectives

In previous sections, we have discussed how cosmic rays are accelerated at Galactic acceleration sites and their subsequent propagation throughout the Galaxy, effectively creating a cosmic ray sea. While propagating, cosmic rays perform random diffusion owing to the large-scale turbulent magnetic field while producing secondary cosmic ray particles through different interaction mechanisms. Not only that, but cosmic rays can also produce various important astrophysical messengers like photons across multi-wavelength and non-interacting particles such as neutrinos. These messengers provide us with evidence of various high-energy astrophysical phenomena occuring in Galactic sources, thereby unveiling the proper nature, acceleration, and emission mechanism at work, and also the information about the ambient medium surrounding the sources. Below, we discuss the motivation behind the research reported in this thesis, as well as the structure of the thesis.

1.4.1 Motivation

We summarize below the motivation for surveying the Galactic sources in a multi-messenger and a multi-wavelength context. Thus, the foundations are laid that guide the research work undertaken.

- Since multiple successful missions were completed by various space-based satellites, such as PAMELA and later AMS-02, dedicated to observing high energy cosmic rays arriving on the Earth, many exciting results have been unveiled for scientists to decipher. Interesting features in the spectrum of the cosmic ray species give us a hint about the acceleration mechanism of the cosmic rays and further put forth certain constraints on the propagation of the accelerated cosmic rays. Moreover, the large-scale structure of the Galactic magnetic field, distribution of the accelerating sources, and interstellar gas can also be studied from the data observed by these satellites. One such enigmatic feature observed is the excess in the positron flux, where the positron flux increases with energy from $\sim$ 20 GeV, finally reaching a peak around $\sim$ 200-300 GeV and then showing a subsequent cutoff in the spectrum. This feature in positron flux, in turn, affects the positron fraction measurements observed by both PAMELA and AMS-02. The positron excess poses a conflict with the theoretical understanding of secondary production by the primary cosmic rays diffusing through the Galaxy. Consequently, it has been obvious for a very long time that a nearby, additional class of astrophysical source(s) must be responsible for the excess observed in the positron flux. Pulsars and dark matter have been conventionally considered to be the leading candidates in explaining the positron excess. However, recent observations and theoretical arguments have rendered the pulsar or dark matter origin of the positron excess questionable. Geminga and Monogem are typically considered to be two nearby sub-kpc pulsars responsible for the observed positron excess. However, a slow diffusion region, known as the pulsar halo, was discovered around both Monogem and Geminga, which indicates that the lepton contributions from these pulsars would not be significant enough to explain the positron excess [170]. Moreover, recently AMS-02 discovered that the observed positron flux is isotropic in nature, whereas explaining the excess with Geminga and/or Monogem would introduce a certain anisotropy in the excess positron flux [171, 172]. Furthermore, AMS-02 has found that the additional source(s) responsible for producing positrons relevant for explaining the excess should also produce antiprotons at a constant fraction ($\sim$ 2) compared to the produced positrons in

60 - 525 GeV range [172]. But pulsars are unable to produce antiprotons. So the pulsar interpretation of positron excess still remains debatable. On the other hand, if dark matter is responsible for the positron excess, the isotropic condition would be satisfied. Nevertheless, it has been argued that apart from producing leptons, dark matter annihilation would also produce gamma rays, which would indirectly prove the existence of the dark matter [173]. Nevertheless, no nearby dark matter clumps, shining in gamma rays, were discovered by *Fermi*-LAT or any other gamma-ray observatories. So, the dark matter interpretation continues to remain an exotic possibility that will explain the positron excess. As a result, new and alternative routes in terms of probable sources responsible for the positron excess must be explored to properly explain it, all the while being consistent with other observables measured by AMS-02 or PAMELA.

- As discussed earlier, photons observed across multiple wavelengths help unveil the nature of unidentified Galactic sources. One such enigmatic Galactic source class is the gamma-ray binaries. There are very few confirmed gamma-ray binaries observed in the Galaxy, e.g., LS 5039, LS I +61°303, PSR B1259-63, HESS J0632-057, HESS J1832-093, PSR J2032+4127, etc, [174–182]. As discussed in section 1.3, it can be further divided into two categories, microquasars (black holes as compact objects) and high-mass gamma-ray binaries (pulsars as compact objects). In high-mass gamma-ray binaries (HMGBs), there are two ways by which gamma-ray emission can occur, 1) disk-fed emission or 2) wind-fed emission. Most of the HMGBs show disk-fed emission, where gamma-ray emission occurs when the pulsar passes through the Be disk of the companion star. On the other hand, wind-fed emission happens when the wind generated by the companion star interacts with the rotating magnetosphere of the pulsar. The question remains, is this it, or is there any other way by which gamma-ray emission can happen? Since gamma-ray binaries are low in number, the possible emission mechanism occuring in them is poorly understood. So, further investigation is needed to unearth whether any other interaction mechanism can also produce gamma-ray in HMGBs, depending on the geometry of the binary system. Simultaneous long-term observations in multiple wavelengths are necessary to properly study interesting possibilities regarding these types of sources.

- Since the air shower array such as LHAASO has been operational, it has discovered dozens of sources that emit ultra-high-energy gamma-rays, with maximum energy exceeding $\sim$ 1 PeV [142]. The presence of ultra-high energy gamma-ray sources in the Galaxy indicates that there are sources in the Galaxy that can accelerate particles up to PeV energies, which are also known as "PeVatrons". Crab pulsar wind nebula is the only source that has been confirmed to be a PeVatron [183], which is why it is understandable to think that every pulsar wind nebula can potentially be a PeVatron accelerator. It has already been posited that the presence of a powerful pulsar in the near vicinity of ultra-high energy gamma-ray sources might be a universal feature [184]. On top of that, it is believed that the spectral index of protons accelerated at supernova shocks will tend to become softer with age, so SNRs will not be able to accelerate particles up to PeV energies. At first glance, this would make it seem that no other Galactic sources can be of PeVatron type other than pulsar wind nebulae. However, with closer inspection, evidence has been found that this might not be the case, making the origin of PeVatrons to be mysterious. Detailed theoretical modeling of acceleration and interaction occuring at SNRs, or PWNe, considering proper conditions, can help alleviate the mystery of PeVatrons. Additionally, further observations in multiple wavelengths, with a closer look at the morphology of the sources, as well as the spectral features, will prove to be beneficial in solving the acceleration and interaction at play, thus revealing the exact nature of these PeVatron sources found in the Galaxy. Detection of additional messengers, such as neutrinos, can also be used to distinguish different interactions occuring at these sources, thus effectively ruling out possibilities that might not have been ruled out otherwise.

1.4.2 Structure of the thesis

The above-mentioned issues in the multi-messenger and multi-wavelength study of Galactic sources have paved the way for further research in this field. We try to establish a framework, following which the thesis has been structured.

- *Chapter 2:* In this chapter, we have provided a model that explains the observed positron excess using the secondary positrons produced inside the nearby Galactic Molecular Clouds. We have shown that if cosmic ray protons are reaccelerated due to magnetized turbulence inside nearby GMCs, then the resulting secondary positrons will be able to explain the observed excess. Our self-consistent model is also able to explain other cosmic ray observables observed by AMS-02, and PAMELA, such as the proton, antiproton, electron spectra, as well as secondary-to-primary ratios such as B/C ratio, and ^{10}Be/^{9}Be ratio. This chapter is based on the paper [185].

- *Chapter 3:* In this chapter, we have studied an unidentified VHE Galactic source, observed by H.E.S.S., dubbed as HESS J1828-099. A high mass X-ray binary XTE J1829-098 has already been detected near the vicinity of the HESS source, as reported in previous studies. We have analyzed *Fermi*-LAT, THOR, and GLOSTAR data and reported possible HE gamma-ray and radio counterparts of this source. By performing NuSTAR X-ray data analysis, we have proved the presence of shock-accelerated electrons in the source region, which interact with the ambient medium to produce the emission observed from this source. Further, we have analyzed the MWL SED of this source with a typical gamma-ray binary model and have shown that HESS J2818-099 can be a possible accreting, high-mass gamma-ray binary, the first of its kind. This chapter is based on the paper [186].

- *Chapter 4:* In this chapter, we have provided a theoretical model to explain the MWL SED of a recently detected UHE gamma-ray source, LHAASO J1908+0621. The source is coincident with SNR G40.5-0.5 and associated molecular clouds, as well as PWN J1907+0602. We have shown that emissions from both SNR and PWN are necessary to explain the MWL SED of the source. Moreover, we have shown hadronic interaction occuring in SNR, and molecular cloud might be responsible for the UHE gamma-ray detected by LHAASO, which indicates that SNR can be a possible PeVatron candidate. This chapter is based on the paper [187].

- *Chapter 5:* In this chapter, we have assumed that emission from the UHE gamma-ray source, LHAASO J2226+6057, to be entirely originating from nearby PWN J2229+6114. Under this assumption, we have provided a detailed PWN model to explain the MWL SED of the UHE gamma-ray source. We have found that in order to explain the SED with emission from the PWN, the corresponding radius and magnetic field of the PWN must be very high and very low, respectively, which contradicts observations. This result indicates that some additional component, other than that from PWN, might be needed to explain the emission observed from LHAASO J2226+6057. This chapter is based on the paper [188].

We use the **DRAGON**[1] code, which uses a Crank-Nicholson scheme, to solve the diffusion-transport equation as given in equation 1.19, for the Galactic propagation of cosmic ray from their sources to the Earth. The solver allows us to mimic suitable astrophysical environments by including plausible source classes in the Galaxy with intended injection parameters, templates of the Galactic magnetic field and interstellar material, and various energy loss processes of cosmic rays, among others. It also takes into account modulation due to solar activity using a force-field approximation. Finally, the cosmic ray fluxes of different species expected to be observed on the Earth are given as output, which can then be plotted to explain the observed data from different observatories. We have also used **Fermipy**[2] package, associated with ***Fermi*-tools**[3] to analyze HE gamma-ray data observed by *Fermi*-LAT. SED, lightcurve, extension, and location of a GeV gamma-ray source can be estimated from the output of **Fermipy**. We have also analyzed the X-ray spectrum constructed by the data obtained by NuSTAR, using **`XSPEC 12.11.1`**[4] tool included in the **HEASOFT 6.28**[5] package. **GAMERA**[6] code was used for modeling of

[1] https://github.com/cosmicrays/DRAGON
[2] https://fermipy.readthedocs.io/en/latest/
[3] https://fermi.gsfc.nasa.gov/ssc/data/
[4] https://heasarc.gsfc.nasa.gov/xanadu/xspec/
[5] https://heasarc.gsfc.nasa.gov/docs/software/heasoft/
[6] http://libgamera.github.io/GAMERA/docs/main_page.html

non-thermal radiation spectrum from gamma-ray sources. We have also used a novel code titled **TIDE-PWN**[7] to perform leptonic, time-dependent modeling of PWN systems. The code seeks a solution for the lepton distribution function considering the full-time-energy-dependent diffusion-loss equation. The code further includes injection, energy losses, and escape for realistic modeling of PWNe. Appropriate reference of data files, wherever used for analysis purposes, are duly mentioned. We discuss the impact of our results and draw our conclusions in Chapter 6.

[7]Private code

2

Positron excess explained by Galactic Molecular Clouds

The observed data by *Alpha Magnetic Spectrometer* (AMS-02) confirms that cosmic ray positron flux rises with energy and shows a peak near a few hundred GeV. This rising positron flux cannot be explained by interactions of cosmic rays with interstellar hydrogen gas. Pulsars, dark matter, and many other innovative physical scenarios have been studied to explain this rising of the positron flux, also known as positron excess. We have studied whether secondary production due to cosmic ray interactions in nearby Galactic Molecular Clouds (GMCs) can contribute significantly to the observed positron spectrum on Earth. Using a large-scale CO survey, 1064 GMCs were detected in the Galaxy, which reside in the Galactic plane. Alongside that, a survey implemented the optical/IR dust extinction measurements to trace 567 GMCs within 4 kpc of Earth, also residing in the Galactic plane. Moreover, new GMCs have been discovered by *Fermi*-LAT near the Galactic plane, which we have also included in our study. It has been speculated earlier that cosmic rays may be reaccelerated in some GMCs. We select 7 GMCs out of 567 GMCs recently reported, within 4 kpc of Earth, where reacceleration due to magnetized turbulence is assumed. We have included a small hardened component of secondary positrons produced from the interaction of reaccelerated CRs in those 7 GMCs. Finally, we use **DRAGON** code for our simulation setup to study CR propagation in the Galaxy and show that the observed positron spectrum can be well explained by our self-consistent model.

2.1 Background

Galactic cosmic rays (CRs) are generally considered to be accelerated in shocks near the supernova remnants (SNRs) [15, 70, 189–191] and propagated throughout the Galaxy. During their propagation, they are deflected by the Galactic magnetic field (GMF), and they also interact with interstellar hydrogen gas. The secondary CRs, produced in subsequent interactions of primary CRs with interstellar hydrogen gas [192], are important probes of CR acceleration. Other than the interaction with the distribution of interstellar matter, there is also diffusion of CRs in the Galaxy, which depends on the magnetic field structure. Even after more than a hundred years of discovery of CRs, new observational data brings in new challenges for theoretical interpretations [17]; due to this reason, this field has remained an active area of research.

Electrons are injected by CR sources; also, they are produced in interactions of CR protons and nuclei with interstellar matter during their propagation in the Galaxy. While CR protons and nuclei can propagate long distances without losing energy significantly, electrons lose energy within a much shorter distance due to radiative losses. Positrons and antiprotons are secondary particles produced in interactions of CR protons and nuclei with interstellar matter. Being antiparticles, they are useful probes of new physics.

Payload for Antimatter Matter Exploration and Light-nuclei Astrophysics (PAMELA) is a satellite-borne apparatus for recording charged CRs. The positron fraction measured by PAMELA between 1.5 and 100 GeV was the first result showing deviation from the conventional secondary production model [123, 124]. More recent PAMELA observations confirm that additional sources, either astrophysical or exotic, may be required to explain the CR positron spectra [125].

Fermi-LAT collaboration reported the CR electron and positron spectrum separately and also the positron fraction in the energy range of 20-200 GeV [193]. They confirmed that the positron fraction rises with the energy in the 20-100 GeV energy range, and the three spectral points in that spectrum between 100 and 200 GeV are also consistent with the same feature.

The *Alpha Magnetic Spectrometer* (AMS) on the International Space Station has measured CR fluxes with high precision over a wide energy range. The AMS collaboration published their results on high precision measurements of fluxes of CR protons (p) [107], helium (He)[108], Boron (B) to Carbon (C) flux ratio [109], and also antiprotons ($\bar{p}$) [110]. Their first results on precise measurements of positron fraction in primary CRs in the energy range of 0.5-350 GeV showed that the positron fraction steadily increases in the energy range of 10 to 250 GeV, however beyond 20 GeV, the slope decreases by order of magnitude [104]. Their subsequent results gave better statistics over an extended energy range [103, 105, 106]. Their recent results of CR electron [117] and positron spectra [118] provide high-quality measurements of fluxes up to TeV energy. The positron flux shows significant excess starting from 25.2±1.8 GeV and a sharp decrease above 284^{+91}_{-64} GeV. The flux has a cutoff at 810^{+310}_{-180} GeV. The data shows that at high energy, the positrons may be originated either from dark matter (DM) annihilation or from other astrophysical sources.

The DM origin of positron excess was studied in many earlier papers [194–199]. Both DM and pulsar scenarios could be the possible origin of the positron excess. Anisotropy could be another useful probe to discriminate these two scenarios [200]. Geminga pulsar has long been identified as a nearby gamma-ray source. The possibility of explaining the GeV positron excess with the TeV gamma-ray source Geminga was explored by Yüksel *et al.* [201]. Hooper *et al.* [202] suggested that a significant contribution to the positron flux between 10 to 100 GeV might be originated from mature pulsars such as Geminga and B0656+14. *The Advanced Thin Ionization Calorimeter* (ATIC) reported a “bump" in the high energy flux of electrons and positrons [203]. Several candidate pulsars were listed in [204] that could individually or coherently contribute to explaining the PAMELA and ATIC data. After more precise observation by AMS-02, the role of nearby pulsars was further explored, and they were identified as a possible origin of the positron excess [205–207].

Previously, very high energy gamma-ray data from *High Altitude Water Cherenkov* (HAWC) [208] detector also indicated that significant high energy positron flux from nearby pulsars such as Monogem and Geminga could explain the positron excess at 10-100 GeV energy range [209]. However, the recent measurement of the surface brightness profile of TeV nebulae surrounding Geminga and PSR B0656+14 by HAWC [210] suggests inefficient diffusion of particles from these sources. When the HAWC and *Fermi*-LAT data are combined, Geminga and PSR B0656+14 are disfavoured as major sources of positron excess in the energy range of 50-500 GeV [170] for Kolmogorov type diffusion. In a more recent work, the pulsar PSR B1055-52 is found to be a promising source for explaining positron excess [211]. In the future, gamma-ray astronomy can shed more light on the origin of positron excess.

Micro-quasars were also considered to be viable sources for explaining the positron excess. It was shown that photo-hadronic interactions in the jets of micro-quasars could produce the excess positron flux, which can explain the rise above 10 GeV [212].

Galactic molecular clouds (GMCs) are dense reservoirs of cold protons distributed throughout the Galactic plane. Such concentrated clumps of protons can be an ideal laboratory for different particle interactions. We have tried to construct a self-consistent model in which we show that the secondary positrons produced from interactions of CRs in nearby GMCs can explain the rise of positron flux above 10 GeV. Our self-consistent model of CR propagation also fits the data of CR electrons, positron fraction, protons, antiprotons, B/C, and ^{10}Be/^{9}Be ratio as measured by AMS-02 and PAMELA.

We consider Galactic SNRs as the primary sources of CRs. During their random movement in the interstellar medium (ISM), CRs interact with ambient gas and also inside the GMCs. We represent our analysis by dividing it into three parts, namely CASE 1, CASE 2, and CASE 3. CASE 1 considers interactions of primary CRs with interstellar hydrogen gas. CASE 2, then, takes into account the interactions inside GMCs residing on the Galactic plane and listed by Rice *et al.* [213], Chen *et al.* [214] and Aharonian *et al.* [165]. Nearby GMCs in the Gould Belt complex, Taurus, Lupus, and Orion A have not been included in CASE 2. Since these three GMCs are nearby and have been extensively studied with gamma-ray data from *Fermi*-LAT experiment [165], the effect of these GMCs needs separate modeling. Also, in earlier works [97, 166–168, 215], it has been discussed that CRs can get reaccelerated inside GMCs due to magnetized turbulence. As a result, the CR spectrum will be hardened. The secondary particles produced from the interaction of these CRs will also have a hardened spectrum. Based on the following three conditions, (1) detection incapability of *Fermi*-LAT (2) radius ≥ 10 pc, and (3) distance from the Earth ≤ 1 kpc, we select 7 GMCs from [214], inside which we assume CRs are reaccelerated. We omit these 7 GMCs from CASE 2 too. We find that the total flux of positrons from CASE 1 and CASE 2 is not sufficient to explain the positron excess above 10 GeV. Subsequently, we incorporate the contributions of secondary CRs from three nearby GMCs Taurus, Lupus, Orion A, and also 7 selected GMCs from [214]. The lepton flux from these GMCs has been calculated analytically, which is our CASE 3. We show that the total flux from CASE 1, CASE 2, and CASE 3 can explain the positron excess observed by AMS-02 and PAMELA data. Also, our model fits the data of proton, antiproton, electron spectra, and also B/C and ^{10}Be/^{9}Be ratio quite well. The possibility of GMCs being important contributors to the observed CR spectra can facilitate future observations and analysis that will expand the landscape of cosmic ray theory and experiments in a new direction.

2.2 Modeling of cosmic ray propagation

2.2.1 Model setup

The propagation of CRs can be studied, for a given source distribution, the density distribution of interstellar medium (ISM), GMF, and injection spectrum of primary cosmic rays from their sources, by solving the CR transport equation [15, 191]. Here, we study high energy CR propagation in our Galaxy by solving the transport equation numerically, using **DRAGON**[1] (Diffusion of cosmic RAys in Galaxy modelizatiON) [216–218]. **DRAGON** incorporates various physical processes such as propagation and scattering of CRs in regular and turbulent magnetic fields, CRs interacting with ISM and GMCs, energy losses due to radioactive decay of the nuclei, ionization loss, Coulomb loss, Bremsstrahlung loss, synchrotron and IC loss, reacceleration and convection in the Galactic medium, to obtain the solution of the transport equation for the CR propagation in the Galaxy. In this subsection, we give an overview of the source distribution model, GMF model, ISM gas density distribution, and diffusion coefficient we have chosen.

DRAGON solves the transport equation in 3D geometry, where the Galaxy is assumed to be cylindrical in shape. The outermost radial boundary is denoted as R_{max}, the vertical boundary as L, and the halo height as z_t, where $L = 3z_t$ [219]. The location of the observer is specified at Sun's position with respect to the Galactic center (GC), with x = 8.3 kpc, y = 0, and z = 0. We are propagating CRs with atomic numbers ranging from Z = 1 to Z = 14, considering the propagation of particles with higher mass numbers does not affect our results. Primary CRs in our work are assumed to be produced from SNRs in our Galaxy. Assuming SNRs as the major sources of CRs with a universal injection spectrum, the source term is used from the paper by K. Ferriere [47].

Interstellar gas plays an important role in the process of CR interactions and secondary production. During propagation, CRs interact with different gas components of the ISM. The gaseous components are mainly atomic hydrogen (HI), ionized hydrogen (HII), and molecular hydrogen (H_2). As discussed earlier, we divide the contribution

[1]The 3D version of the **DRAGON** code is available at https://github.com/cosmicrays/DRAGON for download.

from the interaction of primary CRs with these components into three cases, CASE 1 for contribution from ISM gas density distribution, and CASE 2 for contribution from interactions in GMCs listed in Rice *et al.* [213],Chen *et al.* [214] and Aharonian *et al.* [165], apart from Taurus, Lupus, Orion A, and 7 GMCs selected from [214]. These 10 GMCs are modeled separately as our CASE 3.

HI density distribution: Neutral or atomic hydrogen cannot be detected in optical wavelengths. Generally, HI can be detected by the observation of Lyman α [39, 40] and 21-cm line [41, 42]. Previously, many models have been given to describe HI gas distribution [43, 48, 220]. In our calculation, the radial dependence of HI number density in the Galactic plane is defined by a Table in ref. [221], which is renormalized to make it consistent with the data of ref. [41]. The z-dependence is calculated using the approximation by [41] for R < 8 kpc, by [42] for R > 10 kpc, and interpolated in between.

HII density distribution: Radio signals from pulsars and other Galactic and extra-galactic compact objects give us information about the ionized component of hydrogen gas. Some of the models for the distribution of ionized hydrogen components are [43–45]. Cordes *et al.* [46] provided the space averaged free electron density depending on dispersion, distance, and scattering measurements of pulsars. The distribution of ionized component HII is calculated using the cylindrically symmetrical model for space averaged free electron density [46].

H_2 ***density distribution***: Molecular hydrogen (H_2) is the most abundant molecule in our Galaxy. The second most abundant molecule is CO. Study of H_2 cannot be done reliably from UV and optical observations because UV and optical observations suffer from interstellar extinction. H_2 is studied indirectly by radio observation of CO molecules as CO molecule has (J = 1 $\rightarrow$ 0) rotational transition at the radio wavelength of 2.6 mm [47]. Such transition of CO acts as a tracer of H_2, where CO-to-H_2 conversion factor, X_{CO} is used to obtain information of H_2 distribution in Galaxy [43, 48–51]. Most of the H_2 contribution in our Galaxy comes from GMCs.

The Galactic magnetic field (GMF) plays a crucial role in CR propagation. CR leptons lose energy by synchrotron emission in GMF. There are several methods to constrain the intensity and the orientation of GMF: Zeeman splitting observations [222], infrared, synchrotron and starlight polarisation studies [34–36], and Faraday rotation measures of the Galactic and extragalactic sources [37, 38]. The Galactic magnetic field $\vec{B}$ is usually described as a sum of two components: a large-scale regular and a small-scale turbulent, both having a strength of the order of μG in the Galaxy [223].

In this work, we use the GMF model as given by [38]. The GMF has three components, namely disc, halo, and turbulent. The normalizations of the three components are denoted as $B_0^{\rm disc}$, $B_0^{\rm halo}$ and $B_0^{\rm turbulent}$ respectively. $B_0^{\rm disc}$ and $B_0^{\rm halo}$ lie in the range of 2-11 μG but their role in CR propagation is insignificant [219]. Among these components, the turbulent component of the GMF plays an important role in CR propagation. Observationally, the most relevant information on the turbulent component of GMF comes from Faraday Rotation measurements. A functional relation between the magnitude of the turbulent magnetic field and halo height (z_t) is given in [219] by theoretical modeling of the propagation of the Galactic CR electrons and positrons to fit their observed fluxes their synchrotron emission and its angular distribution. This expression from [219],

$$\left(\frac{B_0^{turbulent}}{1\ \mu G}\right)^2 = 148.06\left(\frac{1\ kpc}{z_t}\right) + 19.12\,, \tag{2.1}$$

has been used to calculate the intensity of the random magnetic field. The shape of the vertical profile is poorly constrained. We have used the exponential profile of the random component of the magnetic field, which is compatible with presently available data.

We have used the following form of diffusion coefficient to study the CR propagation in the Milky Way Galaxy.

$$D(\rho, z) = \beta^{\eta} D_0 \left(\frac{\rho}{\rho_0}\right)^{\delta} exp\left(\frac{z}{z_t}\right)\,, \tag{2.2}$$

where, ρ being the rigidity, z is the vertical height above the Galactic plane and δ denotes the power law index. z_t and β are Galactic halo height and dimensionless particle velocity, respectively. The power η of β accounts for the uncertainties that arise due to the propagation of CRs at low energies [224]. D_0 denotes the normalisation of diffusion coefficient and ρ_0 is the reference rigidity. Also note that to avoid the boundary effects, we set L = $3z_t$ in our work [219]. The z-component of the diffusion coefficient and the turbulent magnetic field are related by

$$D(z)^{-1} \propto B^{\text{turbulent}}(z) \propto exp(-z/z_t). \tag{2.3}$$

In our study, we have used injection spectra of protons and heavy nuclei in the following form [225]:

$$\frac{dN^k}{d\rho} \propto \begin{cases} (\rho/\rho^k_{br,1})^{-\alpha^k_1} & \rho < \rho^k_{br,1}, \\ (\rho/\rho^k_{br,1})^{-\alpha^k_2} & \rho^k_{br,1} \le \rho. \end{cases} \tag{2.4}$$

In **DRAGON**, $\alpha^k_1, \alpha^k_2, \rho^k_{br,1}$ are free parameters, which have been tuned to fit the observed CR spectra. In the above relation, k denotes protons and heavy nuclei (k = 1, 2, .., 14), whose spectra we assumed to be similar in our case. Similarly, for electron injection spectra, we use a similar form:

$$\frac{dN^e}{d\rho} \propto \begin{cases} (\rho/\rho^e_{br,1})^{-\alpha^e_1} & \rho \le \rho^e_{br,1}, \\ (\rho/\rho^e_{br,1})^{-\alpha^e_2} & \rho^e_{br,1} < \rho < \rho^e_{br,2}, \\ (\rho/\rho^e_{br,2})^{-\alpha^e_3}(\rho^e_{br,2}/\rho^e_{br,1})^{-\alpha^e_2} & \rho^e_{br,2} \le \rho. \end{cases} \tag{2.5}$$

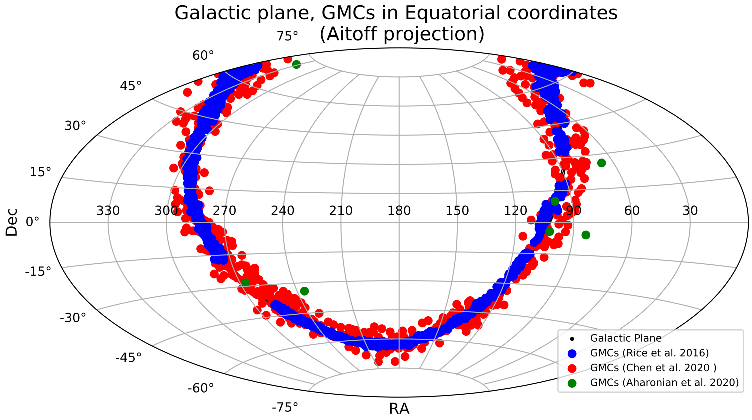

Figure 2.1 All-sky map of the GMCs taken for this work from Rice *et al* [213], Chen *et al* [214] and Aharonian *et al* [165].

We also need to take into account the solar modulation effect, which is dominant below 10 GeV. In accordance with the force-field approximation, we have implemented the solar modulation with a potential (ϕ) such that the observed spectrum can be written as [226],

$$J_k(T_k, \phi) = J_{LIS,k}(T_k + \Phi)\,\frac{(T_k)\,(T_k + 2T_p)}{(T_k + \Phi)(T_k + \Phi + 2T_p)}, \tag{2.6}$$

where ϕ is the solar modulation potential, J_k is the differential intensity of the CR nuclei, T_k is the kinetic energy of CR nuclei with charge number Z and mass number A and $\Phi = (Ze/A)\,\phi$. T_p is the proton rest mass energy and $J_{LIS,k}$ is local interstellar spectrum of CR nuclei type k. Similarly, for electrons and positrons, the equation will take the form,

$$J_e(T_e, \phi) = J_{LIS,e}(T_e + \phi)\,\frac{(T_e)\,(T_e + 2T_q)}{(T_e + \phi)(T_e + \phi + 2T_q)}, \tag{2.7}$$

where ϕ is the solar modulation potential, J_e is the differential intensity of the electron-positron, T_e is the kinetic energy of electron-positron, T_q is the electron rest mass energy and $J_{LIS,e}$ is local interstellar spectrum of electron-positron.

2.2.2 Distribution of Galactic Molecular clouds

GMCs are the main sources of molecular hydrogen in our Galaxy. Secondary CRs are produced in interactions with primary CRs in the molecular cloud environment, which contribute to the observed CR spectrum. In this work, we consider all the GMCs recently reported in Rice *et al.* [213], Chen *et al.* [214] and Aharonian *et al.* [165]. First, we use the catalog of GMCs from Rice *et al.* [213], where they presented a list of 1064 GMCs, by using a dendrogram-based decomposition of a previous most uniform, large-scale all-Galaxy CO survey [164]. The objects are distributed in the Galactic disk between $180^\circ > l > 13^\circ$ and $348^\circ > l > 180^\circ$ within $-5^\circ < b < 5^\circ$, widely spread in the Galaxy covering distances from ~ 1 to ~ 16 kpc. Next, we take GMCs closer to Earth, which are reported by Chen *et al.* [214]. These GMCs have been traced by optical/near-infrared (IR) dust extinction

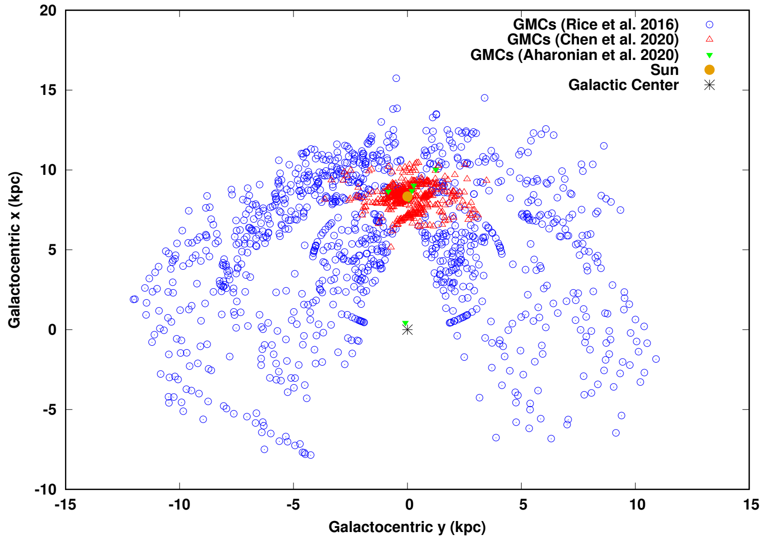

Figure 2.2 Positional distribution of the GMCs in a 2D X-Y plane. The GMCs shown here are taken from Rice *et al* [213], Chen *et al* [214] and Aharonian *et al* [165], similar to Figure 2.1.

measurements. The distances to these GMCs have been accurately measured by 3D dust extinction mapping methods. These GMCs have been identified based on 3D dust reddening maps of the Galactic plane and estimates of color excess, although these GMCs have not been analyzed by *Fermi*-LAT. In work by Chen *et al.* [214], 567 GMCs have been detected within 4 kpc from the Earth. The GMCs are distributed in the Galactic disk, in the range of Galactic longitude $0° < l < 360°$ and Galactic latitude $-10° < b < 10°$. In addition to this, we also take into account the GMCs from the recent work by Aharonian *et al.* [165], where they have analyzed the *Fermi*-LAT gamma-ray data from nearby GMCs. Using the information of the Galactic latitude (b) and longitude (l) from these catalogs, we can calculate the positions of the GMCs in the Galaxy in a galactocentric coordinate system. We use the equations from [213, 227, 228], taking into account that the Sun is at $z_0 \sim 25$ pc above the Galactic plane. The equations are

$$\begin{aligned} x_{gal} &= R_0 \cos\theta - d_\odot(\cos l \cos b \cos\theta + \sin b \sin\theta)\,, \\ y_{gal} &= -d_\odot \sin l \cos b\,, \\ z_{gal} &= R_0 \sin\theta - d_\odot(\cos l \cos b \sin\theta - \sin b \cos\theta)\,, \end{aligned} \tag{2.8}$$

where, $\theta = sin^{-1}\frac{z_0}{R_0}$, $R_0 = 8.34$ kpc is the distance of the Sun from the GC, $d_\odot$ is the kinematic distance of the individual GMCs from the Sun. The positional distribution of these GMCs is given in Figure 2.1 and Figure 2.2.

Generally, by tracing the CO emission in the Galaxy and multiplying the CO emissivity with the CO-to-H_2 conversion factor, the gas density of molecular hydrogen is modeled

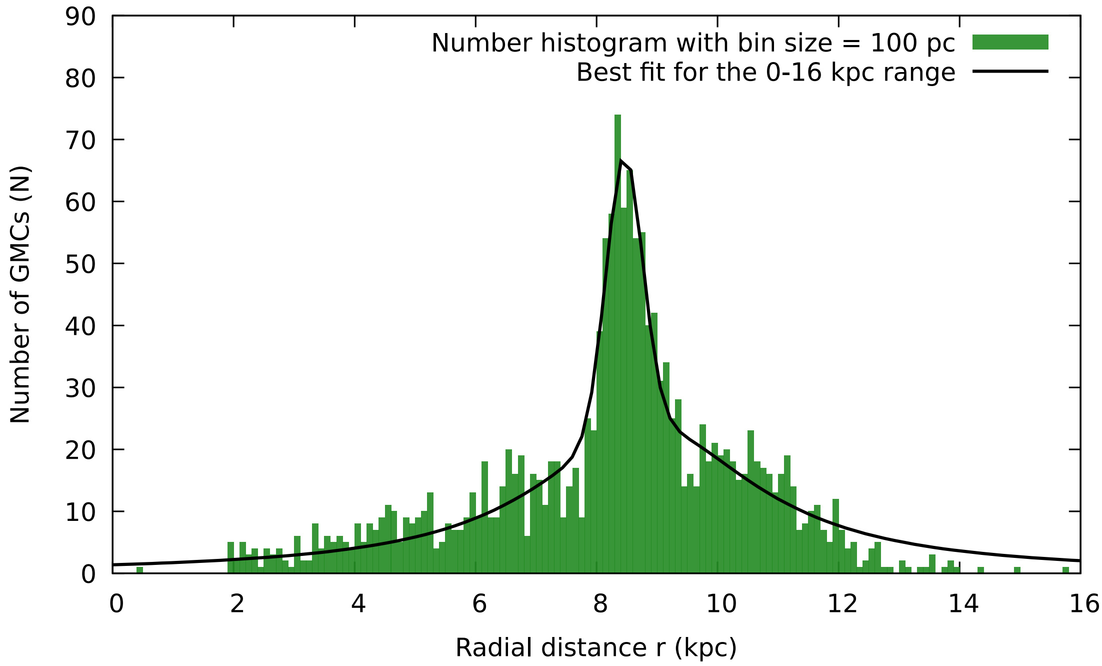

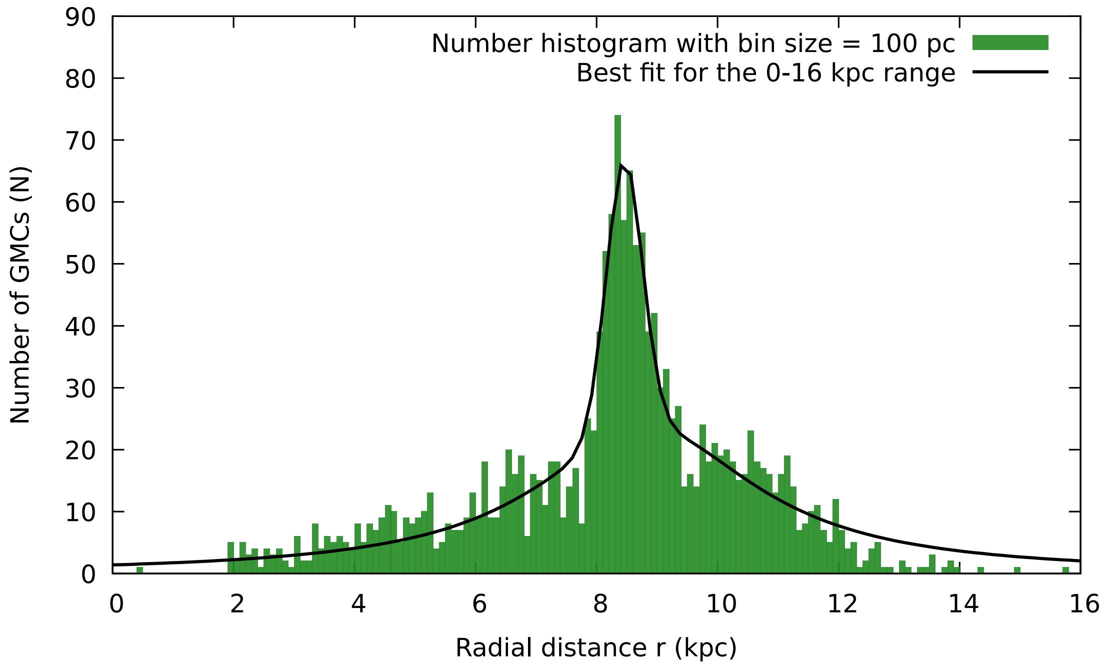

Figure 2.3 Radial number profile of GMCs in Galaxy. *Upper Panel:* Histogram 1 : All of the GMCs from [213], [214] and [165] have been taken into account in this case. *Lower Panel:* Histogram 2 : All of the GMCs from [213], [214] and [165], other than 10 GMCs considered for CASE 3, have been taken into account in this case. In both cases, the black line denotes the linear combination of Gaussian and Lorentzian distribution functions. This black line depicts the functional fit of the histogram in the entire spatial range.

Table 2.1 Best fit parameters for the linear combination of Gaussian and Lorentzian distributions.

Histogram	a_1	σ	μ	a_2	r_0	γ
Histogram 1	33.5319	0.301458	8.45895	23.7586	8.8329	2.19179
Histogram 2	32.9649	0.29976	8.45858	23.5482	8.8312	2.20913

[43, 48–51]. In this work, it can be seen that the GMCs taken from Rice *et al* [213], Chen *et al* [214], and Aharonian *et al* [165], predominantly reside in or very close to the Galactic plane. We consider only the radial distribution of the GMCs. We assume concentric circles of constant bin size of 100 pc, centered at the GC, and build histograms for the number of GMCs residing in each bin in the Galactic plane, covering the radial distance from the GC to the outer region of the Galaxy. The region adjacent to the GC (within 12°) is excluded in the catalog [213]; hence there is a large wedge-shaped gap between the first and fourth quadrant, whereas GMCs reported in Chen *et al* [214] span the entire Galactic longitude, hence there is no gap. First, we consider all of the GMCs from Aharonian *et al* [165], Rice *et al* [213] and Chen *et al* [214], and build number histogram with them, i.e., we consider CASE 2 and CASE 3 GMCs in one histogram. The histogram gives us the variation of the number of GMCs with radial distance. We name this number histogram, where we have included all of the GMCs considered in our work, Histogram 1. Due to the inclusion of many GMCs in the near-Earth region, a peak can be observed near r = 8 kpc. We have fitted the number histogram with a linear combination of the Gaussian distribution function and Lorentzian distribution function, which extends from the center of the Galaxy to the outer region of the Galaxy. The Gaussian radial distribution function has the general form $N_1(r) = \frac{a_1}{\sigma\sqrt{2\pi}} e^{-(r-\mu)^2 / 2\sigma^2}$, where σ is the variance, μ is the mean, 'a_1' is the normalization factor and the Lorentzian radial distribution is given by $N_2(r) = \frac{a_2\,\gamma^2}{(r-r_0)^2+\gamma^2}$, where '$a_2$' is the normalization factor, r_0 is the location of the peak of the distribution, and γ denotes half width of the distribution at half of the maximum height. The cumulative distribution function is written by N(r) = N_1(r) + N_2(r). This distribution function is fitted on the number histogram titled Histogram 1, and the corresponding plot is shown in the Figure 2.3 upper panel. The fit parameters for 100 pc bin size are given in the following Table 2.1. Integrating this number profile N(r) per unit bin width over the entire spatial region, we get back very closely the total number of GMCs considered. The functional fit of Histogram 1 will be used in determining proton, antiproton fluxes, and B/C, ^{10}Be/^{9}Be ratios.

Next, we consider another scenario in which we omit nearby GMCs, Taurus, Lupus, and Orion A. Moreover, we omit the 7 GMCs out of the 567 GMCs reported in [214], where we have assumed reacceleration due to magnetized turbulence is occuring. Apart from these 10 GMCs, we take all of the other GMCs considered in this work and, following the previous method, build a number histogram, taking 100 pc as bin width, which is our

CASE 2. As we can see, the nature of the number histogram in the second scenario does not change much from that of the first scenario, as the omission of 10 GMCs does not alter much of the content of the molecular hydrogen component. We label this second number histogram as Histogram 2. As the nature of the Histogram 2 is very similar to that of Histogram 1, we fit this number histogram with the linear combination of Gaussian and Lorentzian distribution functions, the same as before. The fit parameters are given in Table 2.1, considering 100 pc bin width, and the fit of the histogram has been shown in Figure 2.3 lower panel. As can be seen, there is a very slight change in the fit parameters, which is expected. This functional fit of the Histogram 2 will be used in determining electron and positron spectra and positron fraction in the later sections.

In order to obtain the radial, average n_{H_2} gas density profile in our Galaxy, we have used the following expression,

$$n_{H_2}(r) =< n_{H_2} > \times \left(\frac{N(r)}{N_{total}} \right) , \tag{2.9}$$

where N(r) represents the linear combination of Gaussian distribution fits and Lorentzian distribution fits for the number of GMCs in the Galaxy considered in our work, N_{total} is the total number of GMCs considered, and $< n_{H_2} >$ is the average number density. The number density generally considered for GMCs is $\sim 100\ cm^{-3}$ [163]. Since we have essentially smoothed out each discrete clump of GMCs into a radially continuous distribution of molecular hydrogen, ranging from ∼ 0 kpc to ∼ 16 kpc, the average density of the distribution is taken as $< n_{H_2} > \sim 10\ cm^{-3}$.

The inclusion of vertical distribution of GMCs does not affect the density distribution used in our study since all the GMCs considered in this work reside near the Galactic plane, as previously stated. While building Histogram 1, all of the GMCs (CASE 2 + CASE 3) were taken into account. But for the second scenario, 10 GMCs were omitted while building Histogram 2; hence only CASE 2 GMCs were considered. Secondary lepton production in the 10 nearby GMCs omitted from CASE 2 is modeled individually, which is our CASE 3 and has been discussed in more detail in the next section.

2.3 Contributions from nearby, sub-kpc GMCs

After combining CASE 1 and CASE 2, we find that the total positron flux is insufficient to fit the observed data. Hence, in order to fit the observed flux, we consider the contributions from nearby GMCs (d ≤ 1 kpc), which was defined as CASE 3 previously. CASE 3 includes Taurus, Lupus, and Orion A, which are members of the Gould Belt complex, and the 7 GMCs selected from the catalog given by Chen *et al.* [214]. GMCs are dense, concentrated clumps of cold protons in the Galaxy. When primary CR protons injected from the SNRs propagate through these clumps of cold protons, gamma-rays, and leptons are produced by hadronic interactions (*pp*). Cosmic ray reacceleration is also a proposed mechanism that can occur inside GMCs due to magnetized turbulence [166]. We include the contribution of individual nearby GMCs to the total lepton spectra and positron fraction.

First, we include three of the nearby GMCs, Taurus, Lupus, and Orion A, which act as local sources of secondary CRs, and contribute to the total fluxes of leptons and gamma-rays. We note that these GMCs are not included in the catalog of Rice *et al*. [213] or Chen *et al* [214], hence there has been no double counting in our work. These three GMCs are members of the Gould Belt complex, and being our nearest GMCs, they contribute significantly to the positron and electron flux. The gamma-ray analysis of these GMCs was done in detail in [165]. Previously, Taurus and Orion A were studied in [229, 230], while Lupus was studied for the first time in [165]. Following the definition given in [165], $B \equiv \frac{M_5}{d_{kpc}^2}$, where $M_5 = \frac{M}{10^5\,M_\odot}$ and $d_{kpc} = \frac{d}{1kpc}$, M is the mass of the GMCs, d is the distance of these three GMCs from the Earth and $M_\odot$ is the solar mass, these three GMCs from the Gould Belt complex has 'B' parameter sufficiently higher than 1, which makes them detectable by *Fermi*-LAT. The position coordinates, masses, distances from the Earth, and GC, values of the parameter 'B' of these three GMCs are given in Table 2.2.

Table 2.2 GMC parameters: Galactic coordinates (l, b), masses M, distances from the Earth (d), Galactocentric distance (R_{GC}) and the B parameter from [165] and references therein.

Cloud	l (deg)	b (deg)	Mass ($10^5 M_\odot$)	d (kpc)	R_{GC} (kpc)	B
Taurus	171.6	-15.8	0.11	0.141±0.007	8.4	5.6
Lupus	338.9	16.5	0.04	0.189±0.009	8.2	1.0
Orion A	209.1	-19.9	0.55	0.43±0.02	8.4	3.0

The gamma-ray fluxes produced in these GMCs in *pp* interactions through the production of neutral pions and their subsequent decay have been calculated in [165] and fitted to *Fermi*-LAT data. They have calculated the parent CR proton density spectrum $J_p(E_p)$ for each of these GMCs by fitting the observed gamma-ray spectrum,

$$J_p(E_p) = \rho_{0,CR} \left(\frac{E_p}{E_0}\right)^{-\alpha}, \tag{2.10}$$

where $\rho_{0,CR}$ is the normalisation constant, $E_0 = 10$ GeV is the reference energy, and α is the spectral index. The values for CR proton density $\rho_{0,CR}$ at 10 GeV and spectral index α for the three GMCs used in our work are given in Table 2.3.

In *pp* interactions, charged pions are produced along with neutral pions, which subsequently decay to charged muons. Electrons and positrons are produced from the decay of these charged muons. We have calculated the electron and positron fluxes produced in these three GMCs from *pp* interactions following the formalism given in [231] and using the proton density spectrum given in [165]. The cross section for the production of leptons

Table 2.3 The spectral indices and CR proton densities at 10 GeV derived from the gamma-ray and CO data at the location of the GMCs [165], errors on the normalization result from the sum in quadrature of the statistical error deriving from the fit and the 30% uncertainty on the B parameter (see Table III of [165]).

Cloud	$\rho_{0,CR}$ $[10^{-12} GeV^{-1} cm^{-3}]$	α
Taurus	1.43 ± 0.5	2.89 ± 0.05
Lupus	1.09 ± 0.4	2.74 ± 0.1
Orion A	1.55 ± 0.5	2.83 ± 0.05

was taken from [231], which can be written as,

$$\begin{aligned}\sigma_{inel}(E_p) &= 34.3 + 1.88\,L + 0.25\,L^2 \text{ mb},\\ &\quad \text{for } E \geq 100 \text{ GeV}\\ &= (34.3 + 1.88\,L + 0.25\,L^2)\\ &\quad \times \left[1 - \left(\frac{E_{th}}{E_p}\right)^4\right]^2 \text{ mb},\\ &\quad \text{for } E \leq 100 \text{ GeV}\end{aligned} \tag{2.11}$$

where L = $\ln(E_p/1 \text{ TeV})$, and $E_{th} = m_p + 2m_\pi + m_\pi^2/2m_p = 1.22 \times 10^{-3}$ TeV, which is the threshold energy of production of π mesons. [231] obtained this approximation with the fit of the numerical data included in the SIBYLL code. We note that if we include more GMCs that are further away from the Earth and away from the Galactic plane, our result does not change significantly, as the effect of the nearest GMCs is most dominant on the electron and positron fluxes.

GMCs are highly magnetized dense astrophysical objects with complex inhomogeneous structures. Parent CRs injected inside GMCs, traverse through weakly ionized turbulent plasma, which also contains a high magnetic field. As a result, particle energies may increase, or reacceleration may happen due to fluctuating electromagnetic fields inside the GMCs. Although gamma-ray data analysis has not shown the effects of such reacceleration happening inside GMCs till now, [166] argued that it is physically possible. The gravitational energy of the GMCs is very high (ranging in $\sim 10^{50}$ - 10^{51} erg). If at least a very small part of this gravitational energy can be transformed into the energy of the accelerated particles, then the GMCs can effectively act as particle accelerators. It is necessary for the GMCs to be strongly turbulent in nature in order to accelerate the particles effectively. Such turbulence may occur with the cloud collapse phenomena. Since the energy of the turbulence is comparable to cloud gravitational energy, it may significantly slow down the cloud collapse. Hence part of the gravitational energy may get transformed into turbulent energy of the GMCs. [166] argued that if there existed a mechanism by which this turbulent energy was transformed into particle energy, then there would be an effective acceleration inside the GMCs. Although this mechanism is theoretically possible, as suggested by [166], it has not been observed yet. We assume that the conditions for the reacceleration of CRs are satisfied in a small number of GMCs.

In order to apply this mechanism in our work, we have selected the GMCs carefully. In general, we applied three necessary conditions to select 7 GMCs from [214], in which we assumed reacceleration of the particles is happening. We will show that a small contribution from these GMCs is enough to explain the positron excess adequately. The conditions for selection are the following,

1) The B parameter, defined above, must be less than 0.2. It has been mentioned in [165] that in the cases of sources of angular extensions smaller than 1°, *Fermi*-LAT is able to detect the GMCs with $B \geq 0.4$. In the case where the compact GMCs are located in uncrowded regions, *Fermi*-LAT detection threshold can be as small as $B \approx 0.2$. Again for very close GMCs ($d << 1$ kpc), the detection threshold can exceed $B \approx 1$ to compensate for the loss of the sensitivity of *Fermi*-LAT due to large extensions of the GMCs. Just to ensure the fact that these GMCs are always outside the detection threshold of *Fermi*-LAT as of now, we select only the GMCs for which $B < 0.2$. Thus this condition takes into account the fact that there may be GMCs in which reacceleration is happening, but they are not detected by *Fermi*-LAT.

2) Next, we select only the GMCs within 1 kpc of the Earth. Since leptons lose energy very efficiently by radiative losses, it is necessary to select nearby GMCs, so that they contribute significantly to the observed lepton spectrum. Reacceleration can happen in far away GMCs too, but their contribution will not be significant.

3) As mentioned in [166], the turbulence occuring in the GMCs has a scale length. If the size of the GMCs is less than the maximum scale length of the plasma turbulence, then the particles will escape the GMCs, before getting reaccelerated properly. The maximum scale length of plasma turbulence inside GMCs is of the order of ~ 10 pc [166]. That is why we selected only the GMCs which have a radius greater than 10 pc. In this way, we take into account the fact that the particles are getting reaccelerated before escaping from the GMCs.

Based on these three conditions, we have selected 7 GMCs, in which we assume reacceleration is happening. The physical description of these GMCs is listed in Table 2.4. There is no other GMC that passes through these selection criteria in our set of GMCs.

It has been shown in [166] that due to the effect of reacceleration, the spectrum of injected particles gets harder. It has been calculated that the spectral index of the injected positron is -1.7, which is indicative of a hard spectrum. We use these hardened spectra from 7 selected GMCs and show that even if a very small flux of positrons is injected with this hardened spectrum, then taking their contribution into account, the positron excess can be explained. Next, we give the equations needed to calculate the flux of leptons after

Table 2.4 7 selected GMCs parameters: Galactic coordinates (l, b), radius, distances from the Earth (d), mass, and the B parameter from [214].

GMC ID	l (deg)	b (deg)	Radius (pc)	d (pc)	Mass ($M_\odot$)	B
27	121.498	-7.378	15.027	983.0±23.2	12313.7	0.12
233	-147.177	-9.806	10.750	866.7±20.5	8483.8	0.11
286	174.871	5.824	11.969	982.0±23.2	14307.2	0.14
288	-75.048	7.070	12.095	911.5±21.5	8152.1	0.098
295	47.013	-5.399	11.434	914.5±21.6	9601.4	0.11
342	-96.318	4.705	11.041	952.7±22.5	14479.9	0.15
385	142.282	1.032	11.859	967.4±39.6	12580.0	0.13

traversing the distance from the nearby GMCs to the Earth.

The magnetic field inside the GMCs is higher compared to the mean interstellar magnetic field [232]. The secondary electrons and positrons produced in nearby GMCs are expected to lose energy before they are injected into the ISM. The radiative loss of higher energy leptons is more than the lower energy ones; as a result, we expect an exponential cutoff in their spectrum at high energy. Also, strong gradients may be present in the CR distribution inside the GMCs, which may enhance the generation of plasma waves and, thus, suppress the diffusion coefficient ([233], [234]). This suppressed diffusion coefficient inside the GMCs will lead to suppression of secondary leptons that will actually get injected into ISM because not all of the secondary leptons produced will be able to escape the GMC environment due to diffusive confinement and get injected in the ISM. So, in order to take this realistic situation into account, we have assumed that not all but a majority fraction (~ 90 %) of the total secondary lepton spectra produced will be injected from the GMCs into the ISM. This suppression of secondary leptons will reflect in the normalization of injected lepton spectra considered below.

The injection spectra are expressed as a power law in Lorentz factor of the injected electrons and positrons $\gamma_e = E_e/m_e c^2$,

$$Q(\gamma_e, d) = Q_0 \gamma_e^{-\beta_e}\, exp\left(-\frac{\gamma_e}{\gamma_{e,c}}\right) \delta(d), \tag{2.12}$$

where the cutoff Lorentz factor $\gamma_{e,c} = E_{e,c}/m_e c^2$, a unit of Q_0 is $\mathrm{GeV^{-1}s^{-1}}$, d is the distance of each cloud from the observer and the Dirac delta function, in this case, signifies that we are considering point sources. During propagation in the ISM for time scales (t) less than 10^7 years, the dominant radiative loss processes of relativistic electrons and positrons are synchrotron and inverse Compton (IC) scattering. The formalism for including the propagation effects by solving the transport equation, including radiative losses and diffusion, has been discussed in [235]. The expression for IC and synchrotron energy loss term p_2 has been used from [235],

$$p_2 = 5.2 \times 10^{-20} \frac{w_0}{1 \frac{eV}{cm^3}} s^{-1}, \tag{2.13}$$

where $w_0 = w_B + w_{MBR} + w_{opt}$, w_B is the energy density of the magnetic field, w_{MBR} is microwave background radiation energy density, w_{opt} is energy density of optical-IR radiation in interstellar space. For our study, we assume $w_0 \approx 1 \frac{eV}{cm^3}$.

The diffusion term has been included following [235],

$$D(\gamma_e) = D_0 \left(1 + \left(\frac{\gamma_e}{\gamma_{e,*}}\right)\right)^{\delta}. \tag{2.14}$$

Thus D is constant for $\gamma_e << \gamma_{e,*}$, and energy dependent for $\gamma_e \geq \gamma_{e,*}$, where $\gamma_{e,*} = E_{e,*}/m_e c^2$.

For point sources emitting continuously with a constant rate during the time $0 \leq t' \leq t$, we get the following energy spectrum,

$$f_{st}(d,t,\gamma_e) = \frac{Q_0 \gamma_e^{-\beta_e}}{4\pi\, D(\gamma_e)\, d} \,\mathrm{erfc}\left(\frac{d}{2\sqrt{D(\gamma_e) t_{\gamma_e}}}\right) \times \exp\left(-\frac{\gamma_\mathrm{e}}{\gamma_\mathrm{e,c}}\right), \tag{2.15}$$

where $t_{\gamma_e} = min(t, \frac{a}{p_2 \gamma_e})$ and a = 0.75 [235], in our case $t >> \frac{a}{p_2 \gamma_e}$.

The electron and positron flux from nearby GMCs without including solar modulation effect is,

$$J_{obs}^{e^\pm}(\gamma_e) = \left(\frac{c}{4\pi}\right) f_{st}(d,t,\gamma_e). \tag{2.16}$$

While calculating the total observed spectrum from these nearby GMCs on Earth, we also take into account the solar modulation effect, described by equation (2.7). The values of the relevant parameters used to calculate the secondary electron and positron fluxes from nearby GMCs Taurus, Lupus, Orion A and 7 selected GMCs are listed in Table 2.6. Using equation (2.16), we calculate the total $e^\pm$ fluxes from these 10 nearby GMCs, which is our CASE 3.

Finally, we add the lepton fluxes from CASE 1, CASE 2, and CASE 3 in order to fit the observational data. It must be noted that secondary particles, such as antiprotons, are also produced in these nearby GMCs. But we have checked using the formalism used in [236], that the antiproton flux contribution from Taurus, Lupus, Orion A, and the 7 selected GMCs, is very less. So we take into account these 10 GMCs in Histogram 1, as previously mentioned while calculating different hadronic spectra/ratios as well as antiproton flux so that however negligible their contribution might be, they get consistently included in the process of producing secondary CRs. Secondary Borons produced in these GMCs are taken into account in the same way. Leptons lose energy radiatively very fast; thus,

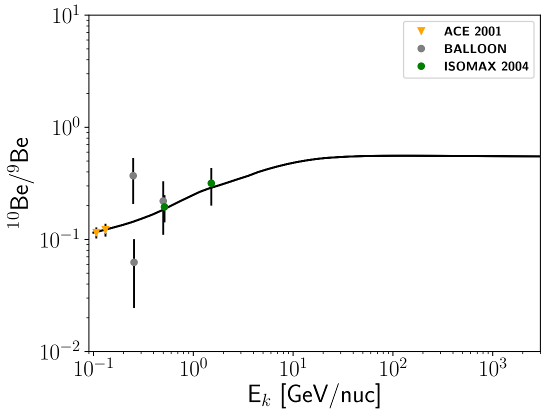

Figure 2.4 ^{10}Be/^{9}Be ratio calculated using **DRAGON** code, and plotted with the observational data given by ACE data [237], several Balloon data, and ISOMAX [238] data. The black line signifies the simulated value of the ratio. The solar modulation potential was considered to be ϕ = 0.2 GV.

nearby GMCs contribute more significantly compared to the GMCs, which are far away from the Earth. Thus these nearby GMCs are modeled individually. Taurus, Lupus, and Orion A are the nearest GMCs analyzed in detail in work by [165]. Also, since we are considering 7 GMCs from [214] as possible reacceleration sites, those GMCs are also modeled separately. In the next section, we discuss the results we have got from our simulated model.

2.4 Results

In this section, we discuss the results that we have got from our model. We have divided our results into four subsections. In the first subsection, we discuss the simulated proton, antiproton fluxes, and B/C, ^{10}Be/^{9}Be ratios. In the second subsection, we discuss the lepton fluxes and positron fraction and show how our model fits the positron spectrum. In the third subsection, we discuss lepton dipole anisotropy from the nearby GMCs. In the last subsection, we discuss the uncertainties in CR propagation model parameters and expected fluxes from the nearby GMCs. We have used the plain diffusion (PD) model to study CR propagation with the **DRAGON** code assuming the sources follow SNR distribution [47]. This model includes diffusion and interactions of CRs but the effect of reacceleration or convection was not considered.

2.4.1 Protons / Cosmic ray nuclei / Antiprotons

In our analysis, we have fitted the observed CR nuclei data in the following way. We have used the standard model given by [41, 42, 221] for neutral and atomic hydrogen and the model given by [46] for the ionized hydrogen. Using these models, we have modeled the ISM hydrogen gas distribution (CASE 1). For molecular hydrogen gas distribution, we have included all the GMCs considered in our work (CASE 2 + CASE 3). We have

Table 2.5 Models and parameter values selected in the PD model to fit the various observed CR nuclei spectra and ratio, using **DRAGON**, are listed in this Table. The parameters used here have been discussed before. D_0, in this case, is the normalization of the diffusion coefficient used for (CASE 1 + CASE 2 + CASE 3). v_A is the Alfven velocity, v_w is the wind or convection velocity, dv_w/dz is vertical gradient of convection velocity.

Model/Parameter	Option/Value
R_{max}	25.0 kpc
z_t	8.0 kpc
L	24.0 kpc
HI gas density type	[41, 42, 221]
HII gas density type	[46]
H_2 gas density type	Equation (2.9)
Source distribution	Ferriere [47]
Diffusion type	Exponential (see equation (2.2))
D_0	2.4 $\times 10^{29}$ cm^2/s
ρ_0	4.0 GV
δ	0.53
η	- 0.40
v_A	0
v_w	0
$\frac{dv_w}{dz}$	0
Magnetic field type	Pshirkov [38]
B_0^{disk}	2×10^{-6} Gauss
B_0^{halo}	4×10^{-6} Gauss
$B_0^{turbulent}$	6.1×10^{-6} Gauss (see equation (2.1))
α_1^k/α_2^k	1.95/2.33
$\rho_{br,1}^k$	7 GV

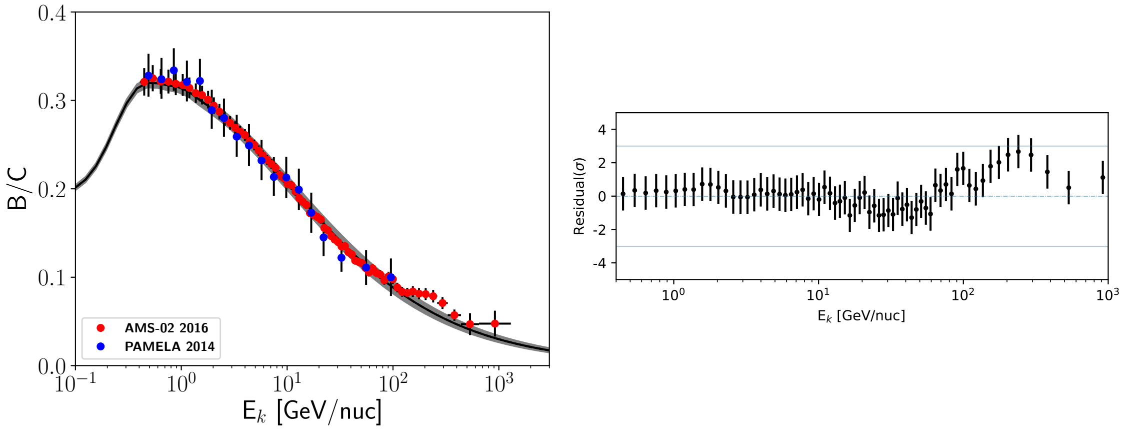

Figure 2.5 *Left panel:* B/C ratio plotted against the observational data reported by AMS-02 [109] and PAMELA [127]. The solid black line is the simulated ratio. The solar modulation potential was considered to be $\phi = 0.0$ GV. The gray-shaded region signifies uncertainties due to variations in CR propagation parameters. *Right panel:* Corresponding residual plot for the fit of simulated B/C ratio to the observed data. The solid blue line signifies a 3σ confidence level. The χ^2/D.O.F. for this fit of B/C ratio is ≈ 0.84.

used the fit parameters of Histogram 1, discussed previously, to take into account the molecular hydrogen content of all of the GMCs. Then we implemented equation (2.9) to model the molecular hydrogen gas density distribution in our simulation.

We have fixed the halo height z_t to a value for which the ^{10}Be/^{9}Be data is well fitted. Such ratios of unstable to a stable isotope of secondary particles is a major constraint for CR propagation. ^{10}Be is the unstable isotope of beryllium, which is unstable to β decay. Since being unstable, ^{10}Be decays faster than its stable counterpart after getting produced from CR interactions inside the Galaxy. The decay time of ^{10}Be becomes longer than the escape time from the Galactic halo for rigidity above 10-100 GV, depending on the size of the halo z_t. This is why the measurement of ^{10}Be/^{9}Be ratio is sensitive to the parameter z_t. Recently [239] has shown that optimum halo height must be around ≈ 7 kpc. That is why we take the halo height considered in our work around that value. We take 8 kpc as our halo height and fit the observed ^{10}Be/^{9}Be ratio. The fit for ^{10}Be/^{9}Be ratio is shown in Figure 2.4, and from there, it can be seen that the choice of our halo height is a good fit for the observed ratio.

We have then subsequently set $B_0^{turbulent}$ using equation (2.1). Next, we have estimated the average diffusion coefficient in the Galaxy by fitting the B/C observed data. Boron is secondarily produced from the spallation of Carbon, which is primary in nature. If the halo height is larger, then the secondary borons are produced more, and also, they spend a long time in the Galaxy, making the secondary-to-primary ratio larger. On the other hand, if the diffusion in the Galaxy is high, then Borons escape the Galaxy faster, and the ratio becomes smaller. Hence it can be seen that the B/C ratio scales with halo height (z_t)

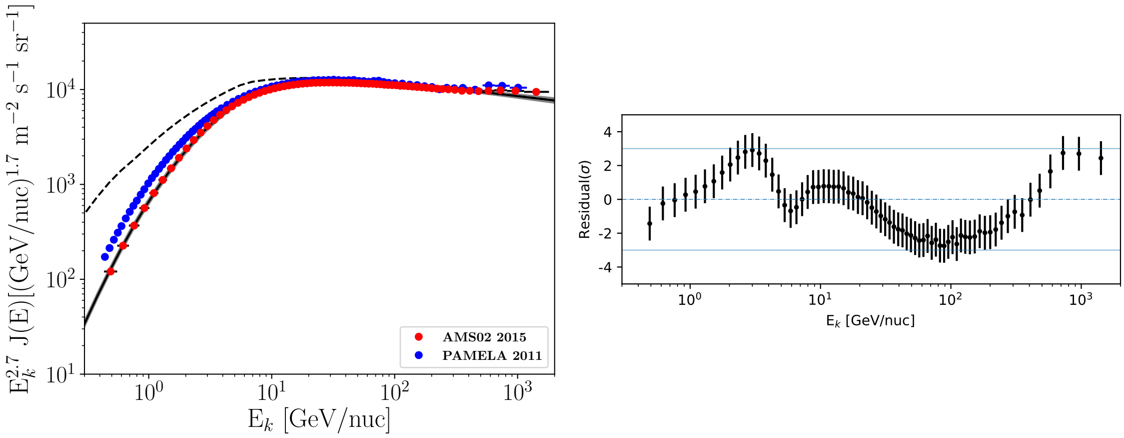

Figure 2.6 *Left panel:* Proton flux calculated using **DRAGON** code, and plotted with the observational data given by AMS-02 [107] and PAMELA [126]. The solar modulation potential considered is ϕ = 0.564 GV. The solid (dashed) black line corresponds to the solar modulated (unmodulated) proton spectrum. The gray-shaded region signifies uncertainties due to variations in CR propagation parameters. *Right panel:* Corresponding residual plot for the fit of simulated proton spectrum to the observed data. The solid blue line signifies a 3σ confidence level. The χ^2/D.O.F. for this fit of proton spectrum $\approx$ 2.9.

and diffusion coefficient D as z_t/D. We have fixed the value of the reference rigidity (ρ_0) and adjusted the normalisation (D_0), δ and η to get a good fit to the observed data of B/C ratio. The ratio and its corresponding residual are plotted in Figure 2.5. From the Figure and the residual plot, it can be seen that our estimation of the average diffusion coefficient is accurate.

Then the spectral indices and breaks of the injected CR spectra are adjusted to get a good fit to the observed proton data given by AMS-02 and PAMELA. We use a low-energy break at around 7 GV. No other high-energy break is used to fit the proton spectrum. The plot for the proton spectrum and its corresponding residual plot are shown in Figure 2.6. Although the residuals show undulation due to small experimental error values associated with proton spectrum data points, it can be seen that the residual calculated for each data point is confined within 3σ confidence level.

We also calculate secondary antiprotons produced in our model. We use CASE 1 + CASE 2 + CASE 3 together to estimate the total flux of antiprotons as a secondary product. Primary CRs interact with ISM gas and molecular hydrogen clumped inside GMCs and produce antiprotons. By taking into account all of the cases together, we get the estimate of antiprotons produced in our model setup. The antiproton spectrum is shown in Figure 2.7 against the data obtained by AMS-02 and PAMELA. The same parameters in Table 2.5 were used to find the total antiproton spectrum.

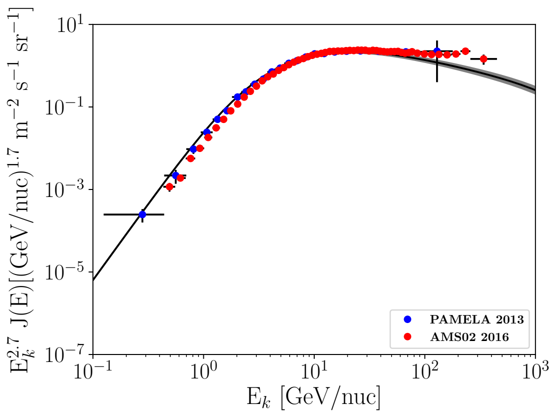

Figure 2.7 Antiproton flux calculated using **DRAGON** code, and plotted with the observational data given by AMS-02 [110] and PAMELA [131]. The solar modulation potential considered is ϕ = 0.564 GV. The solid black line corresponds to the solar-modulated antiproton spectrum. The gray-shaded region signifies uncertainties due to variations in CR propagation parameters.

2.4.2 Leptons

We have adjusted the injection spectrum of primary electrons in our model, given by the broken power law, to get a good fit for the observed data by AMS-02 and PAMELA. The conventional primary electron sources follow the Ferriere distribution [47]. The CR protons and heavy nuclei injected also interact with neutral and ionized hydrogen gas in ISM (CASE 1) and molecular hydrogen in GMCs in the Galactic plane (CASE 2), producing secondary electrons and positrons.

We have used the catalog of GMCs near the Galactic plane from [213], [214], and [165]. We omit 7 GMCs from [214] based on the selection criteria mentioned in the previous section. Also, we omit Taurus, Lupus, and Orion A from [165] and take the contribution of other GMCs into account in CASE 2. We have taken a bin size of 100 pc in radial distance to build the histograms for the number of GMCs in each bin. We have taken all the GMCs of CASE 2 to build the number histogram, which can be fitted by a linear combination of the Gaussian distribution function and Lorentzian distribution function. These distributions are used with the average number density of hydrogen molecules $< n_{H_2} > \sim 10 \;\; cm^{-3}$ to get the molecular hydrogen density distribution in the Galaxy considered in CASE 2. Instead of discrete clumps of GMCs, we have assumed continuous distribution of matter along the Galactic plane, due to this reason, the number density of hydrogen molecules is lower than the typical density of hydrogen molecules in GMCs [163].

The electron spectrum is dominated by primary CR electrons, which are produced in SNRs that follow the Ferriere distribution. Contribution from primary electron sources, along with the contribution of secondary electrons produced in interactions of CRs with

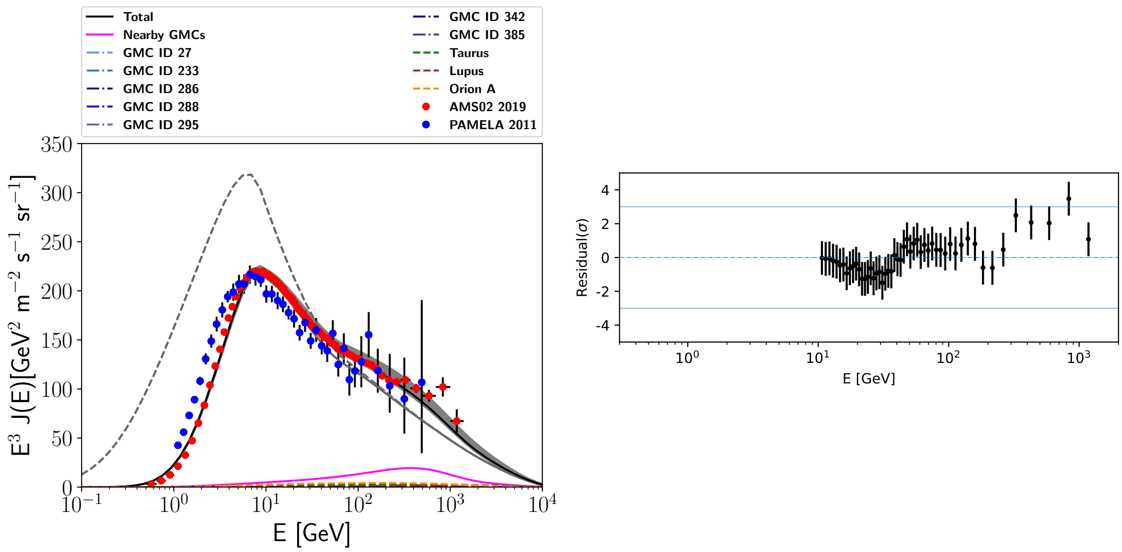

Figure 2.8 *Left panel:* Electron flux calculated using **DRAGON** code, and plotted with the observational data given by AMS-02 [117] and PAMELA [128]. The solid (dashed) gray line is the solar modulated (unmodulated) total flux for (CASE 1 + CASE 2). The Magenta line shows the total flux from nearby GMCs (CASE 3). The black line corresponds to the total flux calculated from our work. The solar modulation potential considered is ϕ = 0.564 GV. The gray-shaded region signifies uncertainties due to variations of CR propagation parameters and uncertainties in the normalization of nearby GMC fluxes. *Right panel:* Corresponding residual plot for the fit of simulated electron spectrum to the observed data from 10 GeV energy and above. The solid blue line signifies a 3σ confidence level. The χ^2/D.O.F. for this fit of electron spectrum above 10 GeV is ≈ 1.22.

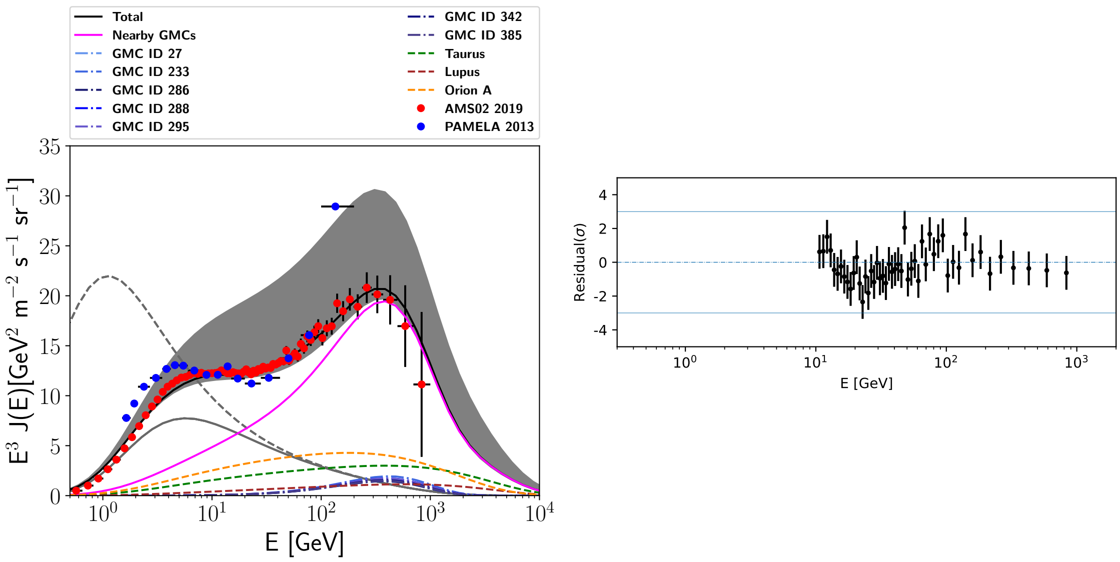

Figure 2.9 *Left panel:* Positron flux using **DRAGON** code, and plotted against the observational data reported by AMS-02 [118] and PAMELA [129]. The solid (dashed) gray line is the solar modulated (unmodulated) total flux for (CASE 1 + CASE 2). The Magenta line shows the total flux from nearby GMCs (CASE 3). The black line corresponds to the total flux calculated from our work. The solar modulation potential considered is $\phi = 0.564$ GV. The gray-shaded region signifies uncertainties due to variations of CR propagation parameters and uncertainties in the normalization of nearby GMC fluxes. *Right panel:* Corresponding residual plot for the fit of simulated positron spectrum to the observed data from 10 GeV energy and above. The solid blue line signifies a 3σ confidence level. The χ^2/D.O.F. for this fit of positron spectrum above 10 GeV is ≈ 0.96.

Table 2.6 Table for the parameters used to calculate total $e^{\pm}$ flux observed on Earth from Taurus, Lupus, Orion A and 7 selected GMCs. Parameters: Q_0 is injection normalization, β_e is the spectral index for $e^{\pm}$ injection from the GMCs, D_0 is the diffusion coefficient normalization, δ is the diffusion index, $E_{e,*}$ is reference energy for the diffusion coefficient, $E_{e,c}$ is the cutoff energy, ϕ is the solar modulation potential. D_0, in this case, is the diffusion coefficient normalization used for CASE 3.

Cloud	Q_0 (GeV$^{-1}s^{-1}$)	β_e	D_0 (cm^2/s)	δ	$E_{e,*}$ (GeV)	$E_{e,c}$ (GeV)	ϕ (GeV)
Taurus	8.5×10^{43}	2.83	2.4×10^{29}	0.53	5×10^3	5×10^3	0.564
Lupus	1×10^{43}	2.72	2.4×10^{29}	0.53	5×10^3	5×10^3	0.564
Orion A	3.6×10^{44}	2.81	2.4×10^{29}	0.53	5×10^3	5×10^3	0.564
GMC ID 27	2.8×10^{38}	1.7	2.4×10^{29}	0.53	5×10^3	6.5×10^2	0.564
GMC ID 233	2.8×10^{38}	1.7	2.4×10^{29}	0.53	5×10^3	6.5×10^2	0.564
GMC ID 286	2.8×10^{38}	1.7	2.4×10^{29}	0.53	5×10^3	6.5×10^2	0.564
GMC ID 288	2.8×10^{38}	1.7	2.4×10^{29}	0.53	5×10^3	6.5×10^2	0.564
GMC ID 295	2.8×10^{38}	1.7	2.4×10^{29}	0.53	5×10^3	6.5×10^2	0.564
GMC ID 342	2.8×10^{38}	1.7	2.4×10^{29}	0.53	5×10^3	6.5×10^2	0.564
GMC ID 385	2.8×10^{38}	1.7	2.4×10^{29}	0.53	5×10^3	6.5×10^2	0.564

ISM gas, are included in our CASE 1. The contribution of secondary electrons produced from primary CRs interacting with GMCs considered in Histogram 2 are included in our CASE 2. Positrons are also produced as secondaries in interactions between primary CR nuclei and atomic, ionized components of hydrogen in the ISM (CASE 1) and also molecular hydrogen components distributed in the Galaxy (CASE 2). We add up the contributions from CASE 1 and CASE 2 to fit the electron and positron spectra. The combined contribution of CASE 1 + CASE 2 is shown with the gray line in the plots of electron and positron spectra. The parameters used for simulating CASE 1 + CASE 2 for electron and positron spectra are presented in tables 2.5 and 2.7.

It is obvious that CR positrons require more nearby sources to explain the observed data. Hence, we consider the contribution of CR interactions in GMCs close to the Earth, which have been analyzed with *Fermi*-LAT data in the work by [165]. We have considered three GMCs, Taurus, Lupus, and Orion A, which are closest to the Earth, for which gamma-ray data have been analyzed. Other GMCs which have been studied with *Fermi*-LAT data in work by [165], are too far from the Earth to be able to contribute significantly. Due to this reason, we have included them in Histogram 2 of CASE 2 and did not model them individually in CASE 3. Further, we assume there is a reacceleration of CRs due to magnetized turbulence in a few nearby GMCs. Due to this process, the CR spectrum gets hardened inside these GMCs. The secondary leptons produced in CR interactions inside these GMCs also have a hard spectrum. The spectral index of this hardened spectrum

Table 2.7 Models and parameter values selected in the PD model to fit the observed lepton spectra and positron fraction, using **DRAGON**, are listed in this Table. The parameters used here have been discussed before. D_0, in this case, is the diffusion coefficient normalization used for (CASE 1 + CASE 2). v_A is the Alfven velocity, v_w is the wind or convection velocity, dv_w/dz is vertical gradient of convection velocity.

Model/Parameter	Option/Value
R_{max}	25.0 kpc
z_t	8.0 kpc
L	24.0 kpc
HI gas density type	[41, 42, 221]
HII gas density type	[46]
H_2 gas density type	Equation (2.9)
Source distribution	Ferriere [47]
Diffusion type	Exponential (see equation (2.2))
D_0	2.4 $\times 10^{29}$ cm^2/s
ρ_0	4.0 GV
δ	0.53
η	- 0.40
v_A	0
v_w	0
$\frac{dv_w}{dz}$	0
Magnetic field type	Pshirkov [38]
B_0^{disk}	2×10^{-6} Gauss
B_0^{halo}	4×10^{-6} Gauss
$B_0^{turbulent}$	6.1×10^{-6} Gauss (see equation (2.1))
$\alpha_1^e/\alpha_2^e/\alpha_3^e$	2.0/2.7/2.4
$\rho_{br,1}^e/\rho_{br,2}^e$	8/65 GV
ρ_c^e	10 TeV

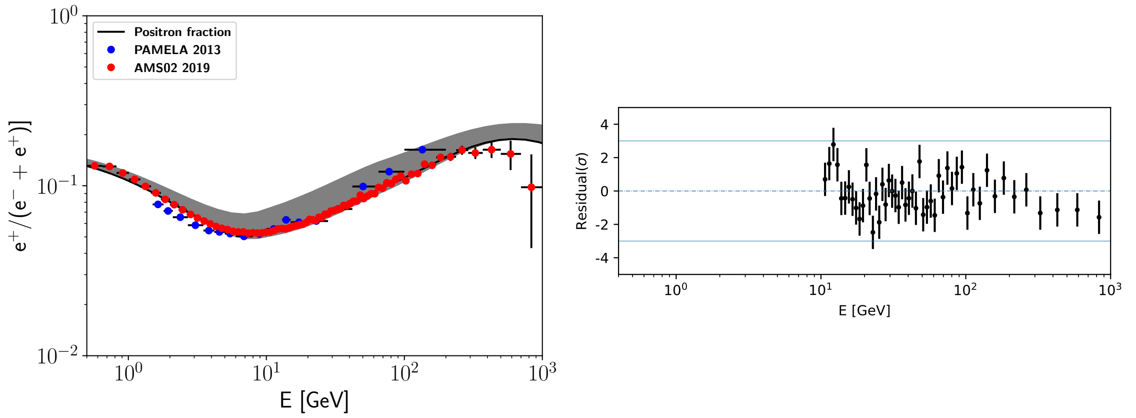

Figure 2.10 *Left panel:* Positron fraction calculated using **DRAGON** code, and plotted with the observational data given by AMS-02 [118] and PAMELA [129]. The gray-shaded region signifies uncertainties due to variations of CR propagation parameters and uncertainties in the normalization of nearby GMC fluxes. *Right panel:* Corresponding residual plot for the fit of simulated positron fraction to the observed data from 10 GeV energy and above. The solid blue line signifies 3σ confidence level.

comes out to be -1.7, which has been calculated in work by [166]. We consider such hardened injection spectrum from 7 GMCs selected from [214], based on three criteria, which have been discussed in the previous section. The total contribution from Taurus, Lupus, Orion A, and a small contribution from these 7 GMCs, due to reacceleration, is considered as CASE 3 in our model. The values of the necessary parameters of these GMCs required to fit the data are given in Table 2.6.

In the figures 2.8 and 2.9, the electron flux and positron flux are shown against the data given by AMS-02 and PAMELA. In Figure 2.10, the corresponding positron fraction is also shown. The residuals for these plots are also shown. Since below 10 GeV, heliospheric modulation plays an important role, and the positron spectrum effectively starts to rise from 10 GeV, we show the residuals from 10 GeV and above. Data points below 10 GeV were not used while plotting the residuals for electron, positron spectra, and positron fraction. Please note the differences between the spectral shapes of Taurus, Lupus, Orion A, and 7 selected GMCs. These differences arise due to the differences between the parameters for the source term of nearby GMCs. For Taurus, Lupus, and Orion A, the injected secondary lepton spectra are soft in nature [165], whereas, for 7 selected GMCs, we get harder injected secondary lepton spectra [166], because of the assumption of reacceleration happening inside these GMCs due to magnetized turbulence. Hence, there are differences in the spectral indices of injected lepton spectra β_e. The cutoff energy $E_{e,c}$ is also different for these 7 GMCs. In 7 GMCs where reacceleration due to magnetized turbulence is assumed, it can be expected that the magnetic field is higher than that of average GMCs; otherwise, every other GMCs would have shown signs of reacceleration in their respective gamma-ray analysis. Since the average magnetic field is higher in these 7

GMCs, compared to that of Taurus, Lupus, and Orion A, radiative losses are more due to the synchrotron process, and thus, the cutoff in the spectrum is expected at comparatively lower energy. This makes the cutoff energy ($E_{e,c}$) of the 7 selected GMCs lower compared to that of Taurus, Lupus, and Orion A. See Table 2.6 for the distinction between the injected spectral indices β_e and cutoff energy $E_{e,c}$ of these GMCs.

2.4.3 Anisotropy due to nearby GMCs

Nearby electron-positron sources can induce anisotropy that can be observed on Earth. This anisotropy is mainly determined by the structure of the magnetic field in the solar neighborhood, which can be calculated by the formalism given in [191], as $\frac{3D}{v}\,\frac{\Delta N}{N}$. Here v is the relativistic speed of the CRs, and D is the diffusion coefficient for effective collision frequency V^2/D of CRs. For nearby GMCs, the anisotropy can be calculated by [191, 207, 240]

$$Anisotropy\ (\delta) = \frac{3\,d}{2\,c\,t_{\gamma_e}}\,\frac{N^{GMC}_{e^-+e^+}}{N^{total}_{e^-+e^+}}. \tag{2.17}$$

Here d is the distance of nearby GMCs from the Earth, t_{γ_e} is the energy loss timescale due to IC and synchrotron processes. The $e^{\pm}$ pair emission ratio $\mathrm{N}^{GMC}_{e^-+e^+}/\mathrm{N}^{total}_{e^-+e^+}$ from all sources observed on Earth, determine the nearby discrete source anisotropy. In Figure 2.11, we show the anisotropy calculated for the nearby GMCs considered in our work, against the upper limits by *Fermi*-LAT ([241], [242]). Note that the anisotropy in lepton spectra from Taurus, Lupus, and Orion A increases with energy because of their soft secondary lepton spectra, while due to the hard secondary lepton spectra from the 7 GMCs of [214], the anisotropy decreases sharply with energy.

2.4.4 Uncertainties in Propagation Model Parameters and Fluxes from GMCs

We discuss the uncertainties that were considered in our work in model parameters of CR propagation and expected fluxes from nearby GMCs (Taurus, Lupus, and Orion A).

First, we have performed a systematic χ^2 analysis around the best-fit values for the fit of the B/C ratio. The standard χ^2 analysis is given by,

$$\chi^2 = \sum_{i=1}^{n}\left[\frac{y_i^{obs}(E) - y_i^{mod}(E, a_M)}{\sigma_i}\right]^2, \tag{2.18}$$

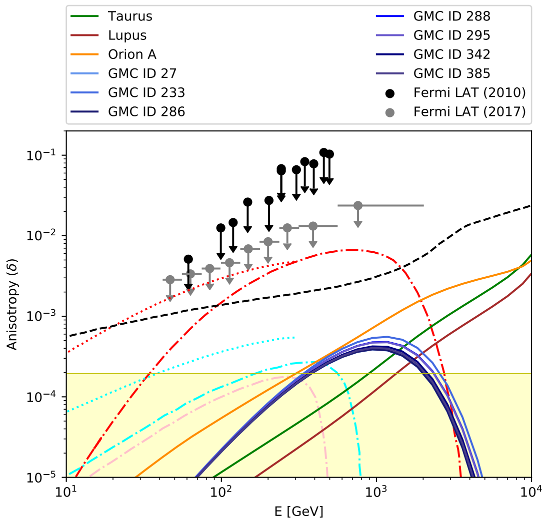

Figure 2.11 Cosmic ray electron + positron anisotropy for nearby GMCs (CASE 3) in comparison with *Fermi*-LAT upper limits. The upper limits are taken from [241] and [242]. We also show electron + positron anisotropy generated from other candidates for positron excess, pulsars, and dark matter. The black dashed line is the anisotropy calculated for the dark matter distributed in Milky Way Galaxy [241]. The dot-dashed lines are for astrophysical objects such as pulsars, Monogem (red), Geminga (cyan), and B1055-52 (pink) [207]. The dotted lines are also for pulsars but taken from the work of [202](see Figure 5 from [202]). The red dotted line is for Monogem (B0656+14) like source, and the cyan dotted line is for the Geminga-like source. The yellow filled region signifies the δ threshold at the 2σ level, for $\dot{N_{ev}} = 3 \times 10^7$ electrons and positrons per year above 10 GeV, and $t_{obs} = 7$ years. Above this region, the Fermi gamma-ray telescope should be able to detect dipole anisotropies at 2σ confidence level [202].

where $y_i^{obs}(E)$ is the B/C ratio data observed by AMS-02, $y_i^{mod}(E, a_M)$ is the simulated values of our model at specific energies respectively, and a_M are the values of M parameters in the simulation. The standard error of each observed value is given by σ_i.

As mentioned earlier, the fit for the B/C ratio depends on halo height (z_t) and parameters of diffusion (D_0, δ). We have varied the CR propagation parameters z_t, D_0, and δ around their best-fit values. In order to find the allowed range of these parameters, we have restricted the value of the reduced χ^2 to be less than 3 for the B/C data, similar to the treatment that has been done in [243]. Note that this value of the reduced χ^2 has only been selected to constrain the allowed values of CR propagation parameters within a reasonable limit and is purely by choice. The minimum and maximum values for these three parameters, for which the reduced χ^2 values are within 3, are given in Table 2.8. The effect of the uncertainties in these CR propagation parameters is shown with a gray region in the B/C ratio plot in Figure 2.5. Also, the effect of this variation of CR propagation parameters on the proton spectrum and antiproton spectrum are shown with gray regions in figures 2.6 and 2.7, respectively.

We consider the uncertainties in these propagation parameters while calculating the Lepton spectra and the positron fraction. We also consider the uncertainties in the normalization of the parent proton flux inside the nearby GMCs Taurus, Lupus, and Orion A. The uncertainties in the parent proton spectra inside these three GMCs are given in Table 2.3 of [165] from *Fermi*-LAT observations of gamma-ray spectra. The uncertainties in these parent proton spectra lead to uncertainties in the injected secondary lepton spectra from these three GMCs. We have considered a significant fraction (~ 90 %) of the allowed maximum and minimum values corresponding to the normalization of the injected lepton spectra from Taurus, Lupus, and Orion A, along with the uncertainties in the CR propagation parameters to estimate the total uncertainties in the electron, positron spectra and the positron fraction. The total uncertainty in the electron spectrum, positron spectrum, and positron fraction are shown with gray regions in figures 2.8, 2.9, and 2.10, respectively. The maximum and minimum values of the normalization of the injected lepton spectra (considering the suppression) from Taurus, Lupus, and Orion A, due to uncertainty in the parent proton spectra are given in Table 2.8.

The only free parameter in our model is the normalization of the injected lepton spectra from the 7 selected GMCs, taken from the catalog of [214]. As mentioned before, we have assumed reacceleration due to magnetized turbulence inside these GMCs. Since the phenomena of reacceleration occuring inside the GMCs is yet to be observed by *Fermi*-LAT, we can not constrain this normalization parameter from the observed gamma-ray data. But we can get an idea about this parameter if we assume that the luminosity of each of the 7 selected GMCs is comparable to the luminosity of Taurus or Lupus or Orion A. The lepton luminosity of the GMCs is related to the normalization constant Q_0 in $\mathrm{GeV}^{-1}s^{-1}$ through the relation,

$$L_{e,GMC} = \int_{1\,\mathrm{GeV}}^{10^4\,\mathrm{GeV}} E_e\, Q(\gamma_e, d)\, dE_e, \tag{2.19}$$

in unit of GeV s^{-1}. The order of magnitude of the luminosity in leptons of each of the 7 GMCs in our work is the same as that of Taurus or Lupus, and it is one order of magnitude lower than that of Orion A. Hence the value of normalization Q_0 used in our work (see Table 2.6) for the 7 selected GMCs is not unphysical, and it gives the best fit to the observed positron data. This is why while calculating uncertainties, this normalization was fixed at the best-fit value. Future observations and possible detection of reacceleration inside GMCs may give stronger constraints on the injection parameters of such GMCs.

Table 2.8 Allowed values for the CR propagation parameters and normalization of nearby GMCs for our model.

Par./Val.	z_t (kpc)	D_0 (cm^2/s)	δ	Q_0^{Taurus} (GeV$^{-1}s^{-1}$)	Q_0^{Lupus} (GeV$^{-1}s^{-1}$)	Q_0^{OrionA} (GeV$^{-1}s^{-1}$)
Minimum Value	7	2.2×10^{29}	0.51	$8.5{\times}10^{43}$	$1{\times}10^{43}$	$3.6{\times}10^{44}$
Best-fit Value	8	2.4×10^{29}	0.53	$8.5{\times}10^{43}$	$1{\times}10^{43}$	$3.6{\times}10^{44}$
Maximum Value	9	2.6×10^{29}	0.55	$1.7{\times}10^{44}$	$2.1{\times}10^{43}$	$7{\times}10^{44}$

2.5 Discussion and conclusion

2.5.1 Summary

In this work, we have comprehensively discussed the origin of the most prominent feature in the electron and positron spectra, as seen by AMS-02 and PAMELA data in a different light compared to the existing literature. Supernova remnants in the Galaxy were considered to be the sites for the acceleration of primary CRs. Primary CRs accelerated in SNRs are injected into the ISM, and then these primary CRs interact with ISM hydrogen gas to produce secondary CRs. GMCs scattered in the Galactic plane were considered to be major sites for secondary particle production from CR interactions. Primary CRs interact with cold protons inside GMCs and produce secondary CRs such as leptons, antiprotons, and gamma rays. In this chapter, we show that the total contribution from nearby GMCs (CASE 3), along with contributions from ISM (CASE 1) and all the other reported GMCs (CASE 2), can explain the positron flux very well.

First, we build a CR transport scenario using publicly available code **DRAGON** while considering CASE 1, CASE 2, and CASE 3. Using that CR transport setup, we reproduce ^{10}Be/^{9}Be ratio, B/C ratio and proton spectrum. We show our simulated spectra and ratio against the data points provided by AMS-02 and PAMELA. We also show the corresponding residuals in our model with respect to the observed data for each fit. Residual is defined by the “distance" between simulated value and observed data, divided by total experimental error. As it can be seen from the residual plots, residuals are always confined within 3σ, confirming a good accuracy of the fitting [239]. We also compare the secondary antiproton spectrum produced from the interactions of primary CRs with the intervening medium (CASE 1 + CASE 2 + CASE 3) in our model with the recent data by AMS-02 and PAMELA.

Next, we consider the electron and positron data observed by AMS-02 and PAMELA. Positron data shows a rise above 10 GeV and then a fall at around 200 to 300 GeV. We simulate CASE 1 and CASE 2 with **DRAGON** and model CASE 3 analytically. We consider that primary electrons are injected from SNRs with a broken power law injection spectrum. Also, secondary electrons and positrons are produced from interactions of primary CRs with ISM gas (CASE 1) and GMCs considered in CASE 2. Next, we calculate the contribution from nearby GMCs separately using the formalism given by [235]. We take 3 nearest GMCs, for which *Fermi*-LAT analysis was performed by [165]. Leptons are produced inside these GMCs through *pp* interactions. Apart from this, we select 7 GMCs from work by [214], in which reacceleration due to magnetized turbulence was considered. We refer to the work done by [166] and consider a small hardened component from these GMCs, which is due to reacceleration. Finally, combining all of the above contributions, we show that the electron spectrum, positron spectrum, and positron fraction can be well-fitted by our model. The rise of the observed positron spectrum and subsequent fall can be well explained by the positron spectrum simulated in our model. Also, the corresponding residuals are shown in the figures. Since we are concerned with the positron excess phenomena, which is dominant from 10 GeV and above, and moreover, below 10 GeV, heliospheric modulation can alter the spectrum, we show the residuals of lepton fluxes and positron fraction, from 10 GeV and above, and neglect the residuals calculated below 10 GeV. Finally, we show the electron and positron anisotropy induced by nearby GMCs considered in our work. We have calculated the electron and positron anisotropy following the formalism given by [207, 240] and plotted the calculated anisotropy against the upper limits obtained by *Fermi*-LAT. It can be seen that the anisotropy induced by the nearby GMCs considered in our work is lower than the upper limits provided by *Fermi*-LAT; hence our model is very much plausible in terms of anisotropy signal. The positions of these nearby GMCs considered in our model have been shown in Figure 2.12.

2.5.2 Distinguishing between different models in terms of anisotropy

As pointed out by [202], fitting of the positron spectrum and positron fraction presented by AMS-02 and PAMELA alone may be insufficient to distinguish between different scenarios considered for explaining this interesting phenomenon. As we have discussed earlier, dark matter distributed in the Galaxy and astrophysical objects such as pulsars are two conventional candidates for explaining the observed positron excess. However, in this work, we have presented an alternative model, which explains the positron excess using the secondary positrons produced from nearby and faraway GMCs distributed in the Milky Way Galaxy. Since explaining the positron excess through fitting the positron spectrum and positron fraction using contribution from nearby GMCs is inadequate, we will discuss anisotropy signals as an additional measurement for solving this problem.

As discussed earlier, contrary to hadronic CRs, high-energy CR electrons and positrons propagating through GMF lose energy rapidly through synchrotron radiation and IC collision with low-energy photons of interstellar radiation field (ISRF). Thus, in order to contribute significantly to the positron spectrum, the contributing sources must be nearby, which will, in turn, induce anisotropy signals. Therefore, depending on the propagation properties in the GMF, detection of excess CR leptons, with energy sufficiently high enough to minimize the geomagnetic field and heliospheric modulation effects, will uncover the nature and the presence of such nearby CR sources [241]. In other words, even after taking into account diffusion in the ISM, a dipole anisotropy should be present in the direction of dominant nearby sources at sufficiently high energies. Although anisotropy signal, which is not associated with nearby sources, can also be expected to result from the Compton-Getting effect [244], where the relative motion of the observer with respect to CR plasma changes the intensity of the CR fluxes, with larger intensity arriving from the direction of motion and lower intensity arriving from the opposite direction. But in general, an anisotropy signal should be a useful probe to distinguish between several distinct models that are being used to explain the positron excess from nearby sources. In particular, as [202] pointed out, that anisotropy at 2σ level can be detected if one fulfills the condition $\delta \gtrsim 2\sqrt{2}\,(\dot{N_{ev}}.t_{obs})^{-1/2}$, where $\dot{N_{ev}}$ is the rate of events detected per unit time above a given threshold and t_{obs} is the observation time. In accordance with [202], we have taken a rate of approximately $3{\times}10^7$ electrons per year above 10 GeV, and an observation time of 7 years [242]. This implies that dipole anisotropy should get detected at the 2σ confidence level in the electron-positron flux above 10 GeV if $\delta \gtrsim 0.02$ %. We show this threshold with a yellow region in Figure 2.11. If anisotropies calculated from any candidates cross this threshold at sufficiently high energies, then it can be predicted that dipole anisotropies from those directions can be detected at a 2σ level. Otherwise, anisotropies from the sources will not be significant enough to be detected and will be mixed with background isotropy due to diffusion. It can be readily seen from Figure 2.11 that anisotropies calculated from all the nearby GMCs considered in this work are well above this threshold. Hence our model predicts that in the GMC scenario proposed in this work, dipole anisotropy may be observed in the directions of the nearby GMCs considered.

As shown by previous works, pulsars can be possible candidates for explaining positron excess. These nearby pulsars, specifically Monogem and Geminga, can explain the positron spectrum, also their anisotropy signals are below the upper anisotropy limit given *Fermi*-LAT ([241] and [242]). [207] has also shown that the pulsar B1055-52 can also be a nearby source that can contribute to the explanation of the positron spectrum. It is shown in [202] that a small dipole anisotropy may be observed by *Fermi*-LAT at sufficiently high energies in the direction of Monogem and Geminga. [207] has calculated the anisotropy of Monogem, Geminga, and B1055-52 pulsars in their respective directions for an injection time of 85 kyr. Also, since Monogem and Geminga lie in similar directions in the sky, they are expected to contribute the same overall anisotropy. The anisotropy calculated from the works by [202] and [207] have been shown in Figure 2.11. The positions of these pulsars are shown in Figure 2.12. From Figure 2.11, it can also be seen that Monogem and Geminga do induce a small dipole anisotropy in their respective direction at high energies. But the anisotropy signal from pulsar B1055-52 can not be detected at 2σ level, as it is below the anisotropy threshold.

Alternatively, also annihilations or decay by Galactic dark matter distributed all over the Milky Way halo can also be primarily responsible for the positron excess observed. If this is to be the case, a dipole anisotropy must be generated towards the direction of the Galactic center since the dark matter is denser in that direction. A model anisotropy calculated from the dark matter distributed in the Galaxy [241] is shown in Figure 2.11, which also is above the anisotropy threshold. Since, as seen from Figure 2.12, apart from Taurus, every other GMCs considered in this work, and all the nearby candidate pulsars are in different directions compared to the direction of Galactic Center, a distinction can be made in terms of anisotropy between dark matter and GMCs and/or pulsars. Also, by considering the difference in proximity and anisotropy signal between Taurus and dark matter residing in the Galactic center, it is possible to distinguish both of them. However, if there are any nearby subhalo of dark matter in the direction of posited GMCs and/or pulsars, then it would be hard to make any distinction among them in terms of anisotropy. Fortunately, the chance of nearby and luminous dark matter clumps that can explain the positron excess is very small for ordinary pair-annihilation cross section [245]. For larger annihilation cross sections, the predicted associated gamma-ray flux from dark matter annihilation will exceed the point source sensitivity of *Fermi*-LAT, i.e., it would have very likely been observed shining in gamma-rays. In particular, [173] has shown that if an anisotropy from such a clump were detected, and if such anisotropy did not generate from anisotropic diffusion effects, then the clump would be clearly detectable as an anomalous, bright gamma-ray source with the *Fermi*-LAT. So it is very much possible to distinguish between the dark matter origination of positrons and that from nearby GMCs considered in this work and/or pulsars considered in the literature.

The only other two candidates remaining for explaining the positron excess are pulsars considered in previous literature and GMCs considered in this work. Both of the models where pulsars are considered and the model given in this work, where GMCs are considered, have successfully produced positron spectrum and positron fraction. Nearby pulsars and GMCs can both induce anisotropy and as seen from Figure 2.11, anisotropy from both of these models are below the *Fermi*-LAT upper limits. Also, anisotropies calculated from both of these models supersede the anisotropy threshold for detection at 2σ level. So, none of these models can be excluded in terms of anisotropy yet. However, with the development of better instrumentation, future observatories should be able to constrain these upper limits to a point where any anisotropy in the sky can be clearly discerned from the isotropic background due to diffusion. Already [246] has shown that a next-generation CR observatory, high-energy cosmic-radiation detection (HERD) facility is expected to be better capable of detecting anisotropy than *Fermi*-LAT. Since, from Figure 2.12, it can be seen that nearby GMCs considered in this work and the pulsars are positioned at different RA and dec in the sky; it will be possible to distinguish anisotropy signals coming from those directions. So in the future, using updated, next-generation instruments based on anisotropies in different positions of the sky, it will be possible to unambiguously discern predictions from the model introduced in this work from that of the pulsar scenario.

The CR positron flux measured in GeV^2 m^{-2} sec^{-1} sr^{-1} rises with energy and peaks near 200 to 300 GeV. CR positrons are secondary particles produced in interactions of CR protons and heavy nuclei with hydrogen gas in ISM, and also in GMCs. It is difficult to explain the rise in CR positron flux unless there are sources close to the Earth. Earlier, pulsars and DM have been suggested as the origin of the rising positron flux or excess. In fact, recently, [248] has shown a complete solution in terms of the Pulsar scenario. In this work, we discuss an alternative, self-consistent scenario of CR propagation, where CR positrons are produced in nearby GMCs in CR interactions and contribute significantly to the observed positron excess. CR proton and antiproton fluxes, B/C ratio, ^{10}Be/^{9}Be ratio, electron, positron fluxes, and positron fraction calculated using our model fit well to the observed data from different observations considered in this work. Thus we conclude that nearby GMCs may play an important role in explaining the positron spectrum over the entire energy range of 1 to 1000 GeV.

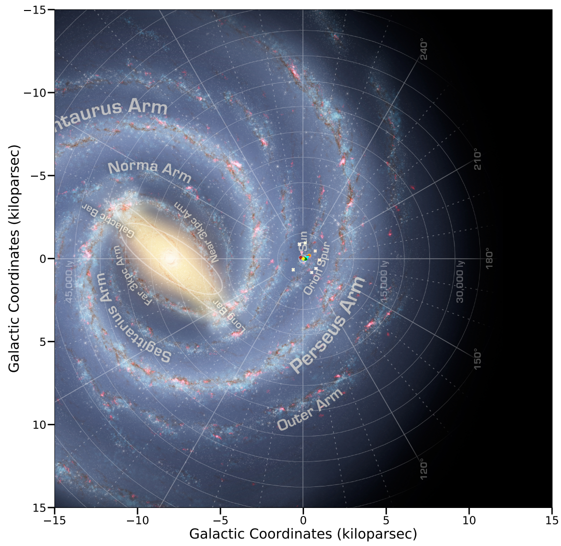

(a)

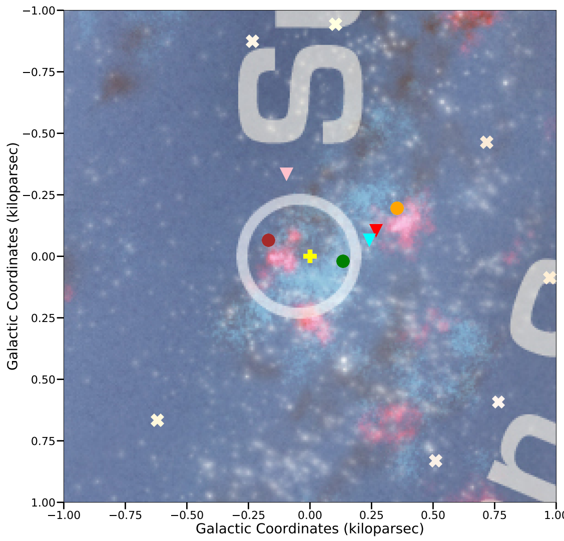

(b)

Figure 2.12 (a) GMCs considered in this work are plotted on the background of the Milky Way Galaxy, along with the candidate pulsars, which are conventionally considered while explaining the positron excess. Background illustration [247] produced by Robert Hurt of the Spitzer Science Center, reflecting the current understanding of Galactic structure. The color scheme is the same as Figure 2.11, other than 7 selected GMCs, where the color scheme is GMC ID 27 (linen), GMC ID 233 (antique white), GMC ID 286 (papaya whip), GMC ID 288 (old lace), GMC ID 295 (cornsilk), GMC ID 342 (light yellow) and GMC ID 385 (seashell). The filled circles signify nearby GMCs, where *pp* interaction is considered (Taurus, Lupus, and Orion A), cross marks signify 7 selected nearby GMCs where reacceleration is considered, and filled triangles signify the nearby pulsars (Monogem, Geminga, and B1055-52). The yellow plus mark is the position of the Sun. (b) Zoomed view of the region (radius of 1 kpc) around the Sun.

3

Discovery of an accreting high mass gamma-ray binary HESS J1828-099

The High Energy Stereoscopic System (H.E.S.S.) observatory has carried a deep survey of the Galactic plane, in the course of which the existence of a significant number of (∼ 78) TeV gamma-ray sources was confirmed, many of which remain unidentified. HESS J1828-099 is a point-like (Gaussian stand. dev. < 0.07°) unidentified source among the 17 confirmed point-like sources in the H.E.S.S. Galactic Plane Survey (HGPS) catalog. This source is also unique because it does not seem to have any apparent association with any object detected at other wavelengths. We investigate the nature and association of HESS J1828-099 with multi-wavelength observational data. A high mass X-Ray binary (HMXB), comprising of pulsar XTE J1829-098 and a companion O or Be star, has been observed earlier in the X-ray and infrared bands, 14′ away from HESS J1828-099. With 12 years of *Fermi*-LAT gamma-ray data, we explore the possibility of 4FGL J1830.2-1005 being the GeV counterpart of HESS J1828-099. Within the RXTE confidence region, a steep spectrum (α_{radio} = - 0.746 ± 0.284) plausible counterpart is detected in data from existing radio frequency surveys. We have probed, for the first time using multi-wavelength data, whether HESS J1828-099, 4FGL J1830.2-1005, and the HMXB system have a common origin. Our study indicates that HESS J1828-099 might be a TeV high-mass gamma-ray binary source.

3.1 Background

High mass gamma-ray binaries (HMGBs) belong to a special class of HMXBs, which mainly emit in gamma-ray energies [32]. Such objects comprise of compact objects such as a neutron star or a black hole and an O or Be-type star as the companion. The gamma-ray emission in such binaries is usually assumed to be powered by wind-driven shocks [32]. The compact object in the HMGBs, usually a rotation-powered pulsar, dissipates its rotational energy by energizing pair plasma, which interacts with wind from the companion star [249–251]. In a close orbit system, a wind collision region is created due to this interaction, which in turn terminates the pulsar and stellar winds by a shock [251–253]. Particles can be accelerated to ultra-relativistic energies at these shock sites due to diffusive shock acceleration, later producing observed emission through various radiative processes [251, 254]. Another favored emission scenario can occur if the massive companion star is Be star with a disk. In this scenario, the primary interaction happens as the pulsar crosses the circumstellar disk of the Be star, as in the cases of PSR B1259-63

[255] and PSR J2032+4127 [176]. The multi-wavelength emission for these two sources differs from other HMGBs, perhaps due to the geometry of the circumstellar decretion disk. For example, in the case of PSR B1259-63, the light curve in the radio, X-ray, and TeV regimes is typically double-peaked and driven by synchrotron (radio and X-ray emissions) and Inverse Compton (TeV emission) cooling [256]. The emission in the GeV range is peculiar given that flares that exceed the pulsar spindown luminosity have been observed with *Fermi*-LAT [257–260]. Alternatively, the microquasar model, in which interaction primarily occurs in the jets produced by accretion onto a black hole, also cannot be ruled out [261, 262]. Only a handful of objects, which have been detected above 100 MeV, are firmly established as HMGBs. Some of the observed HMGBs are: HESS J0632-057, 1FGL J1018-5658, PSR B1259-63, LS I +61°303, LS 5039 [174, 175], PSR J2032+4127 [176–178], a point source in the Large Magellanic Cloud [179, 263], 4FGL J1405.1-6119 [180] and HESS J1832-093 [181, 182, 264]. All of these sources have soft spectra in TeV energies and hard, absorbed spectra in X-ray energies.

HESS J1828-099 is a new Very High Energy (VHE) TeV gamma-ray source that has been detected in the HGPS [265] at the position of R.A. = $18^h28^m58.72^s$ and Decl. = -09°59′33.8″ (J2000). This H.E.S.S. source is detected at a confidence level of 8.9σ, and the size of the source is 0.05° ± 0.01°, making it one of the 17 point-like VHE gamma-ray sources found in HGPS catalog. The flux from this TeV source was recorded for a livetime of 46.3 hours, and its 0.20 - 61.90 TeV spectrum is well fitted by a power law ($\propto E^{-\Gamma_{TeV}}$) having a photon index of Γ_{TeV} = 2.25 ± 0.12. Its flux is 1.9 ± 0.3 % that of the Crab Nebula above 1 TeV, and a 1-dimensional Gaussian model was used as a spatial template to fit the extent of this VHE source. This H.E.S.S. source is still unidentified as it does not seem to have any apparent association with any other source at lower energies. Earlier, [266] claimed that 1FGL J1829.6-1006 (slightly more than 0.25° away from the H.E.S.S. source) could be the GeV counterpart of the TeV source. They also found that the pulsar J1828-1007 is located at 0.1° from the H.E.S.S. source. Moreover, they claimed the spatial separation between the low and high energy emission regions indicates that this source is possibly a pulsar wind nebula (PWN). However, this was not confirmed by the version of the *Fermi*-LAT catalog available at that time, i.e., 3FGL catalog [267] or 2FHL catalog [268]. This pulsar is also absent in the latest 4FGL catalog [269].

In this work, we report our investigations on the origin of the VHE source HESS J1828-099. Analysis of the *Fermi*-LAT data revealed a possible GeV counterpart, 4FGL J1830.2-1005, spatially coincident with the H.E.S.S. source. A Galactic X-ray source XTE J1829-098 was also observed by Chandra X-ray observatory, within the 68% containment radius of 4FGL J1830.2-1005 and 14′ away from the centroid of HESS J1828-099 [270], making it a very likely lower energy counterpart of both the 4FGL and H.E.S.S. sources, based on its position. Pulsar XTE J1829-098 was observed as a transient source by the Rossi X-ray Timing Explorer (RXTE) observatory during the scan of the Galactic plane in 2003

July - 2003 August [271]. The best-fit pulsar position was found to be R.A. = $18^h29^m35^s$ and Decl. = -09°51′0.00″ (J2000), with a 99% confidence region of approximately elliptical shape, with semimajor axes of 3.8′ (RA) and 3′ (Decl.) [271]. Subsequent X-ray Multi-Mirror Mission (XMM-Newton) observations found the position of this source to be R.A. = $18^h29^m44.1^s$ and Decl. = -09°51′24.1″ (J2000), with a 90% uncertainty radius of 3.2″ [270]. It was discovered in the RXTE data that this pulsar has a rotation period of ∼ 7.8 s [271], which was later confirmed by various other observations [270, 272]. Analyzing XMM-Newton data, a hard power-law photon index, Γ_X^{XMM}, of 0.76 ± 0.13 and a hydrogen column density N_H, of (6.0 ± 0.6) × 10^{22} cm^{-2} were estimated in the soft X-ray range (2 - 10 keV), both given with their 1σ uncertainties [270]. This suggests that this pulsar is part of an HMXB, as the best-fit value of N_H exceeds the measured Galactic 21 cm HI column density, in the pulsar's direction, of ∼ 1.81 × 10^{22} cm^{-2} [273], ∼ 1.43 × 10^{22} cm^{-2} [Leiden/Argentine/Bonn (LAB) survey; 274], ∼ 1.79 × 10^{22} cm^{-2} [HI4PI survey; 275], indicating that some absorption is intrinsic to the binary, either from the wind or circumstellar disk of the companion star. A candidate source, 2.1″ away from the XMM-Newton location of the XTE pulsar, was detected in the analysis of the data obtained by Chandra [270]. The Chandra location of this source was found to be R.A. = $18^h29^m43.97^s$ and Decl. = -09°51′23.2″ (J2000), with a 90% positional uncertainty of 0.6″. Assuming the same best-fit XMM-Newton parameters, the average flux of the source, detected by Chandra in the soft X-Ray range, was found to be consistent with that from the XMM-Newton observations [270]. A hard, absorbed spectrum estimated from the analysis of archival data obtained by Swift-X-Ray Telescope (XRT) (Γ_X^{Swift} = $1.1^{+0.9}_{-0.8}$, N$_H$ = 10^{+6}_{-4} × 10^{22} cm^{-2}) reinforces this source's identification as an HMXB [276]. This source has shown frequent outbursts over the years, observed by different observatories. The MAXI gas slit camera (GSC) detected 4 outbursts from this source in 11 years of observation, including one on 2021 April 12 [277]. The time intervals between these outbursts match the proposed orbital period (≈ 246 days) of the binary system [271, 277]. [276] had checked the 15 - 50 keV XTE source light curve on a daily timescale from Swift-Burst Alert Telescope (BAT) archive and found that the duration of the outburst was very likely of the order of 3 - 4 days, which is almost the same order of duration estimated by [278] (∼ 7 days). In August 2018, an X-ray outburst from this source triggered a ToO observation with the Nuclear Spectroscopic Telescope Array (NuSTAR), which showed the existence of a cyclotron absorption line at E_{cyc} = 15.05 ± 0.06 keV, which implies that the magnetic field on the neutron star surface is B ≃ 1.7 × 10^{12} Gauss [272]. The detection of the cyclotron absorption line in the X-Ray spectrum of the pulsar confirmed that this pulsar is part of an HMXB.

A star was found in infrared (IR) analysis within 0.2″ of the Chandra localization of XTE J1829-098 [270]. This bright, infrared counterpart was detected in the Two Micron All Sky Survey (2MASS), but it is not visible in the optical range. The measured IR magnitudes of this companion star are K = 12.7, H = 13.9, I > 21.9 and R > 23.2 [270]. From the measured magnitude in the H and K bands, the distance of this companion was estimated to be approximately 10 kpc. Assuming this distance, the maximum observed X-Ray luminosity in the 2 - 10 keV range was found to be 2×10^{36} erg s^{-1} and minimum luminosity as 3×10^{32} erg s^{-1}, similar to a wind-driven system or a Be binary transient [270]. Later observations by [276] found that reddening free near-infrared (NIR) diagnostic color criterion Q has a value of -0.7, which is very typical of an early-type OB star, although it can also be a Be star. According to the Corbet diagram [279–281], for a possible orbital period of $\approx$ 246 days, there is a greater likelihood that the donor star is a Be star. Moreover, the absence of an Hα emission line in the NIR spectra of the 2MASS counterpart is indicative of the NIR counterpart being a Be star.

Data analysis and the corresponding results are discussed in section 3.2. In subsection 3.2.1, we present the results of the analysis of NuSTAR data and report the detection of a sub-dominant, intrabinary shock emission component. Based on this detection and spatial association, we suggest that this HMXB has a common origin with both the 4FGL and H.E.S.S. sources. In subsection 3.2.2, we present the results of the analysis of $\sim$ 12 years of *Fermi*-LAT data. We have also used multi-wavelength radio continuum data to identify any radio counterpart of the H.E.S.S. source. In subsection 3.2.3, we discuss the detection of a nearby source in multi-radio frequency surveys and investigate this as the likely radio counterpart of the H.E.S.S. source based on its position. In section 3.3, we present the results of one-zone leptonic modeling to fit the multi-wavelength spectral energy distribution (SED) and show that the required values of parameters are consistent with those of other established HMGBs [282]. Finally, in section 3.4, we discuss the results and the caveats of our model. We also suggest the additional observations that are required to completely explain the multi-wavelength SED of the system. Finally, we conclude that HESS J1828-099 is possibly a TeV HMGB based on spatial coincidence and spectral properties.

3.2 Data analysis and results

3.2.1 X-Ray data analysis

Although the XTE J1829-098 was confirmed to be an HMXB, the presence of an iron Kα emission line, the cyclotron absorption line, and the exponential cutoff, as reported in [272], point towards the fact that the pulsar is accreting and the dominant X-ray flux seen from this source is due to the accretion. However, in previous analyses of established TeV HMGBs [283–285], no spectral lines and/or cutoff or spectral turnover at higher energies were found, indicating, as in general for TeV HMGBs, that the pulsar usually is not accreting. Also, the best-fit cutoff power law spectral index obtained from NuSTAR data analysis is notably different compared to what is predicted if we assume that the observed X-rays represent synchrotron emission. These factors put the TeV HMGB interpretation of HESS J1828-099 into question.

To resolve this discrepancy, we tried to find whether or not the pulsar, in this case, is actively accreting by comparing the Alfven radius (R_{Alf}) with the corotation radius (R_{co}). If $R_{Alf} < R_{co}$, then material from the companion star accretes on the pulsar surface; if $R_{Alf} >> R_{co}$, then the stellar material directly interacts with pulsar's rotating magnetosphere and subsequently gets ejected; known as the propeller phase. Finally, if $R_{Alf} \simeq R_{co}$, then these two effects happen simultaneously, and intermittent accretion occurs, which is the intermediate stage of the accretor and propeller phases.

The corotation radius (R_{co}) is defined as the radius at which the spin angular velocity ($\Omega_s = 2\pi/P_s$) of the pulsar is equal to the Keplerian angular velocity ($\Omega_k = \sqrt{GM_*/r^3}$) of the material being accreted. Assuming a standard pulsar mass of 1.5$M_\odot$ and using the observed XTE J1829-098 rotation period (P_s) of 7.8 s, we get,

$$R_{co} = \left(\frac{GM_*}{4\pi^2} \times P_s^2\right)^{\frac{1}{3}} \simeq 6 \times 10^8 \text{cm}. \tag{3.1}$$

The Alfven radius (R_{Alf}) is defined as the radius where the ram pressure of the infalling material from the companion star (ρv^2) balances with the magnetic pressure of the pulsar magnetosphere ($B^2/8\pi$). Assuming typical values for a pulsar, mass of $1.5M_\odot$ and radius $R_* = 10^6$ cm, the observed magnetic field of $B \simeq 1.7 \times 10^{12}$ G, resulting in a magnetic moment, μ, of $B\,R_*^3 \simeq 1.7 \times 10^{30}$ G cm^3 and observed X-ray luminosity $L_X \simeq 4.3 \times 10^{36}$ erg/s [272], we get the Alfven radius as [286, 287],

$$R_{Alf} = 2.6 \times 10^8 \left(\frac{\Lambda}{1}\right) \left(\frac{M_*}{M_\odot}\right)^{\frac{1}{7}} \left(\frac{R_*}{10^6 \text{ cm}}\right)^{-\frac{2}{7}} \left(\frac{L_X}{10^{37} \text{ erg/s}}\right)^{-\frac{2}{7}} \left(\frac{\mu}{10^{30} \text{ G cm}^3}\right)^{\frac{4}{7}} \text{cm} \simeq 5 \times 10^8 \text{cm}, \tag{3.2}$$

where the constant Λ signifies the geometry of the accretion flow. Following [287], there is an uncertainty on the value of Λ, which is $\Lambda = 1$ for spherical accretion, and $\Lambda < 1$ for disk accretion. Since very distinct accretion disks usually do not form in the case of HMXBs [288, 289], we assume a wind-fed spherical accretion ($\Lambda = 1$) for simplicity. R_{Alf} for spherical accretion, as given in equation 3.2, is very close to R_{co}, making this a case for intermittent accretion. In this regime, a turbulent and magnetized transition zone can be formed close to R_{Alf} due to the balance between the magnetic pressure and the pressure inserted by accreting matter. Part of the infalling matter accumulated at the transition zone can further accrete onto the pulsar surface (accretor phase). However, the rotating pulsar magnetosphere can also strongly shock the infalling material at the transition region, ejecting some of it beyond the accretion radius (propeller phase). Electrons can get shock-accelerated to very high energies at this transition region and can further produce X-rays via the synchrotron mechanism [290–293]. Although X-rays produced from accretion are the dominant component observed during the outburst phase, a sub-dominant X-ray

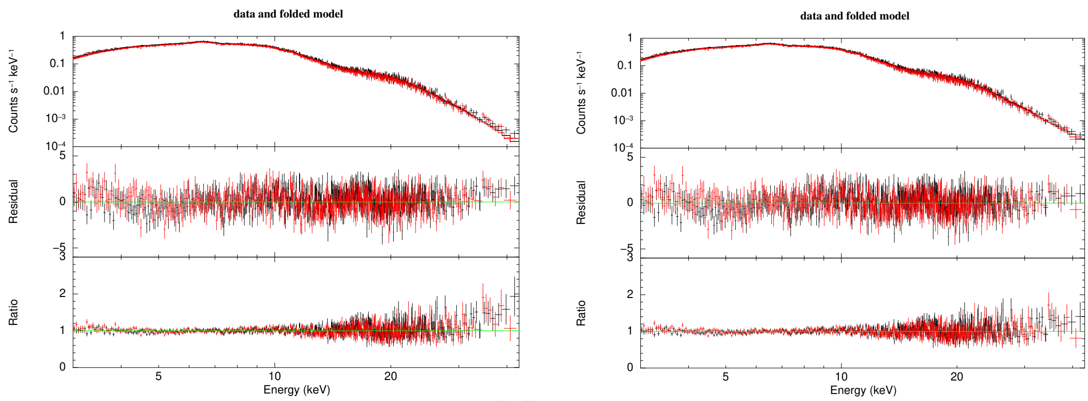

Figure 3.1 *Left Panel:* Data and model spectrum fit, the residual, and the ratio (data/model) for the best-fit values given in the upper panel of Table 3.1. The model used in this case is `constant*tbabs*(cutoffpl*gabs + gauss)`. FPMA and FPMB data points and best fits are shown in black and red, respectively. *Right Panel:* Data and model spectrum fit, the residual and the ratio (data/model), after the addition of a power law component with the best-fit model used in (a). Model used in this case is `constant*tbabs*(cutoffpl*gabs + gauss + pow)`. The color scheme is the same as in (a).

component at higher energies, produced from shocked electrons, should also be present in the data observed by NuSTAR during the same outburst phase.

To confirm this observationally, we have analyzed the data obtained by NuSTAR on 2018 August 16 (ObsID 90401332002), with an on-source exposure time of $\sim$ 27.8 ks and an average count rate of $\sim$ 8 cts s^{-1} per module [272]. To extract the spectra, we have used the **NuSTAR-DAS 2.0.0** software as distributed with the **HEASOFT 6.28** package, with the CALDB version 20210315. The source data was extracted from a circular region of radius 50 arcsec, centered on the source position. The background data was extracted similarly from a circular region of radius 70 arcsec, away from the source position. The NuSTAR observations are not affected by stray light. The obtained spectra were grouped to have 25 counts per bin using `grppha` tool. The spectral analysis was done using the **XSPEC 12.11.1** tool included in the **HEASOFT 6.28** package. Since the background starts to dominate the source counts above 50 keV, we have considered the 3 - 45 keV energy range for spectral analysis.

According to [272], the spectrum of XTE J1829-098 can be explained by a power law with an exponential cutoff (`cutoffpl` model), modified by the fluorescent iron emission line (Gaussian line profile model `gauss`) and an absorption line (Gaussian absorption line model `gabs`), which is interpreted as a Cyclotron Resonant Scattering Feature (CRSF). So we have analyzed the phase-averaged NuSTAR data and tried to fit the spectrum with the model `constant*tbabs*(cutoffpl*gabs + gauss)`, representing the accretion component. We have used the `tbabs` model to take into account the X-ray absorption by the interstellar medium (ISM). To keep the best-fit values of the model consistent with

Table 3.1 *Upper Panel* : Best-fit parameters of the model `constant*tbabs*(cutoffpl*gabs + gauss)`, along with their 1σ uncertainties. *Lower Panel*: Best-fit photon spectral index of the additional power-law component, along with its 1σ uncertainty.

Parameter	Value
Hydrogen column density, N_H (cm^{-2})	1.43×10^{22}
Photon index of the cutoff power law, $\Gamma_X^{cutoffpl}$	$-0.75^{+0.03}_{-0.03}$
Folding energy of exponential rolloff, E_{fold} (keV)	$4.49^{+0.06}_{-0.06}$
Cyclotron line energy, E_{cyc} (keV)	$15.20^{+0.10}_{-0.10}$
Cyclotron line width, W_{cyc} (keV)	$2.37^{+0.10}_{-0.10}$
Optical depth at Cyclotron line center, τ_{cyc}	$0.55^{+0.05}_{-0.05}$
Fe Kα line energy, E_{Fe} (keV)	$6.52^{+0.04}_{-0.04}$
Fe Kα line width, σ_{Fe} (keV)	$0.22^{+0.04}_{-0.04}$
Photon index of the power law, Γ_X^{pl}	$1.50^{+0.15}_{-0.10}$

the best-fit results obtained by [272], we have kept the value of the hydrogen column density N_H in the direction of XTE J1829-098, fixed at 1.43×10^{22} cm^{-2} [LAB survey; 274]. We have used atomic cross-sections from [294] and elemental abundances from [295]. The best-fit values, along with their 1σ uncertainties (χ^2/D.O.F. = 1196.19/1071 ≈ 1.12), are shown in the upper panel of Table 3.1. Considering the uncertainties, the measured values of the model are consistent with those given in [272]. The flux obtained from the model in the 3 - 79 keV energy range was found to be $F_X^{acc} \simeq (3.66 \pm 0.02) \times 10^{-10}$ erg cm^{-2} s^{-1}. The spectrum fit, along with residual and data/model ratio, are shown in Figure 3.1. Although the best-fit values give a very good fit at low and intermediate energies, the best-fit model deviates from the data at higher energies, which is evident from the residual and ratio plots. This discrepancy hints towards a second emission component from the same source region.

Next, we have added an additional power law spectrum, in the form of the model `pow`, with the above model signifying accretion to fit the data. We have let the parameters of the power law component to freely vary while keeping the best-fit values given in the upper panel of Table 3.1 fixed. The best-fit photon spectral index value of the additional power law is given in the lower panel of Table 3.1. As found in other established HMGBs, the spectral index of the power law can vary between 1.4 and 1.6 [284]. It can be readily seen that the best-fit value, along with the uncertainty of the additional power-law component spectral index agrees well with previous observations. The obtained data and the corresponding best-fit model, along with the residual and the ratio, after fitting the data with the model `constant*tbabs*(cutoffpl*gabs + gauss + pow)`, are shown in Figure 3.1. From the Figure, it can be seen that the data is fitted comparatively well at higher energies after the addition of the power law model (χ^2/D.O.F. = 1187.15/1076 ≈ 1.10). The absorbed flux of the sub-dominant power-law component in the energy range of 3 - 79 keV was found to be $F_X^{pl} \simeq (9.6 \pm 0.8) \times 10^{-12}$ erg cm^{-2} s^{-1}, and the corresponding luminosity is $L_X^{pl} \simeq (1.1 \pm 0.1) \times 10^{35}$ (d/10 kpc)^2 erg s^{-1}.

It was found that the improvement in the χ^2 statistic after the addition of the sub-dominant power law component with the accretion component is small. We have also calculated the F-statistic probability using `ftest` tool present in `XSPEC`. We have used appropriate χ^2 and D.O.F. values for the calculation and found that the F-statistic probability ($\approx 1 \times 10^{-2}$), although $<< 1$, is comparatively high. These results suggest that the addition of the sub-dominant power law component with the accretion component is, although reasonable, of low statistical significance. This is not surprising as the additional power-law component is sub-dominant compared to the dominant accretion component in the outburst phase of the XTE source. Moreover, the marginal improvement in the fit statistics can be attributed to a low number of data points available to constrain the additional power-law component in the hard X-ray range. Nevertheless, the improvement in the residual and the ratio associated with the data and model X-ray spectrum (see Figure 3.1) justify the addition of the sub-dominant power-law component. Observational detection of this power law component, in conjunction with the argument presented above in terms of different characteristic radii, suggests that X-rays produced from shocked electrons through synchrotron cooling are also present in the source region. We also present the significance of the sub-dominant power-law component, obtained using the Monte Carlo simulation method. We note that calculating R_{Alf} with $\Lambda = 0.5$, as what may be expected from disk-fed accretion, yields an Alfven radius of $R_{Alf} \simeq 2 \times 10^8$ cm, which is, although of the same order, somewhat less than R_{co}. This may imply that the infalling material from the companion star accretes on the pulsar surface without being propelled at the transition region. Consequently, no shock is created at the transition region in case of disk-fed accretion. However, the signature of the shock component is observed in the NuSTAR data, represented by the sub-dominant power-law component, indicating that our assumption of a wind-fed spherical accretion is valid. The presence of the sub-dominant, non-thermal power-law emission indicates that this source indeed shows typical characteristics of an HMGB [283–285]. We have also performed pulse phase-resolved spectroscopy of the observed NuSTAR data in four different phase bins of equal sizes, spanning the entire phase range of 0 - 1, using the same model described above. But due to relatively low source photon counts, as well as large uncertainties associated with the data points, the phase dependence of the sub-dominant power law component could not be unambiguously established. Multiple simultaneous X-ray observations can help elucidate the phase dependence of the shock component.

Monte Carlo Simulations

As pointed out in [296], the F-test in some cases does not (even asymptotically) adhere to their nominal χ^2 and F-distributions in many statistical tests common in astrophysics. Thus, in this case, the significance of the additional, sub-dominant power law component

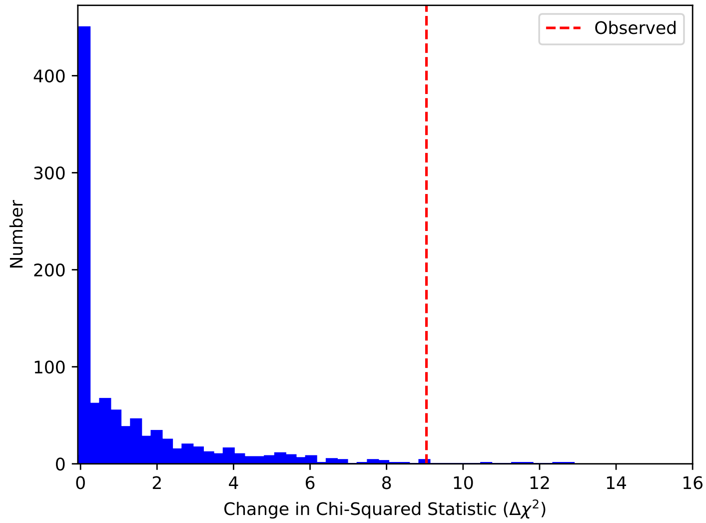

Figure 3.2 Results of 1000 Monte Carlo simulations to test the significance of the sub-dominant power law component depicting shock. The blue solid histogram shows the frequency (y-axis) of $\Delta\chi^2$ values (x-axis) obtained in the simulations. The red dashed line shows the observed $\Delta\chi^2_{obs} = 9.04$.

depicting shock has been assessed through the Monte Carlo simulation method. `XSPEC` tool `simftest` was used to perform this task. We used the model depicting the accretion component as our *null hypothesis*. The model, which includes the additional power-law component with the accretion component, was used as the *alternate hypothesis*. We simulated 1000 trials using `simftest` and calculated the change in χ^2 values for the *null hypothesis* and *alternate hypothesis* models. The maximum change in χ^2 ($\Delta\chi^2$) obtained from our simulations is 12.89. The probability of finding the observed change in χ^2 ($\Delta\chi^2_{obs} = 9.04$) by chance is 6×10^{-3}, which corresponds to 4σ significance. These results justify the addition of a sub-dominant power-law component, which in turn hints towards the presence of shock in the source region of XTE J1829-098.

3.2.2 GeV counterpart of HESS J1828-099

Despite being very prominent in TeV energies, HESS J1828-099 has not been properly identified in GeV energies. For a deeper search of its GeV counterpart, we have analyzed $\sim$ 12 years of *Fermi*-LAT data, observed between 2008 August 4 (MJD 54682) and 2020 October 2 (MJD 59124) in the 0.3 - 500 GeV band. We have used **Fermipy** version 0.20.0[1] [297] to reduce and analyze $\sim$ 12 years of PASS 8 LAT data in the energy range of 0.3-500 GeV. Events with zenith angles greater than 90° were excluded from the analysis to avoid contamination from Earth's albedo gamma rays. The instrument response function, Galactic diffuse emission template (galdiff) and isotropic diffuse emis-

[1] https://fermipy.readthedocs.io/en/latest/

sion template (isodiff) used in this work were “P8R3_SOURCE_V2", “gll_iem_v07.fits" and “iso_P8R3_SOURCE_V2_v1.txt", respectively. We have used the latest 4FGL catalog [269] to search for the possible GeV counterpart of HESS J1828-099.

We have extracted the data from the *Fermi*-LAT website[2], considering a circular region of interest (ROI), having a radius of 10°, with the center of the ROI placed at the position of the H.E.S.S. source. Galdiff, isodiff, as well as all of the 4FGL sources within a rectangular region of 10° × 10°, centered on HESS J1828-099, were included in the analysis. Pulsar J1828-1007 is within 1° of the H.E.S.S. source, but it being a radio pulsar [298] does not affect our analysis. While analyzing the data, we have kept the parameters of all the 4FGL sources within 4° of the H.E.S.S. source free, including that of galdiff and isodiff. Using the source finding algorithm of **Fermipy**, we also tried to find point sources around the H.E.S.S. source that are not included in the 4FGL catalog, having a minimum TS value of 25 and minimum separation of 0.3° between any two point sources. However, no plausible point sources in the GeV range were found in the vicinity of the H.E.S.S. source. All the best-fit values of the spatial and spectral parameters of the 4FGL sources, as well as galdiff and isodiff, were determined using maximum-likelihood analysis. The closest GeV source is 4FGL J1830.2-1005, which was detected at a best-fit position of R.A. = 277.5300° ± 0.0342°, and Decl. = -10.0730° ± 0.0262°, only 0.292° away from the centroid of the H.E.S.S. source. Apart from the possible GeV counterpart 4FGL J1830.2-1005, the rest of the 4FGL sources, including galdiff and isodiff, were considered as background and subsequently subtracted during the analysis. 4FGL J1830.2-1005 was detected with a TS value of 458.53, and its spectral shape is log parabolic, expressed by the form,

$$\frac{dN}{dE} = N_0 \left(\frac{E}{E_b}\right)^{-(\alpha_{\rm GeV}+\beta_{\rm GeV}\log\left(\frac{E}{E_b}\right))}. \tag{3.3}$$

The best-fit parameters are α_{GeV} = 3.491 ± 0.011, β_{GeV} = 0.7651 ± 0.0059, E_b = 1.396 GeV. The average energy flux of this source is F_{γ}^{GeV} = (1.88 ± 0.02) × 10^{-5} MeV cm^{-2} s^{-1}. This flux is included in the spectral energy distribution shown in Figure 3.4.

We have analyzed the extension of the 4FGL J1830.2-1005 using RadialDisk and RadialGaussian models as templates. Fitting the extension with the RadialDisk template gives a maximum TS$_{ext}$ value of 32.41 (∼ 5.692σ), with the best-fit 68% containment radius of the disk being 0.325° ± 0.037°. We have considered radial disks of radius varying from 0° to 0.5° to show how the delta log-likelihood varies with increasing radius (see Figure 3.3 (b)). We have also studied the energy-dependent morphology of the source by estimating the extent in two different energy ranges, 0.3 - 1 GeV and 1 - 500 GeV. We found that the spatial extent in both cases remains almost the same, $0.3063^{+0.0630}_{-0.0692}$ degree in 0.3 - 1 GeV range and $0.2875^{+0.0517}_{-0.0463}$ degree in 1 - 500 GeV range. It was found that the offset in the spatial position of the 4FGL source at different energy ranges varies significantly from the original 4FGL source position (offset ≈ 0.1068° in the energy range 1 - 500 GeV and

[2] https://fermi.gsfc.nasa.gov/ssc/data/access/lat/

offset ≈ 0.0198° in the energy range 0.3 - 1 GeV). The energy-dependent morphology of the sources is shown in Figure 3.3 (a). From the Figure, it can be seen that the 4FGL source and the H.E.S.S. source overlap with each other. Also, with increasing energy (in the 1 - 500 GeV range), we observe an increment in spatial proximity between the 4FGL and the H.E.S.S. sources. Based on the positional coincidence between these two sources, it can be inferred that 4FGL J1830.2-1005 can possibly be the GeV counterpart of HESS J1828-099.

Periodicity search

Since orbital periodicity is a distinguishable feature of HMGBs, in this work, we searched for periodicity in the ∼ 12 years of *Fermi*-LAT gamma-ray data observed from the source 4FGL J1830.2-1005. XTE J1829-098 has a possible orbital period of 246 days, as determined by the interval between consecutive outbursts. Since the 4FGL source is the possible GeV counterpart of the HMXB XTE J1829-098, we tried to find a similar periodic variation in the light curve of the 4FGL source. To that end, we have produced light curves using the likelihood analysis for time bins of sizes ≈ 127 days, balancing low photon statistics and the idea to probe the periodicity of 246 days observed for the XTE source. No significant changes in the flux or spectral index were seen in different time bins. 82.3 days and 177.7 days binned light curves were also produced, and again, no strong variability was found in either of the light curves, similar to the previous case.

Next, we searched for periodicity in the 127 days binned light curve, using a generalized Lomb-Scargle algorithm [299, 300]. AstroML package [301, 302] was used to search for periodicity in the light curve between 1 to 300 days. We applied the statistical bootstrapping method to calculate the significance levels. 1% and 5% significance levels for the highest peak were calculated, determined by 10^5 bootstrap resamplings. No significant peak confirming any hint of periodicity was found in the generated power spectra. Bootstrapping indicates that no periodic signal was detected at 1% or 5% significance. The same method was reapplied for 82.3 days and 177.7 days binned light curves, but even in those cases, no significant periodicity was detected. The non-detection of periodicity could be either due to inadequate statistics or due to a specific geometrical shape of the binary system that would not produce modulated emission in gamma-rays [303]. This is similar to the case of HMGB candidate HESS J1832-093, in which significant periodicity was also not confirmed [264]. However, a detailed epoch-folding method [182] can prove beneficial for finding any periodicity associated with 4FGL J1830.2-1005.

3.2.3 Radio counterpart of HESS J1828-099

We have used multi-wavelength radio data from different surveys to look for possible counterparts of HESS J1828-099. The field is observed as a part of the recent high sensitivity Galactic plane surveys like THOR survey [the HI/OH/Recombination line survey; 147, 148] covering 1 – 2 GHz and the GLOSTAR Galactic Plane survey [A GLObal view of STAR formation 150] covering 4 – 8 GHz. Due to the proximity of the source to the Galactic plane, the field is crowded with multiple resolved and unresolved sources, including Galactic (H II regions, supernova remnants, planetary nebulae) as well as many unclassified Galactic as well as extragalactic sources [304]. Near the position of XTE J1829-098, we detect a radio source within 99% RXTE confidence region in both THOR and the GLOSTAR images and investigate this as a plausible radio counterpart of the HMXB based on its proximity.

THOR provides the radio continuum image of ~ 132 square degree of the Galactic plane observed with the Karl G. Jansky Very Large Array (VLA) in C array configuration. Out of the eight SPWs covering $1-2$ GHz, two are discarded due to excessive RFI. The other six SPWs (with 128 MHz bandwidth, centered at 1.06, 1.31, 1.44, 1.69, 1.82, and 1.95 GHz) are used to make the continuum images. Wang *et al.* [148] used BLOBCAT [305] to identify sources and extract flux densities, as well as to estimate spectral index values from images at a common resolution of 25′. The RMS noise values for individual SPW images are in the range of $0.3-1.0$ mJy/beam. All the images, the flux density, and the spectral index values are available publicly through the latest data release [148]; we have used THOR individual SPW images and the combined THOR (VLA C array) and VGPS [VLA Galactic Plane Survey which are VLA D array and Effelsberg 100-m single dish data combined; 149] image to identify the potential counterpart and adopt the flux density values from THOR catalog.

The C band GLOSTAR survey, similarly, covers ~ 145 square degree of the Galactic plane observed with the VLA B and D configuration along with the Effelsberg 100-m data to provide zero-spacing information. We use the GLOSTAR survey images from the VLA D configuration, with 18′ angular resolution and at an effective frequency of 5.8 GHz (shown in Figure 3.3). The continuum observations with the VLA were carried out using 16 SPWs with 128 MHz bandwidth each. The data are used to make 8 continuum sub-images covering 4.2 - 5.2 GHz and 6.4 - 7.4 GHz. We note that four radio sources are detected within the H.E.S.S. positional error in both THOR and the GLOSTAR survey, but no X-ray counterparts are detected for any of these sources, so it is unlikely that these sources are associated with the H.E.S.S. source.

Figure 3.3 (c) shows the 1.4 GHz THOR+VGPS image of the field at 25′ resolution. There is no radio emission at the Chandra position of XTE J1829-098. However, within the RXTE error region, marked by the ellipse with a crosshair at the center, there is a prominent radio source detected in THOR. The source is marginally resolved, and the L-band peak flux density of this source at an effective frequency of 1.63 GHz is 4.15 ± 0.25 mJy/beam.

The source identified from THOR as the possible counterpart of the binary system, marked by a small white circle in Figure 3.3 (c), is also detected in the GLOSTAR survey and has a peak flux density of 2.30 ± 0.21 mJy/beam (Figure 3.3 (d)). The flux density values from the GLOSTAR sub-images are consistent with the in-band spectral index

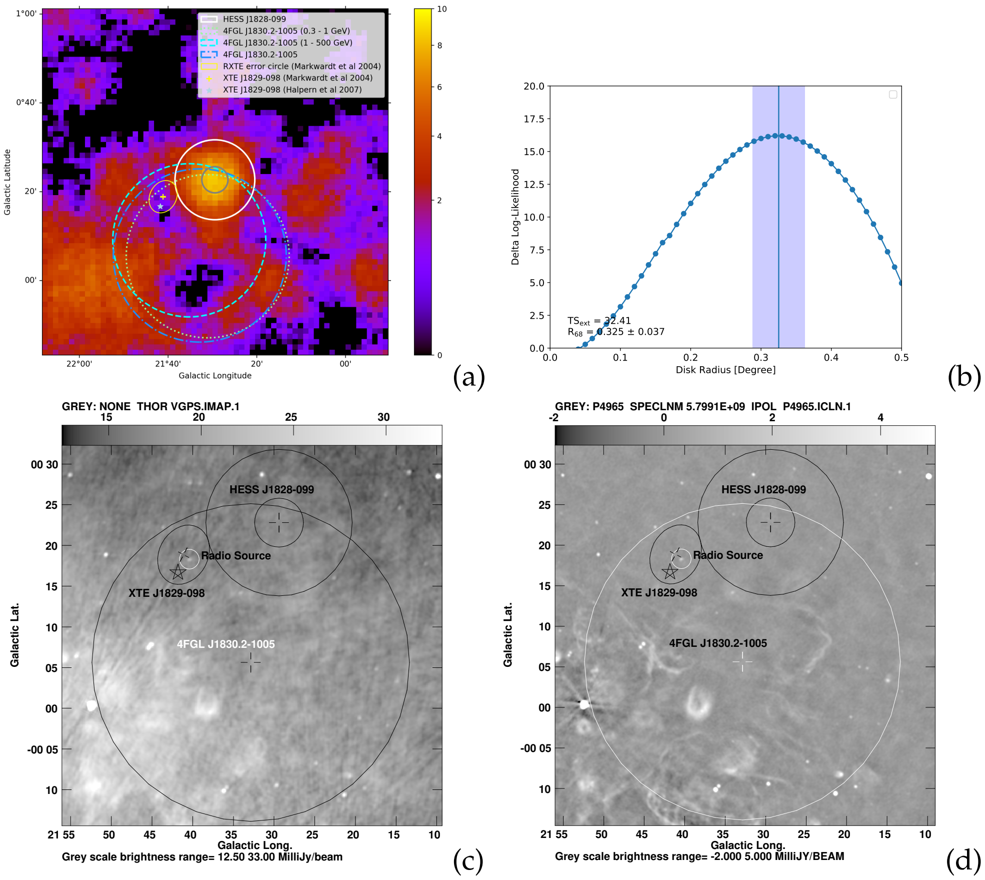

Figure 3.3 (a) H.E.S.S. significance map centered on HESS J1828-099. The color bar denotes the $\sqrt{TS}$ value of the region. The grey circle represents the extent up to which a 1D Gaussian template was fitted, and the white circle signifies the region within which spectral points for HESS J1828-099 were extracted. Morphologies of 4FGL J1830.2-1005 at different energy ranges are shown with a green dotted line (0.3 - 1 GeV) and a cyan dashed line (1 - 500 GeV). The blue dot-dashed line signifies a spatial extension of the 4FGL in the entire considered energy range (0.3 - 500 GeV). RXTE position of pulsar XTE J1829-098 [270], along with 99% confidence region [271] are also shown in yellow. The Chandra position of the pulsar is shown with a light-blue star, (b) Variation of the delta log-likelihood value of 4FGL J1830.2-1005 modeled with radial disks of different radii. The blue-shaded region indicates the uncertainty estimate of the best-fit extension of 4FGL J1830.2-1005. (c) The combined THOR and VGPS 1.4 GHz image and (d) the GLOSTAR 5.8 GHz image showing the radio continuum emission from the field containing HESS J1828-099, 4FGL J1830.2-1005, and the pulsar XTE J1829-098. The Chandra position of the pulsar is marked with a star, and the RXTE error region is shown with a black ellipse. The spatial extents marked for the H.E.S.S. and the 4FGL sources (0.3 - 500 GeV) are the same as in (a). The plausible radio counterpart of the binary system is marked by a white circle.

($\alpha_{\rm radio}$ where $S_\nu \propto \nu^{\alpha_{\rm radio}}$) of -0.746 ± 0.284 estimated from the flux values in different THOR spectral windows (SPWs). The observed radio spectrum is indicative of particle acceleration due to the collision of an ultrarelativistic pulsar wind and the wind/disk of the normal star. The extended nature of the source indicates its possible Galactic origin. In the complete catalog of the D configuration continuum sources (Medina et al., in prep.), it is classified as a candidate planetary nebula based on its Mid-IR properties. However, the non-detection of this source in the earlier 1.4 GHz NVSS image [the NRAO VLA Sky Survey; 306] at 45′ resolution also indicates the variability of this source. We note that the putative radio source is also detected at 147.5 MHz in the TIFR GMRT Sky Survey [TGSS; 307] with a flux density of 51.14 ± 8.45 mJy. The SED in Figure 3.4 includes the multi-wavelength radio data from the TGSS, THOR SPWs, as well as from the GLOSTAR sub-images. Considering the spectral index, possible variability, and the position of the source (within the RXTE error region but not coinciding with the Chandra position of XTE J1829-098), in the subsequent analysis, we consider both the possibilities that this radio source may or may not be a counterpart of HESS J1828-099. For the scenario that it is not associated, we have used the 3σ limits from the GLOSTAR, THOR, and the TGSS to construct (and model) the SED.

3.3 Multi-wavelength SED modeling

We have accumulated the data obtained from different multi-wavelength observations, shown in Figure 3.4 (a) and (b), to perform multi-wavelength SED modeling. We have considered a leptonic, Inverse Compton (IC) dominated, one-zone model, similar to [282], to explain the emission from HESS J1828-099. Since there is an offset between the Chandra position of XTE J1829-098 and the putative radio source found in the RXTE error region, we have explored two different cases to explain the multi-wavelength SEDs. In Model 1, we consider 3σ upper limits for radio flux density at the exact Chandra position of XTE J1829-098 and use these upper limits to construct the SED at radio frequencies, whereas, in Model 2, the radio source within the RXTE error region is assumed to be the radio counterpart of the HMXB and the GLOSTAR/THOR/TGSS data are used to extend the SED to radio wavelengths.

The HMXB XTE J1829-098 is located at a distance of 10 kpc from Earth [270]. Since the companion star of the HMXB probably is a Be star, we assume its age is $t_{age} \leq 10^7$ years and the stellar photon temperature T_* is ≈ 30000 K [308]. We have considered a population of accelerated electrons having a cutoff power-law spectrum, $dN/dE_e \propto E_e^{-\alpha_e} \exp(-E_e/E_{max})$ in the shock region between the pulsar and the companion star. A small distance between the companion star and the pulsar ($\sim 0.2''$) indicates that a photon field with high radiation density is present in the region. The ultra-relativistic electrons are cooling down by synchrotron and IC emission. Radio to X-ray emission is produced due to synchrotron emission, and γ rays are produced by IC emission. As discussed in

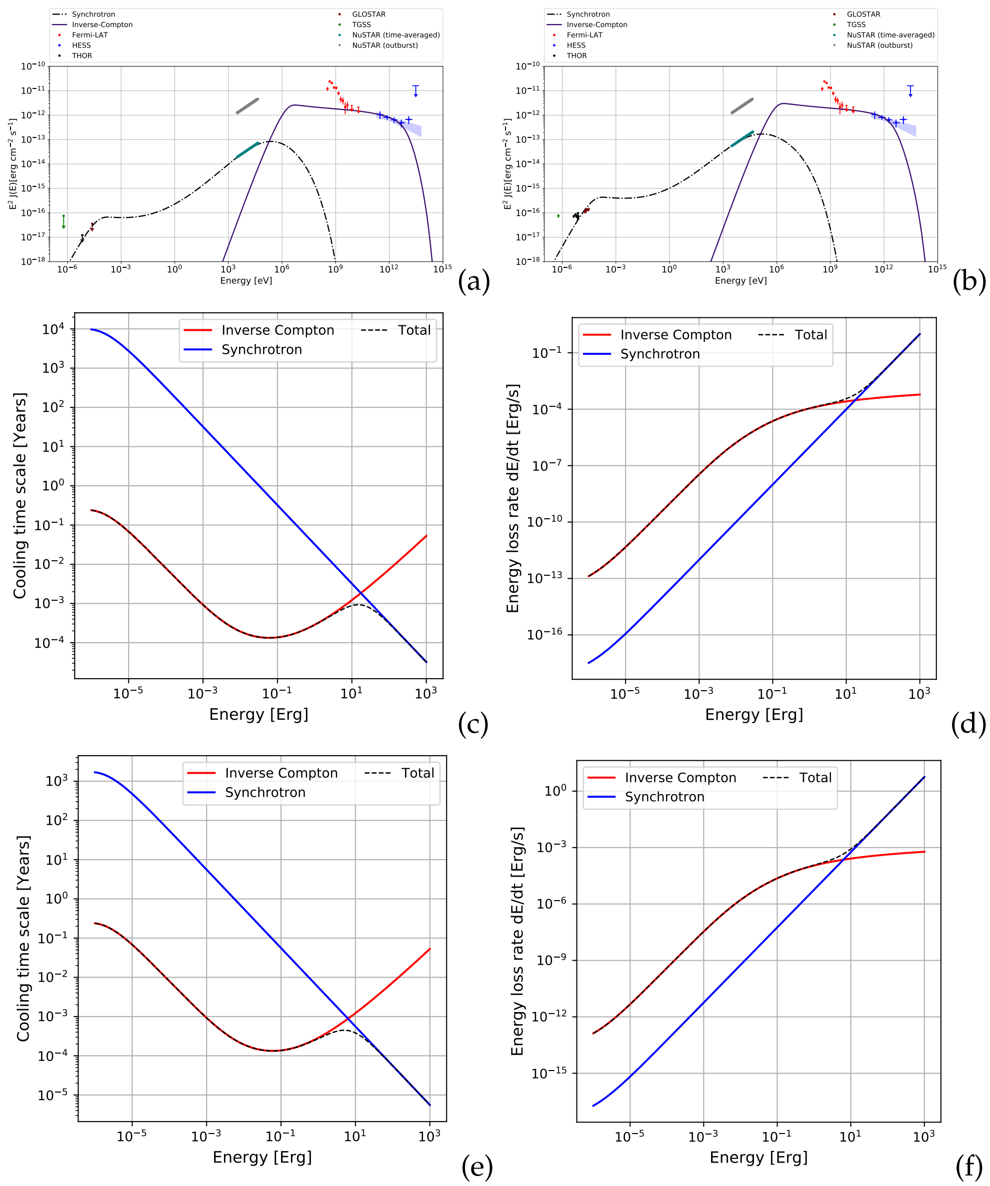

Figure 3.4 Multi-wavelength SED of the source HESS J1828-099 and corresponding IC dominated (a) model 1 and (b) model 2, obtained using **GAMERA**. The unabsorbed power-law X-ray SED obtained from NuSTAR data analysis in the outburst phase of XTE J1829-098 is shown with grey data points. The same unabsorbed X-ray SED, time-averaged over the orbital period of XTE J1829-098 [270], is shown with teal datapoints. The H.E.S.S. data, shown in blue, was taken from [265]. We have analyzed the *Fermi*-LAT data, and the corresponding SED from 4FGL J1830.2-1005 is shown in red. 3σ upper limits at radio range, obtained at the Chandra position of XTE J1829-098, observed by THOR (black), GLOSTAR (maroon), and TGSS (green), are shown in (a) with downward arrows. In (b), flux values of the putative radio source from these surveys are shown with the same color scheme. In (c) and (d), we present the cooling timescale and energy loss rate of model 1, at time t = $t_{age} \approx 10^7$ years. In (e) and (f), we plot the same as (c) and (d) for model 2.

Table 3.2 Parameters used for two models.

Parameter	Model 1	Model 2
E_{min} (GeV)	0.12	0.08
E_{max} (GeV)	5×10^4	5×10^4
α_e	2.2	2.2
B (mG)	25	60
T_* (K)	30000	30000
U_{rad} (erg cm^{-3})	1	1
Age (years)	10^7	10^7
Distance (kpc)	10	10

subsection 3.2.1, we detected a sub-dominant, power law X-ray component with a spectral index of $1.50^{+0.15}_{-0.10}$, which implies that the energy spectrum of parent electrons should have a power law spectral index $\alpha_e = 2\Gamma_X^{pl}$ -1 = $2.0^{+0.3}_{-0.2}$. We have searched within this range to find the best-fit spectral index for the parent electron spectrum for both model 1 and model 2. Moreover, we have also used an exponential cutoff in the parent electron spectrum, as electrons being leptons, lose energy very efficiently. We have assumed E_{max} = 50 TeV, the maximum energy up to which the parent electrons can be accelerated in the shock site.

By analyzing the NuSTAR data, the fluxes of the accretion component ($F_X^{acc} \simeq (3.66 \pm 0.02) \times 10^{-10}$ erg cm^{-2} s^{-1}) and the shock component ($F_X^{pl} \simeq (9.6 \pm 0.8) \times 10^{-12}$ erg cm^{-2} s^{-1}) in 3 - 79 keV range, during the outburst phase, were determined, as discussed in subsection 3.2.1. But XTE J1829-098, being a transient source, shows a very high observed dynamic range ($\sim$ 6800) [270], which indicates that the value of F_X^{acc} can decrease down to $\sim 10^{-14}$ erg cm^{-2} s^{-1} in its most quiescent phase. The flux of the shock component F_X^{pl} will also decrease when the XTE source is not in the outburst phase. Due to the lack of long-term observational data, we assume that the time-averaged flux of the shock component over the entire orbital periodic revolution is (1 - 5) $\times 10^{-2}$ times the flux measured in the outburst phase. This assumption is not unreasonable since the XTE source spends comparatively less time in the outburst phase during its orbital motion, making the time-averaged flux lower than that in the outburst phase. Moreover, other datasets in the radio, GeV, and TeV ranges considered in this chapter for multi-wavelength SED construction are collected from long-term observations, whereas the NuSTAR data for the XTE source is only observed during the outburst phase. Hence, to keep the multi-wavelength SED modeling consistent, we have assumed time-averaged X-ray fluxes from the XTE source. The assumed time-averaged X-ray fluxes used for model 1 and model 2 in the 3 - 79 keV range are, $F_X^{pl,1} \simeq (1.5 \pm 0.1) \times 10^{-13}$ erg cm^{-2} s^{-1} and $F_X^{pl,2} \simeq (4.4 \pm 0.3) \times 10^{-13}$ erg cm^{-2} s^{-1} respectively. Although some uncertainties might be associated with the assumed X-ray flux values, the data is within the dynamic range of the XTE source, which future observations can verify.

Previously, [282] modeled the multi-wavelength data of the TeV HMGB HESS J0632+057 using a one-zone leptonic model. We adopt the same value of the suppression factor due to KN effect from [282], i.e., $f_{KN}(E_e) \sim 10^{-3}$ for $kT_* \sim 3$ eV and $E_e = 1$ TeV. For this value of f_{KN}, the magnetic field was calculated from the relation $B \approx 5(f_{KN}F_X/F_\gamma^{TeV})^{0.5}$ G, where F_X and F_γ^{TeV} are fluxes of X-rays and TeV gamma-rays [265] respectively. We have considered a photon radiation density similar to that of [282], i.e., $U_{rad} \sim 1$ erg cm^{-3}. The IC emission of ultra-relativistic electrons is happening in the deep Klein-Nishina (KN) regime [282]; as a result, the TeV gamma-ray spectrum is softer compared to the X-ray spectrum produced by synchrotron emission. Such spectral variation was seen in X-Ray and TeV ranges for our source [265, 270], which is a characteristic feature of HMGBs.

We have studied the radiation from synchrotron and IC cooling of ultra-relativistic electrons by solving the particle transport equation using publicly available code **GAMERA**[3] [309]. We vary the total injected power in electrons to fit the multi-wavelength data of HESS J1828-099. The parameters required to explain the multi-wavelength data in both cases are given in Table 3.2. Both model 1 and model 2, depicted in Figure 3.4 (a) and (b) respectively, require a power of $\sim$ (4 - 5) $\times$ 10^{35} erg s^{-1}. Although the multi-wavelength one-zone models fail to reproduce the spectrum in the GeV range in both cases, the required luminosity in electrons of the models and the required parameters shown in Table 3.2 are consistent with those of the firmly established TeV HMGBs, thus indicating that HESS J1828-099 is possibly a TeV HMGB [308]. We also present the cooling time scale and energy loss rate of IC and synchrotron mechanisms considered in our models, in Figure 3.4 (c) and (d) respectively for model 1, and in Figure 3.4 (e) and (f) respectively for model 2.

3.4 Discussion and conclusion

The multi-wavelength SED of HESS J1828-099 shown in Figure 3.4 closely resembles that of other known TeV HMGBs, as all of the firmly established HMGBs have hard X-ray spectra and significantly softer spectra in TeV energies. Through a detailed *Fermi*-LAT data analysis, the SED in the GeV energy range was also obtained. This type of spectral shape was seen previously in [264], who assumed that GeV emission is due to some unrelated source such as SNR G22.7-0.2, which is co-spatial with HESS J1832-093 and 4FGL J1832.9-0913.

Since the resultant radiation from the hadronic *p-p* interaction between protons accelerated in the SNR shocks and cold protons clumped in nearby clouds can explain the analyzed GeV data, we have searched SNRs in the vicinity of HESS J1828-099. SNR G021.5-00.1, which has been detected in radio observations, was thought to be spatially coincident with 4FGL J1830.2-1005 [310–312]. Similarly, SNR G20.4+0.1, which is 1° away from HESS J1828-099, was assumed to be associated with the H.E.S.S. source [313]. However, it was

[3] https://github.com/libgamera/GAMERA

found from THOR + VGPS data, as well as in GLIMPSE and WISE data, that these are clumped HII regions and not SNRs [314]. Recently, in the GLOSTAR Galactic plane survey data, 4 SNR candidates were identified: G021.492-0.010, G021.596-0.179, G021.684+0.129, and G021.861+0.169, which fall within the positional uncertainty of 4FGL J1830.2-1005 [315], however further observations are needed to establish a molecular cloud association with these SNRs. Alternatively, since 4FGL J1830.2-1005 is in a crowded region of the Galactic plane, contamination from nearby pulsars can be significant. We tried to find any bright GeV gamma-ray emitting pulsar in the 4FGL catalog in the nearby region of 4FGL J1830.2-1005 but did not find any. If future observations detect a pulsar in the vicinity of the 4FGL source that is contaminating the GeV emission, then it might be possible to explain the GeV data by gating off the pulsar contribution using up-to-date ephemeris. At present, studying these scenarios is beyond the scope of this work. Our model 2 also fails to explain the TGSS data at 147.5 MHz (see Figure 3.4 (b)). Since the HMXBs show strong variability in the X-ray range and the TGSS radio measurements were performed at a different epoch than the X-ray observations, radio variability can be a possible reason behind this discrepancy. Alternatively, a completely different non-thermal low-energy radio component can also explain the TGSS data. Simultaneous observations in the X-ray and radio ranges can help to address this discrepancy. While usually, pulsars are the compact objects in HMGBs such as PSR B1259-63 and PSR J2032+4127; there is a recent debate on the nature of the compact object in LS 5039, which may actually be a magnetar with a spin period of 9 s [283, 316, 317]. Although the spin period of the proposed magnetar is very close to the spin period of XTE J1829-098, the surface magnetic field of the magnetars is typically around 10^{13} - 10^{15} G, whereas for the compact object in this binary source, the magnetic field is lower compared to that ($\approx 10^{12}$ G), confirming that the compact object in this HMXB system, is indeed a pulsar and not a magnetar.

Based on the definition of HMGBs [32, 174, 250, 318], the emission typically dominates above 1 MeV. In the case of HESS J1828-099, the average GeV flux observed by *Fermi*-LAT, F_{γ}^{GeV} ($\simeq (3.01 \pm 0.03) \times 10^{-11}$ erg cm^{-2} s^{-1}), is higher than the time-averaged X-ray flux values used both for model 1 and model 2, $F_X^{pl,1}$ and $F_X^{pl,2}$ respectively. Also, from Figure 3.4 (a) and (b), it can be seen that the multi-wavelength SED peaks above 1 MeV. This nature of emission indicates that HESS J1828-099 can be classified as an HMGB. Furthermore, the required values of parameters presented in Table 3.2 resemble those of known TeV HMGBs [282, 319]. We have kept the distance of the HMXB source ($\sim$ 10 kpc) fixed [270]. The environmental parameters such as magnetic field (B) and radiation density (U_{rad}) were assumed according to [282], and they were also kept fixed. Age (t_{age}) and stellar photon temperature (T_*) were consistent with the Be companion star [308]. The best-fit electron spectral index (α_e) was calculated considering the uncertainty in the power law spectral index of the newly detected, sub-dominant, additional X-ray component produced in the shock region between the rotating pulsar magnetosphere and infalling stellar material.

The magnetic fields used both for model 1 and model 2 are of the same order as in other established HMGBs [282], indicating that our assumption of the time-averaged X-ray flux is reasonable. The electron injection luminosity is the only free parameter that was varied to fit the data. The minimum energy of the parent electron population E_{min} in model 1 is an upper limit, as the radio upper limits do not represent a detection themselves. Considering the offset between the Chandra position of XTE J1829-098 and the putative radio source, model 1 seems to be the favorable interpretation of the source, although model 2 is also plausible. Taking into account the fact that this HMGB is at a larger distance compared to other known binaries, the required electron injection luminosity is consistent with that reported for other established HMGBs [181, 308, 319].

In this work, we have performed GeV, X-ray, and radio data analyses and used results from previous infrared data analyses. From the X-ray data analysis, we have detected a sub-dominant, hard X-ray tail in the NuSTAR source spectrum of XTE J1829-098, which suggests that the X-rays are produced via synchrotron cooling of shocked electrons. However, alternate interpretations for the hard X-ray tail include a compact jet, a hot corona, and an accretion disc, all of which have been observed in HMXBs [320, 321]. Long-term X-ray observations are necessary to confirm the origin of the hard X-ray emission. We have also performed one-zone modeling of the multi-wavelength data of HESS J1828-099, and we have successfully reconciled radio, X-ray, and TeV data. Although our one-zone model strongly suggests that HESS J1828-099 is a TeV HMGB, the GeV data could not be explained by IC emission using this model. Emissions from SNRs associated with molecular clouds and contamination from hitherto undetected nearby pulsars are some of the other possible scenarios that can explain the GeV emission. Nevertheless, based on positional coincidence and spectral information, as well as the agreeable fit of our one-zone model to the observed multi-wavelength data and the consistency of the best-fit model parameters to that of previously studied HMGBs, we conclude that HESS J1828-099 is the TeV counterpart of the HMXB, thus contributing to the increasing number of TeV HMGBs detected. Further deep observations in different wavelengths and detailed modeling of the source are needed to confirm the nature of HESS J1828-099.

4

Hadronic origin of ultra high energy gamma-ray source LHAASO J1908+0621

Recent observations by the Large High Altitude Air Shower Observatory (LHAASO) have paved the way for the observational detection of PeVatrons in the Milky Way Galaxy, thus revolutionizing the field of gamma-ray astrophysics. We study one such detected source, LHAASO J1908+0621, and explore the origin of multi-TeV gamma-ray emission from this source. A middle-aged radio supernova remnant SNR G40.5-0.5 and a GeV pulsar PSR J1907+0602 are co-spatial with LHAASO J1908+0621. Dense molecular clouds are also found to be associated with SNR G40.5-0.5. We explain the multi-TeV gamma-ray emission observed from the direction of LHAASO J1908+0621 by the hadronic interaction between accelerated protons that escaped from the SNR shock front and cold protons present inside the dense molecular clouds and the leptonic emission from the pulsar wind nebula (PWN) associated with the pulsar J1907+0602. Moreover, we explain lower energy gamma-ray emission by considering the radiative cooling of the electrons that escaped from SNR G40.5-0.5. Finally, the combined lepto-hadronic scenario was used to explain the multi-wavelength spectral energy distribution (SED) of LHAASO J1908+0621. Although not yet significant, an IceCube hotspot of neutrino emission is spatially associated with LHAASO J1908+0621, indicating a possible hadronic contribution. In this study, we show that if a hadronic component is present in LHAASO J1908+0621, then the second-generation IceCube observatory will detect neutrino from this source.

4.1 Background

Cosmic rays (CR) are charged atomic nuclei traversing through space with relativistic speed. The CRs consist of 90 % protons, about 8-9 % Helium nuclei, and smaller abundances of heavier elements. The observed local proton spectrum can be well described by a single power law with an index of -2.7, up to around 1 PeV (= 10^{15} eV) energy, which is also known as the "knee" of the CR spectrum. This hints towards the presence of powerful astrophysical proton accelerators in our Galaxy, which can accelerate the CR protons to PeV energies, the so-called "PeVatrons". Despite having been theoretically studied very thoroughly, no Galactic source has been unambiguously confirmed to be a PeVatron, except the possible case of the Galactic center [322–324]. Since CRs, which can accelerate up to PeV energies, can interact with the ambient medium to produce multi-TeV energy gamma-rays, the PeVatrons can be identified by studying the association of gamma-ray sources with them. To that end, successful operations by ground-based observatories such as

H.E.S.S. (High Energy Stereoscopic System), MAGIC (Major Atmospheric Gamma Imaging Cherenkov), Tibet ASγ, HAWC (High-Altitude Water Cherenkov), LHAASO (Large High Altitude Air Shower Observatory) over the past ten years have made the ultra-high energy (UHE) gamma-ray astronomy an active area of research. Since the ultra-high energy gamma rays produced outside our Galaxy get heavily attenuated by the Cosmic Microwave Background (CMB) and Infrared Background (IRB), it is difficult to detect UHE gamma-ray sources outside our Galaxy. However, the recent detections of many gamma-ray sources, emitting gamma-rays with energies ranging from several hundreds of TeV to PeV, have increased the possibilities to unambiguously confirm the presence of PeVatrons residing in our Galaxy.

LHAASO is a state-of-the-art dual-task facility designed for CRs and gamma-ray studies at a few hundred GeV to few PeV, located at 4410 m above sea level in China [141]. Since starting its operation in April 2020, LHAASO has detected more than a dozen of UHE gamma-ray sources in our Galaxy. Many of these sources are associated with PWNe or SNRs. Since the LHAASO observatory is sensitive enough to detect UHE gamma rays coming from a source, the chances of establishing astrophysical sources such as PWN or SNR as possible PeVatrons are very strong. For this work, we study one of such UHE gamma-ray sources observed by LHAASO, which has a strong possibility of being a Galactic PeVatron [142].

LHAASO J1908+0621 is a UHE gamma-ray source, detected in a serendipitous search for gamma-ray sources by LHAASO observatory [142]. This source was detected with 12 other sources with energies $\geq$ 100 TeV and statistical significance $\geq 7\sigma$. The LHAASO source is located at RA = 287.05° and Decl. = 6.35°, with a significance above 100 TeV to be 17.2σ, making it one of the brightest UHE gamma-ray sources in our Galaxy. The gamma-ray spectrum of this source reaches up to a maximum energy of 0.44 ± 0.05 PeV, and the differential photon flux of this source at 100 TeV was found to be 1.36 ± 0.18 Crab Unit (Crab Unit = flux of the Crab nebula at 100 TeV, 1 Crab Unit = 6.1×10^{-17} photons $\mathrm{TeV}^{-1}\ \mathrm{cm}^{-2}\ \mathrm{s}^{-1}$). Since the maximum energy the UHE gamma rays emitted from LHAASO J1908+0621 can attain is greater than 100 TeV, this source shows a strong possibility of being associated with a Galactic PeVatron.

[142] has obtained and fitted the gamma-ray spectrum of LHAASO J1908+0621 with a simple power law model and a log parabola model. The log parabola model gives a better fit compared to a simple power law model due to a gradual steepening of the gamma-ray spectrum between 10 TeV and 500 TeV. Although this steepening can be due to gamma-ray absorption from background photons, the effect of absorption was found to be small, even at very high energies. The best-fit parameters for the log-parabola gamma-ray spectral fit of LHAASO J1908+0621 are a = 2.27 and b = 0.46, where the log parabola model is defined by $(E/10\ \mathrm{TeV})^{-a-b\,log(E/10TeV)}$. The 68% contamination angle for LHAASO J1908+0621 was found to be 0.45°, obtained for gamma-rays over 25 TeV.

HAWC observatory has observed the LHAASO source to have a hard spectrum reaching energies above 100 TeV without any hint of an exponential cutoff, making it a best case for Galactic PeVatrons [325]. This source was first observed by MILAGRO observatory [326] and was later confirmed by H.E.S.S. observatory [327], which detected the source with large angular size ($\sigma = 0.34°$) and a hard spectral index of 2.1, above 300 GeV. ARGO-YBJ observatory [Astrophysical Radiation with Ground-based Observatory at YangBaJing; 328] has found that the TeV luminosity of this source is comparable to Crab Nebula, which makes it one of the most luminous Galactic gamma-ray sources in the TeV regime. The observation by VERITAS [Very Energetic Radiation Imaging Telescope Array System; 329] observatory has also revealed an extended source system ($\sigma = 0.44°$), with three peaks of emission and also, a photon index of 2.2. Additionally, the LHAASO source is associated with an IceCube neutrino hotspot, although the significance is low [330, 331]. The extended nature of the LHAASO source indicates that an SNR and/or PWN should be associated with this source. To that end, the study of possible counterparts of LHAASO J1908+0621 is necessary to establish both the gamma-ray production region and nearby particle accelerators.

LHAASO J1908+0621 is spatially associated with a middle-aged, shell-type supernova remnant SNR G40.5-0.5 [20-40 kyr; 332], which is brighter in the northern region of the TeV source, as observed in the radio data obtained by VLA Galactic Plane Survey [VGPS; 333]. The distance estimation places the SNR at a distance of 3.5 kpc, by CO observations [334] or a more distant position of 5.5-8.5 kpc, using Σ-D relation [332] and 6.1 kpc [335]. The recently discovered relatively young and energetic radio pulsar PSR J1907+0631 (characteristic age τ = 11 kyr, spin-down luminosity $\sim 5 \times 10^{35}$ erg s^{-1}) lies close to the projected center of the SNR [336]. The estimated distance of this pulsar obtained from dispersion measure (DM) is 7.9 kpc, which is compatible with the estimated distance of G40.5-0.5 and hints towards an association between these two objects. Although, in principle, PSR J1907+0631 can power the entire TeV source [337], the considerable offset between the pulsar and the position of the gamma-ray emission disfavors that scenario. Additionally, the distribution of molecular clouds (MCs) has been confirmed from studies involving the distribution of CO gas in the vicinity of SNR G40.5-0.5. [338] have searched for MCs with ^{12}CO (J=1-0), ^{13}CO (J=1-0) and C^{18}O (J=1-0) emission lines, and discovered the MCs to be spatially associated with SNR G40.5-0.5 in the ^{12}CO (J=1-0) and ^{13}CO (J=1-0) maps between the integrated velocity range of 46 and 66 km s^{-1}. A shell-like cavity around the radio morphology of SNR G40.5-0.5 was also observed in the ^{12}CO (J=1-0) and ^{13}CO (J=1-0) maps, indicating a possible SNR swept-up shell [338]. The presence of MCs is also confirmed by [339], in which the MCs were discovered in the ^{12}CO (J=1-0) and ^{13}CO (J=1-0) maps in the velocity range of 58-62 km s^{-1}. This discovery places the SNR+MC association at a near distance of $\sim$ 3-3.5 kpc and far distance of $\sim$ 8-9.5 kpc, and the corresponding mean number density of the MCs was estimated to be 110-180 cm^{-3}

assuming near distance and 45-60 cm^{-3} assuming far distance [338, 339].

Apart from the SNR G40.5-0.5 and PSR J1907+0631, a gamma-ray loud pulsar, PSR J1907+0602, was also found to be spatially associated with LHAASO J1908+0621, located in the southern part of the source [339]. The pulsar has a characteristic age of 19.5 kyr and a spin-down luminosity of 2.8 $\times$ 10^{36} erg s^{-1} [340]. The distance of the pulsar, estimated from DM, was found to be 3.2 $\pm$ 0.6 kpc [340]. [338] performed an off-pulse analysis of the *Fermi*-LAT data of the GeV pulsar PSR J1907+0602 and discovered a previously undetected, extended source spatially associated with the Milagro counterpart of LHAASO J1908+0621, labeled as Fermi J1906+0626. Additionally, another unidentified GeV source 4FGL J1906.2+0631, distance unknown, was located within the positional error of LHAASO J1908+0621 [341].

Due to its complex spatial morphology, the origin of the gamma-ray emission from LHAASO J1908+0621 is uncertain. Leptonic emission from PWN associated with PSR J1907+0602 can be a possible origin of the multi-TeV gamma-ray detected by LHAASO. The electrons can be accelerated up to 1 PeV at the wind termination shock of the PWN. However, electrons being leptons, lose energy radiatively very fast. Thus escape from the acceleration site and then further propagation can pose a real challenge to the scenario [142]. Furthermore, if electrons are the progenitor of the gamma-ray emission, no neutrinos should be detected by IceCube from the source region, and the neutrino hotspot could not be explained. Alternatively, escaped protons from the shock of the SNR G40.5-0.5 can penetrate the associated MCs and, through hadronic interaction, produce multi-TeV gamma rays. Although the SNR itself is too old to produce multi-TeV gamma-rays, protons accelerated at earlier epochs can initiate high energy gamma-ray emission from the MC region [142]. Moreover, in the hadronic scenario, one can also explain the neutrino hotspot near the source region. Intrigued by this fact, in this work, we explore the hadronic origin of LHAASO J1908+0621. We try to see the conditions in which the emission from the LHAASO source can be explained by gamma-rays originating from p-p interaction between accelerated protons from the SNR and cold protons inside the MCs, as well as calculate the corresponding neutrino emission from the hadronic interaction and compare it to the sensitivity of the IceCube Gen-2 observatory [342]. Additionally, we also consider leptonic emission from the PWN associated with PSR J1907+0602, as well as the leptonic emission from the SNR+MC system, along with the hadronic contribution, to understand the radiation mechanism implied by the observed multi-wavelength (MWL) SED.

In section 4.2, we discuss the morphology of the complicated region surrounding LHAASO J1908+0621. In section 4.3, we calculate the multi-TeV gamma-ray emission through hadronic interaction between accelerated protons from SNR and cold protons residing in the MCs. In section 4.4, we calculate the leptonic contributions from both SNR G40.5-0.5 and PWN associated with PSR J1907+0602. In section 4.5, we calculate the corresponding neutrino SED from the hadronic interaction and compare the calculation with the sensitivity of the IceCube observatory. In section 4.6, we discuss and subsequently conclude the obtained results reported in this work.

4.2 Morphology

Detailed morphological study of the region surrounding LHAASO J1908+0621 has been reported in [338], [339], and [142], using various observations by space-based and ground-based observatories. Through detailed *Fermi*-LAT data analysis, [338] has reported the position of the PWN associated with PSR J1907+0602. The position of SNR G40.5-0.5 and the surrounding MCs were also confirmed by radio observations and CO mapping, respectively [338, 339]. In general, a clear separation of high energy radiation from the low energy emission, attributed to their different original objects, must be strongly supported by the morphological observation of the extended source, in which the objects are spatially well separated. However, due to the complex juxtaposition of potential counterparts along the line-of-sight of LHAASO J1908+0621, it is difficult to distinguish among the sources responsible for high energy and low energy emissions from the region. In this section, we discuss the emission mechanisms considered in this chapter to explain the MWL SED of LHAASO J1908+0621 while being consistent with the observed energy morphology of the source region.

Ground-based observatories, such as H.E.S.S. and VERITAS, have good enough angular resolutions ($\sim 0.06^\circ$) to extract a high energy emission region in the direction of the LHAASO source. Although the significance is not very high, the significance map derived from the VERITAS observation indicates that the PWN associated with PSR J1907+0602 could be an important source for the VHE ($E > 100$ GeV) gamma-ray emission [329, 338, 339]. However, as given in [339], although the VERITAS emission lobe obtained from the significance map (significance levels ranging from 3σ to 5.2σ) matches well with the proposed PWN position, there is another VERITAS emission lobe, which is spatially coincident with the contact point between SNR G40.5-0.5 and the surrounding MCs (see figures 1 and 3 of [339]). This indicates that VHE gamma-rays obtained from both PWN J1907+0602 and the SNR+MC system should contribute to the SED obtained by VERITAS. Similar to VERITAS, in the H.E.S.S. significance map obtained by H.E.S.S. Galactic Plane Survey [HGPS; 343], emission lobes were found to be coincident with the position of PWN J1907+0602, as well as the contact region of the SNR+MC system. Moreover, the 68% containment region of the Gaussian morphology measured by H.E.S.S. comfortably overlaps with the SNR+MC system, as well as the PWN. The fact that the H.E.S.S. energy morphology contains two emission lobes spatially attributed to the VHE gamma-ray radiation from both the PWN and the SNR+MC system suggests that emissions from both the PWN and the SNR+MC system should be responsible for the VHE gamma-ray data observed by H.E.S.S [327, 343]. This is why we have considered the contributions from both PWN J1907+0602 and the SNR+MC system to satisfy the VHE SEDs obtained from VERITAS and H.E.S.S. observations. We note that since the Field of View (FoV) of VERITAS observatory [FoV $\sim 3.5°$; 344] is smaller than that of H.E.S.S. observatory [FoV $\sim 5°$; 133], VERITAS underestimates the total flux observed from the source region, as compared to that measured by H.E.S.S. observatory. We have taken the values of the FoVs into account while constructing the MWL SED of the source, and we have crudely scaled the VERITAS SED to visually match that measured by the H.E.S.S. observatory.

For other ground-based observatories such as LHAASO and HAWC, the angular resolution may not be enough to draw a detailed morphological map of the source region, but it should be enough to establish the extent of high energy emission from the source region. [142] has provided a KM2A significance map, which shows the potential counterparts of the UHE (> 100 TeV) gamma-ray source. From the inset of the Extended data, Figure 5 of [142], it can be seen that similar to H.E.S.S., the reported PWN position given by [338] is within the extent of the UHE emission observed by LHAASO, although an offset of 0.18°, or 10 pc (at 3.2 kpc), is also present between the centroid of the LHAASO emission morphology and the best-fit position of the disk morphology used to explain the PWN in [338]. On the other hand, the overlapping region of SNR G40.5-0.5 and the surrounding MCs is also situated well within the maximum significance region observed by LHAASO; however, the centroid of the UHE emission morphology observed by LHAASO is also not coincident with the contact region between SNR G40.5-0.5 and the associated MCs. No distinct lobes of emission, like in the cases of H.E.S.S. and VERITAS, were found in the source morphology observed by LHAASO, making it difficult to ascertain which source, the PWN or the SNR+MC system, is actually contributing to the UHE regime. [345] has tried to explain the UHE gamma-ray data observed by LHAASO using one-zone and two-zone, purely leptonic scenarios originating from PWN J1907+0602. However, it was found that the corresponding synchrotron fluxes obtained from the proposed models exceed the X-ray upper limits measured by XMM-Newton observatory [345]. Consequently, in this work, we explore the contribution of the SNR+MC system, which is another possible candidate overlapped with the image of LHAASO J1908+0621 [142], and determine the conditions for which the SNR+MC system would be responsible for the UHE gamma-ray emission observed by LHAASO. The phenomenological model explored in this chapter does not violate the observed X-ray upper limits.

As stated earlier, [338] had discovered an extended source by performing *Fermi*-LAT data analysis during the off-peak phases of the PSR J1907+0602. They have shown that this extended source, Fermi J1906+0626, shows a significant peak coincident with the molecular material distribution obtained from the CO mapping. This clearly implies that Fermi J1906+0626 is a result of interaction between accelerated particles from SNR G40.5-0.5 and the associated MCs. Moreover, as seen from Figure 2 of [338], the significance peak of Fermi J1906+0626 in 0.1 - 2 GeV energy range is outside of the TeV significance contours presented by VERITAS, as well as UHE emission morphology of LHAASO. So in this work, we explain the lower energy emission from the direction of LHAASO J1908+0621 by the leptonic interaction between escaped electrons from the SNR shock front and the molecular material. Since inside MCs, bremsstrahlung radiation will dominate IC cooling due to enhanced material number density, we have explained the lower energy gamma-ray SED (0.1 - 10 GeV) using bremsstrahlung emission in the present work. Below, we discuss the theoretical framework of our model, used to explain the MWL SED of LHAASO J1908+0621.

4.3 Hadronic modeling

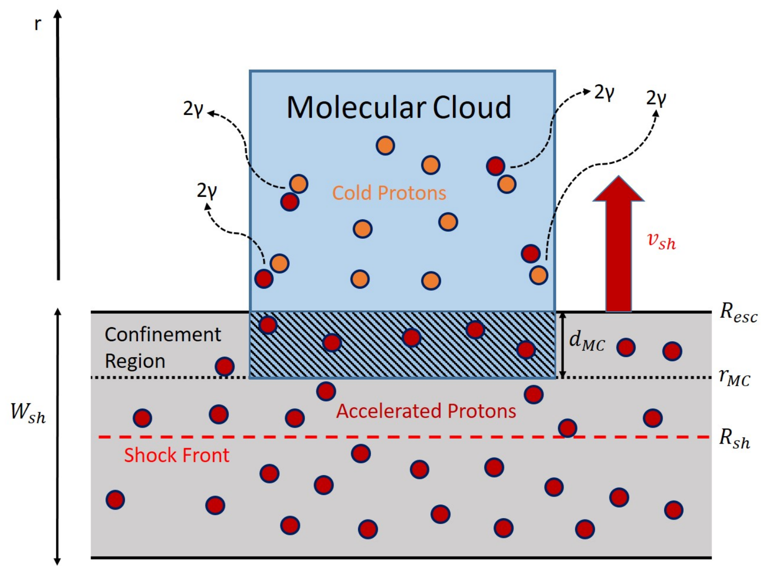

Figure 4.1 Schematic diagram showing the interaction between the SNR and associated MCs, following [346].

In this section, we calculate the hadronic contribution to the total gamma-ray flux observed by LHAASO from LHAASO J1908+0621. The hadronic component comprises the gamma-ray produced from the interaction between escaped protons from SNR G40.5-0.5 and cold protons residing inside the associated MCs. We assume that the SNR and MCs are at a distance of 8 kpc from the Earth, similar to [338]. For that distance, the number density of the associated MCs was assumed to be 45 cm^{-3} [338]. As evident by the radio observations, the SNR shows a shell-like structure, outside of which the MCs are present. Due to this fact, we assumed that the supernova exploded at the center of the cavity of the shell, which is surrounded by MCs, similar to [347]. After the explosion, the shock expands inside the cavity and finally hits the surrounding MCs, which are assumed to be ~ 22 pc from the cavity center.

After the explosion, the supernova is in the free expansion phase, in which the ejecta from the explosion expands freely without any deceleration. After time t_{Sedov}, the supernova enters the adiabatic Sedov phase, in which the mass of the swept-up ISM material by the shock wave increases and reaches densities that impede the free expansion. Rayleigh-Taylor instabilities arise once the mass of the swept-up ISM approaches that of the ejected material. In this phase, the cooling timescales are essentially much longer than the dynamical timescales, which makes this phase adiabatic in nature. This phase lasts until t_{Rad}, after which the supernova enters the radiative phase. When the shock expands through various phases of supernova evolution, its radius and velocity change with time. The time dependence of shock velocity is given by [347, 348],

$$v_{sh}(t) = \begin{cases} v_i & (t < t_{Sedov}), \\ v_i (t/t_{Sedov})^{-3/5} & (t_{Sedov} < t), \end{cases} \tag{4.1}$$

where v_{sh} is the velocity of the shock and v_i denotes the initial velocity of the ejecta. We assume $v_i = 10^9$ cm s^{-1} [347]. We can obtain the time dependence of the shock radius by integrating equation 4.1.

$$R_{sh}(t) \propto \begin{cases} (t/t_{Sedov}) & (t < t_{Sedov}), \\ (t/t_{Sedov})^{2/5} & (t_{Sedov} < t). \end{cases} \tag{4.2}$$

For this work, we assume the radius of the shock and time at the beginning of the Sedov phase, R_{Sedov} and t_{Sedov}, to be 2.1 pc and 210 yr following [346, 349].

The CR protons are accelerated through Diffusive Shock Acceleration (DSA) mechanism when the supernova is in the Sedov phase. The CRs are scattered back and forth across the shock front by magnetic turbulence during the acceleration as the shock front expands towards the surrounding MCs. Following [346, 348], we assume CR protons need to cross an escape boundary outside the shock front to escape from the SNR. To that end, we assume a geometrical confinement condition $l_{esc} = \kappa R_{sh}$ and adopt $\kappa = 0.04$ [346], where l_{esc} is the distance of the escape boundary from the shock front. Using this definition and equation 4.2, we can write the escaping radius,

$$R_{esc}(t) = (1 + \kappa) R_{sh}(t). \tag{4.3}$$

We assume that the accelerated CR protons need to cross this escaping radius to contribute to further astrophysical processes.

After traversing through the cavity, the SNR shock eventually hits the surrounding MCs. The shock has to travel a distance of ∼ 22 pc (= r_{MC}, distance of the MCs from the cavity center) to collide with the MCs. Setting $R_{esc} = r_{MC}$, from equation 4.2 and 4.3, the time of the collision can be found to be $t_{coll} \sim 7.5 \times 10^3$ yrs. Using t_{coll} in equation 4.1, the velocity of the shock at the point of collision can be calculated to be $v_{sh}(t_{coll}) \sim 1.2 \times 10^8$ cm/s. Following [347], we assume the SNR is at the end of the Sedov phase at $t = t_{coll}$, so the particle acceleration stops at $t \sim t_{coll}$. Hence the protons accelerated at $t \leq t_{coll}$ ($\sim t_{rad}$) will illuminate the MCs. However, in order to interact with the cold protons inside MCs, the accelerated CR protons have to escape from the SNR shock first. The protons which have higher energies will have more probability to escape the confinement region and take part in the hadronic interaction. Protons with lower energies will not be energetic enough to escape the confinement region. Since we are considering the interaction at a time when the outermost boundary of the confinement region (R_{esc}) collides with the MC surface (r_{MC}), i.e., t_{coll}, only the higher energy protons will take part in the hadronic interaction at t_{coll}, and the lower energy protons will still be confined around the SNR. Consequently, a dominant hadronic contribution, primarily in the highest energy, while a suppression in the escaped proton population in the lower energies, is expected from this scenario. This condition not only puts a constraint on the lower energy limit of the escaped proton population from the SNR shock but also on the spectral shape of the escaped protons. The CRs with higher energies escape the confinement region and start seeping into the MC when the escaping boundary (R_{esc}) contacts the surface of the MC (r_{MC}) [346]. The schematic diagram explaining the collision, as well as the escape of the accelerated proton population, is shown in Figure 4.1.

To estimate the minimum energy needed to escape the SNR shock, we use a phenomenological model, where the escape energy is expected to be a decreasing function of the shock radius [346]. This approach is based on the assumption that SNRs are responsible for observed CRs below the knee [234, 348]. The maximum energy of CR protons E_{max} is expected to increase up to the knee energy ($= 10^{15.5}$ eV) until the beginning of the Sedov phase, and then it decreases from that epoch. The escape energy can be given by a phenomenological power-law relation,

$$E_{esc} = E_{max} \left(\frac{R_{sh}}{R_{Sedov}} \right)^{-\alpha}, \tag{4.4}$$

where α is a parameter describing the evolution of the maximum energy during the Sedov phase [346, 348]. In this chapter, we assume that $\alpha = 2$, which also dictates the suppression of the escaped proton population at lower energies. Hence, assuming $E_{max} = 10^{15.5}$ eV, $R_{sh} = R_{esc} = r_{MC}$ and $R_{Sedov} = 2.1$ pc, we get the minimum energy needed by the CR protons to escape from the confinement region formed around the SNR shock front, when the escape boundary contacts the surrounding MC surface, i.e., $E_{esc} \approx 30$ TeV. We assume $E_{esc} = E_{min}$ while calculating the total hadronic contribution from the escaped CR proton population. We can also calculate the spectral index of the escaped CR proton population to ascertain its spectral shape. Since the protons are accelerated by the DSA mechanism, we assume that the CR proton spectrum at the shock front is represented by a power-law $\propto E^{-s}$. Then the spectrum of the escaped protons, i.e., the protons having the energy greater than E_{esc} is given by [346, 348],

$$N_{esc}(E) \propto E^{-[s+(\beta/\alpha)]}, \tag{4.5}$$

where β represents a thermal leakage model of CR injection and is given by β = 3(3 - s)/2. For s = 2, we get β = 1.5. Plugging in the value of s, α, and β in equation 4.5, we get the spectral index of the escaped CR protons to be ≈ 2.75. Note that the spectral shape and the minimum energy of the escaped protons are calculated when the escape boundary hits the surface of the surrounding MCs (t = t_{coll}).

After the collision at t_{coll}, the shock enters the momentum-conserving, radiative pressure-driven "snowplow" phase of evolution at t > t_{coll}. Similar to [347], we can express the shock in the cloud as a shell centered on r = $|\vec{r}|$ = 0, where $\vec{r}$ represents the radially outward direction from the cavity center. Furthermore, from the momentum conservation, the radius of the shocked shell R_{shell}(t) inside the MCs can be written as [347],

$$\begin{aligned}&\frac{4\pi}{3}\left[n_{MC}(R_{shell}(t)^3 - R_{sh}(t_{coll})^3) + n_{cav}R_{sh}(t_{coll})^3\right]\dot{R}_{shell}(t)\\&= \frac{4\pi}{3}n_{cav}R_{sh}(t_{coll})^3 v_{sh}(t_{coll}),\end{aligned} \tag{4.6}$$

with R_{shell} = r_{MC} at t = t_{coll}. n_{MC} = 45 cm^{-3}, is the number density of the associated MCs, and n_{cav} = 1 cm^{-3} represents the number density inside the cavity, which we choose to be same as that of the interstellar medium (ISM). We solve the equation 4.6 numerically at t > t_{coll}. We found that it takes the time t_{stop} ∼ 3.3×10^4 kyr for the shell radius to reach the radius of the observed shocked shell radius of ∼ 25 pc [334], and the calculated shell velocity of the shocked shell inside the MCs was found to be ∼ 55 km s^{-1}, which is very close to the observed internal gas velocity of the clouds of 10 km s^{-1} [334]. t_{stop}, which essentially indicates the age of the SNR+MC system, agrees well with the current age of the SNR G40.5-0.5 (20 - 40 kyr), and also, the shocked shell velocity agrees well with the observation. If the velocity of the shocked shell was equal to the internal gas velocity of the clouds, then no shell would have been observed. But since a shocked shell inside the surrounding MCs has been observed, it is expected for the velocity of the shell to be somewhat higher. This shows that the model is consistent with present-day observations of SNR G40.5-0.5. The variation of the shocked shell with time has been given in Figure 4.2 (b).

Now in this work, we have assumed that escaped CR protons that have entered clouds do not escape from the clouds before they lose energy through rapid radiative cooling [346, 347]. For that, the diffusion coefficient inside the MCs has to be very low compared to that observed in the ISM. Alternatively, it can be represented by the condition t_{diff} ≥ t_{stop}, where t_{diff} is the diffusion time of CRs inside a cloud, and it is given by t_{diff} ∼ L_{MC}^2/6D(E). L_{MC} is the size of the MCs, and D(E) is the energy-dependent diffusion coefficient [347].

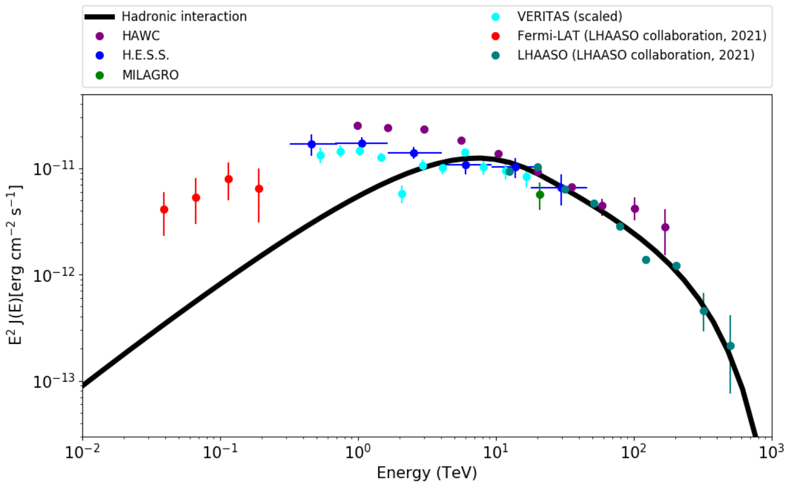

(a)

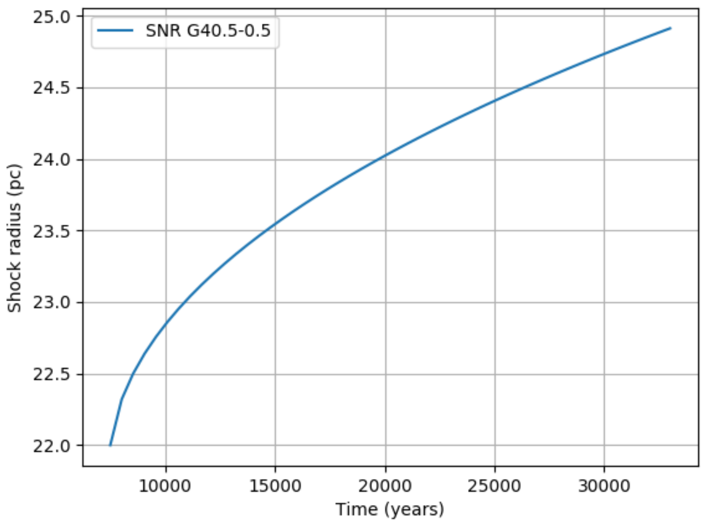

(b)

Figure 4.2 (a) Model gamma-ray SED obtained from hadronic p-p interaction inside the MCs surrounding the SNR G40.5-0.5. Along with the calculated SED, datapoints obtained from *Fermi*-LAT (red) [142], VERITAS (cyan) [329], H.E.S.S. (blue) [327], MILAGRO (green) [326], HAWC (purple) [325] and LHAASO (teal) [142] are also shown. The VERITAS data points have been scaled to visually match with that measured by the H.E.S.S. observatory. (b) The time evolution of the shocked shell associated with the SNR G40.5-0.5 inside the surrounding MCs is shown.

From the observed secondary-to-primary ratio of CR in the Galaxy, the energy-dependent diffusion coefficient in the Galaxy has been found to be D(E) $\approx 10^{28}\chi$(E/10 GeV)$^{\delta}$ cm^{2}s^{-1}, where δ can be between 0.3-0.6 and χ is a multiplicative factor [185]. It has been estimated before that although the value of χ is 1 in the Galaxy, inside dense MCs, the value is $\chi < 1$ [234]. The small value of χ can be attributed to the reduction of diffusion coefficient by the plasma waves generated by a stream of escaping CRs near the vicinity of the SNR [347, 350]. In order to fulfill the condition $t_{diff} \geq t_{stop}$, we found that the value of χ must follow the condition $\chi \leq 0.01$ [347]. This suppression of diffusion coefficient can be easily realized inside a dense molecular cloud environment, as the value of the diffusion coefficient inside MCs is estimated to be of the order of 10^{25} - 10^{26} cm^{2}s^{-1} [234]. If this is the case, then we can comfortably state that the injected CR protons inside the MCs lose their energy before escaping from the MCs. Moreover, since there is no effect of diffusion on the injected CR proton population, the spectral shape of the proton population does not change before they lose their energy radiatively. So we can assume the injected CR proton population attains a steady state before losing energy through hadronic p-p interaction. Thus, we calculate the total gamma-ray produced from this proton population through hadronic p-p interaction while keeping in mind that the gamma-ray spectrum calculated at the present age will be the same as that calculated at t $\sim t_{coll}$.

We have used **GAMERA** [351] to calculate the steady-state gamma-ray spectra from the population of injected CR protons inside the MCs that surround the SNR G40.5-0.5. We have used a CR proton population having power-law spectrum in the form of $N_p \propto E^{-\alpha_p}$, with a spectral index of $\alpha_p \approx 2.75$, the minimum energy of $E_{min} \approx 30$ TeV and maximum energy of $E_{max} \approx 10^{15.5}$ eV, i.e., the knee energy. We have considered the semi-analytical method developed by [90] to perform the hadronic interaction calculation. The magnetic field inside the cloud was assumed to be $B_{MC} \sim 60$ μG [347] and the number density used was $n_{MC} = 45$ cm^{-3} [338]. The total energy of the injected protons needed to fit the data observed by various observatories is $W_p \sim 2.5 \times 10^{49}$ erg, which is consistent with the usual 1 - 10 % of the kinetic energy released in SNRs ($E_{SN} = 10^{51}$ erg) [352]. The calculated spectrum, along with the observed data points, are given in Figure 4.2 (a).

From the Figure, it can be seen that the gamma-ray data observed by LHAASO, HAWC, H.E.S.S., and VERITAS were partially explained by the hadronic model due to the suppression of the parent proton population at sub-TeV energies. It is also evident from the Figure that an additional emission component is required for explaining the GeV - TeV part of the SED observed by *Fermi*-LAT, H.E.S.S., and VERITAS. Moreover, lower energy gamma-ray data points (not shown in Figure 4.2 (a)) obtained by [338] could not be explained by the same hadronic model, further indicating the necessity of additional emission components. In the next section, we aim to explain the sub-TeV, as well as lower energy (0.1 - 10 GeV) gamma-ray datapoints using leptonic contributions from both SNR

G40.5-0.5 and the PWN associated with PSR 1907+0602.

4.4 Leptonic modeling

4.4.1 PWN J1907+0602

Along with the hadronic contribution discussed in section 4.3, we also take into account the contribution from the leptonic emission of relativistic electron population from the PWN powered by the rotation-powered GeV pulsar PSR J1907+0602. The offset between the centroid of this extended source and PSR J1907+0602 indicates that this is a relic PWN [338]. We have considered a steady-state relativistic electron population from this PWN and calculated the total leptonic contribution from this source.

We have considered different leptonic cooling mechanisms, such as IC, synchrotron, and bremsstrahlung [91, 354, 355], and obtained the total gamma-ray SED from the electron population associated with the PWN using **GAMERA** [351]. The distance and the age of the PWN were set at 3.2 kpc and 19.5 kyr, respectively [340], same as that of PSR J1907+0602. The value of the magnetic field associated with a PWN, in general, is low ($\sim \mu$G) due to the adiabatic expansion of the PWN with time [356]. The magnetic field associated with PWN J1907+0602 was assumed to be $B_{PWN} \approx 3\ \mu$G, in order to be consistent with previous works by [338] and [339]. The number density inside the PWN was assumed to be n_{PWN} = 0.1 cm^{-3}. To calculate the IC contribution from the PWN, we have considered the ISRF model from [357]. We have also considered the contribution from Cosmic Microwave Background (CMB), having the temperature T_{CMB} = 2.7 K and energy density of U_{CMB} = 0.25 eV cm^{-3}. The spectrum of the electron population was assumed to be a simple power law with an exponential cutoff in the form of $N_e \propto E^{-\alpha_e^{PWN}} \exp(-E/E_{max}^{e,PWN})$. The spectral index of the spectrum was taken as $\alpha_e^{PWN} \approx 1.5$, and the maximum energy of the population was considered to be $E_{max}^{e,PWN} \approx 10$ TeV, which is constrained by the observed X-ray upper limits. The minimum energy of the electron population $E_{min}^{e,PWN}$ was given by the rest-mass energy. The energy budget of this relativistic electron population needed to satisfy the observed VHE data was found to be $W_e^{PWN} \sim 7.5 \times 10^{47}$ erg.

4.4.2 SNR G40.5-0.5

An extended object, labeled Fermi J1906+0626, illuminated in the GeV gamma-ray range, was reported from the off-pulse phase-resolved analysis done by [338]. In their work, the spectrum of this extended object, bright in the lower energy, was described by hadronic interaction between the SNR+MC system, modified by the diffusion inside the clouds. However, in this work, we consider that the lower energy spectrum is due to the contribution of the electrons escaping from the shock front of SNR G40.5-0.5, a scenario that has not been explored in previous works. Escaped electron population from the confinement region around the shock gets injected inside the surrounding MCs and

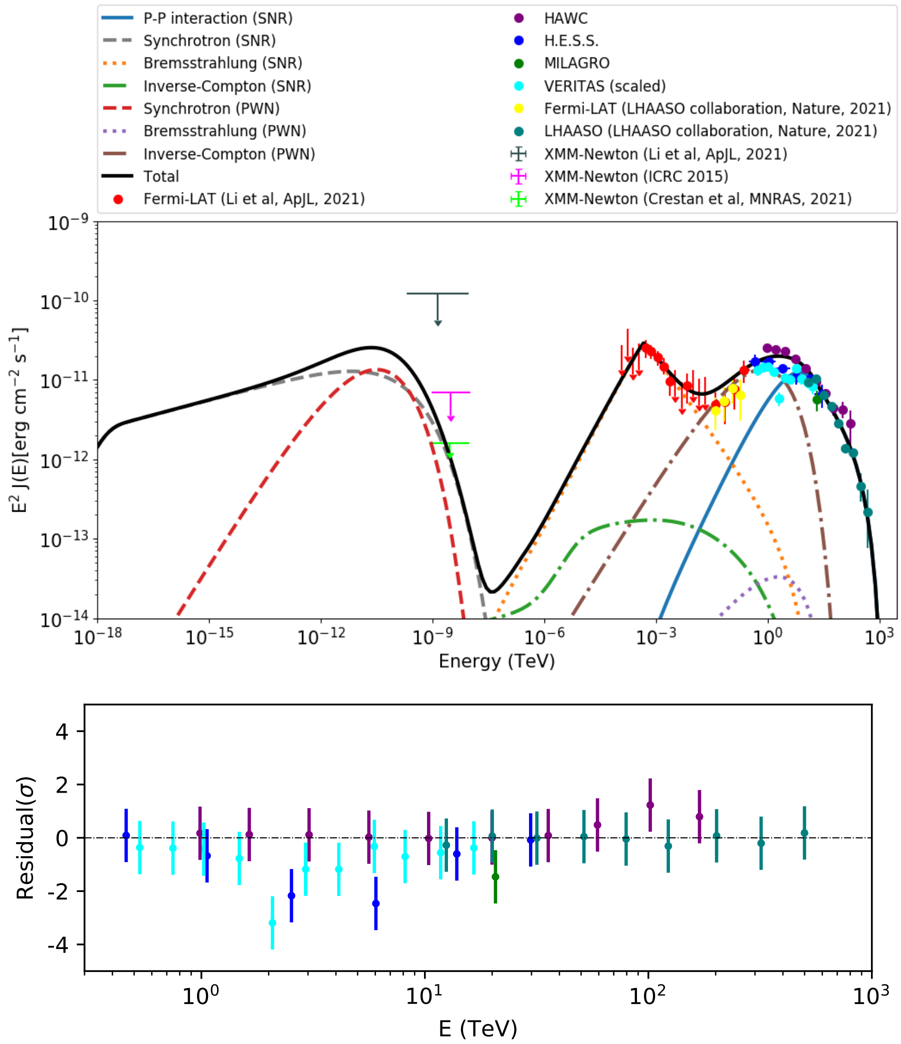

Figure 4.3 *Upper Panel:* MWL SED of LHAASO J1908+0621. Datapoints obtained from different observations by *Fermi*-LAT (red [338], yellow [142]), HAWC (purple) [325], H.E.S.S. (blue) [327], MILAGRO (green) [326], VERITAS (cyan) [329] and LHAASO (teal) [142] are shown in the Figure. The VERITAS data points have been scaled to visually match with that measured by the H.E.S.S. observatory. The XMM-Newton upper limit obtained from [338] is shown in dark slate grey. XMM-Newton upper limits obtained from [339] and [353] are shown in lime and magenta respectively. The solid blue line corresponds to the hadronic component from SNR G40.5-0.5. The synchrotron (grey dashed), bremsstrahlung (orange dotted), and IC (light green dot-dashed) components from SNR G40.5-0.5 are shown. Also, synchrotron (red dashed), bremsstrahlung (violet dotted), and IC (brown dot-dashed) components from PWN J1907+0602 are shown. The total combination of all of these components is shown with a solid black line. *Lower Panel:* The corresponding residual plot for the fit of the total model SED to the observed data from different observatories. The color scheme of the data points is the same as that described in the *Upper Panel*.

Table 4.1 Parameters used in the model, corresponding to the hadronic and the leptonic components from the SNR+MC association and the PWN, are provided in the Table below.

Source	Component	Parameter	Value
SNR G40.5-0.5 + MCs	Hadronic	Injection spectral index (α_p)	2.75
		Minimum energy (E_{min})	30 TeV
		Maximum energy (E_{max})	3.2 PeV
		Energy budget (W_p)	2.5×10^{49} erg
		Magnetic field (B_{MC})	60 μG
		Number density (n_{MC})	45 cm^{-3}
	Leptonic	Injection spectral index (α_e^{SNR})	2.75
		Minimum energy ($E_{min}^{e,SNR}$)	500 MeV
		Maximum energy ($E_{max}^{e,SNR}$)	6.9 TeV (Equation 4.7)
		Energy budget (W_e^{SNR})	1×10^{49} erg
		Magnetic field (B_{MC})	60 μG
		Number density (n_{MC})	45 cm^{-3}
PWN J1907+0602	Leptonic	Injection spectral index (α_e^{PWN})	1.5
		Minimum energy ($E_{min}^{e,PWN}$)	0.511 MeV
		Maximum energy ($E_{max}^{e,PWN}$)	10 TeV
		Energy budget (W_e^{PWN})	7.5×10^{47} erg
		Magnetic field (B_{PWN})	3 μG
		Number density (n_{PWN})	0.1 cm^{-3}

then interacts with the ambient medium of the same MCs. Emission is produced through synchrotron [91, 354] and IC [91] cooling of the injected electron population. Since the number density of the MCs is much higher compared to that of ISM, bremsstrahlung emission [355] dominates the lower energy gamma-ray SED. We have used **GAMERA** [351] as before to calculate the leptonic emissions.

Since the electrons go through the same evolution process as the protons before escaping from the SNR shock front, we assume that the spectral index of escaped CR electrons is the same as that of the protons [348], i.e., $\alpha_e^{SNR} \approx 2.75$. However, since the electrons, being leptons, lose energy radiatively very fast compared to protons, we have considered a simple power law with the exponential cutoff as the spectrum of the runaway electron population in the form of $N_e \propto E^{-\alpha_e^{SNR}} \exp(-E/E_{max}^{e,SNR})$. The maximum energy associated with the runaway electron population spectrum is given by the relation [347, 358],

$$E_{max}^{e,SNR} = 14 h^{-1/2} \left(\frac{v_{sh}}{10^8 \text{ cm/s}}\right) \left(\frac{B}{10\ \mu\text{G}}\right)^{-1/2} \text{TeV}, \tag{4.7}$$

where h($\sim$ 1) is determined by the shock angle and the gyro-factor, v_{sh} is the velocity of the shock front, and B is the downstream magnetic field. Since we calculate the maximum energy of the lepton population at the collision time, we considered $v_{sh}(t_{coll})$ as velocity in the above relation. We consider the magnetic field (B_{MC}) and number density (n_{MC}) inside the MCs same as that considered in section 4.3, so we use $B = B_{MC}$ in the above relation. The minimum energy of the electron population was assumed to be $E_{min}^{e,SNR}$ = 500 MeV. For the IC contribution, we have adopted the interstellar radiation field (ISRF) modeled in [357] at the position of SNR G40.5-0.5. The CMB contribution was also taken into account. The necessary energy budget of the runaway electron population to explain the lower energy gamma-ray SED was found to be $W_e^{SNR} \sim 1 \times 10^{49}$ erg.

After considering synchrotron, IC, and bremsstrahlung contributions from the runaway electron population from SNR G40.5-0.5, the lower energy (0.1 - 10 GeV) gamma-ray SED obtained by [338] could be explained adequately. The dominant contribution in explaining the SED in the 0.1 - 10 GeV range came from the bremsstrahlung component, which is expected, as the morphology associated with this lower energy gamma-ray emission was found to be spatially coincident with the molecular material enhancement observed inside the dense clumps surrounding SNR G40.5-0.5. The IC contribution was rather negligible in this case. The necessary model parameters used in this work have been summarized in Table 4.1.

The MWL SED of the source LHAASO J1908+0621 is shown in Figure 4.3, along with calculated SEDs from various leptonic and hadronic contributions from SNR G40.5-0.5 and PWN J1907+0602. From the Figure, it can be seen that the total model flux satisfies the observed gamma-ray SED data points from lower energies to the VHE-UHE regime. Most notably, the UHE gamma-ray spectrum observed by LHAASO can be explained by the hadronic component from the SNR+MC system. *Fermi*-LAT data points above 30 GeV, as obtained by [338], as well as [142], were explained by the leptonic contribution from the PWN, which also conforms with the *Fermi*-LAT morphology map obtained by [338] (see Figure 2 of that paper). Moreover, both PWN J1907+0602 and the SNR+MC system contribute to explaining the gamma-ray SED observed by VERITAS and H.E.S.S. The bremsstrahlung emission from the escaped electron population associated with SNR G40.5-0.5 also satisfies the lower energy gamma-ray SED. Very crucially, the combined synchrotron emission obtained from our model satisfies all of the upper limits obtained from various XMM-Newton data analysis [338, 339, 353], further confirming the validity of our model.

As can be seen from the upper panel of Figure 4.3, there remains a discrepancy between the data obtained by the Imaging Atmospheric Cherenkov Telescope (IACT) experiments and HAWC in the energy band of 1 to 10 TeV. Since HAWC has observed a larger source extent [359], the data observed by both H.E.S.S. and VERITAS are inconsistent with that observed by HAWC [339]. Consequently, in this particular work, we have tried to fit the data in this important band of 1-10 TeV by favoring more the HAWC data than the IACT

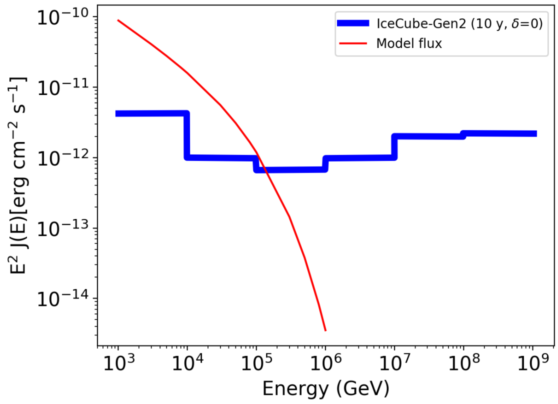

Figure 4.4 The estimated total muonic neutrino flux reaching the Earth from SNR G40.5-0.5. The continuous red line represents the total muonic neutrino flux produced due to the interactions of the escaped CR protons from SNR G40.5-0.5 with the cold protons in the associated molecular clouds. The blue solid, dashed line indicates the sensitivity of IceCube-Gen2 to detect the neutrino flux from a point source at the celestial equator with an average significance of 5σ after 10 years of observations.

data. The corresponding residual, i.e. (data-model)/error, the plot is given in the lower panel of Figure 4.3. From the Figure, it can be clearly seen that the total model SED is more consistent with the HAWC data, as compared to the data observed by H.E.S.S. and VERITAS in the 1-10 TeV range.

4.5 Neutrino flux

Neutrinos are also produced in hadronic p-p interactions, along with gamma rays. Consequently, if there are gamma-ray sources that are powered by hadronic interactions, neutrino emission from the same source region is also expected. MGRO J1908+06, the MILAGRO counterpart of LHAASO J1908+0621, maybe a neutrino source due to its extended nature and hard TeV gamma-ray spectrum [360, 361]. IceCube neutrino telescope searched for point-like source emission in the vicinity of this source. The astrophysical muon neutrino flux observed from this source region has been found to have the second-best p-value, being a Galactic source [330]. However, the emission is still consistent with the background. Although not quite significant yet, the presence of a neutrino hotspot associated with the source indicates hadronic emission in the highest energy range. The hadronic p-p interaction considered in the SNR+MC system to explain the UHE gamma-rays observed by LHAASO also produces neutrinos in the source region. In this section, we calculate the total muonic neutrino flux produced from the interactions between the escaped CR parent proton population from the SNR G40.5-0.5 and the cold protons residing inside the surrounding MCs.

To calculate the flux of the muonic neutrinos $\nu_\mu + \tilde{\nu}_\mu$, we use the semi-analytical formulation developed in [89]. Following [89], we have included the muonic neutrinos produced from direct decay of charged pions ($\pi \longrightarrow \mu\ \nu_\mu$) labeled as $\nu_\mu^{(1)}$ and from the decay of muons ($\mu \longrightarrow e\ \nu_\mu\ \nu_e$) labeled as $\nu_\mu^{(2)}$. E_p and E_ν denote the energies of the proton population and produced neutrinos, respectively. The total neutrino production rate from inelastic hadronic p-p interaction can be calculated using the equation [89],

$$\Phi_\nu(E_\nu) = \frac{c n_{MC}}{4\pi d^2} \int \sigma_{inel}(E_\nu/x) J_p(E_\nu/x) F_\nu(x, E_\nu/x) \frac{dx}{x}, \tag{4.8}$$

where the variable $x = E_\nu/E_p$, c is the velocity of light, n_{MC} is the density of the molecular clouds, d(= 8 kpc) is the distance of the SNR+MC system, $\sigma_{inel}(E_p)$ is the inelastic cross-section of p-p interaction, which is given by,

$$\sigma_{inel}(E_p) = 34.3 + 1.88L + 0.25L^2 \text{ mb}, \tag{4.9}$$

where $L = \ln(E_p/1 \text{ TeV})$. $J_p(E_p)$ signifies the spectrum of the parent proton population, and it is given by $J_p(E_p) = A(E_p/1 \text{ TeV})^{-\alpha_p}$. The normalization A (in the unit of erg^{-1}) can be calculated by performing the integration $W_p = A \int_{E_{min}}^{E_{max}} E_p\ (E_p/1 \text{ TeV})^{-\alpha_p}\ dE_p$, where the integration parameters are the same as that discussed in section 4.3. The condition that the maximum energy of the parent proton population can reach up to $E_{max} \approx 10^{15.5}$ eV is taken into account while considering the proton spectrum. F_ν represents the function that explains the spectra of $\nu_\mu^{(1)}$ and $\nu_\mu^{(2)}$, which get produced from the decays of charged pions and muons respectively [89]. Note that while for $\nu_\mu^{(2)}$, the lower and upper integration limits for equation 4.8 are 0 and 1 respectively, for $\nu_\mu^{(1)}$, the upper limit is 0.427. This is because the spectrum of $F_{\nu_\mu^{(1)}}$ sharply cuts off at $x = 0.427$ [89]. By integrating equation 4.8 with appropriate limits, we get the total muonic neutrino flux $\nu_\mu + \tilde{\nu}_\mu$, obtained from both channels of decays, and it is given by $\Phi_{\nu_\mu+\tilde{\nu}_\mu} = \Phi_{\nu_\mu^{(1)}+\tilde{\nu}_\mu^{(1)}} + \Phi_{\nu_\mu^{(2)}+\tilde{\nu}_\mu^{(2)}}$. Our estimated muon neutrino flux is shown in Figure 4.4 along with the IceCube-Gen2 sensitivity limit [342].

From Figure 4.4, it can be seen that the model neutrino flux exceeds the sensitivity limit of IceCube-Gen2. This implies that if the hadronic component from the SNR+MC system contributes to the total observed emission from the direction of LHAASO J1908+0621 in the TeV - PeV range, then the corresponding neutrino flux will be detectable by IceCube below PeV energies. This is an important differentiator between the leptonic and hadronic scenarios in the UHE range, as no neutrinos would get produced if the UHE gamma-ray emission from the LHAASO source is due to the IC cooling of one-zone or two-zone leptonic population [345]. Future observations by IceCube will help to confirm the exact nature of LHAASO J1908+0621.

4.6 Discussion and conclusion

In earlier literature [338, 340], it has been posited that the multi-TeV, VHE-UHE gamma-ray data points are most likely represented entirely by the leptonic emission from a population of relativistic electrons associated with the PWN of PSR J1907+0602. [338]

have explained the VHE-UHE gamma-ray data points with a leptonic component from the PWN since the spectrum measured by Cherenkov instruments resembles the spectral signature associated with IC emission from GeV/TeV PWNe. This approach was also considered in [339], as well as in [345]. However, [339] disfavored a one-zone leptonic scenario to explain the VHE-UHE gamma-ray spectra by the spatial morphology of the multi-TeV emission. The multi-TeV emission region associated with the PWN extends far from the pulsar position, but emission itself does not show any signs of spectral softening with the distance from the pulsar, as is expected from the cooling of electrons [339]. Moreover, due to the Klein-Nishina suppression of the IC cross-section at higher energies, the maximum energy of the electron population will attain a large value in order to fit the observed VHE-UHE gamma-ray data entirely by a one-zone electron population from PWN J1907+0602. Furthermore, if the multi-TeV, VHE-UHE gamma-ray datapoints were explained with a one-zone leptonic model from PWN J1907+0602, then the corresponding synchrotron flux would be incompatible with the X-ray upper limits obtained by [339, 353] in the keV energy range. These issues were echoed in [345], in which the authors also favored a two-population scenario to explain the VHE-UHE gamma-ray emission. Note that [339] also explored a one-zone hadronic model to explain the VHE-UHE gamma-rays and found that a very hard photon index is needed in their model, which was not seen in other TeV sources associated with SNRs. Hence, they concluded that a fully hadronic model is also disfavoured. [345] also stated that a one-zone hadronic model to explain the UHE gamma-rays observed by HAWC is not favored due to a lack of sufficient energy to power the hadronic emission and fit the observed data. It is clear that in order to explain the VHE-UHE gamma-ray emission, a two-population model is required. Any one-zone leptonic, as well as the hadronic scenario, is not sufficient for explaining the MWL SED of LHAASO J1908+0621 consistently.

In this study, we explore a lepto-hadronic scenario of CR interaction to produce VHE-UHE gamma-rays observed from the direction of LHAASO J1908+0621, with a particular focus on proper hadronic modeling required to explain both UHE gamma-rays observed by LHAASO, as well as the neutrino hotspot coincident with the source position, detected by IceCube. We have considered that the emission in the 10 GeV - 10 TeV energy range has originated due to the leptonic emission from PWN J1907+0602, whereas above 10 TeV, the emission has a hadronic origin. We use a physically viable and detailed model of CR interaction inside an SNR+MC system [346–348] to partially explain the observed UHE gamma-ray data points. The choice of the free parameter α constrains the minimum energy and the spectrum of the escaped CR proton population, which consistently reproduces the gamma-ray SED in the multi-TeV energy range. Moreover, the model matches the present-day observation of the state of the shocked shell inside the MCs. In addition, we have also included emissions due to leptonic cooling from PWN J1907+0602. Finally, we have shown that by considering these two scenarios, the gamma-ray data points extending from 10 GeV to 1 PeV can be explained well.

[338] had shown previously that in the 0.1 - 10 GeV range, an extended source, Fermi J1906+0626, is present overlapping the source region of MGRO J1908+06. The authors described SED from this source by a soft spectrum, which is similar to the ones observed in evolved SNRs. Moreover, they reported that from the *Fermi*-LAT analysis of this extended source, a significant peak was found coinciding with an enhancement of molecular cloud material, thus justifying the tentative hadronic origin of this low energy component. They further fitted the SED with a steep power law proton spectrum, which is modified by diffusion. The same model was considered in [345], where lower energy data points were fitted by a hadronic component from the SNR+MC system. However, in this work, we explain the gamma-ray SED in the 0.1 - 10 GeV range, with leptonic contribution from the SNR G40.5-0.5 and its surrounding MC system. We considered a power law spectrum with an exponential cutoff to explain the relativistic electron population associated with the SNR+MC system. We considered that, like protons, electrons could also escape from the confinement region around the shock front of the SNR and get injected into the MCs. After considering various leptonic cooling mechanisms inside the MCs, we found that the leptonic component from SNR G40.5-0.5 is adequate to explain the lower energy gamma-ray emission. Since bremsstrahlung emission dominates the IC cooling inside a dense molecular medium, it was primarily used to explain the lower energy gamma-ray SED. Moreover, this emission scenario was also corroborated by the spatial morphology observed by *Fermi*-LAT [338]. The combined lepto-hadronic scenario explored in our model not only satisfactorily explains the observed gamma-ray SED from low to ultra-high energy, but the synchrotron emission obtained from our model is also consistent with the observed X-ray upper limits.

Since there is a possibility of an IceCube neutrino hotspot present in the source region, we also calculated the total muonic neutrino flux from the hadronic interaction considered in this study. If the UHE emission is due to leptonic emission, then no neutrino would be seen from the source region. Although the hotspot is not significant yet, as observed by previous generation IceCube, the IceCube-Gen2 has a better sensitivity for detecting neutrino from a Galactic source. From our calculation, we found that the total neutrino flux exceeds the sensitivity limit of IceCube-Gen2, which implies that if the emission from LHAASO J1908+0621 is partially hadronic in origin, then IceCube-Gen2 will be able to detect neutrino from the source region. Future observation by IceCube will be crucial to divide the two emission contributions from the SNR+MC system and the PWN currently considered.

Although the model explored in this work satisfies the observed gamma-ray data points, as well as the X-ray upper limits, a lot of issues are still needed to be clarified by future experiments in the MWL bands. Since the source region is very complex, with the PWN and the SNR+MC system juxtaposed within the 68% containment region of many observatories, further morphological observations are very crucial to better constrain the model. More detailed morphological observations in UHE gamma-ray regime, which we expect that Cherenkov Telescope Array (CTA) will provide in the near future, will be important in discerning the source localizations, as well as their contributions. Moreover, long-term X-ray and radio observations are very crucial to constrain the modeling of this source. X-ray and radio observations will not only constrain the magnetic field but will also affect the minimum energy, the injection spectral index, and the energy budget of the parent lepton population of both the PWN and SNR+MC systems. Furthermore, astrophysical neutrino detection at the source region will, in turn, confirm the contribution of the hadronic component from the SNR+MC system at the UHE regime.

In conclusion, in this work, we have studied the underlying emission mechanism of LHAASO J1908+0621 suggested by the observed data and subsequently explored a simple, analytical, phenomenological model that is compatible with the MWL data points hitherto observed. In our model, the leptonic component from PWN J1907+0602 is dominant in the 10 GeV to 10 TeV range, whereas the hadronic component is used to explain the observed UHE SED above 10 TeV to 1 PeV energy range. The leptonic contribution from the SNR+MC system explains the lower energy part (0.1 - 10 GeV) of the gamma-ray SED. Our model also satisfies the observed X-ray upper limits. However, as discussed earlier, more detailed observations about the gamma-ray emitters in energy ranges from 0.5 TeV to 1 PeV will reveal more insight into the complex source region in the near future. Additionally, the crucial observations in X-ray and radio bands will play a huge role in unveiling the radiation mechanism of this source region through detailed MWL analyses. Future observations by the CTA observatory, as well as neutrino observation by IceCube-Gen2 at the source position, will be important to untangle the exact nature of this enigmatic source in both low and high energies.

5

Pulsar Wind Nebula interpretation of ultra high energy gamma-ray source LHAASO J2226+6057

The Large High Altitude Air Shower Observatory has reported the detection of cosmic-ray sources in the Milky Way that can accelerate particles up to PeV (= 10^{15} eV) energies. These sources, so-called "PeVatrons", are mostly unidentified. Several classes of sources, such as supernova remnants, pulsar wind nebula, or young stellar clusters, can potentially be the counterparts of these PeVatrons. The aim of this work is to study a pulsar wind nebula interpretation of one of these PeVatrons, LHAASO J2226+6057, which has a relatively well-covered multifrequency spectrum. We have performed leptonic, time-dependent modeling of the pulsar wind nebula (PWN) associated with PSR J2229+6114 considering a time-energy-dependent diffusion-loss equation. Injection, energy losses, as well as the escape of particles were considered to balance the time-dependent lepton population. We have also included the dynamics of the PWN and the associated supernova remnant (SNR) and their interaction via the reverse shock to study the reverberation phase of the system. We have considered different values of the braking index (n) and true age (t_{age}) for the fitting of the Multi-wavelength (MWL) spectral energy distribution (SED) of LHAASO J2226+6057. The best-fit PWN model parameters and their 1σ confidence intervals have been evaluated. We have also demonstrated the impact of reverberation on the MWL SED with increasing time. Additionally, we have discussed the resultant large radius and the low magnetic field associated with the PWN in question as caveats for the possible physical connection of the pulsar as the origin of this high energy source.

5.1 Background

Recent observations by state-of-the-art observatories, such as the Large High Altitude Air Shower Observatory (LHAASO), Tibet ASγ, the High Altitude Water Cherenkov (HAWC), among others, have paved the way for the detection of multiple Galactic ultra-high energy (UHE; $E_\gamma \geq 100$ TeV) gamma-ray sources [142, 362–364]. Upcoming observatories such as the Cherenkov Telescope Array [CTA; 365] and the Southern Wide-field Gamma-ray Observatory [SWGO; 366] will be of importance to identify and characterize these PeVatrons: Galactic CR sources that accelerate particles up to PeV energies.

As discussed earlier, LHAASO is a state-of-the-art dual-task facility designed for CRs and gamma-ray studies at a few hundred GeV to a few PeV, located at 4410 m above sea level in China [367]. The recent data reported by the LHAASO observatory show the existence of 12 significantly detected sources (> 7σ) that emit gamma rays with energies above several hundred TeVs [142]. Most of the sources reported by LHAASO have significantly extended gamma-ray emission regions up to $\sim 1^{\circ}$. The very high energy (VHE; 100 GeV $\leq E_{\gamma} \leq$ 100 TeV) counterparts of these sources residing in the Galactic plane have been associated with pulsar wind nebulae (PWNe), based on the spatial proximity with highly energetic pulsars and typically extended morphological features [322]. It has already been posited that UHE gamma-ray emission spatially coincident or in very close proximity of energetic pulsars with a high spin-down luminosity ($\dot{E} > 10^{36}$ erg s^{-1}) may be a universal feature; for more details, readers can refer to [184], for example. Moreover, the Crab nebula, associated with pulsar PSR B0531+21, was confirmed to be a PeVatron by recent LHAASO observations [142]. Bearing all of this in mind, it is natural to consider PWNe as possible Galactic PeVatrons, from which UHE gamma rays are detected.

PWNe, considered to be one of the most efficient lepton accelerators in the Galaxy, are powered by highly energetic pulsars. Pulsars dissipate most of their rotational energy via the injection of ultrarelativistic electron-positron pairs, which form a cold, ultrarelativistic wind of particles. Since the bulk velocity of this ultrarelativistic wind is supersonic with respect to the ambient medium, this wind creates a termination shock. Injected particles can be accelerated to very high energies at this termination shock. The accelerated leptons can then interact with the ambient matter, photon fields, and the magnetic field through Bremsstrahlung, inverse-Compton (IC), and synchrotron processes. The cooling of the accelerated leptons results in an MWL spectrum ranging from radio to gamma-ray energies. Here, we consider LHAASO J2226+6057 as our source of interest, as this is the only UHE gamma-ray source for which data have been observed across radio, X-ray, and gamma-ray energy ranges. It has been observed that LHAASO J2226+6057 is situated in a complex morphological region. Due to the close spatial proximity of Boomerang PWN, as well as supernova remnant (SNR) G106.3+2.7 and associated molecular clouds (MCs), it is hard to confirm the exact source responsible for the UHE gamma-ray emission observed. From the observations of Imaging Air Cherenkov Telescopes (IACTs), such as MAGIC and VERITAS, it was found that the emission region was divided into two morphological regions: the head and the tail. The head region contains Boomerang PWN and PSR J2229+6114, and the tail region contains VER J2227+608, which is likely to be associated with SNR G106.3+2.7 and the MCs in the region. Faint and diffuse radio and X-ray emissions were also observed from the tail region. It is possible that the emission from Boomerang PWN illuminates the head region, whereas the hadronic interaction occurring between the SNR and the MCs are responsible for the gamma-ray emission in the tail. Although it is difficult to confirm which source is actually responsible for the UHE gamma-ray emission, comprehensive studies are needed to explore both scenarios. New data from upcoming observations with a high angular resolution by MAGIC and VERITAS will be crucial to shed new light on this source. We discuss the features of LHAASO J2226+6057, as well as the previous works done for this source in Sec. 5.2. Then we comment on the PWN model used in this work in Sec. 5.3 and present the results in Sec. 5.4. We finally discuss and conclude in Sec. 5.5.

5.2 LHAASO J2226+6057 features

LHAASO J2226+6057 was detected at RA = 336.75° and Decl. = 60.95° with a significance of 13.6σ above 100 TeV. Its gamma-ray spectrum reaches up to a maximum energy of 0.57 ± 0.19 PeV [142]. This source is spatially associated with SNR G106.3+2.7, as well as the pulsar J2229+6114 and its wind nebula, known as the "Boomerang" nebula [368]. PSR J2229+6114 is a bright gamma-ray pulsar with a spin period of 51.6 ms, a characteristic age of 10460 yr, and a spin-down luminosity of 2.2×10^{37} erg s^{-1} [369]. Pulsed GeV gamma-ray emission from this pulsar was detected by *Fermi*-LAT [370]. In the VHE range, SNR G106.3+2.7 was observed by VERITAS as VER J2227+608, located 0.4° away from PSR J2229+6114 [371]. Gamma rays with GeV energies [372], diffuse non-thermal X-rays [373], as well as radio data [374] have also been observed from the source region. The distance of the source suffers from great uncertainty. It was estimated to be 7.5 kpc [based on the pulsar dispersion measure; 370], 3 kpc [based on X-ray absorption measurements; 369], and 0.8 kpc [based on measurements of radial velocities of atomic hydrogen and molecular material; 368]. In this work, we consider the distance to be 3 kpc, similar to [375] and [376].

The possible connection between LHAASO J2226+6057 and PSR J2229+6114 has previously been studied by [377], [375], and [376]. [377] performed a time-independent one-zone treatment, which is a steady-state leptonic scenario from the PWN, to explain only the highest energy gamma-ray data. The evolution of the source was neglected, and also MWL data were not used. [375] used a time-dependent one-zone leptonic scenario from the PWN. However, the authors did not consider the effect of escape for LHAASO J2226+6057, which they only accounted for LHAASO J1908+0621, nor did they explore the effect of age and the braking index on the evolution of the injected leptonic population. The impact of the SNR reverse shock and its effects on the PWN radius evolution were not taken into account, assuming that such effects are important only if the age of the PWN is greater than 10 kyr, which is not necessarily the case; for more details, readers can refer to [378], for example. [376] also performed a similar study. The authors argue that a distorted nebula, which was created due to the impact of an SNR reverse shock, is responsible for the GeV gamma-ray emission observed from the source region by [372]. Their results are similar to those of [375]. Our PWN model here intends to test their conclusions after relaxing assumptions or adding additional physical details.

A recent paper by [143] has proposed a hadronic origin of the LHAASO source based on the spatial proximity of a molecular cloud (MC) with the gamma-ray centroid of the source. However, as pointed out by [377], the associated SNR is quite old to produce the observed hard gamma-ray spectrum at the highest energies. Consequently, a hadronic scenario from an SNR+MC association would need peculiar modeling to explain the UHE gamma-ray spectrum observed from the source. A novel approach was explored in [187] to explain the hadronic origin of LHAASO J1908+0621, and perhaps, a similar approach may participate here as well.

5.3 Brief description of the model

For this work, we have used the code **TIDE**, for which earlier applications can be found in [379], [378], and [380], for example. The numerical code solves the evolution of leptonic pair distribution in the PWN as a function of Lorentz factor γ at time t described by the following equation:

$$\frac{\partial N(\gamma,t)}{\partial t} = Q(\gamma,t) - \frac{\partial}{\partial \gamma}[\dot{\gamma}(\gamma,t)N(\gamma,t)] - \frac{N(\gamma,t)}{\tau(\gamma,t)}. \tag{5.1}$$

The left-hand side of equation 5.1 describes the variation of lepton distribution in time. The first term on the right-hand side is the Lepton injection function Q(γ, t), which is usually assumed as a broken power law:

$$Q(\gamma,t) = Q_0(t)\begin{cases}(\gamma/\gamma_b)^{-\alpha_1} & \gamma \le \gamma_b, \\ (\gamma/\gamma_b)^{-\alpha_2} & \gamma > \gamma_b.\end{cases} \tag{5.2}$$

The second and third terms on the right-hand side take radiative losses into account – such as synchrotron, IC, Bremsstrahlung, adiabatic losses, or heating – as well as the escape of the particles (we assume Bohm diffusion), respectively (see [356] for the incorporated formulae). The normalization factor Q_0(t) is calculated using the spin-down luminosity L(t) of the pulsar through the equation, $(1-\eta)L(t) = \int_{\gamma min}^{\gamma_{max}} \gamma m_e c^2 Q(\gamma,t) d\gamma$, where η is the fraction of spin-down power that goes on to power the magnetic field of the PWN. The magnetic field varies in time as a result of the balance between the magnetic field power and adiabatic gains or losses of the field due to the contraction or the expansion of the PWN [381]. The reverberation phase of the PWN included in the model has been considered to be the same as that in [382]. The variation of the PWN radius is calculated by taking into account the age, SNR explosion energy, ambient medium density, expansion velocity of the nebula, and pressure profiles of the SNR at the position of the PWN. The model takes into account the change in pressure profiles depending on whether the PWN shell is surrounded by unshocked ejecta (i.e., R < R_{RS}) or the shocked ejecta (i.e., R_{RS} < R < R_{SNR}), where R_{RS} and R_{SNR} are the radii of the SNR reverse shock and the SNR, respectively. After reverberation, an assumed Sedov expansion follows when the PWN reaches the pressure of the SNR. For more details, readers can refer to [378], [382], and [380], for example. For a more thorough description of the reverberation period, we need to account for the fact that the ejecta pressure is not constant [383, 384]. This is beyond the scope of this work since, at the moment, a prescription to deal with this fact in the context of radiative PWN is unavailable. Given the likely young age of the source, a PWN would be before the time of the largest compression (see below), and thus we expect the current approach to be acceptable.

5.4 Results

5.4.1 Braking index and true age exploration

In the works of [375] and [376], the true age and the braking index were chosen to be 7000 years and 3, respectively. Since the choice of the true age is essential for a time evolutionary model of PWNe, we explore other values here as well. On the other hand, if the pulsar is assumed to be a dipole in a vacuum, and considered to be spinning down by emitting only magnetic dipole radiation (MDR), then the corresponding braking index associated with the spin down is calculated to be 3 [385]. Alternatively, the spin-down of a pulsar driven entirely by a particle wind would result in a braking index of 1 [386, 387]. A combination of magnetic dipole radiation and wind braking would result in a braking index with a value between 1 and 3 [388]. Most of the observed pulsar braking indices fall within this range ([389, 390], and references therein). Although, there are exceptions: for example, PSR J1640–4631, which has a braking index of n = 3.15 ± 0.03 [388], and PSR J1734–3333, which has a braking index of n = 0.9 ± 0.2 [391]. For this work, we only consider the braking index range $1 < n < 3$. Since the choice of the braking index affects the characteristics of the pulsar spin down, it is also important to explore whether the variation of n affects the SED.

To explore the effect of n and t_{age} on the MWL SED, we have chosen $t_{age} = 1000, 4000,$ and 7000 years, and $n = 1.5, 2.0, 2.5,$ and 3.0. Given the characteristic age $\tau_c \approx 10.5$ kyr and the present-day spin-down luminosity $L(t_{age}) \approx 2.25 \times 10^{37}$ erg/s, the initial spin-down age (τ_0) and initial spin-down luminosity (L_0) were calculated using the relations,

$$L(t) = L_0 \left(1 + \frac{t}{\tau_0}\right)^{-\frac{n+1}{n-1}}, \tag{5.3}$$

and,

$$\tau_0 = \frac{2\tau_c}{n-1} - t, \tag{5.4}$$

for a specific choice of n and t_{age}. We also assume the values of the following parameters are the same throughout the work: minimum Lorentz factor $\gamma_{min} = 1$; SN explosion energy $E_{SN} = 10^{51}$ erg; interstellar medium (ISM) ambient density $\rho_{ISM} = 0.1$ cm^{-3}; SNR core density index = 0; SNR envelope density index = 9 (we assume a type II SN as the progenitor, as in [393–395]); PWN adiabatic index = 1.333 and SNR adiabatic index = 1.667; containment factor ϵ (ratio of the Larmor radius of particles to the radius of the termination shock) = 0.5: and magnetic compression ratio $\kappa = 3$ (strong shock condition). The ejected mass of the progenitor SNR was also fixed at $M_{ej} = 8M_\odot$ for the $n - t_{age}$ exploration. For the target radiation fields for the IC interaction, we considered the cosmic microwave background, far-infrared (FIR) and near-infrared (NIR) radiation fields at the

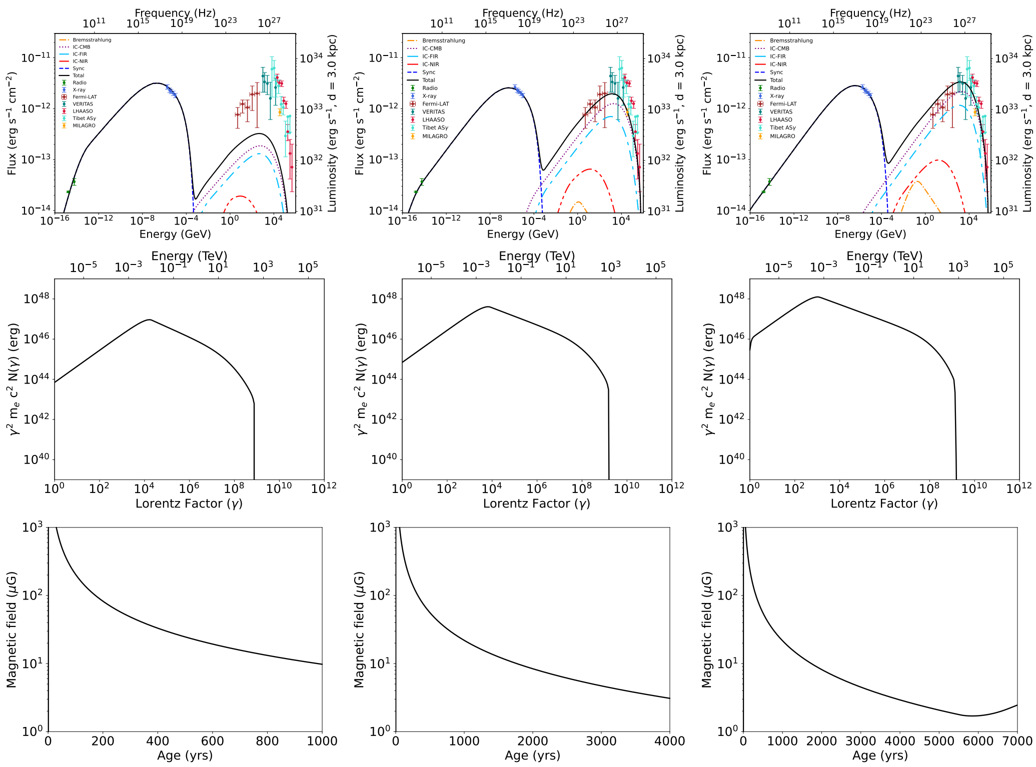

Figure 5.1 LHAASO J2226+6057 MWL SEDs along with the calculated model flux (top row), present lepton spectrum (middle row), and magnetic field evolution with time (bottom row) are given for t_{age} = 1000 years (left column), 4000 years (middle column) and 7000 years (right column), for a fixed braking index n = 2.5. The radio data (green) and X-ray data (royal blue) are taken from [374] and [373], respectively. Fermi-LAT (brown), VERITAS (teal), Tibet ASγ (turquoise), MILAGRO (orange), and LHAASO (crimson) data are taken from [372], [371], [143], [392] and [142], respectively.

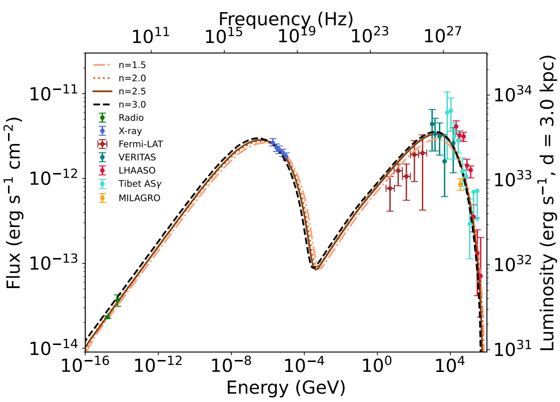

Figure 5.2 MWL SEDs of LHAASO J2226+6057 for n = 1.5, 2.0, 2.5, and 3.0. The color scheme of the data points is the same as given in Figure 5.1.

source position with temperatures of $T_{FIR} = 25$ K and $T_{NIR} = 5000$ K, respectively. The energy densities associated with the FIR and NIR field were taken from [396] and fixed at those values for $n - t_{age}$ exploration. It has almost always been observed (see [379]) that the energy densities of the FIR and NIR fields required to explain the IC emission from PWNe, differ from the interstellar radiation fields reported by [396]. [397] also argue that an enhancement of the radiation field is needed to explain the hard gamma-ray spectrum observed at the highest energies. However, since the aim of this subsection is to compare the effect of n and t_{age} on the computed SED, we have fixed the energy densities of FIR and NIR fields at the values given by [396], that is $\omega_{FIR} = 0.29$ eV cm^{-3} and $\omega_{NIR} = 0.45$ eV cm^{-3}, so there are fewer free parameters left for varying. The maximum Lorentz factor of the lepton distribution was fixed by the most restrictive condition between the synchrotron limit [398] or gyroradius limit [399] during the evolution. For a specific choice of n and t_{age}, we varied the injection function parameters, that is to say, low energy index α_1, high energy index α_2, energy break γ_b, as well as magnetic fraction η, to describe the MWL SED of the source.

First, we fixed the braking index at the value of $n = 2.5$ and considered three different cases of t_{age}. The MWL SED, along with the computed model flux, injected lepton spectrum, and magnetic field at the considered t_{age}, are shown in Figure 5.1. From the Figure, it can be seen that the fit corresponding to $t_{age} = 7000$ years is the best out of the three ages considered. For $t_{age} = 1000$ years and $t_{age} = 4000$ years, the X-ray and radio data can be adequately explained. However, for $t_{age} = 1000$ years, the IC emission is not significant enough to explain the high-energy data. Also, for $t_{age} = 4000$ years, the IC emission only partially explains it. From this exploration, it is apparent that the age of the PWN lies between 4000 and 7000 years. In this particular work, we consider $t_{age} = 7000$ years to compare our results with those obtained by [375] and [376], albeit these authors did not explore other options. We also discuss the results of considering the true age as a free parameter in a later subsection.

After limiting the age of the system, we subsequently explored the effect of the braking index on the evolution of the source. Assuming a fixed $t_{age} = 7000$ years, we changed the braking index and tried to describe the MWL SED. We calculated L_0 and τ_0 using equations 5.3 and 5.4. We again changed α_1, α_2, γ_b, and η, similarly to the previous case. The calculated spectra for $n = 1.5, 2.0, 2.5$, and 3.0 are given in Figure 5.2. We note that n does not significantly affect the computed SEDs, and we have selected $n = 2.5$ for further study.

5.4.2 χ^2 fitting of the MWL SED

We have considered typical PWN parameters as initial input, and, using the **TIDEFIT** code [400], subsequently varied them to solve equation 5.1 and computed the best χ^2-fitted model spectrum. To find the best-fit spectra, we used $t_{age} = 7000$ years and $n = 2.5$. Similar to the previous discussion, L_0 and τ_0 have been fixed at the value calculated by equation 5.3 and 5.4. The PWN parameters that had already been fixed in the above discussion have also been fixed in this calculation as well, except for the cases of the ejected mass and FIR and NIR energy densities (between 0.01 eV cm^{-3} to 5 eV cm^{-3}). Since the ejected mass of the progenitor SNR directly affects the size, as well as the magnetic field of the PWN, it was left free within the typical ejected mass range of 7M$_\odot$ to 15M$_\odot$. Apart from these changes and similarly to the previous discussion, α_1, α_2, γ_b, and η were left free to vary so as to find the best-fit MWL spectrum. The parameters used in the model are reported in Table 5.1, in which we have divided the parameters among measured or assumed, derived, and fitted values. The resulting plots are given in Figure 5.3. The time evolutions of the calculated MWL spectrum and injection spectrum are given in Figure 5.4.

From the top row of Figure 5.3, it can be seen that the computed MWL spectrum using the model, along with the 1σ confidence interval, matches with the observed MWL data well. The goodness of fit can also be seen from the bottom residual plot. The systematic uncertainty associated with the model is 0.32, and the χ^2/D.O.F. for the given fit is 35.65/30. Also, from the Figure, as well as from Table 5.1, it can be seen that FIR and NIR radiation fields do not contribute to the IC emission needed to explain the VHE-UHE data, rather it was found that the CMB is most likely solely responsible as the target photon field required. Recent work by [401] has also considered CMB photons as the most relevant target for IC scattering. However, such a result is somewhat different from what was assumed by [375], who considered radiation fields 1.5-3.0 times that of CMB to fit the data.

From the bottom row of Figure 5.3 and Table 5.1, it can be seen that the PWN would be very extended at the present age according to the model, and concurrently the associated magnetic field would be very low and close to the average Galactic value. The large radius of the PWN may agree with the large extension measured by LHAASO, but it contradicts the radio and X-ray sizes observed for the Boomerang PWN [369, 402], as these sizes are much smaller compared to the calculated PWN radius. The required magnetic field to fit the data is also uncomfortably low (we discuss this below) and begs the question of how the particles are confined in such a diluted PWN.

5.4.3 Possible impact of reverberation

From Figure 5.3, and from the resulting values given in Table 5.1, it can be seen that the radius of the SNR reverse shock is smaller than the PWN radius, which means that the reverse shock has just reached the position of the PWN shell at the onset of the reverberation phase of the PWN. If the age of the system is increased further from the considered age, the effect of reverberation will be apparent on the MWL spectrum. Since the PWN has just started to contract at the considered age of 7000 years, it is unlikely that it is heavily distorted.

We considered t_{age} = 7000, 8000, 9000, and 10500 years to study the effect of rever-

Table 5.1 Physical parameters used by and resulting from the fit. The bracketed terms in the fitted parameters section signify the lower and upper bounds of a 1σ confidence interval.

Definition	Parameter	Value
Measured or assumed parameters:		
Age	t_{age} [kyr]	7
Characteristic age	τ_c [kyr]	10.5
Braking index	n	2.5
Present day spin-down luminosity	L(t_{age}) [erg s^{-1}]	2.25×10^{37}
Distance	D [kpc]	3
Minimum energy at injection	γ_{min}	1
SN explosion energy	E_{SN} [erg]	10^{51}
ISM density	ρ_{ISM} [cm^{-3}]	0.1
SNR core density index	w_{core}	0
SNR envelope density index	w_{env}	9
PWN adiabatic index	γ_{PWN}	1.333
SNR adiabatic index	γ_{SNR}	1.667
Containment factor	ϵ	0.5
Magnetic compression ratio	κ	3
CMB temperature	T_{CMB} [K]	2.73
CMB energy density	ω_{CMB} [eV cm^{-3}]	0.25
FIR temperature	T_{FIR} [K]	25
NIR temperature	T_{NIR} [K]	5000
Derived parameters:		
Initial spin-down luminosity	L_0 [erg s^{-1}]	1.13×10^{38}
Initial spin-down age	τ_0 [kyr]	7
Fitted parameters:		
Energy break at injection	γ_b	3338.00 (2082.91, 10597.30)
Low energy index at injection	α_1	1.4522 (1.0000, 1.6432)
High energy index at injection	α_2	2.3727 (2.3316, 2.3890)
Ejected mass	M_{ej} [$M_\odot$]	8.8927 (8.1735, 9.3202)
Magnetic fraction	η	0.0033 (0.0026, 0.0060)
FIR energy density	ω_{FIR} [eV cm^{-3}]	0.0100 (0.0100, 0.4611)
NIR energy density	ω_{NIR} [eV cm^{-3}]	0.0100 (0.0100, 5.0000)
Resulting features:		
PWN radius	R_{PWN} (t_{age}) [pc]	9.33
SNR forward shock radius	R_{FS} (t_{age}) [pc]	16.23
SNR reverse shock radius	R_{RS} (t_{age}) [pc]	8.98
PWN magnetic field	B_{PWN} (t_{age}) [μG]	1.91

beration on the MWL spectrum. The braking index was chosen to be 2.5, and L_0 and τ_0 were calculated using equation 5.3 and 5.4 for a specific choice of t_{age}. Since we are only interested in comparing the effect of reverberation on the MWL spectrum based on the assumption of different ages of the PWN, we assumed the values of [396] for the FIR and NIR energy densities. Similarly to subsection 5.4.1, α_1, α_2, γ_b, and η were varied to find the most adequately fitted MWL spectrum for each case of t_{age}. The resulting plot is given in the left panel of Figure 5.5. The MWL spectrum gradually deviates away from the observed MWL SED, and consequently, the fit worsens. Since the magnetic field increases due to the compression of the PWN during the reverberation phase, the chosen input of the magnetic fraction η was decreased with an increasing considered age so as to control the fraction of spin-down luminosity that goes on to power the magnetic field of the nebula. Nevertheless, due to the compression of the nebula and high synchrotron burning, the power law index at high energy gradually softens with age, indicating the efficient cooling of the injected high-energy electrons to lower energies during reverberation. This, in turn, affects the spectrum of the resultant synchrotron and IC photons produced. This fact is apparent from the Figure, as the calculated MWL spectrum is unable to explain the observed X-ray and the VHE-UHE data present in the SED.

We have also considered t_{age} = 6500, 6800, 7200, and 7500 years and fitted the SED to study how the magnetic field and radius change. The corresponding plot is given in the right panel of Figure 5.5. The final PWN radius increases with increasing age, and it also corresponds to the onset of the PWN contraction due to reverberation in all cases. The PWN must be at the beginning stage of the contraction if the observed SED is to be explained. In all cases, the magnetic field is still low and close to, or lower than, the Galactic average value.

5.4.4 t_{age} as a free parameter

From the above discussion, it is apparent that the true age of the PWN cannot be much greater than 7000 years due to reverberation beginning afterward. As discussed in subsection 5.4.1, the true age cannot also be lower than 4000 years. Thus, we have used **TIDEFIT**, leaving the true age parameter free. Apart from t_{age}, the free parameters considered in this case are the same as that discussed in subsection 5.4.2. The best-fit t_{age} from the fitting of the MWL SED is 4880.3 (3871.4, 6060.4) years. This value is consistent with the range of the said parameter discussed above. The best-fitted model spectrum is similar to that shown in Figure 5.3. Although, the best-fit values of the free parameters obtained from the χ^2-fitting of the MWL SED, in this case, are not exactly the same as those obtained assuming t_{age} = 7000 years (see subsection 5.4.2 and Table 5.1), the 1σ confidence intervals of these free parameters for the two cases overlap with each other. Both solutions are essentially the same within uncertainties. So we decided not to report the best-fit results obtained in this case. We have also obtained a comparatively large PWN radius (R_{PWN} = 8.26 pc) and low magnetic field (B_{PWN} = 1.87 μG) associated with the PWN at the best fitted t_{age}, similar to the case discussed in subsection 5.4.2 for t_{age} = 7000 years, which we discuss next.

5.5 Discussion and conclusion

In this chapter, we have provided a detailed, time-dependent, one-zone model to explain the UHE gamma-ray emission observed from the direction of LHAASO J2226+6057 using the emission from PWN associated with PSR J2229+6114. We summarize the main points obtained in this work and compare them with previous studies.

1. The effects due to the variation of the true age and braking index were not explored in previous studies performed for this source. From our study, we found that a true age between 4000 and 7000 years is most suitable for the fitting of the SED of the source. Considering t_{age} as a free parameter during the fitting of the MWL SED also revealed a compatible result. Our study found that no significant effects can be seen on the MWL spectrum if we consider different braking indices.

2. We used the **TIDEFIT** code to fit the observed MWL SED by computing the best χ^2 fit model spectrum. From the fit, we found that CMB is the target photon field responsible for the IC cooling of the injected leptons from the PWN, whereas the effects of FIR and NIR radiation fields are negligible in this case. Additionally, we have found that the PWN at its current age must be extended (R_{PWN} ~ 10 pc), as are the extended source regions observed by VERITAS (~ 14 pc (0.27°)) [371] and LHAASO (~ 25.6 pc (0.49°)) [142]. The obtained PWN radius is larger when compared to, for example, X-ray radii observed for the Boomerang PWN, which is normal in one-zone models.

3. We have taken the effect of reverberation into account in our modeling. It was found that the PWN is at the onset of compression due to the impact of a reverse shock hitting the shell of the PWN. The effect of reverberation on the MWL spectrum was also explored by gradually increasing the true age of the PWN to the characteristic age. The MWL description worsened with increasing age. The true age cannot be much larger than the considered age of 7000 years if a PWN is responsible for the gamma-ray emission detected. Since reverberation does not provide a better fit, its inclusion does not solve the large radius and low magnetic field issue.

4. We have also found that a very low magnetic field (~ 2 μG) is needed to explain the MWL SED of the source, which is comparable with the Galactic average magnetic field value. A similarly low magnetic field (a few μG) was found in previous studies as the one needed to describe this source [375, 376]. Moreover, a low magnetic field was found for other LHAASO-detected PeVatron candidates as well [187, 338, 339, 375], which is an a priori obvious outcome of requesting a leptonically

generated high energy emission. Further complications of the model, as we have discussed, do not significantly alleviate this.

As discussed earlier, uncertainty regarding the distance of the source remains. We have explored this uncertainty by considering two very different values, D = 800 pc and D = 7.5 kpc. For D = 7.5 kpc, we have found the fit is comparatively worse compared to that discussed in subsection 5.4.2, with χ^2/D.O.F. = 36.78/30 and a systematic uncertainty of 0.41. On the other hand, the fit in the case of D = 800 pc is comparable to that discussed in subsection 5.4.2, with χ^2/D.O.F. = 35.88/30 and a systematic uncertainty of 0.32. There is no clear evidence to overrule one distance over the other, so we only report the case of D = 3 kpc in detail to directly compare our results with those of [375] and [376]. It is to be noted that the power law lepton injection spectrum is more favored in the case of D = 800 pc rather than a broken power law spectrum. However, the issue of a large radius and low magnetic field remains in this case as well.

The large estimated PWN size appears to be a caveat of the PWN interpretation of the LHAASO source. It is likely that both the head and the tail regions contribute to the total observed emission from the source. In light of such a complicated source morphology, a one-zone treatment of the source region considered in the model proves to be a simplistic take on the same. The large PWN radius obtained from the calculation could be a consequence of such a simplistic assumption. Nevertheless, our model tends to be the most definitive PWN approach considered thus far to explain the MWL emission from the LHAASO source, complete with a reverberation consideration and PWN true age estimation. It is to be noted that the PWN radius obtained by [375] ($\sim$ 3.1 pc) is different from that obtained in this work. Although one zone model has been considered in both cases, the differences in the formalism adopted to compute the radius evolution in the presence of the background SNR may be the reason behind this. In any case, further investigation will be important to properly address the complexity of the source morphology.

The Galactic magnetic field (GMF) plays an important role in the cosmic ray propagation. The intensity and orientation of GMF are constrained by several methods such as Zeeman-splitting observations [33]; infrared, synchrotron, and starlight polarization studies [34–36]; and Faraday rotation measures [37, 38]. The GMF model typically has three components, namely the disc (B_{Disc}), halo (B_{Halo}), and turbulent (B_{Turb}) contributions. Typical values for B_{Disc} and B_{Halo} lie within the range of 2-11 μG [185, 219]; although, the value of the turbulent component depends on the halo height of the Galaxy [219], for example, for a typical halo height of 8 kpc, the value of B_{Turb} comes out to be ≈ 6 μG [185]. Although the exact structure of the small-scale GMF is not known yet, from the models given by [38] and [403], and also from the observed secondary-to-primary ratio ([185], and references therein), the large-scale, average GMF can be estimated to be in the range 2-6 μG. The PWN magnetic field ($\sim$ 2 μG) would be marginally close to, or even lower than, any of the estimates of the average GMF value.

We see two possible ways out of this. On the one side, the local environment of the PWN could have been evacuated by the explosion of the supernova and/or by earlier explosions so that the local field in the vicinity is actually much lower than a few μG, allowing for a magnetic field contrast to appear between the PWN and its environment. On the other hand, there is still a chance that the approximate representation of reverberation that we have adopted here is still misleading. We know that assuming the ejecta pressure as constant (as all models of PWNe have so far done) is, in fact, an oversimplification [383, 384]. A better treatment of the ejecta pressure could plausibly change the reverberation results, and we shall explore this in the future. Of course, it is also possible that the PWN explanation of the source is not realized at all, and an additional hadronic component provides the dominant contribution. For the moment, a conflicting low value for the PWN magnetic field (not solved by age, braking indices, or the currently assumed behavior of the reverberation process) leaves the PWN origin of LHASSO J2226+6057, and other similar sources, in search of further observational tests.

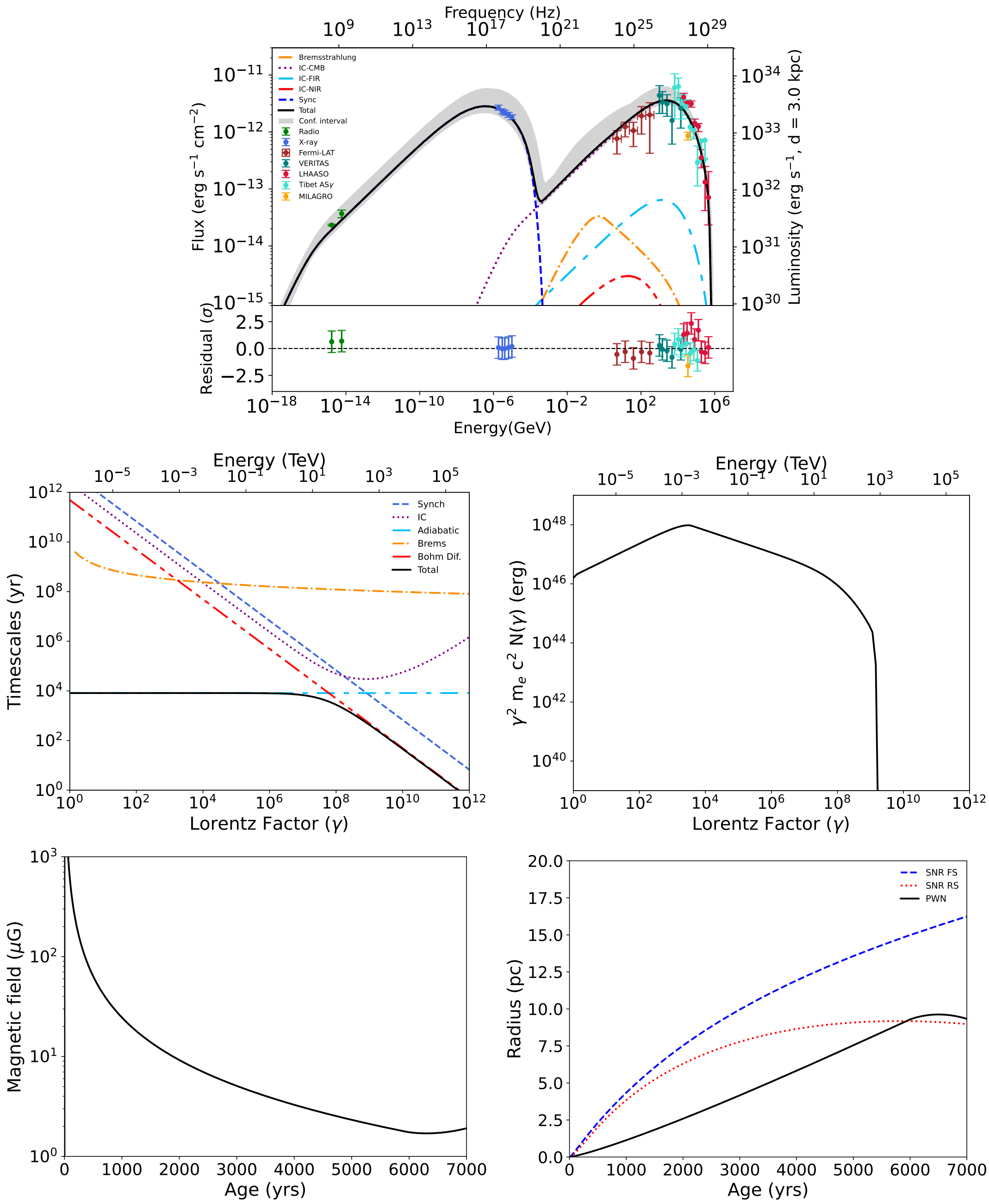

Figure 5.3 Calculated best-fit MWL spectrum is shown at the top row, along with the MWL data points. The color scheme of the data points is the same as that in Figure 5.1. In the bottom panel of the figure, the residuals are also plotted. The color scheme of the residuals is the same as the data points. The middle row shows the timescales of radiative losses, adiabatic losses, and the escape of particles considered in the model (left) and the injected lepton spectrum at the present age (right). Also, the time evolution of the magnetic field (left), as well as the SNR forward shock, SNR reverse shock, and PWN radius (right), are given in the bottom row.

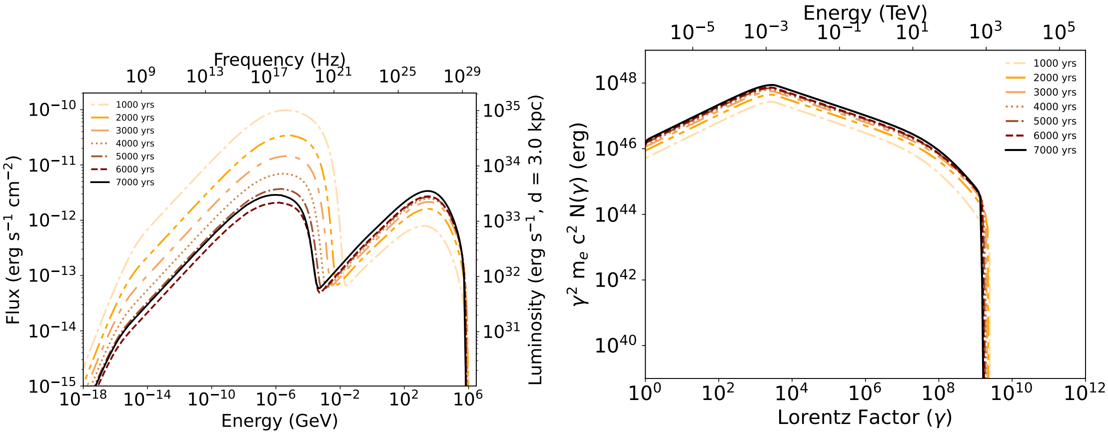

Figure 5.4 Time evolution of calculated MWL spectrum (left), as well as the injected lepton spectrum (right), are shown in the figure, assuming the parameters given in Table 5.1.

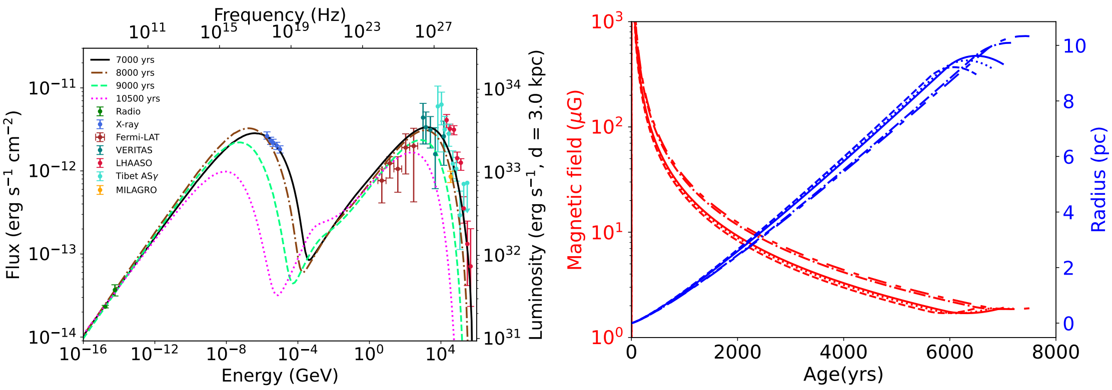

Figure 5.5 Impact of reverberation on the PWN MWL spectrum with increasing age is shown (left). The time evolution of the PWN magnetic field (red) and radius (blue) is shown (right) for t_{age} = 6500 years (dashed), 6800 years (dotted), 7000 years (solid), 7200 years (dot-dashed), and 7500 years (long-dashed).

6
Summary & Outlook

In this thesis, we have studied acceleration, propagation, and interaction mechanisms associated with various Galactic astrophysical sources in multi-messenger (cosmic rays, photons, neutrinos) and multi-wavelength (gamma-ray, X-ray, radio) contexts. The results presented in this thesis are divided into four chapters. In the first part, we presented a self-consistent model, where the positron excess phenomenon was explained by secondary positrons produced by interaction inside the nearby GMCs. Different cosmic ray observables were also consistently explained by the model. In the second part, we have reported a discovery of a new gamma-ray binary through detailed multi-wavelength modeling. Our work shows that the selected source, HESS J1828-099, maybe the first ever detected, accreting high-mass gamma-ray binary. In the third and fourth parts, we have tackled the issue of PeVatrons in the Galaxy. We have studied an ultra-high energy gamma-ray source LHAASO J1908+0621, and we have found that a combined combination of emission from SNR G40.5-0.5 and the associated molecular clouds and PWN associated with PSR J1907+0602 is responsible for the observed MWL SED. Further, we showed that neutrino flux would be observed by the next generation of IceCube, further confirming the SNR origin of emission from LHAASO J1908+0621. We have also studied another UHE gamma-ray source LHAASO J2226+6057 by assuming that PWN associated with PSR J2229+6114 is responsible for the emission. We have found that if that is the case, then the PWN must have a large radius and a low magnetic field, which is contrary to the observations. Our work shows that SNRs, along with PWNe, should also be a leading candidate source class for being a PeVatron observed in the Galaxy.

6.1 Impact & Novelty of Research

⊙ In Chapter 2, we provide an alternative model to explain the observed positron excess. We have considered contributions from all of the GMCs observed from large-scale CO surveys reported in multiple catalogs to the cosmic ray observables such as the proton, antiproton fluxes, and B/C, ^{10}Be/^{9}Be ratios. Lepton fluxes produced from *pp* interactions inside the GMCs has also been considered to explain the electron and positron spectra. Nearby GMCs to the Earth that have been observed in gamma rays have been treated with special attention due to their close proximity. Additionally, reacceleration due to magnetic turbulence has been considered in 7 nearby GMCs that are yet to be detected by *Fermi*-LAT due to their particular $M_5/d^2_{kpc} < 0.2$ value. We have shown that even if a small portion of protons injected into these GMCs are reaccelerated, then the resulting secondary positron flux will be able to explain the observed positron excess. We have also shown that the ($e^+ + e^-$) anisotropy of these nearby GMCs does not violate the *Fermi*-LAT upper limits.

⊙ In Chapter 3, we report our investigation regarding the nature and association of HESS J1828-099 with multi-wavelength observational data. We located a high mass X-ray binary (HMXB), consisting of pulsar XTE J1829-098 and a companion star, in close spatial proximity to HESS J1828-099. This HMXB has shown frequent outbursts and is primarily accreting. We detected GeV gamma-ray and radio counterparts consistent with the HMXB and HESS J1828-099 by analyzing $\sim$ 12 years of *Fermi*-LAT data and radio data from THOR and GLOSTAR observatories, respectively. By explaining the multi-wavelength spectral energy distribution of the source, we were able to posit that all of these counterparts have a common origin. We concluded that HESS J1828-099 might be the first ever detected, accreting HMGB.

⊙ In Chapter 4, we have reported our exploration regarding the ultra high energy gamma-ray emission from a LHAASO detected source, LHAASO J1908+0621. The multi-TeV VHE-UHE gamma-ray emission was explained by the combination of the hadronic interaction occuring in SNR G40.5-0.5 and the associated molecular clouds system, as well as the leptonic contribution from the PWN associated with the pulsar J1907+0602. The lower energy, GeV gamma-ray data was explained by the bremsstrahlung cooling of electrons accelerated at supernova shock. Our theoretical model is consistent with observed X-ray upper limits. Our model is also consistent with the IceCube neutrino hotspot coincident with the source. The study shows that an escape-limited scenario of cosmic ray acceleration at the SNR shocks can explain the observed UHE gamma-ray emission, thus indicating that besides PWNe, SNRs can also be a viable candidate for being PeVatrons.

⊙ In Chapter 5, we have explored the pulsar wind nebula interpretation of yet another ultra high energy gamma-ray source LHAASO J2226+6057. By solving a time-energy-dependent diffusion-loss equation, we have performed leptonic, time-dependent modeling of the PWN associated with PSR J2229+6114. Particle injection, energy losses, and escape of particles were considered to balance the time-dependent lepton population. We have also included the dynamics of the PWN and the associated SNR and their interaction via the reverse shock to study the reverberation phase of the system. After detailed theoretical modeling, we have found that if the multi-wavelength emission from LHAASO J2226+6057 is indeed due to the PWN associated with PSR J2229+6114, then the PWN must have an associated magnetic field of very small magnitude (potentially lower than the average Galactic magnetic field), and a very high radius, which defies the radio and X-ray observations. So, we concluded that it is unlikely that the PWN is the PeVatron source responsible for the UHE gamma-ray emission observed from the direction of LHAASO J2226+6057.

6.2 Future directions

Even after putting forth efforts behind the projects presented in this thesis, there continue to remain many open questions regarding multi-messenger and multi-wavelength research in the field of high-energy astrophysics.

The origin of cosmic rays has been a longstanding problem in the field of high-energy astrophysics. SNRs are thought to be responsible for accelerating particles up to PeV energies, which would also explain the break in the all-particle cosmic ray spectra, i.e., the "knee". Although this idea is theoretically possible, further experiments are needed to confirm its overall plausibility. These updated experiments should also be able to check whether there are any other source classes (i.e., PWNe, massive stellar clusters) that can be legitimate contenders for being Galactic accelerators, which produce cosmic rays that can contribute significantly to the Galactic cosmic ray sea. Moreover, several high-energy astrophysical sources, such as blazars [404, 405], starburst galaxies [406–409], tidal disruption events [410–413], gamma-ray bursts [414–418], etc., can accelerate ultra high energy cosmic rays, which contribute to the all-particle cosmic ray spectra above the "ankle" ($\sim 3 \times 10^{18}$ eV). This begs the question, which source(s) is responsible for the cosmic rays above the "knee", and below the "ankle"? Are there any hidden Galactic sources that can accelerate particles even beyond the "knee" energy, thus contributing to this energy range? How does the cosmic ray composition change from the "knee" to the highest energies? New detectors in the near future, such as KASCADE-Grande, IceTop/IceCube, extensions of Auger-South, and extension of the Telescope Array, will be able to elucidate these topics and provide additional information on the transition of cosmic rays from Galactic to the extragalactic regime. Not only the origin but also the propagation of cosmic rays in the Galaxy contains many problems that are needed to be addressed. As discussed earlier, cosmic rays interact with the materials of the ISM while getting diffused by the large-scale magnetic field of the Galaxy. Proper modeling of interstellar gas and the turbulent magnetic field in the Galaxy will help in understanding the cosmic ray propagation, as well as help in estimating secondary production in the Galaxy. Recent observations suggest that some cosmic rays may also be accelerated in the Galactic halo. The origin of these cosmic rays and their acceleration mechanism in the halo is still unclear and thus in need of further investigation.

Apart from cosmic ray observations, the detection of photons in multiple wavelengths, as well as neutrinos, is necessary to study various Galactic sources. The recent revolution in gamma-ray astronomy due to observations by different IACTs and air shower arrays has proven to be fundamental in detecting new sources in the Galaxy and beyond. Many point-like and extended sources have been revealed by these observations, most of which are unidentified. Observing these unknown sources in multiple wavelengths will be crucial in understanding their association with known astronomical sources, energy morphologies, and spectra. Further, modeling these sources using detailed theoretical models will be useful to study the interaction mechanisms at play in these sources, thus further confirming their nature and emission. By explaining the multi-wavelength data observed from these sources, novel interaction mechanisms can also be revealed in the future. Gamma-ray observations will be especially important to ascertain new emission mechanisms in Galactic sources. For example, the emission mechanism that produces gamma rays in novae outbursts, which are explosive events that occur on the surface of a white dwarf star in a binary system [419] or in rotating pulsars observed in gamma-ray [420], are yet to be fully understood. Other than specific Galactic sources, the origin of diffuse, extended gamma-ray emission that is observed in the Galactic plane is not well understood, but it is believed to be produced by cosmic ray interactions with interstellar gas and radiation fields. The Galactic center region is a bright source of gamma-ray emission, and recent observations have revealed an excess of gamma rays that cannot be explained by known astrophysical sources. The origin of this excess emission is still a subject of debate among researchers. Neutrino emission is a smoking gun evidence for hadronic interaction in astrophysical sources. Consequently, new generation observatories such as IceCube-Gen2 [342], KM3Net [421], etc., will be essential in determining proper emission occuring in sources observed in Galaxy.

The presence of PeVatrons in the Galaxy is a hot topic in the current state of research in high-energy astrophysics. As discussed earlier, the Crab Nebula is the only known source that has been confirmed to be a PeVatron candidate, following the successful detection of a UHE gamma-ray source associated with it. Consequently, PWNe has been naturally assumed to be the leading candidate for being PeVatron class of sources. However, we have shown that the association of SNR and molecular clouds can be a viable candidate for being a PeVatron source [420, 422]. We have further shown that it is not necessary that PWNe always have to be PeVatrons, as there can be cases where MWL data observed from a UHE gamma-ray source can not be explained by PWN emission. Although we have provided theoretical efforts on the subject, further observational confirmation is needed to properly identify the nature and the emission of the PeVatrons. To that end, observations by next-generation observatories such as CTA [365] and SWGO [366] will be beneficial in understanding the acceleration and emission process occuring in PeVatron sources in the Galaxy. If confirmed, then the idea, that Galactic sources explain cosmic ray spectrum observed until the “knee” energy, can also be understood. Further analytical and numerical studies of particle acceleration and emission processes of cosmic rays, neutrinos, and gamma rays at even higher energies in feasible astrophysical environments, and simultaneous observation of cosmic rays, neutrinos, gamma rays, and gravitational waves, from cosmic events, will be of utmost importance in deciphering the mysteries currently lurking in the field high energy, multi-messenger, and multi-wavelength astrophysics.

References

[1] A. H. Compton, Phys. Rev. **43**, 387 (1933).

[2] A. H. Compton, Review of Scientific Instruments **7**, 71 (1936).

[3] P. Carlson and A. de Angelis, European Physical Journal H **35**, 309 (2010), arXiv:1012.5068 [physics.hist-ph] .

[4] M. Walter and A. W. Wolfendale, European Physical Journal H **37**, 323 (2012).

[5] M. D. Maria, M. G. Ianniello, and A. Russo, Historical Studies in the Physical and Biological Sciences **22**, 165 (1991).

[6] A. De Angelis, Nuovo Cimento Rivista Serie **33**, 713 (2010), arXiv:1103.4392 [physics.hist-ph] .

[7] R. D. E. Atkinson and F. G. Houtermans, Zeitschrift fur Physik **54**, 656 (1929).

[8] P. Carlson, in *Centenary Symposium 2012: Discovery of Cosmic Rays*, American Institute of Physics Conference Series, Vol. 1516, edited by J. F. Ormes (2013) pp. 9–16, arXiv:1302.5808 [math.GR] .

[9] M. Schein, W. P. Jesse, and E. O. Wollan, Phys. Rev. **59**, 615 (1941).

[10] K. Greisen, Physical Review Letters **16**, 748 (1966).

[11] G. T. Zatsepin and V. A. Kuz'min, Soviet Journal of Experimental and Theoretical Physics Letters **4**, 78 (1966).

[12] C. Evoli, "The cosmic-ray energy spectrum," (2020).

[13] T. K. Gaisser and T. Stanev, Nuclear Physics A **777**, 98 (2006), arXiv:astro-ph/0510321 [astro-ph] .

[14] T. K. Gaisser, R. Engel, and E. Resconi, *Cosmic Rays and Particle Physics* (2016).

[15] V. L. Ginzburg and S. I. Syrovatskii, *The Origin of Cosmic Rays* (1964).

[16] V. L. Ginzburg and S. I. Syrovatskii, Annual Review of Astronomy and Astrophysics **3**, 297 (1965).

[17] P. Blasi, The Astronomy and Astrophysics Review **21**, 70 (2013), arXiv:1311.7346 [astro-ph.HE] .

[18] M. Ackermann *et al.*, Science **339**, 807 (2013).

[19] M. Tavani *et al.*, The Astrophysical Journal Letters **710**, L151 (2010), arXiv:1001.5150 [astro-ph.HE] .

[20] F. Giordano, M. Naumann-Godo, J. Ballet, K. Bechtol, S. Funk, J. Lande, M. N. Mazziotta, S. Rainò, T. Tanaka, O. Tibolla, and Y. Uchiyama, The Astrophysical Journal Letters **744**, L2 (2012), arXiv:1108.0265 [astro-ph.HE] .

[21] V. A. Acciari *et al.*, The Astrophysical Journal Letters **730**, L20 (2011), arXiv:1102.3871 [astro-ph.HE] .

[22] G. Morlino and D. Caprioli, Astronomy & Astrophysics **538**, A81 (2012), arXiv:1105.6342 [astro-ph.HE] .

[23] E. G. Berezhko, L. T. Ksenofontov, and H. J. Völk, The Astrophysical Journal **763**, 14 (2013), arXiv:1211.5398 [astro-ph.HE] .

[24] V. S. Beskin and R. R. Rafikov, Monthly Notices of the Royal Astronomical Society **313**, 433 (2000), arXiv:astro-ph/0002525 [astro-ph] .

[25] J. P. Ostriker, in *International Cosmic Ray Conference*, International Cosmic Ray Conference, Vol. 1 (1970) p. 69.

[26] S. Manconi, M. Di Mauro, and F. Donato, Physical Review D **102**, 023015 (2020), arXiv:2001.09985 [astro-ph.HE] .

[27] S. Manconi, M. Di Mauro, and F. Donato, Journal of Cosmology & Astroparticle Physics **2019**, 024 (2019), arXiv:1803.01009 [astro-ph.HE] .

[28] M. Di Mauro, S. Manconi, and F. Donato, Physical Review D **101**, 103035 (2020), arXiv:1908.03216 [astro-ph.HE] .

[29] M. Di Mauro, S. Manconi, and F. Donato, Physical Review D **100**, 123015 (2019), arXiv:1903.05647 [astro-ph.HE] .

[30] A. M. Bykov, The Astronomy and Astrophysics Review **22**, 77 (2014), arXiv:1511.04608 [astro-ph.HE] .

[31] M. Ackermann *et al.*, Science **334**, 1103 (2011).

[32] G. Dubus, The Astronomy and Astrophysics Review **21** (2013), 10.1007/s00159-013-0064-5.

[33] R. M. Crutcher, The Astrophysical Journal

520, 706 (1999).
[34] S. Nishiyama, H. Hatano, M. Tamura, N. Matsunaga, T. Yoshikawa, T. Suenaga, J. H. Hough, K. Sugitani, T. Nagayama, D. Kato, and T. Nagata, The Astrophysical Journal Letters **722**, L23 (2010), arXiv:1009.0584 [astro-ph.GA] .
[35] T. R. Jaffe, J. P. Leahy, A. J. Banday, S. M. Leach, S. R. Lowe, and A. Wilkinson, Monthly Notices of the Royal Astronomical Society **401**, 1013 (2010), https://academic.oup.com/mnras/article-pdf/401/2/1013/3958026/mnras0401-1013.pdf .
[36] C. Heiles, The Astrophysical Journal **462**, 316 (1996).
[37] J. L. Han, R. N. Manchester, A. G. Lyne, G. J. Qiao, and W. van Straten, The Astrophysical Journal **642**, 868 (2006).
[38] M. S. Pshirkov, P. G. Tinyakov, P. P. Kronberg, and K. J. Newton-McGee, The Astrophysical Journal **738**, 192 (2011), arXiv:1103.0814 [astro-ph.GA] .
[39] B. D. Savage and E. B. Jenkins, ApJ **172**, 491 (1972).
[40] E. B. Jenkins and B. D. Savage, ApJ **187**, 243 (1974).
[41] J. M. Dickey and F. J. Lockman, Annual Rev. Astron. Astrophys. **28**, 215 (1990).
[42] P. Cox, E. Kruegel, and P. G. Mezger, Astronomy and Astrophysics **155**, 380 (1986).
[43] K. Ferrière, ApJ **497**, 759 (1998).
[44] J. M. Cordes and T. J. W. Lazio, arXiv e-prints , astro-ph/0207156 (2002), arXiv:astro-ph/0207156 [astro-ph] .
[45] J. M. Cordes and T. J. W. Lazio, arXiv e-prints , astro-ph/0301598 (2003), arXiv:astro-ph/0301598 [astro-ph] .
[46] J. M. Cordes, J. M. Weisberg, D. A. Frail, S. R. Spangler, and M. Ryan, Nature **354**, 121 (1991).
[47] K. M. Ferrière, Reviews of Modern Physics **73**, 1031 (2001), arXiv:astro-ph/0106359 [astro-ph] .
[48] M. Pohl, P. Englmaier, and N. Bissantz, ApJ **677**, 283 (2008), arXiv:0712.4264 [astro-ph] .
[49] L. Bronfman, R. S. Cohen, H. Alvarez, J. May, and P. Thaddeus, ApJ **324**, 248 (1988).
[50] H. Nakanishi and Y. Sofue, Publications of the Astronomical Society of Japan **58**, 847 (2006), arXiv:astro-ph/0610769 [astro-ph] .
[51] K. Ferrière, W. Gillard, and P. Jean, Astronomy and Astrophysics **467**, 611 (2007), arXiv:astro-ph/0702532 [astro-ph] .
[52] E. Fermi, Physical Review **75**, 1169 (1949).
[53] E. Fermi, The Astrophysical Journal **119**, 1 (1954).
[54] T. Winchen and S. Buitink, Astroparticle Physics **102**, 25 (2018), arXiv:1612.03675 [astro-ph.HE] .
[55] R. Cowsik, Astronomy & Astrophysics **155**, 344 (1986).
[56] E. S. Seo and V. S. Ptuskin, The Astrophysical Journal **431**, 705 (1994).
[57] C. Fransson and R. I. Epstein, The Astrophysical Journal **242**, 411 (1980).
[58] L. Alfredo Anchordoqui, arXiv e-prints , arXiv:1104.0509 (2011), arXiv:1104.0509 [hep-ph] .
[59] E. Möbius and R. Kallenbach, ISSI Scientific Reports Series (2005).
[60] M. G. Baring, in *Very High Energy Phenomena in the Universe; Moriond Workshop*, edited by Y. Giraud-Heraud and J. Tran Thanh van (1997) p. 97, arXiv:astro-ph/9711177 [astro-ph] .
[61] A. Wandel, in *IAU Colloq. 101: Supernova Remnants and the Interstellar Medium*, edited by R. S. Roger and T. L. Landecker (1988) p. 325.
[62] R. A. Chevalier, Annual review of astronomy and astrophysics **15**, 175 (1977).
[63] T. Jones, L. Rudnick, B. Jun, K. Borkowski, G. Dubner, D. Frail, H. Kang, N. Kassim, and R. McCray, Publications of the Astronomical Society of the Pacific **110**, 125 (1998).
[64] S. P. Reynolds, Annual review of astronomy and astrophysics **46**, 89 (2008).
[65] P. O. Lagage and C. J. Cesarsky, Astronomy & Astrophysics **125**, 249 (1983).
[66] A. R. Bell, Astroparticle Physics **43**, 56 (2013).
[67] A. R. Bell, A. T. Araudo, J. H. Matthews, and K. M. Blundell, Monthly Notices of the Royal Astronomical Society **473**, 2364 (2018), arXiv:1709.07793 [astro-ph.HE] .

[68] J. Bednarz and M. Ostrowski, Monthly Notices of the Royal Astronomical Society **283**, 447 (1996), arXiv:astro-ph/9608078 [astro-ph] .

[69] R. D. Blandford and J. P. Ostriker, The Astrophysical Journal Letters **221**, L29 (1978).

[70] A. R. Bell, Monthly Notices of the Royal Astronomical Society **182**, 443 (1978), https://academic.oup.com/mnras/article-pdf/182/3/443/3856040/mnras182-0443.pdf .

[71] G. F. Krymskii, Akademiia Nauk SSSR Doklady **234**, 1306 (1977).

[72] W. I. Axford, E. Leer, and J. F. McKenzie, Astronomy & Astrophysics **111**, 317 (1982).

[73] A. R. Bell, K. M. Schure, and B. Reville, Monthly Notices of the Royal Astronomical Society **418**, 1208 (2011), arXiv:1108.0582 [astro-ph.HE] .

[74] D. C. Ellison and G. P. Double, Astroparticle Physics **22**, 323 (2004), arXiv:astro-ph/0408527 [astro-ph] .

[75] K. M. Schure, A. R. Bell, L. O'C Drury, and A. M. Bykov, Space Science Reviews **173**, 491 (2012), arXiv:1203.1637 [astro-ph.HE] .

[76] V. N. Zirakashvili, V. S. Ptuskin, and H. J. Völk, The Astrophysical Journal **678**, 255 (2008), arXiv:0801.4486 [astro-ph] .

[77] E. Amato and P. Blasi, Monthly Notices of the Royal Astronomical Society **392**, 1591 (2009), arXiv:0806.1223 [astro-ph] .

[78] A. M. Hillas, Journal of Physics G Nuclear Physics **31**, R95 (2005).

[79] R. Cowsik, Y. Pal, S. N. Tandon, and R. P. Verma, Phys. Rev. Lett. **17**, 1298 (1966).

[80] M. M. Shapiro and R. Silberberg, Annual Review of Nuclear and Particle Science **20**, 323 (1970).

[81] A. Codino and F. Plouin, in *International Cosmic Ray Conference*, International Cosmic Ray Conference, Vol. 2 (2008) pp. 191–194, arXiv:0806.1346 [astro-ph] .

[82] V. S. Ptuskin, O. N. Strelnikova, and L. G. Sveshnikova, Astroparticle Physics **31**, 284 (2009).

[83] R. Cowsik and L. W. Wilson, in *International Cosmic Ray Conference*, International Cosmic Ray Conference, Vol. 2 (1975) p. 659.

[84] V. Ptuskin, in *26th International Cosmic Ray Conference (ICRC26), Volume 4*, International Cosmic Ray Conference, Vol. 4 (1999) p. 291.

[85] F. C. Jones, in *International Cosmic Ray Conference*, International Cosmic Ray Conference, Vol. 2 (1991) p. 268.

[86] F. C. Jones, A. Lukasiak, V. Ptuskin, and W. Webber, The Astrophysical Journal **547**, 264 (2001), arXiv:astro-ph/0007293 [astro-ph] .

[87] V. S. Ptuskin, F. C. Jones, and J. F. Ormes, The Astrophysical Journal **465**, 972 (1996).

[88] F. A. Aharonian, *Very high energy cosmic gamma radiation : a crucial window on the extreme Universe* (2004).

[89] S. R. Kelner, F. A. Aharonian, and V. V. Bugayov, Physical Review D **74**, 034018 (2006), arXiv:astro-ph/0606058 [astro-ph] .

[90] E. Kafexhiu, F. Aharonian, A. M. Taylor, and G. S. Vila, Physical Review D **90**, 123014 (2014), arXiv:1406.7369 [astro-ph.HE] .

[91] G. R. Blumenthal and R. J. Gould, Reviews of Modern Physics **42**, 237 (1970).

[92] E. S. Seo, Astroparticle Physics **39**, 76 (2012).

[93] A. C. Cummings, B. Webber, B. C. Heikkila, E. C. Stone, and N. Lal, in *42nd COSPAR Scientific Assembly*, Vol. 42 (2018) pp. E1.5–43–18.

[94] S. M. Krimigis, T. P. Armstrong, W. I. Axford, C. O. Bostrom, C. Y. Fan, G. Gloeckler, and L. J. Lanzerotti, Space Science Reviews **21**, 329 (1977).

[95] R. L. Heacock (1980).

[96] N. Weber, *A Measurement of the Antiproton and Proton Fluxes in Cosmic Rays using the CAPRICE Experiment*, Ph.D. thesis, TU Stockholm (1997).

[97] M. A. DuVernois *et al.*, ApJ **559**, 296 (2001).

[98] K. Abe *et al.*, Physics Letters B **670**, 103 (2008), arXiv:0805.1754 [astro-ph] .

[99] H. S. Ahn *et al.*, Astroparticle Physics **30**, 133 (2008), arXiv:0808.1718 [astro-ph] .

[100] A. D. Panov *et al.*, Bulletin of the Russian Academy of Sciences, Physics **73**, 564 (2009), arXiv:1101.3246 [astro-ph.HE] .

[101] D. Kang *et al.*, in *37th International*

Cosmic Ray Conference (2022) p. 313, arXiv:2109.02518 [astro-ph.HE] .
[102] M. Duranti, EPJ Web Conf. **209**, 01014 (2019).
[103] L. Accardo *et al.*, Phys. Rev. Lett. **113**, 121101 (2014).
[104] M. Aguilar *et al.*, Phys. Rev. Lett. **110**, 141102 (2013).
[105] M. Aguilar *et al.*, Phys. Rev. Lett. **113**, 121102 (2014).
[106] M. Aguilar *et al.*, Phys. Rev. Lett. **113**, 221102 (2014).
[107] M. Aguilar *et al.*, Phys. Rev. Lett. **114**, 171103 (2015).
[108] M. Aguilar *et al.*, Phys. Rev. Lett. **115**, 211101 (2015).
[109] M. Aguilar *et al.*, Phys. Rev. Lett. **117**, 231102 (2016).
[110] M. Aguilar *et al.*, Phys. Rev. Lett. **117**, 091103 (2016).
[111] M. Aguilar *et al.* (AMS Collaboration), Phys. Rev. Lett. **119**, 251101 (2017).
[112] M. Aguilar *et al.* (AMS Collaboration), Phys. Rev. Lett. **121**, 051103 (2018).
[113] M. Aguilar *et al.* (AMS Collaboration), Phys. Rev. Lett. **121**, 051101 (2018).
[114] M. Aguilar *et al.* (AMS Collaboration), Phys. Rev. Lett. **120**, 021101 (2018).
[115] M. Aguilar *et al.*, Physical Review Letters **121**, 051102 (2018).
[116] Z. Weng (AMS), PoS **ICHEP2018**, 364 (2019).
[117] M. Aguilar *et al.*, Phys. Rev. Lett. **122**, 101101 (2019).
[118] M. Aguilar *et al.* (AMS Collaboration), Phys. Rev. Lett. **122**, 041102 (2019).
[119] M. Aguilar *et al.* (AMS Collaboration), Phys. Rev. Lett. **124**, 211102 (2020).
[120] B. Beischer, arXiv e-prints , arXiv:2007.08392 (2020), arXiv:2007.08392 [astro-ph.HE] .
[121] O. Adriani *et al.*, Nucl. Instrum. Meth. A **478**, 114 (2002).
[122] O. Adriani *et al.*, Physics Reports **544**, 323 (2014).
[123] O. Adriani *et al.*, Nature **458**, 607 (2009), arXiv:0810.4995 [astro-ph] .
[124] O. Adriani *et al.*, Astroparticle Physics **34**, 1 (2010), arXiv:1001.3522 [astro-ph.HE] .
[125] O. Adriani *et al.*, Phys. Rev. Lett. **111**, 081102 (2013), arXiv:1308.0133 [astro-ph.HE] .
[126] O. Adriani *et al.*, Science **332**, 69 (2011).
[127] O. Adriani *et al.*, ApJ **791**, 93 (2014), arXiv:1407.1657 [astro-ph.HE] .
[128] O. Adriani *et al.*, Physical Review Letters **106** (2011), 10.1103/physrevlett.106.201101.
[129] O. Adriani *et al.*, Phys. Rev. Lett. **111**, 081102 (2013), arXiv:1308.0133 [astro-ph.HE] .
[130] O. Adriani *et al.*, Phys. Rev. Lett. **105**, 121101 (2010), arXiv:1007.0821 [astro-ph.HE] .
[131] O. Adriani *et al.*, Soviet Journal of Experimental and Theoretical Physics Letters **96**, 621 (2013).
[132] W. B. Atwood *et al.*, The Astrophysical Journal **697**, 1071 (2009), arXiv:0902.1089 [astro-ph.IM] .
[133] M. De Naurois, PoS **ICRC2019**, 656 (2019).
[134] W. Hofmann and H. E. S. S. Collaboration, in *International Cosmic Ray Conference*, International Cosmic Ray Conference, Vol. 7 (2001) p. 2785.
[135] D. Ferenc and MAGIC Collaboration, in *AAS/High Energy Astrophysics Division #9*, AAS/High Energy Astrophysics Division, Vol. 9 (2006) p. 18.42.
[136] J. Cortina, F. Goebel, and T. Schweizer, arXiv e-prints , arXiv:0907.1211 (2009), arXiv:0907.1211 [astro-ph.IM] .
[137] J. Holder *et al.*, Astroparticle Physics **25**, 391 (2006), arXiv:astro-ph/0604119 [astro-ph] .
[138] A. Acharyya *et al.*, Research Notes of the American Astronomical Society **7**, 6 (2023), arXiv:2301.04498 [astro-ph.HE] .
[139] B. M. Baughman, in *32nd International Cosmic Ray Conference*, Vol. 9 (2011) p. 123.
[140] M. Durocher and P. Harding, in *The 36th Annual New Mexico Symposium*, edited by A. D. Kapinska (2021) p. 20.
[141] Z. Cao, Chinese Physics C **34**, 249 (2010).
[142] Z. Cao *et al.*, Nature **594**, 33 (2021).
[143] Tibet ASγ Collaboration *et al.*, Nature Astronomy **5**, 460 (2021), arXiv:2109.02898 [astro-ph.HE] .
[144] X. A. Huo *et al.*, in *International Cosmic Ray Conference*, International Cosmic Ray Conference, Vol. 2 (1990) p. 427.
[145] F. A. Harrison *et al.*, arXiv e-prints ,

arXiv:1008.1362 (2010), arXiv:1008.1362 [astro-ph.IM] .

[146] F. A. Harrison *et al.*, The Astrophysical Journal **770**, 103 (2013), arXiv:1301.7307 [astro-ph.IM] .

[147] H. Beuther *et al.*, Astronomy & Astrophysics **595**, A32 (2016).

[148] Y. Wang *et al.*, Astronomy & Astrophysics **634**, A83 (2020), arXiv:1912.08223 [astro-ph.GA] .

[149] J. M. Stil, A. R. Taylor, J. M. Dickey, D. W. Kavars, P. G. Martin, T. A. Rothwell, A. I. Boothroyd, F. J. Lockman, and N. M. McClure-Griffiths, The Astronomical Journal **132**, 1158 (2006).

[150] A. Brunthaler *et al.*, Astronomy & Astrophysics **651**, A85 (2021), arXiv:2106.00377 [astro-ph.GA] .

[151] S. N. X. Medina *et al.*, Astronomy & Astrophysics **627**, A175 (2019), arXiv:1905.09281 [astro-ph.GA] .

[152] M. G. Aartsen *et al.* (IceCube), Adv. Space Res. **62**, 2902 (2018), arXiv:1701.03731 [astro-ph.HE] .

[153] L. Drury, Space Science Reviews **36**, 57 (1983).

[154] L. O. Drury, F. A. Aharonian, and H. J. Voelk, Astronomy & Astrophysics **287**, 959 (1994), arXiv:astro-ph/9305037 [astro-ph] .

[155] M. A. Malkov and L. O. Drury, Reports on Progress in Physics **64**, 429 (2001).

[156] K. Koyama, R. Petre, E. V. Gotthelf, U. Hwang, M. Matsuura, M. Ozaki, and S. S. Holt, Nature **378**, 255 (1995).

[157] U. Hwang, A. Decourchelle, S. S. Holt, and R. Petre, The Astrophysical Journal **581**, 1101 (2002).

[158] M. J. Rees and J. E. Gunn, Monthly Notices of the Royal Astronomical Society **167**, 1 (1974).

[159] M. Meyer, D. Horns, and H. S. Zechlin, Astronomy & Astrophysics **523**, A2 (2010), arXiv:1008.4524 [astro-ph.HE] .

[160] A. M. Hillas *et al.*, The Astrophysical Journal **503**, 744 (1998).

[161] W. Bednarek and M. Bartosik, Astronomy & Astrophysics **405**, 689 (2003), arXiv:astro-ph/0304049 [astro-ph] .

[162] J. Albert *et al.*, Science **312**, 1771 (2006), arXiv:astro-ph/0605549 [astro-ph] .

[163] M. Heyer and T. Dame, Annual Review of Astronomy and Astrophysics **53**, 583 (2015), https://doi.org/10.1146/annurev-astro-082214-122324 .

[164] T. M. Dame, D. Hartmann, and P. Thaddeus, ApJ **547**, 792 (2001), arXiv:astro-ph/0009217 [astro-ph] .

[165] F. Aharonian, G. Peron, R. Yang, S. Casanova, and R. Zanin, Phys. Rev. D **101**, 083018 (2020).

[166] V. A. Dogiel, A. V. Gurevich, Y. N. Istomin, and K. P. Zybin, Monthly Notices of the Royal Astronomical Society **228**, 843 (1987), https://academic.oup.com/mnras/article-pdf/228/4/843/3497077/mnras228-0843.pdf .

[167] V. A. Dogiel and G. S. Sharov, Astronomy and Astrophysics **229**, 259 (1990).

[168] V. A. Dogiel, A. V. Gurevich, Y. N. Istomin, and K. P. Zybin, Astrophysics and Space Science **297**, 201 (2005).

[169] V. Baghmanyan, G. Peron, S. Casanova, F. Aharonian, and R. Zanin, The Astrophysical Journal Letters **901**, L4 (2020), arXiv:2009.08893 [astro-ph.HE] .

[170] S.-Q. Xi, R.-Y. Liu, Z.-Q. Huang, K. Fang, and X.-Y. Wang, ApJ **878**, 104 (2019), arXiv:1810.10928 [astro-ph.HE] .

[171] M. Molero Gonzalez, J. Casaus, C. Mana, and M. Velasco, PoS **ICRC2021**, 120 (2021).

[172] Z. Weng, PoS **ICRC2021**, 122 (2021).

[173] S. Profumo, Journal of Cosmology and Astroparticle Physics **2015**, 043 (2015).

[174] G. Dubus, Comptes Rendus Physique **16**, 661 (2015), gamma-ray astronomy / Astronomie des rayons gamma.

[175] J. Li, D. F. Torres, K.-S. Cheng, E. de Oña Wilhelmi, P. Kretschmar, X. Hou, and J. Takata, The Astrophysical Journal **846**, 169 (2017).

[176] A. G. Lyne, B. W. Stappers, M. J. Keith, P. S. Ray, M. Kerr, F. Camilo, and T. J. Johnson, Monthly Notices of the Royal Astronomical Society **451**, 581 (2015), arXiv:1502.01465 [astro-ph.HE] .

[177] W. C. G. Ho, C.-Y. Ng, A. G. Lyne, B. W. Stappers, M. J. Coe, J. P. Halpern, T. J. Johnson, and I. A.

Steele, Monthly Notices of the Royal Astronomical Society **464**, 1211 (2016), https://academic.oup.com/mnras/article-pdf/464/1/1211/18518503/stw2420.pdf .

[178] A. U. Abeysekara *et al.*, The Astrophysical Journal **867**, L19 (2018).

[179] R. H. D. Corbet, L. Chomiuk, M. J. Coe, J. B. Coley, G. Dubus, P. G. Edwards, P. Martin, V. A. McBride, J. Stevens, J. Strader, L. J. Townsend, and A. Udalski, The Astrophysical Journal **829**, 105 (2016).

[180] R. H. D. Corbet, L. Chomiuk, M. J. Coe, J. B. Coley, G. Dubus, P. G. Edwards, P. Martin, V. A. McBride, J. Stevens, J. Strader, and L. J. Townsend, The Astrophysical Journal **884**, 93 (2019).

[181] P. Eger, H. Laffon, P. Bordas, E. de Ona Whilhelmi, J. Hinton, and G. Puhlhofer, Monthly Notices of the Royal Astronomical Society **457**, 1753 (2016), https://academic.oup.com/mnras/article-pdf/457/2/1753/2927636/stw125.pdf .

[182] G. Marti-Devesa and O. Reimer, Astronomy & Astrophysics **637**, A23 (2020).

[183] Z. Cao *et al.*, Science **373**, 425 (2021), arXiv:2111.06545 [astro-ph.HE] .

[184] A. Albert *et al.*, The Astrophysical Journal Letters **911**, L27 (2021).

[185] A. De Sarkar, S. Biswas, and N. Gupta, Journal of High Energy Astrophysics **29**, 1 (2021), arXiv:1911.12977 [astro-ph.HE] .

[186] A. De Sarkar, N. Roy, P. Majumdar, N. Gupta, A. Brunthaler, K. M. Menten, S. A. Dzib, S. N. X. Medina, and F. Wyrowski, The Astrophysical Journal Letters **927**, L35 (2022), arXiv:2202.13376 [astro-ph.HE] .

[187] A. De Sarkar and N. Gupta, The Astrophysical Journal **934**, 118 (2022), arXiv:2205.01923 [astro-ph.HE] .

[188] A. De Sarkar, W. Zhang, J. Martín, D. F. Torres, J. Li, and X. Hou, Astronomy & Astrophysics **668**, A23 (2022), arXiv:2209.13285 [astro-ph.HE] .

[189] A. R. Bell, Monthly Notices of the Royal Astronomical Society **182**, 147 (1978), https://academic.oup.com/mnras/article-pdf/182/2/147/3710138/mnras182-0147.pdf .

[190] R. Blandford and D. Eichler, Physics Reports **154**, 1 (1987).

[191] V. S. Berezinskii, S. V. Bulanov, V. A. Dogiel, and V. S. Ptuskin, *Astrophysics of cosmic rays* (1990).

[192] A. W. Strong, I. V. Moskalenko, and V. S. Ptuskin, Annual Review of Nuclear and Particle Science **57**, 285 (2007), arXiv:astro-ph/0701517 [astro-ph] .

[193] M. Ackermann *et al.*, Phys. Rev. Lett. **108**, 011103 (2012), arXiv:1109.0521 [astro-ph.HE] .

[194] I. Cholis, L. Goodenough, D. Hooper, M. Simet, and N. Weiner, Phys. Rev. D **80**, 123511 (2009), arXiv:0809.1683 [hep-ph] .

[195] L. Bergström, T. Bringmann, and J. Edsjö, Phys. Rev. D **78**, 103520 (2008), arXiv:0808.3725 [astro-ph] .

[196] T. A. Porter, R. P. Johnson, and P. W. Graham, Annual Review of Astronomy and Astrophysics **49**, 155 (2011), arXiv:1104.2836 [astro-ph.HE] .

[197] I. Cholis and D. Hooper, Phys. Rev. D **88**, 023013 (2013), arXiv:1304.1840 [astro-ph.HE] .

[198] D. Malyshev, I. Cholis, and J. Gelfand, Phys. Rev. D **80**, 063005 (2009), arXiv:0903.1310 [astro-ph.HE] .

[199] S.-J. Lin, Q. Yuan, and X.-J. Bi, Phys. Rev. D **91**, 063508 (2015), arXiv:1409.6248 [astro-ph.HE] .

[200] D. Grasso *et al.*, Astroparticle Physics **32**, 140 (2009), arXiv:0905.0636 [astro-ph.HE] .

[201] H. Yüksel, M. D. Kistler, and T. Stanev, Phys. Rev. Lett. **103**, 051101 (2009), arXiv:0810.2784 [astro-ph] .

[202] D. Hooper, P. Blasi, and P. D. Serpico, JCAP **2009**, 025 (2009), arXiv:0810.1527 [astro-ph] .

[203] J. Chang *et al.*, Nature **456**, 362 (2008).

[204] S. Profumo, Central European Journal of Physics **10**, 1 (2012), arXiv:0812.4457 [astro-ph] .

[205] C. Venter, A. Kopp, A. K. Harding, P. L. Gonthier, and I. Büsching, ApJ **807**, 130 (2015), arXiv:1506.01211 [astro-ph.HE] .

[206] J. Feng and H.-H. Zhang, European Physical Journal C **76**, 229 (2016), arXiv:1504.03312 [hep-ph] .

[207] J. C. Joshi and S. Razzaque, JCAP **2017**, 029 (2017), arXiv:1706.01981 [astro-ph.HE] .

[208] A. U. Abeysekara *et al.*, The Astrophysical Journal **843**, 40 (2017).

[209] D. Hooper, I. Cholis, T. Linden, and K. Fang, Phys. Rev. D **96**, 103013 (2017), arXiv:1702.08436 [astro-ph.HE] .

[210] A. U. Abeysekara *et al.*, Science **358**, 911 (2017), arXiv:1711.06223 [astro-ph.HE] .

[211] K. Fang, X.-J. Bi, and P.-F. Yin, ApJ **884**, 124 (2019), arXiv:1906.08542 [astro-ph.HE] .

[212] N. Gupta and D. F. Torres, Monthly Notices of the Royal Astronomical Society **441**, 3122 (2014).

[213] T. S. Rice, A. A. Goodman, E. A. Bergin, C. Beaumont, and T. M. Dame, ApJ **822**, 52 (2016), arXiv:1602.02791 [astro-ph.GA] .

[214] B. Q. Chen, G. X. Li, H. B. Yuan, Y. Huang, Z. J. Tian, H. F. Wang, H. W. Zhang, C. Wang, and X. W. Liu, MNRAS **493**, 351 (2020), arXiv:2001.11682 [astro-ph.GA] .

[215] S. Coutu *et al.*, Astroparticle Physics **11**, 429 (1999), arXiv:astro-ph/9902162 [astro-ph] .

[216] G. Di Bernardo, C. Evoli, D. Gaggero, D. Grasso, and L. Maccione, Astroparticle Physics **34**, 274 (2010), arXiv:0909.4548 [astro-ph.HE] .

[217] C. Evoli, D. Gaggero, A. Vittino, G. Di Bernardo, M. Di Mauro, A. Ligorini, P. Ullio, and D. Grasso, JCAP **2017**, 015 (2017), arXiv:1607.07886 [astro-ph.HE] .

[218] D. Gaggero, *Cosmic Ray Diffusion in the Galaxy and Diffuse Gamma Emission* (2012).

[219] G. Di Bernardo, C. Evoli, D. Gaggero, D. Grasso, and L. Maccione, Journal of Cosmology and Astroparticle Physics **2013**, 036 (2013), arXiv:1210.4546 [astro-ph.HE] .

[220] H. Nakanishi and Y. Sofue, Publications of the Astronomical Society of Japan **55**, 191 (2003), arXiv:astro-ph/0304338 [astro-ph] .

[221] M. A. Gordon and W. B. Burton, Apj **208**, 346 (1976).

[222] R. M. Crutcher, Astrophys. J. **520**, 706 (1991).

[223] R. Beck, Astrophysics and Space Sciences Transactions **5**, 43 (2009).

[224] G. di Bernardo, C. Evoli, D. Gaggero, D. Grasso, L. Maccione, and M. N. Mazziotta, Astroparticle Physics **34**, 528 (2011), arXiv:1010.0174 [astro-ph.HE] .

[225] I. Cholis, M. Tavakoli, C. Evoli, L. Maccione, and P. Ullio, Journal of Cosmology and Astroparticle Physics **2012**, 004 (2012).

[226] I. G. Usoskin, K. Alanko-Huotari, G. A. Kovaltsov, and K. Mursula, Journal of Geophysical Research (Space Physics) **110**, A12108 (2005).

[227] T. P. Ellsworth-Bowers, J. Glenn, E. Rosolowsky, S. Mairs, N. J. Evans, C. Battersby, A. Ginsburg, Y. L. Shirley, and J. Bally, The Astrophysical Journal **770**, 39 (2013).

[228] A. A. Goodman, J. Alves, C. N. Beaumont, R. A. Benjamin, M. A. Borkin, A. Burkert, T. M. Dame, J. Jackson, J. Kauffmann, T. Robitaille, and R. J. Smith, ApJ **797**, 53 (2014), arXiv:1408.0001 [astro-ph.GA] .

[229] A. Neronov, D. Malyshev, and D. V. Semikoz, Astronomy & Astrophysics **606**, A22 (2017), arXiv:1705.02200 [astro-ph.HE] .

[230] R.-z. Yang, E. de Oña Wilhelmi, and F. Aharonian, Astronomy & Astrophysics **566**, A142 (2014), arXiv:1303.7323 [astro-ph.HE] .

[231] S. R. Kelner, F. A. Aharonian, and V. V. Bugayov, Phys. Rev. D **74**, 034018 (2006), arXiv:astro-ph/0606058 [astro-ph] .

[232] R. M. Crutcher, Annual Review of Astronomy and Astrophysics **50**, 29 (2012), https://doi.org/10.1146/annurev-astro-081811-125514 .

[233] S. Gabici, F. A. Aharonian, and P. Blasi, Astrophysics and Space Science **309**, 365 (2007).

[234] S. Gabici, F. A. Aharonian, and S. Casanova, Monthly Notices of the Royal Astronomical Society **396**, 1629 (2009), https://academic.oup.com/mnras/article-pdf/396/3/1629/5800874/mnras0396-1629.pdf .

[235] A. M. Atoyan, F. A. Aharonian, and H. J. Völk, Phys. Rev. D **52**, 3265 (1995).

[236] J. C. Joshi and N. Gupta, Astroparticle Physics **65**, 108 (2015), arXiv:1411.5176 [astro-ph.HE] .

[237] N. E. Yanasak *et al.*, ApJ **563**, 768 (2001).

[238] T. Hams *et al.*, ApJ **611**, 892 (2004).
[239] C. Evoli, G. Morlino, P. Blasi, and R. Aloisio, Phys. Rev. D **101**, 023013 (2020).
[240] D. Grasso *et al.*, Astroparticle Physics **32**, 140 (2009).
[241] M. Ackermann *et al.* (The Fermi LAT Collaboration), Phys. Rev. D **82**, 092003 (2010).
[242] S. Abdollahi *et al.*, Phys. Rev. Lett. **118**, 091103 (2017).
[243] A. M. Lionetto, A. Morselli, and V. Zdravkovic, Journal of Cosmology and Astroparticle Physics **2005**, 010 (2005).
[244] A. H. Compton and I. A. Getting, Phys. Rev. **47**, 817 (1935).
[245] P. Brun, T. Delahaye, J. Diemand, S. Profumo, and P. Salati, Phys. Rev. D **80**, 035023 (2009).
[246] K. Fang, X.-J. Bi, and P.-F. Yin, Monthly Notices of the Royal Astronomical Society **478**, 5660 (2018).
[247] E. Churchwell *et al.*, Publications of the Astronomical Society of the Pacific **121**, 213 (2009).
[248] D. Hooper and T. Linden, Phys. Rev. D **98**, 043005 (2018).
[249] L. Maraschi and A. Treves, Monthly Notices of the Royal Astronomical Society **194**, 1P (1981), https://academic.oup.com/mnras/article-pdf/194/1/1P/3084915/mnras194-001P.pdf .
[250] G. Dubus, Astronomy & Astrophysics **451**, 9 (2006).
[251] D. Huber, Kissmann, R., Reimer, A., and Reimer, O., Astronomy & Astrophysics **646**, A91 (2021).
[252] S. V. Bogovalov, D. V. Khangulyan, A. V. Koldoba, G. V. Ustyugova, and F. A. Aharonian, Monthly Notices of the Royal Astronomical Society **387**, 63 (2008), https://academic.oup.com/mnras/article-pdf/387/1/63/3182385/mnras0387-0063.pdf .
[253] V. Bosch-Ramon, Barkov, M. V., Khangulyan, D., and Perucho, M., Astronomy & Astrophysics **544**, A59 (2012).
[254] L. Sironi and A. Spitkovsky, The Astrophysical Journal **741**, 39 (2011).
[255] F. Aharonian *et al.*, Astronomy & Astrophysics **442**, 1 (2005), arXiv:astro-ph/0506280 [astro-ph] .
[256] M. Chernyakova *et al.*, Monthly Notices of the Royal Astronomical Society **439**, 432 (2014), arXiv:1401.1386 [astro-ph.HE] .
[257] A. A. Abdo *et al.*, The Astrophysical Journal: Letters **736**, L11 (2011), arXiv:1103.4108 [astro-ph.HE] .
[258] G. A. Caliandro, C. C. Cheung, J. Li, J. D. Scargle, D. F. Torres, K. S. Wood, and M. Chernyakova, The Astrophysical Journal **811**, 68 (2015), arXiv:1509.02856 [astro-ph.HE] .
[259] T. J. Johnson, K. S. Wood, M. Kerr, R. H. D. Corbet, C. C. Cheung, P. S. Ray, and N. Omodei, The Astrophysical Journal **863**, 27 (2018), arXiv:1805.03537 [astro-ph.HE] .
[260] Z. Chang, S. Zhang, Y.-P. Chen, L. Ji, L.-D. Kong, and P.-J. Wang, Universe **7**, 472 (2021), arXiv:2112.02295 [astro-ph.HE] .
[261] Romero, Torres, D. F., Kaufman Bernadó, M. M., and Mirabel, I. F., Astronomy & Astrophysics **410**, L1 (2003).
[262] Bosch-Ramon and Paredes, Astronomy & Astrophysics **417**, 1075 (2004).
[263] H.E.S.S. Collaboration *et al.*, Astronomy & Astrophysics **610**, L17 (2018).
[264] P.-H. T. Tam, K. K. Lee, Y. Cui, C. P. Hu, A. K. H. Kong, K. L. Li, V. Tudor, X. He, and P. S. Pal, The Astrophysical Journal **899**, 75 (2020).
[265] H. Abdalla *et al.*, Astronomy & Astrophysics **612**, A1 (2018).
[266] A. Neronov and D. V. Semikoz, "Galactic sources of e>100 gev gamma-rays seen by fermi telescope," (2010), arXiv:1011.0210 [astro-ph.HE] .
[267] F. Acero *et al.*, The Astrophysical Journal Supplement Series **218**, 23 (2015).
[268] M. Ackermann *et al.*, The Astrophysical Journal Supplement Series **222**, 5 (2016).
[269] S. Abdollahi *et al.*, The Astrophysical Journal Supplement Series **247**, 33 (2020).
[270] J. P. Halpern and E. V. Gotthelf, The Astrophysical Journal **669**, 579 (2007), arXiv:0707.2935 [astro-ph] .
[271] C. B. Markwardt, J. H. Swank, and E. A. Smith, The Astronomer's Telegram **317**, 1 (2004).
[272] A. E. Shtykovsky, A. A. Lutovinov,

S. S. Tsygankov, and S. V. Molkov, Monthly Notices of the Royal Astronomical Society: Letters **482**, L14 (2018), https://academic.oup.com/mnrasl/article-pdf/482/1/L14/25998686/sly182.pdf .

[273] J. M. Dickey and F. J. Lockman, Annual Review of Astronomy and Astrophysics **28**, 215 (1990).

[274] P. M. W. Kalberla, W. B. Burton, D. Hartmann, E. M. Arnal, E. Bajaja, R. Morras, and W. G. L. Pöppel, Astronomy & Astrophysics **440**, 775 (2005), arXiv:astro-ph/0504140 [astro-ph] .

[275] N. Ben Bekhti *et al.*, Astronomy & Astrophysics **594**, A116 (2016), arXiv:1610.06175 [astro-ph.GA] .

[276] V. Sguera, L. Sidoli, A. J. Bird, A. Paizis, and A. Bazzano, Monthly Notices of the Royal Astronomical Society **491**, 4543 (2019), https://academic.oup.com/mnras/article-pdf/491/3/4543/31559445/stz3330.pdf .

[277] M. Nakajima *et al.*, The Astronomer's Telegram **14554**, 1 (2021).

[278] C. B. Markwardt, J. Halpern, and J. H. Swank, The Astronomer's Telegram **2007**, 1 (2009).

[279] R. H. D. Corbet, Astronomy & Astrophysics **141**, 91 (1984).

[280] R. H. D. Corbet, Space Science Reviews **40**, 409 (1985).

[281] R. H. D. Corbet, Monthly Notices of the Royal Astronomical Society **220**, 1047 (1986), https://academic.oup.com/mnras/article-pdf/220/4/1047/3129823/mnras220-1047.pdf .

[282] J. A. Hinton, J. L. Skilton, S. Funk, J. Brucker, F. A. Aharonian, G. Dubus, A. Fiasson, Y. Gallant, W. Hofmann, A. Marcowith, and O. Reimer, The Astrophysical Journal: Letters **690**, L101 (2009), arXiv:0809.0584 [astro-ph] .

[283] I. Volkov, O. Kargaltsev, G. Younes, J. Hare, and G. Pavlov, The Astrophysical Journal **915**, 61 (2021).

[284] T. Takahashi, T. Kishishita, Y. Uchiyama, T. Tanaka, K. Yamaoka, D. Khangulyan, F. A. Aharonian, V. Bosch-Ramon, and J. A. Hinton, The Astrophysical Journal **697**, 592 (2009).

[285] H. An, E. Bellm, V. Bhalerao, S. E. Boggs, F. E. Christensen, W. W. Craig, F. Fuerst, C. J. Hailey, F. A. Harrison, V. M. Kaspi, L. Natalucci, D. Stern, J. A. Tomsick, and W. W. Zhang, The Astrophysical Journal **806**, 166 (2015).

[286] F. K. Lamb, C. J. Pethick, and D. Pines, The Astrophysical Journal **184**, 271 (1973).

[287] P. A. Becker, Klochkov, D., Schönherr, G., Nishimura, O., Ferrigno, C., Caballero, I., Kretschmar, P., Wolff, M. T., Wilms, J., and Staubert, R., Astronomy & Astrophysics **544**, A123 (2012).

[288] S. Karino, K. Nakamura, and A. Taani, Publications of the Astronomical Society of Japan **71**, 58 (2019), arXiv:1903.03455 [astro-ph.HE] .

[289] P. Reig, Astrophysics and Space Science **332**, 1 (2011), arXiv:1101.5036 [astro-ph.HE] .

[290] M. M. Romanova and S. P. Owocki, Space Science Reviews **191**, 339 (2015), arXiv:1605.04979 [astro-ph.SR] .

[291] D. F. Torres, N. Rea, P. Esposito, J. Li, Y. Chen, and S. Zhang, The Astrophysical Journal **744**, 106 (2012).

[292] R. V. E. Lovelace, M. M. Romanova, and G. S. Bisnovatyi-Kogan, The Astrophysical Journal **625**, 957 (2005).

[293] Bednarek, Astronomy & Astrophysics **495**, 919 (2009).

[294] D. A. Verner, G. J. Ferland, K. T. Korista, and D. G. Yakovlev, The Astrophysical Journal **465**, 487 (1996), arXiv:astro-ph/9601009 [astro-ph] .

[295] J. Wilms, A. Allen, and R. McCray, The Astrophysical Journal **542**, 914 (2000), arXiv:astro-ph/0008425 [astro-ph] .

[296] R. Protassov, D. A. van Dyk, A. Connors, V. L. Kashyap, and A. Siemiginowska, The Astrophysical Journal **571**, 545 (2002), arXiv:astro-ph/0201547 [astro-ph] .

[297] M. Wood, R. Caputo, E. Charles, M. Di Mauro, J. Magill, J. S. Perkins, and Fermi-LAT Collaboration, in *35th International Cosmic Ray Conference (ICRC2017)*, International Cosmic Ray Conference, Vol. 301 (2017) p. 824, arXiv:1707.09551 [astro-ph.IM] .

[298] T. Prinz and W. Becker, arXiv e-prints , arXiv:1511.07713 (2015), arXiv:1511.07713 [astro-ph.HE] .
[299] N. R. Lomb, Astrophysics and Space Science **39**, 447 (1976).
[300] J. D. Scargle, The Astrophysical Journal **263**, 835 (1982).
[301] J. Vanderplas, A. Connolly, Ž. Ivezić, and A. Gray, in *Conference on Intelligent Data Understanding (CIDU)* (2012) pp. 47 –54.
[302] Ž. Ivezić, A. Connolly, J. Vanderplas, and A. Gray, *Statistics, Data Mining and Machine Learning in Astronomy* (Princeton University Press, 2014).
[303] HESS Collaboration *et al.*, Monthly Notices of the Royal Astronomical Society **446**, 1163 (2015), arXiv:1411.0572 [astro-ph.HE] .
[304] A. Chakraborty *et al.*, Monthly Notices of the Royal Astronomical Society **492**, 2236 (2020), arXiv:2001.02358 [astro-ph.GA] .
[305] C. A. Hales, T. Murphy, J. R. Curran, E. Middelberg, B. M. Gaensler, and R. P. Norris, Monthly Notices of the Royal Astronomical Society **425**, 979 (2012), arXiv:1205.5313 [astro-ph.IM] .
[306] J. J. Condon, W. D. Cotton, E. W. Greisen, Q. F. Yin, R. A. Perley, G. B. Taylor, and J. J. Broderick, The Astronomical Journal **115**, 1693 (1998).
[307] H. T. Intema, P. Jagannathan, K. P. Mooley, and D. A. Frail, Astronomy & Astrophysics **598**, A78 (2017), arXiv:1603.04368 [astro-ph.CO] .
[308] J. Takata, P. H. T. Tam, C. W. Ng, K. L. Li, A. K. H. Kong, C. Y. Hui, and K. S. Cheng, The Astrophysical Journal **836**, 241 (2017).
[309] J. Hahn, in *34th International Cosmic Ray Conference (ICRC2015)*, International Cosmic Ray Conference, Vol. 34 (2015) p. 917.
[310] J. W. Hewitt and F. Yusef-Zadeh, The Astrophysical Journal **694**, L16 (2009).
[311] C. D. Kilpatrick, J. H. Bieging, and G. H. Rieke, The Astrophysical Journal **816**, 1 (2015).
[312] F. Acero *et al.*, The Astrophysical Journal Supplement Series **224**, 8 (2016).
[313] H. Abdalla, A. Abramowski, F. Aharonian, F. Ait Benkhali, E. O. Angüner, M. Arakawa, M. Arrieta, P. Aubert, M. Backes, *et al.*, Astronomy & Astrophysics **612**, A3 (2018).
[314] L. D. Anderson, Y. Wang, S. Bihr, M. Rugel, H. Beuther, F. Bigiel, E. Churchwell, S. C. O. Glover, A. A. Goodman, T. Henning, *et al.*, Astronomy & Astrophysics **605**, A58 (2017).
[315] R. Dokara *et al.*, Astronomy & Astrophysics **651**, A86 (2021), arXiv:2103.06267 [astro-ph.GA] .
[316] H. Yoneda, K. Makishima, T. Enoto, D. Khangulyan, T. Matsumoto, and T. Takahashi, Physical Review Letters **125**, 111103 (2020).
[317] H. Yoneda, D. Khangulyan, T. Enoto, K. Makishima, K. Mine, T. Mizuno, and T. Takahashi, The Astrophysical Journal **917**, 90 (2021).
[318] G. Dubus, N. Guillard, P.-O. Petrucci, and P. Martin, Astronomy & Astrophysics **608**, A59 (2017), arXiv:1707.05744 [astro-ph.HE] .
[319] J. L. Skilton, M. Pandey-Pommier, J. A. Hinton, C. C. Cheung, F. A. Aharonian, J. Brucker, G. Dubus, A. Fiasson, S. Funk, Y. Gallant, A. Marcowith, and O. Reimer, Monthly Notices of the Royal Astronomical Society **399**, 317 (2009), https://academic.oup.com/mnras/article-pdf/399/1/317/3810284/mnras0399-0317.pdf .
[320] P. R. den Hartog, W. Hermsen, L. Kuiper, J. Vink, J. J. M. in't Zand, and W. Collmar, Astronomy & Astrophysics **451**, 587 (2006), arXiv:astro-ph/0601644 [astro-ph] .
[321] J. Wang, G. Fabbiano, G. Risaliti, M. Elvis, M. Karovska, A. Zezas, C. G. Mundell, G. Dumas, and E. Schinnerer, The Astrophysical Journal **729**, 75 (2011).
[322] H.E.S.S. Collaboration *et al.*, Nature **531**, 476 (2016), arXiv:1603.07730 [astro-ph.HE] .
[323] H.E.S.S. Collaboration *et al.*, Astronomy & Astrophysics **612**, A9 (2018), arXiv:1706.04535 [astro-ph.HE] .
[324] MAGIC Collaboration *et al.*, Astronomy & Astrophysics **642**, A190 (2020), arXiv:2006.00623 [astro-ph.HE] .
[325] HAWC Collaboration *et al.*, arXiv e-prints , arXiv:1909.08609 (2019), arXiv:1909.08609 [astro-ph.HE] .

[326] A. A. Abdo *et al.*, The Astrophysical Journal **664**, L91 (2007).

[327] Aharonian *et al.*, Astronomy & Astrophysics **499**, 723 (2009).

[328] B. Bartoli *et al.*, The Astrophysical Journal **760**, 110 (2012), arXiv:1207.6280 [astro-ph.HE] .

[329] E. Aliu *et al.*, The Astrophysical Journal **787**, 166 (2014), arXiv:1404.7185 [astro-ph.HE] .

[330] M. G. Aartsen *et al.*, European Physical Journal C **79**, 234 (2019), arXiv:1811.07979 [hep-ph] .

[331] M. G. Aartsen *et al.*, Physical Review Letters **124**, 051103 (2020), arXiv:1910.08488 [astro-ph.HE] .

[332] A. J. B. Downes, T. Pauls, and C. J. Salter, Astronomy & Astrophysics **92**, 47 (1980).

[333] J. M. Stil, A. R. Taylor, J. M. Dickey, D. W. Kavars, P. G. Martin, T. A. Rothwell, A. I. Boothroyd, F. J. Lockman, and N. M. McClure-Griffiths, The Astronomical Journal **132**, 1158 (2006), arXiv:astro-ph/0605422 [astro-ph] .

[334] J. Yang, J.-L. Zhang, Z.-Y. Cai, D.-R. Lu, and Y.-H. Tan, Chinese Journal of Astronomy and Astrophysics **6**, 210 (2006).

[335] G. L. Case and D. Bhattacharya, The Astrophysical Journal **504**, 761 (1998), arXiv:astro-ph/9807162 [astro-ph] .

[336] A. G. Lyne *et al.*, The Astrophysical Journal **834**, 137 (2017), arXiv:1608.09007 [astro-ph.HE] .

[337] L. Duvidovich, A. Petriella, and E. Giacani, Monthly Notices of the Royal Astronomical Society **491**, 5732 (2020), https://academic.oup.com/mnras/article-pdf/491/4/5732/31614371/stz3414.pdf .

[338] J. Li, R.-Y. Liu, E. de Oña Wilhelmi, D. F. Torres, Q.-C. Liu, M. Kerr, R. Bühler, Y. Su, H.-N. He, and M.-Y. Xiao, The Astrophysical Journal Letters **913**, L33 (2021), arXiv:2102.05615 [astro-ph.HE] .

[339] S. Crestan, A. Giuliani, S. Mereghetti, L. Sidoli, F. Pintore, and N. La Palombara, Monthly Notices of the Royal Astronomical Society **505**, 2309 (2021), arXiv:2105.07001 [astro-ph.HE] .

[340] A. A. Abdo *et al.*, The Astrophysical Journal **711**, 64 (2010), arXiv:1001.0792 [astro-ph.HE] .

[341] S. Abdollahi *et al.*, The Astrophysical Journal: Supplement Series **247**, 33 (2020), arXiv:1902.10045 [astro-ph.HE] .

[342] M. G. Aartsen *et al.*, arXiv e-prints , arXiv:1911.02561 (2019), arXiv:1911.02561 [astro-ph.HE] .

[343] H. Abdalla *et al.*, Astronomy & Astrophysics **612**, A1 (2018), arXiv:1804.02432 [astro-ph.HE] .

[344] N. Galante and VERITAS Collaboration, in *High Energy Gamma-Ray Astronomy: 5th International Meeting on High Energy Gamma-Ray Astronomy*, American Institute of Physics Conference Series, Vol. 1505, edited by F. A. Aharonian, W. Hofmann, and F. M. Rieger (2012) pp. 202–208, arXiv:1210.5480 [astro-ph.HE] .

[345] HAWC Collaboration *et al.*, arXiv e-prints , arXiv:2112.00674 (2021), arXiv:2112.00674 [astro-ph.HE] .

[346] K. Makino, Y. Fujita, K. K. Nobukawa, H. Matsumoto, and Y. Ohira, Publications of the Astronomical Society of Japan **71**, 78 (2019), arXiv:1901.10477 [astro-ph.HE] .

[347] Y. Fujita, Y. Ohira, S. J. Tanaka, and F. Takahara, The Astrophysical Journal: Letters **707**, L179 (2009), arXiv:0911.4482 [astro-ph.HE] .

[348] Y. Ohira, R. Yamazaki, N. Kawanaka, and K. Ioka, Monthly Notices of the Royal Astronomical Society **427**, 91 (2012).

[349] Y. Ohira, K. Murase, and R. Yamazaki, Monthly Notices of the Royal Astronomical Society **410**, 1577 (2011), arXiv:1007.4869 [astro-ph.HE] .

[350] D. G. Wentzel, Annual Review of Astronomy and Astrophysics **12**, 71 (1974).

[351] J. Hahn, PoS **ICRC2015**, 917 (2016).

[352] F. A. Aharonian *et al.*, Nature **432**, 75 (2004), arXiv:astro-ph/0411533 [astro-ph] .

[353] D. Pandel, in *34th International Cosmic Ray Conference (ICRC2015)*, International Cosmic Ray Conference, Vol. 34 (2015) p. 743, arXiv:1512.08140 [astro-ph.HE] .

[354] G. Ghisellini, P. W. Guilbert, and R. Svensson, The Astrophysical Journal: Letters **334**, L5 (1988).

[355] M. G. Baring, D. C. Ellison, S. P.

Reynolds, I. A. Grenier, and P. Goret, The Astrophysical Journal **513**, 311 (1999), arXiv:astro-ph/9810158 [astro-ph] .

[356] J. Martín, D. F. Torres, and N. Rea, Monthly Notices of the Royal Astronomical Society **427**, 415 (2012), arXiv:1209.0300 [astro-ph.HE] .

[357] C. C. Popescu, R. Yang, R. J. Tuffs, G. Natale, M. Rushton, and F. Aharonian, Monthly Notices of the Royal Astronomical Society **470**, 2539 (2017), https://academic.oup.com/mnras/article-pdf/470/3/2539/18245516/stx1282.pdf .

[358] R. Yamazaki, K. Kohri, A. Bamba, T. Yoshida, T. Tsuribe, and F. Takahara, Monthly Notices of the Royal Astronomical Society **371**, 1975 (2006), arXiv:astro-ph/0601704 [astro-ph] .

[359] A. U. Abeysekara *et al.*, arXiv e-prints , arXiv:1909.08609 (2019), arXiv:1909.08609 [astro-ph.HE] .

[360] M. C. Gonzalez-Garcia, F. Halzen, and S. Mohapatra, Astroparticle Physics **31**, 437 (2009), arXiv:0902.1176 [astro-ph.HE] .

[361] F. Halzen, A. Kheirandish, and V. Niro, Astroparticle Physics **86**, 46 (2017).

[362] A. U. Abeysekara *et al.*, Physical Review Letters **124**, 021102 (2020), arXiv:1909.08609 [astro-ph.HE] .

[363] M. Amenomori *et al.*, Physical Review Letters **123**, 051101 (2019), arXiv:1906.05521 [astro-ph.HE] .

[364] M. Amenomori *et al.*, Physical Review Letters **126**, 141101 (2021), arXiv:2104.05181 [astro-ph.HE] .

[365] Cherenkov Telescope Array Consortium, *Science with the Cherenkov Telescope Array* (2019).

[366] A. Albert *et al.*, arXiv e-prints , arXiv:1902.08429 (2019), arXiv:1902.08429 [astro-ph.HE] .

[367] Z. Cao, Chinese Physics C **34**, 249 (2010).

[368] R. Kothes, B. Uyaniker, and S. Pineault, The Astrophysical Journal **560**, 236 (2001).

[369] J. P. Halpern, F. Camilo, E. V. Gotthelf, D. J. Helfand, M. Kramer, A. G. Lyne, K. M. Leighly, and M. Eracleous, The Astrophysical Journal Letters **552**, L125 (2001), arXiv:astro-ph/0104109 [astro-ph] .

[370] A. A. Abdo *et al.*, The Astrophysical Journal **706**, 1331 (2009), arXiv:0910.2249 [astro-ph.HE] .

[371] V. A. Acciari *et al.*, The Astrophysical Journal Letters **703**, L6 (2009), arXiv:0911.4695 [astro-ph.HE] .

[372] Y. Xin, H. Zeng, S. Liu, Y. Fan, and D. Wei, The Astrophysical Journal **885**, 162 (2019), arXiv:1907.04972 [astro-ph.HE] .

[373] Y. Fujita, A. Bamba, K. K. Nobukawa, and H. Matsumoto, The Astrophysical Journal **912**, 133 (2021).

[374] S. Pineault and G. Joncas, The Astronomical Journal **120**, 3218 (2000).

[375] J. C. Joshi, S. J. Tanaka, L. S. Miranda, and S. Razzaque, arXiv e-prints , arXiv:2205.00521 (2022), arXiv:2205.00521 [astro-ph.HE] .

[376] H. Yu, K. Wu, L. Wen, and J. Fang, New Astronomy **90**, 101669 (2022).

[377] M. Breuhaus, B. Reville, and J. A. Hinton, Astronomy & Astrophysics **660**, A8 (2022), arXiv:2109.05296 [astro-ph.HE] .

[378] J. Martín, D. F. Torres, and G. Pedaletti, Monthly Notices of the Royal Astronomical Society **459**, 3868 (2016), arXiv:1603.09328 [astro-ph.HE] .

[379] D. F. Torres, A. Cillis, J. Martín, and E. de Oña Wilhelmi, Journal of High Energy Astrophysics **1**, 31 (2014), arXiv:1402.5485 [astro-ph.HE] .

[380] D. F. Torres and T. Lin, The Astrophysical Journal Letters **864**, L2 (2018), arXiv:1808.10613 [astro-ph.HE] .

[381] D. F. Torres, A. N. Cillis, and J. M. Rodriguez, The Astrophysical Journal Letters **763**, L4 (2012).

[382] D. F. Torres, The Astrophysical Journal **835**, 54 (2017), arXiv:1612.02835 [astro-ph.HE] .

[383] R. Bandiera, N. Bucciantini, J. Martín, B. Olmi, and D. F. Torres, Monthly Notices of the Royal Astronomical Society **499**, 2051 (2020), arXiv:2009.10992 [astro-ph.HE] .

[384] R. Bandiera, N. Bucciantini, J. Martín, B. Olmi, and D. F. Torres, Submitted to MNRAS (2022).

[385] R. N. Manchester and J. H. Taylor, (1977).

[386] F. C. Michel, The Astrophysical Journal **158**, 727 (1969).

[387] R. N. Manchester, J. M. Durdin, and L. M. Newton, Nature **313**, 374 (1985).

[388] R. F. Archibald, E. V. Gotthelf, R. D. Ferdman, V. M. Kaspi, S. Guillot, F. A. Harrison, E. F. Keane, M. J. Pivovaroff, D. Stern, S. P. Tendulkar, and J. A. Tomsick, The Astrophysical Journal Letters **819**, L16 (2016), arXiv:1603.00305 [astro-ph.HE] .

[389] C. M. Espinoza, A. G. Lyne, B. W. Stappers, and M. Kramer, Monthly Notices of the Royal Astronomical Society **414**, 1679 (2011), https://academic.oup.com/mnras/article-pdf/414/2/1679/3015039/mnras0414-1679.pdf .

[390] J. A. Pons, D. Viganò, and U. Geppert, Astronomy & Astrophysics **547**, A9 (2012), arXiv:1209.2273 [astro-ph.SR] .

[391] C. M. Espinoza, A. G. Lyne, M. Kramer, R. N. Manchester, and V. M. Kaspi, The Astrophysical Journal Letters **741**, L13 (2011), arXiv:1109.2740 [astro-ph.HE] .

[392] A. A. Abdo *et al.*, The Astrophysical Journal Letters **700**, L127 (2009), arXiv:0904.1018 [astro-ph.HE] .

[393] R. A. Chevalier and C. Fransson, The Astrophysical Journal **395**, 540 (1992).

[394] J. M. Blondin, R. A. Chevalier, and D. M. Frierson, The Astrophysical Journal **563**, 806 (2001), arXiv:astro-ph/0107076 [astro-ph] .

[395] J. D. Gelfand, P. O. Slane, and W. Zhang, The Astrophysical Journal **703**, 2051 (2009), arXiv:0904.4053 [astro-ph.HE] .

[396] T. A. Porter, I. V. Moskalenko, and A. W. Strong, The Astrophysical Journal **648**, L29 (2006).

[397] M. Breuhaus, J. Hahn, C. Romoli, B. Reville, G. Giacinti, R. Tuffs, and J. A. Hinton, The Astrophysical Journal Letters **908**, L49 (2021), arXiv:2010.13960 [astro-ph.HE] .

[398] O. C. de Jager, A. K. Harding, P. F. Michelson, H. I. Nel, P. L. Nolan, P. Sreekumar, and D. J. Thompson, The Astrophysical Journal **457**, 253 (1996).

[399] O. C. de Jager and A. Djannati-Ataï, in *Astrophysics and Space Science Library*, Astrophysics and Space Science Library, Vol. 357, edited by W. Becker (2009) p. 451, arXiv:0803.0116 [astro-ph] .

[400] J. Martin and D. F. Torres, Journal of High Energy Astrophysics, in press , arXiv:2209.12397 (2022), arXiv:2209.12397 [astro-ph.HE] .

[401] E. de Oña Wilhelmi, R. López-Coto, E. Amato, and F. Aharonian, The Astrophysical Journal Letters **930**, L2 (2022), arXiv:2204.09440 [astro-ph.HE] .

[402] J. P. Halpern, E. V. Gotthelf, K. M. Leighly, and D. J. Helfand, The Astrophysical Journal **547**, 323 (2001).

[403] R. Jansson and G. R. Farrar, The Astrophysical Journal **757**, 14 (2012), arXiv:1204.3662 [astro-ph.GA] .

[404] K. Murase, C. D. Dermer, H. Takami, and G. Migliori, The Astrophysical Journal **749**, 63 (2012).

[405] S. Razzaque, C. D. Dermer, and J. D. Finke, The Astrophysical Journal **745**, 196 (2012).

[406] D. F. Torres and L. A. Anchordoqui, arXiv e-prints , astro-ph/0505283 (2005), arXiv:astro-ph/0505283 [astro-ph] .

[407] L. A. Anchordoqui and D. F. Torres, Physical Review D **102**, 023034 (2020), arXiv:2004.09378 [astro-ph.GA] .

[408] G. E. Romero and D. F. Torres, The Astrophysical Journal Letters **586**, L33 (2003), arXiv:astro-ph/0302149 [astro-ph] .

[409] E. Peretti, P. Blasi, F. Aharonian, and G. Morlino, Monthly Notices of the Royal Astronomical Society **487**, 168 (2019), arXiv:1812.01996 [astro-ph.HE] .

[410] G. R. Farrar and T. Piran, arXiv e-prints , arXiv:1411.0704 (2014), arXiv:1411.0704 [astro-ph.HE] .

[411] R. Alves Batista and J. Silk, Physical Review D **96**, 103003 (2017), arXiv:1702.06978 [astro-ph.HE] .

[412] D. Biehl, D. Boncioli, A. Fedynitch, L. Morejon, and W. Winter, in *European Physical Journal Web of Conferences*, European Physical Journal Web of Conferences, Vol. 208 (2019) p. 04002, arXiv:1809.10259 [astro-ph.HE] .

[413] C. Guépin, K. Kotera, E. Barausse, K. Fang, and K. Murase, Astronomy & Astrophysics **616**, A179 (2018), arXiv:1711.11274 [astro-ph.HE] .

[414] K. Murase and S. Nagataki, Phys. Rev. Lett. **97**, 051101 (2006).

[415] C. D. Dermer and S. Razzaque, The Astrophysical Journal **724**, 1366 (2010).

[416] N. Gupta and B. Zhang, Monthly Notices of the Royal Astronomical Society **380**, 78 (2007), https://academic.oup.com/mnras/article-pdf/380/1/78/4146342/mnras0380-0078.pdf .

[417] P. Baerwald, M. Bustamante, and W. Winter, The Astrophysical Journal **768**, 186 (2013).

[418] N. Globus, D. Allard, R. Mochkovitch, and E. Parizot, Monthly Notices of the Royal Astronomical Society **451**, 751 (2015), arXiv:1409.1271 [astro-ph.HE] .

[419] A. De Sarkar, A. J. Nayana, N. Roy, S. Razzaque, and G. C. Anupama, The Astrophysical Journal **951**, 62 (2023), arXiv:2305.10735 [astro-ph.HE] .

[420] A. De Sarkar and P. Majumdar, arXiv e-prints , arXiv:2309.04729 (2023), arXiv:2309.04729 [astro-ph.HE] .

[421] S. Aiello *et al.*, Astroparticle Physics **111**, 100 (2019).

[422] A. De Sarkar, Monthly Notices of the Royal Astronomical Society **521**, L5 (2023), arXiv:2301.13451 [astro-ph.HE] .